MAPPING REGIONAL DISTRIBUTIONS OF ENERGY BALANCE COMPONENTS USING OPTICAL REMOTELY SENSED IMAGERY

by
Sung-ho Hong

Advisor: Jan M.H. Hendrickx

Submitted in partial fulfillment
of the requirement for the degree of
PhD in Hydrology

March, 2008

New Mexico Institute of Mining and Technology
Department of Earth and Environmental Science
Socorro, New Mexico

ABSTRACT

Precise spatio-temporal distributions of surface energy balance components in arid/semiarid riparian areas are critical information for sustainable management of water resources as well as for a better understanding of water and heat exchange processes between the land surface and the atmosphere. However the distributions of surface fluxes over large areas are difficult to obtain from ground measurements alone. Therefore their prediction from remote-sensing data is very attractive since it enables large area coverage with a high repetition frequency.

In this study, a remote-sensing image processing algorithm, the Surface Energy Balance Algorithms for Land (SEBAL), was selected to estimate the energy balance components in the arid/semi-arid riparian areas in the southwestern United States. The main objective of this study is to investigate the potential and limitations of remote sensing for the assessment of spatio-temporal distributions of surface energy balance components using optical imagery from Landsat and MODIS satellites. This study first compares instantaneous and daily SEBAL fluxes derived from Landsat 7 imagery to surface-based measurements with eddy covariance flux towers; then it investigates how up- and down-scaling affect the SEBAL-derived maps of evapotranspiration.

For the up-scaling study, "output" and "input" up-scaling procedures were conducted in which aggregation was accomplished by both simple averaging and nearest neighboring resampling techniques. For the down-scaling study, also input and output down-scaling procedures were evaluated in which disaggregated maps were obtained by two different processes: subtraction and regression.

SEBAL yields accurate estimates of energy balance components in riparian areas in the southwestern United States using both Landsat 7 and MODIS images. The up- and down-scaling schemes proposed in this study generate evapotranspiration maps having a good agreement with maps directly derived from Landsat (30 m) and MODIS (250 m) satellites.

ACKNOWLEDGEMENT

First al all, I sincerely owe my loving thanks to my wife Youna Lee, daughter Hee-jue and son Jung-woo. Without their encouragement, patience and understanding it would have been impossible for me to complete this research and study. Also my sincere gratitude is due to my parents (Jai-yun and Kyoung-ja), parents-in-law (Hung-chu and Hyo-sik), sister, brother-in-law and their families for their patient and endless support. They have always believed in me and given me courage to continue.

I am deeply indebted to my supervisor Prof. Dr. Jan Hendrickx for his tremendous support, stimulating suggestions and encouragement during the research for and writing of this dissertation. It was a really great experience working under his direction during my whole degree program.

I warmly thank my other PhD committee members, Dr. Rick Allen, University of Idaho, Dr. Brian Borchers, Dr. Enrique Vivoni and Dr. Rob Bowman for their support throughout my study period. I appreciate their interest in my topic and I thank them for all valuable advice, thoughtful comments and helpful suggestions.

TABLE OF CONTENTS

CHAPTER 3

SURFACE ENERGY BALANCE ALGORITHM FOR LAND (SEBAL)

CHAPTER 4

EVALUTION OF AN EXTREME-CONDITION-INVERSE-CALIBRATION REMOTE SENSING MODEL FOR MAPPING ENERGY BALANCE FLUXES IN ARID RIPARIAN AREAS

CHAPTER 5

UP-SCALING OF SEBAL DERIVED EVAPOTRANSPIRATION MAPS FROM LANDSAT (30M) TO MODIS (250M) SCALE

CHAPTER 6

DOWN-SCALING OF SEBAL DERIVED EVAPOTRANSPIRATION MAPS FROM MODIS (250M) TO LANDSAT (30M) SCALE

CHAPTER 7

SUMMARY, CONCLUSIONS AND RECOMMENDATIONS

LIST OF TABLES

LIST OF FIGURES

LIST OF SYMBOLS AND NOTATIONS

Symbol	Definition	Units
B	radiation emitted from the body	Wm^{-2}
c	speed of light	ms^{-1}
C_n^2	refractive index of air	$m^{-2/3}$
C_P	specific heat capacity of air	$Jkg^{-1}K^{-1}$
C_Q^2	refractive index of humidity	$(gm^{-3})^2 m^{-2/3}$
C_T^2	refractive index of temperature	$K^2 m^{-2/3}$
C_{wind}	wind speed correction coefficient for mountainous region	-
C_{zom}	surface roughness correction coefficient for sloping surfaces	-
d	zero displacement plane	m
D	aperture diameter of the scintillometer	m
DN	digital number	-
DOY	day of year (Julian day)	-
d_r	inverse squared relative distance of the Earth-sun	-
dT	near surface air temperature difference	K
EF	evaporative fraction	-
$ESUN_\lambda$	mean solar exoatmospheric irradiance for band λ	$Wm^2 \mu m^{-1}$
ET	evapotranspiration	mmd^{-1}
ET_r	reference evapotranspiration	mmd^{-1}
ETM+	enhanced thematic mapper	
$f_c(\phi)$	apparent fractional coverage viewed as seen by the radiometer	-
f_g	fraction of green vegetation	-
g	gravitational acceleration	ms^{-2}
G	ground heat flux	Wm^{-2}
G_{sc}	solar constant	Wm^{-2}
h	crop height	m
H	sensible heat flux	Wm^{-2}
I	irrigation rate	mmh^{-1}
k	von Karman's constant	-
K	propagation wave number	m^{-1}
K_H	eddy diffusivities of heat	$m^2 s^{-1}$
K_V	eddy diffusivities of water vapor	$m^2 s^{-1}$
K_{TS}	thermal conductivity of the soil	$Jm^{-1}s^{-1}K^{-1}$
L	Monin-Obukhov length	m
L	distance between the transmitter and the receiver or the path length	m
LAI	leaf area index	-
LE	latent heat flux	Wm^{-2}
L_m	longitude of the measurement site	degree
L_z	longitude of the center of the local time zone	degree
L_λ	at-satellite spectral radiance of the band λ	$Wm^{-2}ster^{-1}\mu m^{-1}$
NDVI	normalized difference vegetation index	-
P	precipitation rate	mmh^{-1}
P	energy consumed by photosynthesis	Wm^{-2}
P	pressure	Nm^{-2}
Q	humidity	gm^{-3}
q*	scalar scales for humidity	gg^{-1}

r_a	aerodynamic resistance	sm^{-1}
r_{ah}	aerodynamic resistance for heat transport	sm^{-1}
r_{ex}	extra resistance	sm^{-1}
r_s	surface resistance	sm^{-1}
R	surface runoff rate	mmh^{-1}
R_a	extraterrestrial solar radiation	Wm^{-2}
$R_L\downarrow$	incoming longwave radiation	Wm^{-2}
$R_L\uparrow$	outgoing longwave radiation	Wm^{-2}
R_n	net radiation	Wm^{-2}
R_{nl}	net longwave radiation	Wm^{-2}
R_{ns}	net shortwave radiation	Wm^{-2}
$R_s\downarrow$	incoming shortwave radiation	Wm^{-2}
$R_s\uparrow$	outgoing shortwave radiation	Wm^{-2}
s	surface slope	radian
S	storage of heat in air and plant biomass	Wm^{-2}
S_c	seasonal correction for solar time	hour
ΔS	change in storage rate	mmh^{-1}
T	standard local time	hour
T	temperature	K
T_a	air temperature	K
T_b	brightness temperature	K
T_c	canopy temperature	K
T_s	surface temperature	K
T_{s_cold}	surface temperature at a reference point (cold pixel)	K
T_{aero}	aerodynamic surface temperature	K
TM	thematic mapper	
T_{rad}	radiometric surface temperature	K
T_{ref}	near surface air temperature at a reference point	K
T_s	surface temperature	K
T_{sdem}	DEM adjusted surface temperature	K
u	wind speed	ms^{-1}
u*	friction velocity	ms^{-1}
u_{200}	wind speed at a "blending" height of 200m	ms^{-1}
$u_{200\_adjusted}$	adjusted wind speed at a "blending" height of 200m	ms^{-1}
W	capillary rise rate	mmh^{-1}
W_λ	weighting coefficient for band λ	-
x	parameter for calculation of Monin-Obukhov length	-
z	height	m
z_{oh}	surface roughness for heat transport	m
z_{0m}	surface roughness for momentum transport	m
Γ'	proportional factor for G/R$_n$ ratio	-
Γ''	extinction factor for G/R$_n$ ratio	-
Ψ_h	stability correction factor for heat transfer	-
Ψ_m	stability correction factor for momentum transfer	-
Ψ_c	stability correction factor for vapor transfer	-
α	surface albedo	-
$\alpha_{path\ radiance}$	albedo path radiance	-
α_{PT}	Priestley-Taylor parameter	-
α_{toa}	albedo at the top of the atmosphere	-
β	Bowen ratio	-
e_a	atmospheric emissivity	-
e_o	surface emissivity	-
ϕ	solar declination	radian
γ	surface aspect	radian
γ	psychrometric constant	kPaK^{-1}

φ	latitude	degree
λ	latent heat of vaporization	Jkg^{-1}
λ	wavelength	μm
Δ	slope of the saturation vapor pressure-temperature curve	-
θ	solar incident angle	radian
θ	volumetric soil water content	-
θ^*	scalar scales for temperature	K
ρ_a	air density	kgm^{-3}
ρ_λ	reflectance of band λ	-
σ	Stefan-Boltzmann constant	$Wm^{-2}K^{-4}$
τ_{sw}	one-way shortwave transmittance of air	-
ω	hour angle of the sun	radian
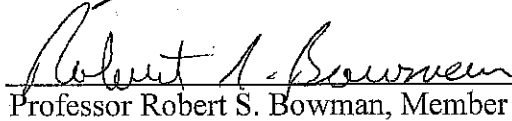
This dissertation is accepted on behalf of the
faculty of the Institute by the following committee.

_____   May 1, 2008
Professor Jan M.H. Hendrickx, Advisor   Date
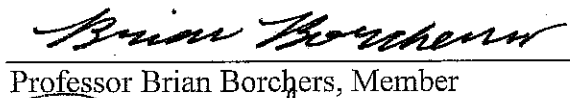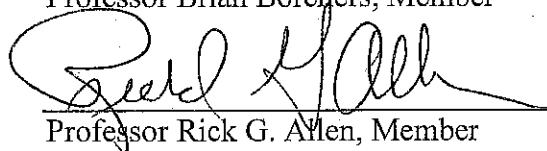
_____
Professor Robert S. Bowman, Member

_____
Professor Enrique R. Vivoni, Member
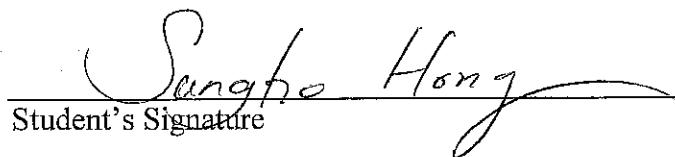
_____
Professor Brian Borchers, Member

_____
Professor Rick G. Allen, Member

I release this document to the New Mexico Institute of Mining and Technology.

_____   May 1, 2008
Student's Signature   Date

CHAPTER 1

INTRODUCTION

Evapotranspiration (ET) is defined as the total amount of water that is transferred from the earth's surface to the atmosphere by evaporation and transpiration. Evaporation occurs at the surfaces of soils, plant leaves and water bodies when water evaporates directly into the atmosphere. Soil surfaces become wet after rain or irrigation or as a result of capillary rise when ground water tables are shallow, while plant leaves intercept water during rain and sprinkler irrigation. Transpiration refers to the transport of water vapor into the atmosphere after liquid water has evaporated through the stomata of plant leaves. Vapor transport through the stomata is determined by a slow diffusion process and plant physiological conditions regulated by air temperature, soil moisture status, vapor pressure deficit, and solar radiation. Under extreme circumstances of heat or solar radiation, plants may reduce –or even close entirely– the stomatal opening and, thus, interfere in an active manner with transpiration.

ET is an important component of the earth's hydrologic budget. For example, in the United States about 65 % of the precipitation received is returned to the atmosphere

through ET in the Northwest and Northeast regions and in the Southwest region ET represents nearly all the soil and surface water loss, where runoff is minimal (Nemani and Running, 1989; Hanson, 1991). Accurate monitoring and mapping of ET is important for society since it allows decision makers and stakeholders (i) to follow where, when, and how much water has moved into the atmosphere by evaporation; (ii) to monitor crop performance and the effects of droughts for famine prediction; (iii) to better evaluate the performance of irrigation systems; and (iv) to enhance weather predictions and increase our understanding of climate change. However, ET is a complex function of soil properties, atmospheric conditions, land use, vegetation, and topography which causes ET to vary in both space and time (Allen et al., 1996). Therefore, it is difficult to estimate or representatively measure ET at the regional scale (Bastiaanssen, 1995; Parlange et al., 1995).

Measurement approaches for ET from the land surface, including eddy covariance (e.g. Kizer and Elliott, 1991), Bowen ratio (e.g. Scott et al., 2000) and weighing lysimeters (e.g. Wright, 1982), are too expensive and time consuming for continuous application at sufficient spatial density at the regional scale. These techniques produce ET measurements over small footprints (m^2 to ha) which are difficult to extrapolate to the regional scale, especially over heterogeneous land surfaces (Moran and Jackson, 1991). For example, in the heterogeneous landscape of the central plateau of Spain as many as 13 ground measurements of ET in a relatively small area of 5000 km^2 were not sufficient to predict accurately the area-averaged ET rate (Pelgrum and Bastiaanssen, 1996).

Since larger scale estimates of ET require alternative measurement and estimation approaches, the potential of satellite image-based remote sensing for examining spatial patterns or regional estimates of sensible (H) and latent (LE) heat fluxes has been pursued by a number of investigators (Choudhury, 1989; Moran and Jackson, 1991; Menenti et al., 1993; Kustas and Norman, 1996; Mecikalski et al., 1999; Granger, 2000; Caparinni and Castelli, 2002; Nishida et al., 2003; Bastiaanssen et al., 2005; Allen et al., 2007). These efforts have resulted in the development of remote sensing algorithms that are quite different in their spatial and temporal scales: 30 m to 1/8th degree (about 13 km in New Mexico) and daily to monthly. Operational algorithms that have produced H and LE maps on local, regional, or national scales are: the North American Land Data Assimilation Systems (NLDAS) (Cosgrove et al., 2003), the Land Information Systems (LIS) (Peters Lidard et al., 2004), the Atmosphere-Land Exchange Inverse (ALEXI) (Norman et al., 1995; Anderson et al., 1997), the disaggregated ALEXI model (DisALEXI) (Kustas et al., 2003; Norman et al., 2003), the Surface Energy Balance System (SEBS) (Su, 2002; Jia et al., 2003; Han and Yang, 2004), the Surface Energy Balance Algorithm for Land (SEBAL) (Bastiaanssen et al., 1998; Bastiaanssen et al., 2005), Mapping EvapoTranspiration at high spatial Resolution with Internalized Calibration (METRIC) (Allen et al., 2005; Allen et al., 2007), as well as algorithms without distinct acronyms (Moran et al., 1989; Jiang and Islam, 2001; Ma et al., 2006; Schüttemeyer et al., 2007).

SEBAL has been developed and pioneered by Bastiaanssen and his colleagues in The Netherlands during the 1990s (Bastiaanssen, 1995; Bastiaanssen et al., 1997; Bastiaanssen et al., 2001; Bastiaanssen et al., 2005). METRIC has been developed by

Allen and his research team in Idaho using SEBAL as its foundation (Allen et al., 2005; Allen et al., 2007). Unlike ALEXI and DisALEXI, SEBAL and METRIC do not require spatial fields of air temperature and atmospheric temperature soundings interpolated across the region of interest. However, applications of SEBAL and METRIC are restricted to clear days over areas of uniform weather condition, preventing application at the continental scale such as done by ALEXI, DisALEXI, NLDAS and LIS.

SEBAL and METRIC calculate the energy balance from extreme thermal and vegetation conditions within an image using a "cold (wet)" and "hot (dry)" pixel. These procedures index H from the land surface (one of the major energy balance components) to satellite measured surface temperatures at specific surface boundary conditions. The main difference between SEBAL and METRIC is that the latter makes use of the reference evapotranspiration (ET_r) calculated using high-quality ground measurements from weather stations (Allen et al., 2005) while the former can be applied without using ground measurements. Since many areas of the world have no adequate ground measurements there is a need for algorithms such as SEBAL. On the other hand, METRIC allows assimilation of ground measurements which can improve the quality of the H and LE maps. The SEBAL approach has demonstrated a high accuracy for evapotranspiration mapping worldwide with typical accuracies of about ±15 % and ±5 % for, respectively, daily and seasonal ET estimates (Bastiaanssen et al., 2005). Validation of METRIC evapotranspiration in Idaho using precision lysimeter measurements (considered the best standard) has shown METRIC evaporation estimates to be within

±10% at the sub-field scale for daily, monthly and annual time scales (Morse et al., 2000; Tasumi et al., 2000; Allen et al., 2003).

In this dissertation I have selected SEBAL to estimate ET over arid riparian areas for the following reasons: (i) SEBAL consists of physically-based image analysis algorithms using standard satellite imagery and requires a minimum of ancillary meteorological information from surface measurements or atmospheric models; (ii) SEBAL deals with a large number of environmental variables and does not assume variables to be constant over space as do many other methods. For example, some methods assume all variables besides surface and air temperatures to be spatially constant (Jackson et al., 1977; Seguin and Itier, 1983); (iii) In SEBAL, the need for atmospheric correction of short-wave and thermal information in images is reduced (Tasumi, 2003) because SEBAL H and LE estimates depend only on radiometric temperature differences in the scene rather than on the absolute value of the surface temperature. This greatly enhances the applicability of SEBAL since the measurements needed for atmospheric corrections are often not available (Allen et al., 2007); (iv) SEBAL uses Landsat images with high spatial resolution which allows it to capture the small scale spatial heterogeneity that is typical for riparian areas in the southwestern United States.

Previous validation studies have mainly been conducted in relatively homogeneous agricultural areas and have focused on comparison of daily ET rates estimated from SEBAL and METRIC with ground measurements using lysimeters (Trezza, 2002; Tasumi, 2003), Bowen ratio and eddy covariance methods (Bastiaanssen

et al., 2002; Droogers and Bastiaanssen, 2002). The overall goal of this study is to conduct a thorough evaluation of the performance of SEBAL in semi-arid riparian areas with a focus on the Middle Rio Grande Valley where vast deserts are transected by narrow river valleys covered by a mosaic of agricultural fields (mostly alfalfa) and riparian vegetation (cottonwood, saltcedar, russian willow and salt grasses) which creates a heterogeneous landscape with a short patch length scale. If SEBAL performs well under these challenging conditions, it provides a possibility to perform well in other arid and semi-arid regions of the world. Another difference with previous studies is my focus on all components of the energy balance during the instant of satellite overpass as well as on a daily basis. I can accomplish this since there is a quality controlled data set consisting of R_n, G, H and LE measurements in the riparian areas of the Middle Rio Grande Basin (New Mexico), San Pedro River Valley (Arizona) and the Owens River Valley (California).

Another important goal of this dissertation is to evaluate up- and down-scaling procedures of ET maps generated from Landsat images (spatial resolution 30, temporal resolution 16 days) and from MODIS images (spatial scale 250 m, temporal resolution daily). The methodology for aggregating simple rectangular grid data is well developed (Bian, 1997; Bian et al., 1999; Mengelkamp et al., 2006). In this dissertation, simple averaging and nearest neighbor methods were selected for the data aggregation scheme, since these methods have been the most popular and convenient to use (Atkinson, 1985; Liang, 2004). The simple averaging method calculates the average value over an area of interest to produce a new coarser resolution data set. Nearest neighbor sampling produces

a subset of the original data; the extremes and subtleties of the data values are therefore preserved.

Numerous studies have used the assumption that large-scale surface fluxes can be expressed as direct area averages of small-scale surface fluxes (Shuttleworth, 1991; Lhomme, 1992; Li and Avissar, 1994). Liang (2000) simply averaged the remotely sensed reflectance values from 30 m to 1 km and explored the aggregation effect. He concluded that the spectral reflectance was basically linear from 30 m resolution to 1000 m resolution. More recently, Mengelkamp et al. (2006) mentioned that area-averaged small-scale ET calculated from local measurements was in good agreement with the area-represented regional values. Nevertheless, few papers have examined the effect of different up-scaling schemes on the relative accuracy of the aggregated data despite its practical importance.

A spatial resolution gap exists between the data requirements of regional-scale models and the output data from remote sensing energy balance algorithms such as SEBAL. For example, general circulation models or regional weather prediction models need input data with a spatial resolution of hundreds of kilometers which is much larger than the spatial resolution of most satellite sensors (Liang, 2004). Therefore, an up-scaling (data aggregation) procedure is needed to fill the scale gap between satellite measurements and input requirements for large scale models. Increasing spatial resolution by data aggregation has shown the potential to generate observed or modeled

surface flux estimates over a range of different spatial resolutions (Gupta et al., 1986; Lhomme, 1992; Ebleringer and Field, 1993).

In this dissertation, high quality scenes of two different dates of Landsat 7 Enhanced Thematic Mapper Plus (ETM+) and Moderate Resolution Imaging Spectroradiometer (MODIS) imagery were selected and SEBAL was applied to estimate daily ET. Landsat-scale pixels (30 m) were aggregated to larger scale (60, 120, 250, 500 and 1000 m). The objectives of this study were first to test the consistency of the SEBAL algorithm for Landsat 7 and MODIS images, and second to investigate the effects of four different up-scaling processes on the spatial distribution of ET, especially how the relative accuracy of ET changes with different up-scaling processes.

Down-scaling is defined as an increase in spatial resolution following disaggregation of the original data set (Bierkens et al., 2000; Liang, 2004). The process of down-scaling accomplishes a restoration of the variation at a specific scale by assuming that the values of the larger scale are the average of the values at the finer scale and that more uncertainties exist in down-scaled products than up-scaled products because infinite solutions of down-scaled products are possible (Bierkens et al., 2000). Down-scaling is generally required for the use of available information at a desired fine resolution (Price et al., 2000; Maayar and Chen, 2006). Traditionally, various down-scaling procedures have been tested in the fields of meteorology and climatology to obtain local climatological information from coarse-resolution remote sensing imagery, but only a

few studies have applied disaggregation schemes to surface parameters to increase resolution (Liang, 2004).

In this study, high quality Landsat 7 and MODIS images were selected to test various down-scaling procedures. Disaggregated daily ET rates from MODIS imagery were compared with the ET rates derived from Landsat imagery. SEBAL-estimated daily ET from Landsat imagery was validated against ground-based eddy covariance measurements in previous research, demonstrating very good agreement (Hendrickx and Hong, 2005). The primary objective of this research was to investigate the effect of various relatively simple down-scaling schemes on the spatial distribution of the SEBAL-derived daily ET rate, especially how the relative accuracy of ET changes with increasing spatial resolution. In Chapter 6, I provide a brief review of some existing down-scaling procedures.

This dissertation consists of seven chapters of which chapters 4, 5, and 6 are prepared as journal publications that stand by themselves. As a consequence some overlap and repetition occurs between the different chapters. Chapter 2 presents a literature review of different ground based and remote sensing methods for the measurement and evaluation of ET. Chapter 3 describes SEBAL with great detail for application with Landsat and MODIS images over flat and mountainous terrain. Chapters 4, 5, and 6 are three journal publications dealing with, respectively, the evaluation of SEBAL versus ground measurements, up-scaling of ET maps from Landsat to MODIS scale, and down-scaling ET maps from MODIS to Landsat scales. The final chapter 7

summarizes conclusions and makes recommendations for further research.

REFERENCES

Allen, R.G., W.O. Pruitt, J.A. Businger, L.J. Fritschen, M.E. Jensen, and F.H. Quinn. 1996. Chapter 4: Evaporation and Transpiration. American Society of Civil Engineering, NY.

Allen, R.G., A. Morse, and M. Tasumi. 2003. Application of SEBAL for western US water rights regulation and planning Proceedings of the International Workshop on Remote Sensing of Crop Evapotranspiration for Large Regions. 54th IEC Meeting of the International Commission on Irrigation and Drainage (ICID), Montpellier, France.

Allen, R.G., M. Tasumi, and R. Trezza. 2005. M E T R I C^{tm} Mapping Evapotranspiration at High Resolution. Applications Manual for Landsat Satellite Imagery. Version 2.0. University of Idaho, Kimberly, Idaho.

Allen, R.G., M. Tasumi, and R. Trezza. 2007. Satellite-based Energy Balance for Mapping Evapotranspiration with Internalized Calibration (METRIC) – Model. Journal of Irrigation and Drainage Engineering 133:380-394.

Anderson, M.C., J.M. Norman, G.R. Diak, W.P. Kustas, and J.R. Mecikalski. 1997. A two-source time-integrated model for estimating surface fluxes using thermal infrared remote sensing. Remote Sensing of Environment 60:195-216.

Atkinson, P.M. 1985. Preliminary Results of the Effect of Resampling on Thematic Mapper Imagery. ACSM-ASPRS Fall Convention Technical Papers:929-936.

Bastiaanssen, W.G.M. 1995. Regionalization of surface flux densities and moisture indicators in composite terrain, Wageningen Agricultural University, Wageningen, Netherlands.

Bastiaanssen, W.G.M., H. Pelgrum, P. Droogers, H.A.R. De Bruin, and M. Menenti. 1997. Area-average estimates of evaporation, wetness indicators and top soil moisture during two golden days in EFEDA. Agricultural and Forest Meteorology 87:119-137.

Bastiaanssen, W.G.M., M. Menenti, R.A. Feddes, and A.A.M. Holtslag. 1998. A remote sensing surface energy balance algorithm for land (SEBAL). Part 1: Formulation. Journal of Hydrology 212-213:198-212.

Bastiaanssen, W.G.M., R.A.L. Brito, M.G. Bos, R.A. Souza, E.B. Cavalanti, and M. Bakker. 2001. Low cost satellite data for monthly irrigation performance monitoring: benchmarks from Nilo Coelho, Brazil. Irrigation and Drainage Systems 15:53-79.

Bastiaanssen, W.G.M., M.-D. Ahmad, and Y. Chemin. 2002. Satellite surveillance of evaporative depletion across the Indus Basin. Water Resources Research 38:1273, doi:10.1029/2001WR000386.

Bastiaanssen, W.G.M., E.J.M. Noordman, H. Pelgrum, G. Davids, B.P. Thoreson, and R.G. Allen. 2005. SEBAL model with remotely sensed data to improve water-resources management under actual field conditions. Journal of Irrigation and Drainage Engineering 131:85-93.

Bian, L. 1997. Multiscale nature of spatial data in scaling up environment models CRC Press, Inc.

Bian, L., R. Butler, D.A. Quattrochi, and P.M. Atkinson. 1999. Comparing effects of aggregation methods on statistical and spatial properties of simulated spatial data. Photogrammetry and Remote Sensing 65:73-84.

Bierkens, M.F.P., P.A. Finke, and D.E. Willigen. 2000. Upscaling and downscaling methods for environmental research. Wageningen University and Research Centre, Kluwer Academic Publishers.

Caparinni, F., and F. Castelli. 2002. Remote sensing used to estimate land surface evaporation. EOS Transactions 83:290-291.

Choudhury, B.J. 1989. Estimating evaporation and carbon assimilation using infrared temperature data: vistas in modeling Wiley, New York.

Cosgrove, B.A., D. Lohmann, K.E. Mitchell, P.R. Houser, E.F. Wood, J. Schaake, A. Robock, C. Marshall, J. Sheffield, L. Luo, Q. Duan, R.T. Pinker, J.D. Tarpley, R.W. Higgins, and J. Meng. 2003. Real-time and retrospective forcing in the North American Land Data Assimilation System (NLDAS) project. Journal of Geophysical Research 108. doi:10.1029/2002JD003118.

Droogers, P., and W.G.M. Bastiaanssen. 2002. Irrigation performance using hydrological and remote sensing modeling. Journal of Irrigation and Drainage Engineering 128:11-18.

Ebleringer, J.R., and C.B. Field. 1993. Scaling Physiological Processes, Leaf to Globe Academic Press, Inc., New York.

Granger, R.J. 2000. Satellite-derived estimates of evapotranspiration in the Gediz basin. Journal of Hydrology 229:70-76.

Gupta, V.K., I. Rodriguez-Iturbe, and E.F. Wood. 1986. Scale Problems in Hydrology D. Reidel Publishing Company, Boston.

Han, H., and L. Yang. 2004. Evaluation of regional scale evapotranspiration using SEBS model in western Chinese Loess Plateau. Geoscience and Remote Sensing Symposium 2 (20-24):1339 - 1342.

Hanson, R.L. 1991. Evapotranspiration and Droughts U.S. Geological Survey Water-Supply Paper 2375.

Hendrickx, J.M.H., and S.-H. Hong. 2005. Mapping sensible and latent heat fluxes in arid areas using optical imagery. Proceedings of International Society for Optical Engineering, SPIE 5811:138-146.

Jackson, R.D., R.J. Reginato, and S.B. Idso. 1977. Wheat canopy temperatures: A practical tool for evaluating water requirements. Water Resources Research 13:651-656.

Jia, L., Z. Su, B.v.d. Hurk, M. Menenti, A. Moene, H.A.R. De Bruin, J.J.B. Yrisarry, M. Ibanez, and A. Cuesta. 2003. Estimation of sensible heat flux using the Surface Energy Balance System (SEBS) and ATSR measurements. Physics and Chemistry of the Earth 28:75-88.

Jiang, L., and S. Islam. 2001. Estimation of surface evaporation map over southern Great Plains using remote sensing data. Water Resources Research 37:329-340.

Kizer, M.A., and R.L. Elliott. 1991. Eddy correlation systems for measuring evapotranspiration. Transactions of American Society of Agricultural Engineers 34:387-392.

Kustas, W.P., and J.M. Norman. 1996. Use of remote sensing for evapotranspiration monitoring over land surfaces. Hydrological Sciences 41:495-516.

Kustas, W.P., J.M. Norman, M.C. Anderson, and A.N. French. 2003. Estimating subpixel surface temperatures and energy fluxes from the vegetation index-radiometric temperature relationship. Remote Sensing of Environment 85:429-440.

Lhomme, J.-P. 1992. Energy balance of heterogeneous terrain: Averaging the controlling parameters. Agricultural and Forest Meteorology 61:11-21.

Li, B., and R. Avissar. 1994. The impact of spatial variability of land-surface characteristics on land-surface fluxes. Journal of Climate 7:527-537.

Liang, S. 2000. Numerical experiments on spatial scaling of land surface albedo and leaf. area index. Remote Sensing Reviews 19:225–242.

Liang, S. 2004. Quantitative Remote Sensing of Land Surfaces John Wiley and Sons, Inc.

Ma, Y., L. Zhong, Z. Su, H. Ishikawa, M. Menenti, and T. Koike. 2006. Determination of regional distributions and seasonal variations of land surface heat fluxes from Landsat-7 Enhanced Thematic Mapper data over the central Tibetan Plateau area. Journal of Geophysical Research 111:D10305, doi:10.1029/2005JD006742.

Maayar, M.E., and J.M. Chen. 2006. Spatial scaling of evapotranspiration as affected by heterogeneities in vegetation, topography, and soil texture. Remote Sensing of Environment 102:33-51.

Mecikalski, J.R., G.R. Diak, M.C. Anderson, and J.M. Norman. 1999. Estimating fluxes on continental scales using remotely-sensed data in an atmospheric-land exchange model. Journal of Applied Meteorology 38:1352-1369.

Menenti, M., S. Azzali, W. Verhoef, and R. van Swol. 1993. Mapping agroecological zones and time lag in vegetation growth by means of Fourier Analysis of time series of NDVI images. Advances in Space Research 13:233-237.

Mengelkamp, H.-T., F. Beyrich, G. Heinemann, F. Ament, J. Bange, F. Berger, J. Bösenberg, T. Foken, B. Hennemuth, C. Heret, S. Huneke, K.-P. Johnsen, M. Kerschgens, W. Kohsiek, J.-P. Leps, C. Liebethal, H. Lohse, M. Mauder, W. Meijninger, S. Raasch, C. Simmer, T. Spieß, A. Tittebrand, J. Uhlenbrock, and P. Zittel. 2006. Evaporation Over A Heterogeneous Land Surface. Bulletin of the American Meteorological Society 87:775-786.

Moran, M.S., R.B. Jackson, L.H. Raymond, L.W. Gay, and P.N. Slater. 1989. Mapping surface energy balance components by combing Landsat Thematic Mapper and ground-based meteorological data. Remote Sensing of Environment 30:77-87.

Moran, M.S., and R.B. Jackson. 1991. Assessing the spatial distribution of evapotranspiration using remotely sensed inputs. Journal of Environmental Quality 20:725-735.

Morse, A., M. Tasumi, R.G. Allen, and W.J. Kramer. 2000. Application of the SEBAL methodology for estimating consumptive use of water and streamflow depletion in the Bear river basin of Idaho through remote sensing. Final report submitted to the Raytheon Systems Company, Earth Observation System Data and Information System Project, by Idaho Department of Water Resources and University of Idaho.

Nemani, R.R., and S.W. Running. 1989. Estimation of surface resistance to evapotranspiration from NDVI and thermal-IR AVHRR data. Journal of Applied Meteorology 28:276-284.

Nishida, K., R.R. Nemani, S.W. Running, and J.M. Glassy. 2003. An operational remote sensing algorithm of land surface evaporation. Journal of Geophysical Research 108 (D9):doi:10.1029/2002JD002062.

Norman, J.M., W.P. Kustas, and K.S. Humes. 1995. A two-source approach for estimating soil and vegetation energy fluxes from observations of directional radiometric surface temperature. Agriculture and Forest Meteorology 77:263-293.

Norman, J.M., M.C. Anderson, W.P. Kustas, A.N. French, J. Mecikalski, R. Torn, G.R. Diak, T.J. Schmugge, and B.C.W. Tanner. 2003. Remote sensing of surface energy fluxes at 10 1-m pixel resolutions. Water Resources Research 39:1221. doi:10.1029/2002WR001775.

Parlange, M.B., W.E. Eichinger, and J.D. Albertson. 1995. Regional scale evaporation and the atmosphere boundary layer. Reviews of Geophysics 33:99-124.

Pelgrum, H., and W.G.M. Bastiaanssen. 1996. An intercomparison of techniques to determine the area-averaged latent heat flux from individual in situ observations: a remote sensing approach using the European Field Experiment in a Desertification-Threatened Area data. Water Resources Research 32:2775-2786.

Peters Lidard, C.D., S. Kumar, Y. Tian, J.L. Eastman, and P. Houser. 2004. Global urban-scale land-atmosphere modeling with the land information system. 84th AMS Annual Meeting 11-15 January 2004, Symposium on Planning, Nowcasting, and Forecasting in the Urban Zone.

Price, D.T., D.W. McKennery, I.A. Nalder, M.T. Hutchinson, and J.L. Kesteven. 2000. A comparison of two statistical methods for spatial interpolation of Canadian monthly mean climate data. Agricultural and Forest Meteorology 101:81-94.

Schüttemeyer, D., C. Schillings, A.F. Moene, and H.A.R. De Bruin. 2007. Satellite-based actual evapotranspiration over drying semiarid terrain in West Africa. Journal of Applied Meteorology and Climatology 46:97-111 DOI: 10.1175/JAM2444.1.

Scott, R.L., J.W. Shuttleworth, G. D.C., and M.I. T. 2000. The water use of two dominant vegetation communities in a semiarid riparian ecosystem. Agricultural and Forest Meteorology 105:241-256.

Seguin, B.D., and B. Itier. 1983. Using midday surface temperature to estimate daily evapotranspiration from satellite thermal IR data. International Journal of Remote Sensing 4:371-383.

Shuttleworth, W.J. 1991. The modllion concept. Review of Geophysics 29:585-606.

Su, Z. 2002. The Surface Energy Balance System (SEBS) for estimation of turbulent heat fluxes. Hydrology and Earth System Sciences 6:85-99.

Tasumi, M., R.G. Allen, and W.G.M. Bastiaanssen. 2000. The theoretical basis of SEBAL. Appendix A of Morse et al. (2000). Idaho Department of Water Resources, Idaho.

Tasumi, M. 2003. Progress in operational estimation of regional evapotranspiration using satellite imagery, Ph.D. Thesis, University of Idaho, Moscow, Idaho.

Trezza, R. 2002. Evapotranspiration using a satellite-based surface energy balance with standardized ground control. Ph.D. Thesis, Utah State University: Logan, Utah.

Wright, J.L. 1982. New evapotranspiration crop coefficients. Journal of Irrigation and Drainage Engineering 108:57-74.

CHAPTER 2

MEASUREMENT AND MODELLING OF EVAPOTRANSPIRATION

Techniques for quantifying actual evapotranspiration (ET) have been around for several decades and scientists are continually seeking to improve these methods (e.g. Rana and Katerji 2000, Courault et al. 2005, Shuttleworth 2007). Although a great variety of different methods are currently available to quantify ET in given space and time scales, accurate determination of the spatio-temporal distribution of ET is still a very challenging task since ET varies widely through both space and time. There are several factors controlling ET in the atmosphere; the amount of solar radiation reaching the earth's surface, the availability of water in the soil, the types of plants, the amount of roots, and weather conditions can all affect ET.

Most conventional direct measurements techniques including eddy covariance, Bowen ratio and weighing lysimeters are too expensive and time consuming for continuous application at sufficient spatial density at the regional scale (Moran and Jackson, 1991). They provide only point measurements and (except for lysimeters) it is difficult to determine the area that measurements represent, especially over heterogeneous regions. For example, in the heterogeneous landscape of the central

plateau of Spain as many as 13 ground measurements of ET in a relatively small area of

5000 km^2 were not sufficient to predict accurately the area-averaged ET rate (Pelgrum

and Bastiaanssen, 1996). Recently developed cost-effective and fast techniques using

remote sensing data have proven to be the only appropriate approach to provide ET

estimation at regional scale with high repetition rate (Choudhury, 1989; Kustas and

Norman, 1996; Anderson et al., 1997; Bastiaanssen et al., 1998).

This chapter review several techniques used to measure and estimate ET at the

local or regional scale. For each method, the advantages and disadvantages for their

usage are discussed. The techniques presented in section 2.1 are categorized as methods

that measure ET with hydrological and micrometeorological approaches, while methods

that estimate ET using remotely sensed data are discussed in section 2.2.

2.1. TECHNIQUES FOR MEASURING EVAPOTRANSPIRATION

2.1.1. Hydrological Approaches

2.1.1.1. Water balance method

The water balance at the Earth's surface can be obtained by calculating the input,

output, and storage changes of water. Water balance is an indirect method. In semi-arid

basins, the major input of water is from precipitation and output is ET. The residual in the

water balance equation and the principle of conservation of mass is used to estimate ET

in the water balance method (Figure 2.1).
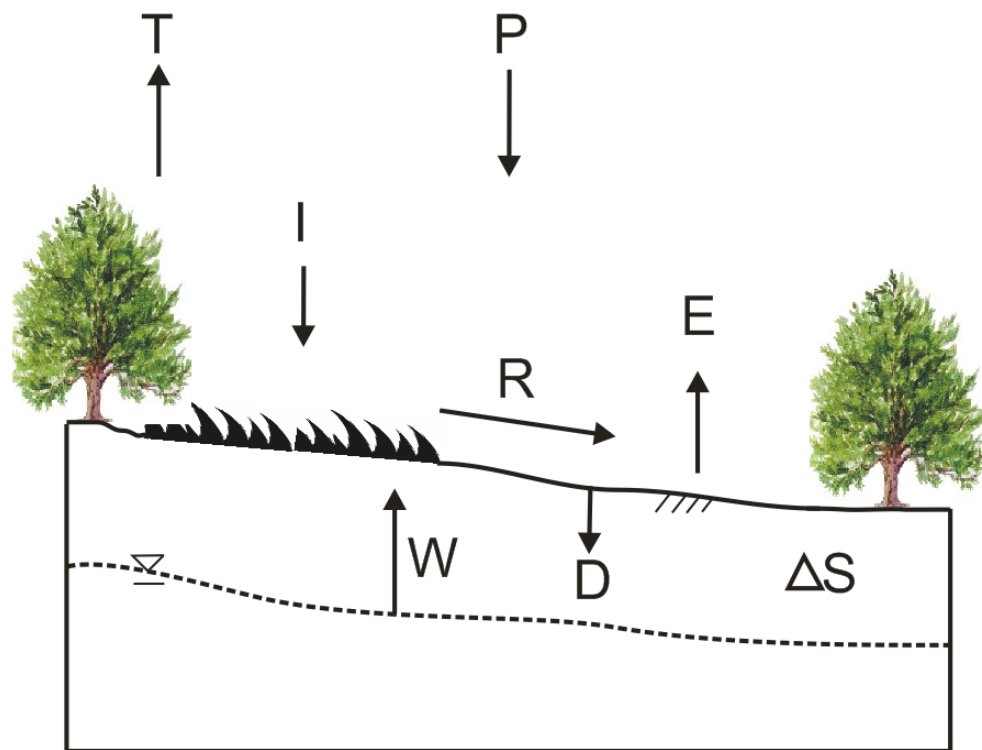
Figure 2.1 Schematic of the water balance

$$P + I + W - R - D \pm \Delta S = ET \qquad\qquad [2.1]$$

where P is the precipitation, I is the irrigation, W is the capillary rise from the ground

water table, ET is the evapotranspiration, R is the surface runoff, D is the drainage

groundwater recharge and ΔS is the change in the soil water storage capacity. All terms

are usually expressed in mm per unit time over a watershed.

The water balance model is very popular since it looks simple. However the water

balance model requires significant input data including precipitation, ground water table

depth, soil moisture conditions and soil-water holding capacity. Some of these input

parameters are difficult to determine over short time scales. For instance, reasonable

agreement was reported between catchment scale water balance flow estimation and

measured annual flows, but agreement with monthly flows was poor (Mather, 1972).

Villagra et al. (1995) also argued that the error of input parameters including soil water

storage, total hydraulic gradients, soil hydraulic conductivity and soil water flux densities

cause a coefficient of variation of the order of 40% in ET estimates. Despite numerous

uncertainties associated with the simple water balance model, many researchers have

applied this type of model to problems ranging from catchment scale to the global water

balance studies (Thornthwaite, 1948; Alley, 1984; Willmott et al., 1985; Mintz and

Walker, 1993; Houser et al., 1998).

2.1.1.2. Weighing lysimeter technique

The weighing lysimeter technique measures ET directly by using the water balance. This technique works by isolating a representative sample from the soil–vegetation interface by placing it into a large 'bucket' and measuring the remaining components of the water balance (*P, I*) independently or through changes in the weight of the bucket (Tanner, 1967; Aboukhaled et al., 1982; Wright, 1991).

$$P + I \pm \Delta S = ET \qquad\qquad\qquad [2.2]$$

The weight of the moisture lost from the lysimeter by ET can be determined either by using a manometer to record pressure variations or with an electric balance. Either of these methods can be set up for daily, hourly, or long term monitoring. Because the weighing lysimeters technique measures water loss directly, it is considered one of the most accurate ways of quantifying ET on small scales (Aboukhaled et al., 1982; Allen et al., 1996). However, larger scale ET estimation using this technique is more challenging because of the high cost, physical difficulties of installation, the resulting disturbance of soil in the area and the limitations of vegetation height and rooting depth. That is the major reason why the weighing lysimeter data sometimes represent the ET of just one point in the field instead of conditions of the whole field (Aboukhaled et al., 1982). The weighing lysimeters technique is generally better for point-scale estimates and loses usefulness as a prediction tool when extrapolated over larger areas (Moran and Jackson, 1991).

2.1.2. Micrometeorological Approaches

2.1.2.1. Energy balance method

The energy inputs and outputs are balanced according to the energy conservation law at the land surface. The surface energy balance describes how the radiative energy flux reaching the earth's surface is transferred into sensible, latent and soil heat fluxes. The radiation balance of the Earth system is an accounting of the incoming and outgoing components of shortwave and longwave radiation. The radiation balance in the vertical direction is expressed by

$$R_n = (1-\alpha)R_S \downarrow + R_L \downarrow - R_L \uparrow - (1-\varepsilon_0)R_L \downarrow \qquad [2.3]$$

Where R_n is the net radiation [Wm^{-2}], $R_S\downarrow$ is the incoming shortwave radiation [Wm^{-2}], $R_L\downarrow$ is the incoming longwave radiation [Wm^{-2}], $R_L\uparrow$ is the longwave radiation emitted directly by the earth [Wm^{-2}], α is the surface albedo [-] and ε_0 is the surface emissivity [-]. The term $(1-\varepsilon_0)$ $R_L\downarrow$ represents the reflected long wave radiation as explained in section 3.1. R_n can be positive or negative. Positive net radiation occurs during sunny daytime when $R_S\downarrow$ is large. At night, net radiation is usually negative since $R_S\downarrow$ is zero. Thus at night the outgoing longwave radiation from the Earth's surface is usually the largest term.

The principal use of the available net radiation flux in the Earth system is in the phase change of water (latent heat flux), changing the temperature of the air (sensible heat flux), subsurface (ground heat flux), canopy (heat storage) and green plant biochemical process (photosynthesis). Here are all components of the energy balance

equation below:

$$LE = R_n - H - G - P \pm \Delta S \qquad\qquad\qquad [2.4]$$

where R_n is the net radiation flux [Wm^{-2}], LE is the latent heat flux [Wm^{-2}], H is the

sensible heat flux [Wm^{-2}], G is the ground heat flux [Wm^{-2}], P is the energy used in the

photosynthetic process [Wm^{-2}] and S is the storage of heat in air and plant biomass [Wm^{-2}]. The term flux refers to flux density, which represents the amount of energy that flows

through a horizontal surface of unit area per unit time. P and S are usually rather small

compared to the other fluxes and are therefore often neglected (Miller, 1977; Monteith

and Unsworth, 1990). Energy terms related to the horizontal transfer of heat also are not

included because the assumed horizontal homogeneity implies these terms are balanced

across the surfaces of the control volume for which the energy balance equation holds.

The combination of all of the energy balance parameters must complete the

balance (Twine et al., 2000). The components of this relationship can be measured

independently. R_n is measured with a net radiometer and G is measured using soil heat

flux plates, thermocouples and soil moisture sensors (Fritschen and Gay, 1979). H can be

measured using a`scintillometer (Meijninger et al., 2002), sonic anemometer with a fine-

wire thermocouple (Kizer and Elliott, 1991; Massman and Lee, 2002) or the flux-gradient

relation (Rana and Katerji, 2000). Since ET is calculated as LE/L, where L is the latent

heat of vaporization, if all other terms (R_n, G and H) are observed and estimated, ET is

estimated as the residual of the land surface energy balance.

2.1.2.2. Aerodynamic method

The aerodynamic method is a micrometeorological technique to measure ET directly. It assumes a flux density is related to the gradient of the concentration in the atmospheric surface layer and based on only measurements of atmospheric gradients without using the information of the surface energy balance measurements (Thornthwaite and Holzman, 1942; Kondo, 1975; Blanc, 1987; Singh and Xu, 1997). In the aerodynamic method, heat fluxes are determined using the vertical profiles of air temperature, humidity and wind speed. It requires at least three or four levels of measurements (Legg et al., 1981; Wieringa, 1993). These parameters for turbulent flows in the surface layer can be derived based on the Monin-Obukhov similarity relations (Monin and Obukhov, 1954; Businger et al., 1971; Yaglom, 1977).

$$u(z) = \frac{u_*}{k}\left[ln\left(\frac{z}{z_0}\right) - \Psi_m\left(\frac{z}{L}\right) + \Psi_m\left(\frac{z_0}{L}\right) \right] \tag{2.5}$$

$$\theta(z_2) - \theta(z_1) = \frac{\theta_*}{k}\left[ln\left(\frac{z_2}{z_1}\right) - \Psi_h\left(\frac{z_2}{L}\right) + \Psi_h\left(\frac{z_1}{L}\right) \right] \tag{2.6}$$

$$q(z_2) - q(z_1) = \frac{q_*}{k}\left[ln\left(\frac{z_2}{z_1}\right) - \Psi_c\left(\frac{z_2}{L}\right) + \Psi_c\left(\frac{z_1}{L}\right) \right] \tag{2.7}$$

where Ψ_m, Ψ_h, and Ψ_c are the Monin-Obukhov similarity functions [-] (stability functions) for momentum, heat, and vapor transport, respectively, k (0.41) is the von Karman constant, L is the Obukov length [m], z_0 is the surface roughness length [m], ρ is the air density [kgm^{-3}], u_* [ms^{-1}], θ_* [k] and q_* [gg^{-1}] are the friction velocity and scalar scales for temperature and humidity, respectively. Then the latent and sensible heat fluxes

can be calculated as follows:

$$LE = -\lambda \cdot \rho \cdot u_* \cdot q_* \qquad\qquad [2.8]$$

$$H = -\rho \cdot c_p \cdot u_* \cdot \theta_* \qquad\qquad [2.9]$$

where λ is the latent heat of vaporization [Jkg^{-1}].

The aerodynamic method provides reliable results when vertical gradients of variables are large, however it does not work well when the temperature or humidity gradients are small (Baldocchi et al., 1988; Garratt, 1992; Rana and Katerji, 1996). Cellier and Brunet (1992) indicated that since the gradients are often small, the amount of uncertainty in heat fluxes estimated by the aerodynamic method is related to the inaccuracy of the measurement devices. Several studies suggested reducing this uncertainty to some extent by calculating the temperature and wind speed changes necessary for sensible heat fluxes (Itier, 1981; Rana and Katerji, 2000). Then the energy balance was used to estimate latent heat as the residual term by indirect way. Nevertheless, the aerodynamic method does not provide a reliable ET on tall vegetation neither with a complete form nor with a simplified form (Thom et al., 1975; Garratt, 1978; Rana and Katerji, 1996).

2.1.2.3. Bowen Ratio method

The Bowen ratio method is an indirect method that has been widely applied and tested in various environment of settings (Tanner, 1960; Fritschen, 1965; Hatton and

Vertessy, 1990). The fundamental equations describing the relationship between vertical temperature and vapor pressure gradients for sensible (H) and latent heat (LE) fluxes, respectively, are expressed as:

$$H = -\rho c_p K_H \frac{\partial T}{\partial Z}$$ [2.10]

$$LE = \frac{-\rho c_p}{\gamma} K_V \frac{\partial e}{\partial Z}$$ [2.11]

where ρ is the air density [kgm^{-3}], c_p is the specific heat of air [Jkg^{-1}K^{-1}], γ is the psychrometric constant [kPaK^{-1}], K_H and K_V are the eddy diffusivities [m^{2}s^{-1}] of heat and water vapor transport, respectively, and $\frac{\partial T}{\partial Z}$ and $\frac{\partial e}{\partial Z}$ are the temperature and water vapor pressure gradients, respectively.

In Eqs. [2.10] and [2.11], H and LE are not easily estimated because turbulent transport coefficients (K_H and K_V) are difficult to determine. However, Bowen (1926) argued that if the transfer coefficients are assumed to be equal, the ratio of H to LE is proportional to the ratio of the vertical gradients of temperature and vapor pressure above a surface. This ratio between H and LE is known as the Bowen ratio (Bowen, 1926) and can be approximated from measurements of air temperature and relative humidity at two different heights.

$$\beta = \frac{c_p p}{\varepsilon L_V} \frac{\partial T / \partial Z}{\partial e / \partial Z} = \gamma \frac{\Delta T}{\Delta e} .$$ [2.12]

Since the Bowen ratio is defined as $\beta = H/LE$, the energy balance equation Eq. [2.4] can be rearranged to give the following expression for LE and H:

$$LE = \frac{R_n - G}{1 + \beta} \qquad [2.13]$$

$$H = \frac{\beta}{1 + \beta}(R_n - G) \qquad [2.14]$$

The Bowen ratio has been proven to be an accurate method to measure ET in various environments (Fuchs and Tanner, 1970; Sinclair et al., 1975) including tall vegetation (Cellier and Brunet, 1992; Rana and Katerji, 1996). One of the advantages of the Bowen ratio technique is it requires only a small number of parameters to derive H and LE. Temperature and humidity measurements at just two heights are sufficient to calculate the Bowen ratio. On the other hand, since the H and LE measurements are directly dependent on the accuracy of β, a small measurement error in β will cause very large errors in the computed fluxes (Tanner, 1988; Singh and Xu, 1997). Sinclair et al. (1975) reported uncertainties up to 10% under ideal surface conditions, while Nie et al. (1992) reported uncertainties up to 20% for heterogeneous surfaces. Extremely dry conditions can vastly increase the error associated with the Bowen ratio technique. Angus and Watts (1984) estimated that the error could be as high as 60% under dry conditions. Kanemasu et al. (1992) indicated that measurement uncertainty using the Bowen ratio is particularly susceptible to errors when atmospheric moisture gradients approach zero. Xu and Qiu (1997) indicated that estimation by Bowen ratio method can be computationally

unstable and generate erroneous results when the Bowen ratio is close to -1. Some studies

attempted to improve flux predictions by proposing criteria for rejecting unrealistic

Bowen ratio values (Unland et al., 1996; Perez et al., 1999). However, determination of

proper criteria is not a trivial step since the criteria of Bowen ratio vary and are dependent

upon sensor resolution and environmental conditions (Perez et al., 1999; Xing et al.,

2008).

2.1.2.4. Eddy covariance method

In the eddy covariance approach (Swinbank, 1951; Tanner, 1988; Kizer and

Elliott, 1991), ET is measured through the turbulent velocity and water vapor fluctuations

caused by the transportation of vapor from the surface to the atmosphere. EC is a very

effective method of directly measuring the water vapor flux at short time scales. The

instrumentation required for the eddy covariance approach is fairly sophisticated.

According to turbulent transfer theory, surface fluxes should be measured by correlating

fluctuations in vertical wind speed with fluctuations in other atmospheric quantities like

water vapor and temperature. In this way, the eddy covariance approach predicts surface

fluxes. An expression for the vertical component of wind speed (w) or an atmospheric

quantity such as heat or water vapor (s) can be related as shown:

$$w = \overline{w} + w' \qquad\qquad [2.15]$$

$$s = \overline{s} + s' \qquad\qquad [2.16]$$

where $\overline{w}$ is the sum of mean wind speed measured over a sampling time t and w' is the

instantaneous deviation from this average.

Similarly, the time-averaged flux (F_s) of an atmospheric variable is dependent on its density, vertical velocity and volumetric content. As shown in Eqs. [2.15] and [2.16] above, each of these factors has a mean and a fluctuating component as:

$$F_S = \rho \overline{w's'} \qquad [2.17]$$

where the over-bar again denotes a time average and the w' and the s' are instantaneous deviations from the mean. In this expression, the averages of the fluctuating terms and the mean vertical wind speed are both assumed to be zero and air density is assumed to be constant in the lower atmosphere. Additionally, assuming a unit volume for the mass of the transported entity allows the density term to be expressed.

The eddy covariance can be expressed in terms of the upward vertical fluxes of water vapor (q_s) in Eq. [2.18] and of temperature (T) in Eq. [2.19]:

$$E = \rho \overline{w'q_s'} \qquad [2.18]$$

$$H = \rho c_p \overline{w'T'} \qquad [2.19]$$

In the field, hygrometers are used to measure specific humidity based on the electromagnetic radiation that the water vapor absorbs. Ultraviolet and infrared absorption hygrometers are effective when measuring humidity fluctuations in narrow

vertical columns of moving air. On the other hand, sonic-anemometers, also used to

measure H, measure the vertical wind velocity by transmitting sonic signals and

measuring them along fixed orthogonal directions. In addition, temperature fluctuations

can be measured if a fine-wire thermocouple is installed.

The theory behind the eddy covariance technique is straightforward, but the

necessary instrumentation is sophisticated. In order for the variables to correlate

accurately, the instrument must be capable of sampling the eddies at high frequency, the

orientation and placement of the sensors must be precise and a sufficiently long

averaging period must be used. Monteith and Unsworth (1990) reported that the response

time of the sensors depends on the range of eddy sizes that carry the flux. The size of

eddies increases with their height above the surface and with any increase in surface

roughness (Brutsaert 1991). The instrument sensitivity to moisture is also an issue with

this technique, which means that measurements cannot be made when precipitation,

irrigation, or dew exist. The krypton hygrometer and fine wire thermocouples

incorporated on the sonic anemometer are particularly sensitive to moisture.

The eddy covariance technique has an advantage over the Bowen ratio because it

can measure the sensible and latent heat fluxes independently using the krypton

hygrometer for the LE and the sonic anemometer for the H. However, Laubach and

Teichmann (1999) and Twine et al. (2000) report problems with closing the energy

balance equation using the eddy covariance technique. Because of the instrumentation's

sensitivity to moisture and the need to orient the eddy covariance devices with wind

direction, obtaining accurate ET estimates using the eddy covariance system is best done on clear days with appropriate wind direction. Loescher et al. (2005) examined EC measurement uncertainties in detail using instrument intercomparisons in laboratory and field. Linear regressions for sensible heat fluxes of eight EC instruments in neutral and unstable stability conditions revealed differences of up to 30%, while typical uncertainties (measured by the standard deviations of the slopes) were 7-11% depending on atmospheric stability.

When making micrometeorological measurements over Earth surfaces, the measurements should represent the properties of the surface of interest. In order to do that the height of the instruments needs to be constrained. This is referred to as the "fetch" requirement. As a rule of thumb, a fetch is usually reported as a ratio of 1:100, so that a vertical measurement height of 1 meter is necessary for 100 meters of homogeneous cover (Wieringa, 1993; Allen et al., 1996; Stannard, 1997). The location and extent of the flux footprint (fetch distance) depends on surface roughness, atmospheric stability, wind speed and wind direction (Schmid and Oke, 1990; Hsieh et al., 2000). There are several types of footprint models. Initially, simple two-dimensional analytical footprint models for neutral atmospheric conditions were developed (Gash, 1986; Schuepp et al., 1990). Later, the analytical footprint model was improved to account for atmospheric stability conditions (Horst and Weil, 1992; Hsieh et al., 2000).

2.1.2.5. Scintillometry method

Scintillometry equipment has been developed over the last 30 years (Wesely, 1976; De Bruin et al., 1995; Nieveen et al., 1998; Meijninger and De Bruin, 2000; Kohsiek et al., 2002; Hendrickx et al., 2007; Kleissl et al., 2008). Basically, scintillometry is a ground-based measurement technique that consists of transmitting a beam of electromagnetic radiation, most commonly in the near-infrared or microwave regions and measuring the variations in intensity of the received signal. These variations are caused by turbulently induced fluctuations in the refractive index of air. These measured refractive index fluctuations, in combination with other related data (e.g. roughness length and wind speed) can be used to estimate sensible and latent fluxes. The characteristics of these variations depend on the wavelength of the signal. For instance, signals in the near-infrared region are more sensitive to heat movement, while the microwave portion tends to respond more accurately to water vapor movement (Hill, 1992; Green et al., 1994; McAneney et al., 1995; Nieveen et al., 1998; Watts et al., 2000; Green et al., 2001; Meijninger et al., 2002; Hendrickx et al., 2007).

One of the most important advantages of scintillometry over the eddy covariance (EC) and Bowen ratio techniques is that footprint area of a scintillometer measurement (for example, footprint of the large aperture scintillometer (LAS) is up to 5000 m in one dimension) is significantly larger than the one from eddy covariance or Bowen ratio (usually less than 500 m) (Hemakumara et al., 2003; Hafeez et al., 2006; Hendrickx et al., 2007). Large footprint of the scintillometer (500 to 10,000 m) makes it possible to be

used as validation and calibration data set for regional scale remote sensing and

distributed hydrological models (Beyrich et al., 2002; Meijninger et al., 2002).

The scintillometer measures the intensity fluctuations of light σ_I^2 [-], from which

the structure parameter of the refractive index of air C_n^2 [m$^{-2/3}$], C_T^2 [K^2 m$^{-2/3}$] and C_Q^2

[(gm^{-3})^{2}m$^{-2/3}$] can be derived (Hill et al., 1980; Hill et al., 1988). Eqs. [2.20] and [2.21]

are used to calculate C_n^2 for the microwave (mw) and near-infrared (ir) scintillometers,

respectively.

$$\sigma_I^2 = 0.5 C_{n_{mw}}^2 K^{7/6} L^{11/6} \qquad [2.20]$$

$$\sigma_I^2 = 0.892 C_{n_{ir}}^2 D^{-7/3} L^3 \qquad [2.21]$$

where $K = 2\pi/\lambda$ [m^{-1}] is the propagation wave number, D is the aperture diameter of the

scintillometer [m] and L the distance between the transmitter and the receiver or the path

length [m].

$$C_n^2 = \frac{A_T^2 C_T^2}{\overline{T}^2} + 2\left(\frac{A_T A_Q C_{TQ}}{\overline{T}\,\overline{Q}\backslash} \right) + \frac{A_Q^2 C_Q^2}{\overline{Q}^2} \qquad [2.22]$$

where

$$C_{TQ} = \pm\sqrt{C_T^2 C_Q^2} \qquad [2.23]$$

and over-bar indicates the temporal averages, Constants A_T and A_Q are functions of

wavelength λ [m], $\overline{T}$ (temperature) [K], $\overline{Q}$ (humidity) [gm^{-3}], $\overline{P}$ (pressure) [Nm^{-2}].

Since fluctuations of the refractive index of air mainly depend on that of temperature and humidity, C_n^2 is related to the structure parameter of temperature and humidity, C_Q^2 and C_T^2, respectively, as below (Wesely, 1976; Hill et al., 1980).

$$C_Q^2 = \frac{A_{T_{mw}}^2 C_{n_{ir}}^2 + A_{T_{ir}}^2 C_{n_{mw}}^2 + 2SA_{T_{mw}} A_{T_{ir}} \sqrt{C_{n_{mw}}^2 C_{n_{ir}}^2}}{(\overline{T}\Pi)^2} \qquad [2.24]$$

$$C_T^2 = \frac{A_{Q_{mw}}^2 C_{n_{ir}}^2 + A_{Q_{ir}}^2 C_{n_{mw}}^2 + 2SA_{Q_{mw}} A_{Q_{ir}} \sqrt{C_{n_{mw}}^2 C_{n_{ir}}^2}}{(\overline{Q}\Pi)^2} \qquad [2.25]$$

where $\Pi = \left[A_{T_{mw}} A_{Q_{ir}} - A_{T_{ir}} A_{Q_{mw}} \right] / \overline{T} \overline{Q}$ and S is the sign ($\pm$) of the T-Q correlation.

According to Monin-Obukhov similarity theory (MOST), it is possible to empirically link C_T^2 and C_Q^2 to the temperature and humidity scales, T_* and Q_* [-]. For unstable condition ($L<0$) (De Bruin et al., 1993):

$$f\left(\frac{z}{L}\right) = \frac{C_T^2}{T_*^2 (z-d)^{-2/3}} = \frac{C_Q^2}{Q_*^2 (z-d)^{-2/3}} = 4.9 \left(1 + 7 \left|\frac{z}{L}\right|\right)^{-2/3} \qquad [2.26]$$

where z is the measurement height [m], d is the zero plane displacement height [m] and L is the Monin-Obukhov length [m] defined as:

$$L = -\frac{T \cdot u_*^2}{k \cdot g \cdot T_*} \qquad [2.27]$$

where

$$u_* = \frac{ku}{\ln\left(\dfrac{z-d}{z_0}\right) - \Psi\left(\dfrac{z-d}{L}\right)}$$ [2.28]

T is the air temperature [K], u_* is the friction velocity [ms^{-1}], k is the von Karman constant (0.41), g the gravitational acceleration (9.81) [ms^{-2}], Ψ is the integrated stability function (Panofsky and Dutton, 1984), u is the wind speed [ms^{-1}] and z_0 is the aerodynamic surface roughness height [m].

The heat fluxes, H [Wm^{-2}] and LE [Wm^{-2}] are obtained iteratively from Eqs. 2.25-2.27 and the following relationship:

$$H = -\rho C_p u_* T_*$$ [2.29]

$$LE = -L_V u_* Q_*$$ [2.30]

where ρ is the air density [kgm^{-3}] and C_p is the specific heat [Jkg^{-1}K^{-1}].

Among several possible options in scintillometry, the large aperture scintillometer (LAS) can have an optical integration path of up to few kilometers. A very large aperture scintillometer (XLAS), was especially designed for use over large distances, up to 10 km (De Bruin et al., 1995; Kohsiek et al., 2002). Kleissl et al. (2007) quantified scintillometer instrument error by intercomparing five Large Aperture Scintillometers in field. They found differences in the regression slopes of up to 21% with typical uncertainties of 5 - 6%. These uncertainties occurred even when great care was taken

during installation and maintenance of the equipment, data processing, and site selection. Larger errors are expected for non-ideal conditions.

The scintillometry method, which is based on the Monin-Obukhov similarity theory (MOST) has been applied and compared to eddy covariance systems by several authors and shown to be a viable method for estimating areal averaged sensible and latent heat fluxes (Meijninger and De Bruin, 2000; Green et al., 2001; Kohsiek et al., 2002; Asanuma and Lemoto, 2006). The scintillometer technique has been used successfully over homogeneous terrain. Recently several investigations have demonstrated the potential of this method over non-uniform surfaces. Watts et al. (2000) compared estimates from LAS with heat fluxes derived from infrared surface temperatures over semi-arid grassland, finding close agreement. Green et al. (2001) also found good agreement with eddy covariance fluxes over pasture land. Asanuma and Lemoto (2006) measured regional sensible heat flux over a semi-arid grassland in Mongolia with large aperture scintillometer and compared with eddy covariance tower measurements and found that results are comparable with each other. Overall, scintillometry appears to provide a useful means of obtaining path averaged fluxes at a scale suitable for satellite remote sensing comparison.

2.2. REMOTE SENSING APPROACHES FOR ESTIMATING ET

Although remote sensing techniques can not measure actual ET directly, the use of remote sensing to estimate ET rates on land surface has recently been the focus of

many investigations. The potential of satellite image-based remote sensing for examining spatial patterns of regional distributions of ET has been investigated by a number of authors (Choudhury, 1989; Moran and Jackson, 1991; Menenti et al., 1993; Kustas and Norman, 1996; Mecikalski et al., 1999; Granger, 2000; Caparinni and Castelli, 2002; Su, 2002; Nishida et al., 2003; Bastiaanssen et al., 2005; Hendrickx and Hong, 2005; Allen et al., 2007). These efforts have resulted in the development of remote sensing ET algorithms that are quite different in their spatial and temporal scales: 30 m to 4 km, daily to yearly. Operational algorithms that have produced evaporation maps on local, regional, or national scales are: the North American Land Data Assimilation Systems (NLDAS) (Cosgrove et al., 2003), the Land Information Systems (LIS) (Peters Lidard et al., 2004), the Atmosphere-Land Exchange Inverse (ALEXI) (Anderson et al., 1997; Norman et al., 2003), the disaggregated ALEXI model (DisALEXI) (Norman et al., 2003), the Surface Energy Balance System (SEBS) (Su, 2002; Jia et al., 2003; Janssen et al., 2004), the Surface Energy Balance Algorithm for Land (SEBAL) (Bastiaanssen et al., 1998; Bastiaanssen et al., 2005; Hendrickx and Hong, 2005), Mapping EvapoTranspiration at high spatial Resolution with Internalized Calibration (METRIC) (Allen et al., 2005; Allen et al., 2007), as well as algorithms without distinct acronym (Jiang and Islam, 2001; Ma et al., 2004; Ma et al., 2006; Schüttemeyer et al., 2007)

Four main categories in remote sensing ET estimation are introduced in the next section. Those categories are based on works by Kustas and Norman (1996) and Courault et al. (2005): (1) Statistical and empirical approaches, (2) Crop coefficient with traditional ET equations, (3) Physically based analytical approaches and (4) Numerical

hydrologic models.

2.2.1. Statistical and Empirical Approaches

The statistical and empirical methods relate the difference between satellite observed surface radiometric temperature at the time of satellite passover and regionally measured air temperature to daily ET (Jackson et al., 1977; Seguin and Itier, 1983; Nieuwenhuis et al., 1985; Reginato et al., 1985; Carlson and Buffum, 1989; Vidal and Perrier, 1989; Thunnissen and Nieuwenhuis, 1990). An early approach for estimating daily ET from instantaneous remote sensing data was presented by Jackson et al. (1977) and later analyzed by Seguin and Itier (1983) and others. The general form of the extrapolation equation from instantaneous surface and air temperatures to daily ET rates is as follows;

$$ET_d = R_{nd} + A - B(T_{rad,i} - T_{a,i})$$ [2.31]

where i represents instantaneous (near midday) values, d represents daily totals, A and B are regression coefficients depending on the local situation and T_a is air temperature at 2 m height. To estimate daily ET in Eq. [2.31], the radiometric surface temperature (T_{rad}) is required from remotely sensed data after atmospheric correction. Eq. [2.31] assumes that the daily total of soil heat flux is negligible ($G_d = 0$) and also that the ratio between sensible heat (H) and net radiation (R_n) is constant throughout the day (Courault et al., 2005).

Other research has been conducted to establish the relationship between ET and NDVI (Kerr et al., 1989; Lo et al., 1993; Seevers and Ottmann, 1994; Srivastava et al., 1997). Kerr et al. (1989) Srivastava et al (1997) and Seevers and Ottmann (1994) showed a good fit of linear relationship between NDVI and ET. The high correlation indicates an almost linear relationship between satellite-measured radiance and water losses to the atmosphere. Lo et al. (1993) generated a non-linear relation between NDVI and ET in the area of whole Africa. Monthly and yearly total of NDVI was obtained from AVHRR imagery and ET was calculated from water budget model suggested by Willmott et al. (1985). They observed a strong correlation between NDVI and ET ($r \approx 0.9$) and noted about one month of time lag between peak ET and peak NDVI.

A major advantage of the statistical and empirical methods is that they require only a few input data, but, apart from surface temperature, all other data, including air temperature, are often assumed spatially constant. Although local measurements can be interpolated with a geostatistical model (Seguin et al., 1994), the accuracy is still around $20 - 30\%$. This limits the application to essentially homogeneous local regions.

2.2.2. Crop Coefficient with Traditional ET Equations

The crop coefficient (K_c) is a parameter frequently used in water resources management to scale actual ET to the reference ET for the particular vegetation. Accurate values of K_c improve plant water consumption estimation and the efficient management of water in both irrigated agriculture and natural vegetation areas. In regional hydrological studies it is not uncommon to make the assumption that crop coefficient is

directly related to daily ET (Garatuza-Payan and Watts, 2005; Compaore et al., 2008). This assumption then makes it possible to derive regional ET estimates based on a crop coefficient distribution.

Neale et al. (1989) calculated K_c for corn using alfalfa ET as the reference ET. Corn ET was measured by lysimeters located at the Northern Colorado Research Center. Reference ET (alfalfa ET) was measured by three lysimeters located in a well-watered alfalfa field and radiometer measured reflectances were used to estimate the vegetation index. Then the reflectance-based K_c was estimated by linear scaling against vegetation index (*NDVI*). The authors argued that the reflectance-based K_c real time coefficients can be used with any combination of crop development and weather conditions. This is one of the main advantages over traditional crop coefficient approaches.

Regional distribution of reference and potential ET calculated from remote sensing data has been attempted to provide a reference level for actual ET in various land surfaces. Mekonnen and Bastiaanssen (2000) tried the Priestly-Taylor (1972) (PT) approach to estimate reference ET at regional scale, because its radiation and temperature parameters can be assessed from remotely sensed data. The authors argued that this equation might behave better than a Penman-Monteith (PM) based equation because the PM equation requires weather parameters, such as vapor pressure and wind speed that are impossible to describe at a regional scale. The authors found first a good correlation between PM-ET and PT-ET using weather data, which indicated that the PT equation could be used under the humid conditions present in the study area. They concluded that

the K_c approach, based in the PT equation for calculating reference ET, can be used in remote sensing to determine regional scale crop water requirements as long as the vapor pressure deficit remains within acceptable limits. Choudhury (1997) estimated the global pattern of potential ET from the PM equation using satellite and assimilated data. The calculated potential ET rates were validated with lysimeter observations from well-watered grass at 35 widely distributed locations in different climatic regimes. The results show that potential ET estimates from remote sensing and assimilated data have reasonable agreement with measured values.

The Priestly-Taylor approach for calculating ET has been widely used because the PT equation is simpler than PM and thus requires limited input parameters (Shouse et al., 1980; Green et al., 1984; Wilson et al., 2001; Liu and Lin, 2005). The PT method was extensively tested for different regions and there exist mixed results of PT performance. Several studies indicated that PT approach has shown reasonable performance (Jensen et al., 1990; McAneney and Itier, 1996) In contrast, Irmak et al. (2003) found underestimation of PT daily ET when compared with FAO-56 PM in Florida and the PT underestimations tended to be higher in dry water-stressed conditions. Yoder et al. (2005) compared PT and PM (FAO-56) with using ground measurement by a large weighing lysimeter, and they indicate that PT overestimated ET and was less accurate than PM (FAO-56). Although the PM approach suggested by Allen et al. (1998) requires wind speed and vapor pressure deficit in addition to air temperature and solar radiation, PM generally yields better results under various climatic conditions than the PT approach (Allen et al., 1994; Mohan and Arumugam, 1996; Itenfisu et al., 2003; Yoder et al., 2005).

2.2.3. Physically-Based Analytical Approaches

The most common physically-based procedures for estimating ET using remote sensing data are based on the surface energy balance. The method for balancing surface energy consists of estimating R_n, G, and H from remotely sensed data and getting LE (ET) as the residual (neglecting photosynthesis, advection and heat storage in the air and canopy):

$$LE = R_n - G - H \qquad [2.32]$$

Because all residual errors are incorporated in the estimate of LE, applying Eq. [2.32] requires the accurate estimation of R_n, G, and H. In particular, much discussion has occurred about estimating H accurately from remotely sensed data since aerodynamic surface temperature (T_{aero}) is difficult to measure from remote sensing. T_{aero} is one of the mandatory parameters in the common H equation (Brutsaert, 1991).

$$H = \rho Cp \frac{T_{aero} - T_a}{r_{ah}} \qquad [2.33]$$

where ρ_a is the density of air [kgm^{-3}], C_p is the specific heat capacity of air [Jkg^{-1} K^{-1}], T_{aero} is the aerodynamic surface temperature [K], T_a is air temperature at the reference height [K] and r$_{ah}$ is the aerodynamic resistance to heat transport [sm^{-1}].

Since remote sensing thermal bands measure radiometric surface temperature

(T_{rad}), several studies have analyzed the effect of sensible heat flux using T_{rad} instead of

T_{aero}. The two temperatures usually differ by 1 to 5 °C, depending on canopy density and

height, canopy dryness, wind speed and sun angle (Kustas et al., 1994; Qualls and

Brutsaert, 1996; Qualls and Hopson, 1998). Unfortunately, an uncertainty of 1 °C in T_{aero}

$- T_a$ can result in a 50 Wm^{-2} uncertainty in H (Campbell and Norman, 1998) which could

be approximately equivalent to an evaporation rate of 1 mm day^{-1}. A way to compensate

for the differences between T_{aero} and T_{rad} is to add an extra resistance term, r_{ex} in Eq.

[2.33]. The r_{ex} can be expressed by ratio of z_{om} and z_{oh} (Kustas et al., 1989):

$$r_{ah} + r_{ex} = \frac{1}{ku_*} \ln\left(\frac{z-d}{z_{om}} - \Psi_h\right) + \frac{1}{ku_*}\left(kB^{-1}\right)$$ [2.34]

where

$$kB^{-1} = ln\left(\frac{z_{om}}{z_{oh}}\right),$$ [2.35]

k is the von Karman constant, and B^{-1} is a parameter expresses the momentum flux

compared to the extra resistance.

Although many investigators have tried to solve this problem by adjusting r_{ah} or

use of an additional resistance term, no generally applicable method has been developed

(Kustas and Norman, 1996). Especially for sparse vegetation, kB^{-1} is difficult to

determine since it is dependent upon vegetation type and canopy stage as well as climate

conditions (Troufleau et al., 1997; Massman, 1999; Lhomme et al., 2000). Therefore the

kB^{-1} approach is quite questionable for sparse canopies (Lhomme et al., 1997; Verhoef et

al., 1997). Campbell and Norman (1998) conclude that a practical method for using satellite surface temperature measurements should have at least three qualities: (i) Accommodate the difference between aerodynamic temperature and radiometric temperature, (ii) not require a measurement of near-surface air temperature and (iii) rely more on differences in surface temperature over time or space rather than absolute surface temperatures to minimize the influence of atmospheric corrections and uncertainties in surface emissivity.

In this chapter, the physically-based analytical approaches using remote sensing are categorized as single-source (Bastiaanssen et al., 1998; Su, 2002; Allen et al., 2007) and dual-source models (Lhomme et al., 1994; Norman et al., 1995; Chebouni et al., 1996). A main difference between the two models are whether the model parameterizes the radiative and turbulent exchanges of soil and vegetation components in a thermal pixel as separate (dual-source) or lumped manner (single-source) (Figure 2.2).

2.2.3.1. Single-source approach

The single-source approach considers each thermal pixel area as a single homogeneous source of heat fluxes. One example of a single-source model called SEBAL (Surface Energy Balance Algorithm for Land) (Bastiaanssen, 1995) deals with the problem of inferring T_{aero} from T_{rad} by estimating dT (the temperature difference between T_1 and T_2, taken at two levels, z_1 and z_2, over the zero plane displacement) directly without measuring the absolute temperature at a given height.
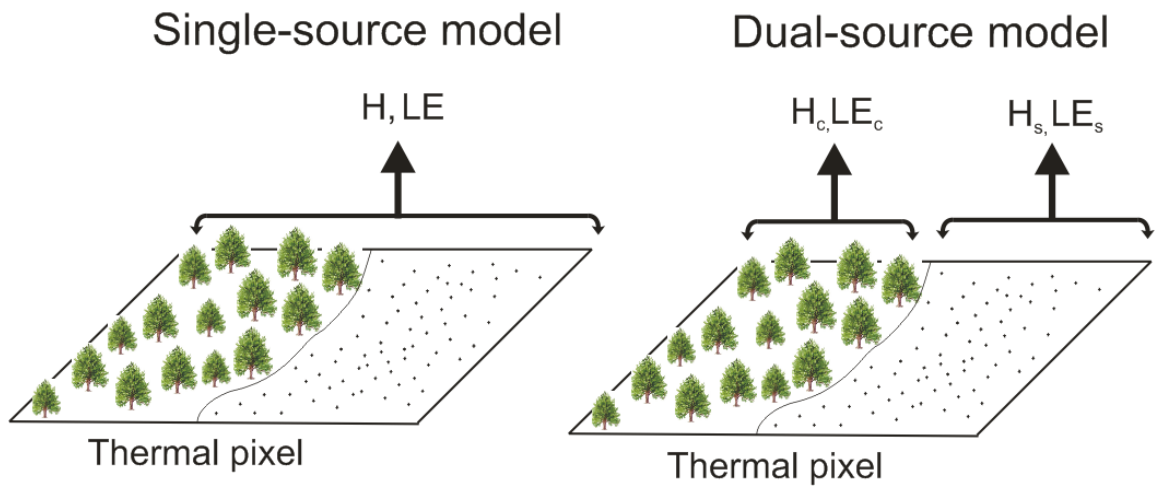
Figure 2.2 Schematic of the single-source (left) and dual-source (right) remote sensing model (subscript c and s is canopy and soil, respectively).

$$T_1 - T_2 = \Delta T_a = \frac{H\, r_{ah}}{\rho\, c_p} \qquad\qquad [2.36]$$

SEBAL selects two reference surface pixels (dry and wet) for internal calibration. The temperature difference (dT) for a dry reference surface (pixel) is calculated in SEBAL from the inversion of the sensible heat flux equation. There is no latent heat flux (LE=0) for the dry surface so that $H = R_n$ - G (Bastiaanssen et al., 1998). Based on the H value for a dry surface, ΔT_a of dry surface can be calculated from Eq. [2.36]. For a wet reference surface, all available energy R_n - G is used for evapotranspiration LE, so that $H \approx 0$ and $\Delta T_a \approx 0$. In order to keep requirements for high quality ground data to a minimum, Bastiaanssen (1995) presumed that $H = 0$ for the wet surface to eliminate the need for a ground-based ET prediction, so that ΔT_a for the wet surface is equal to zero.

Another single-source model METRIC (Mapping EvapoTranspiration at high Resolution with Internalized Calibration) developed by Allen et al. (2001) is similar to SEBAL but uses the used reference crop ET (ET_r) to predict LE for the dry and wet reference surfaces. METRIC calculates $H = R_n$ - G and $H = R_n$ - $G - 1.05 ET_r$ at the dry and wet reference surfaces, respectively, where ET_r is computed at the image time using weather data from local weather stations.

As mentioned above, SEBAL calculates the sensible heat flux for each pixel using the air temperature difference (dT) between heights z_1 and z_2. Several field observations confirm that land surfaces with a high dT are associated with high radiometric

temperatures (T_s) and those with a low dT with low radiometric temperatures. Field measurements in Egypt and Niger (Bastiaanssen et al., 1998), China (Wang et al., 1998), USA (Franks and Beven, 1997) and Kenya (Farah and Bastiaanssen, 2001) have shown that the relationship between T_s and dT is approximately positively linear for different field conditions including irrigated fields, deserts, and mountains. Therefore, SEBAL uses a linear relationship between dT and surface temperature (T_s) for the calculation of dT for each pixel in an image.

$$\Delta T_a = c_1 T_{rad} - c_2 \qquad [2.37]$$

where c_1 and c_2 are empirical coefficients valid for one particular moment (the time and date of an image) and landscape. By using the low and high values for ΔT_a as calculated from the wet and dry reference pixels, the extremes of H are used to find coefficients c_1 and c_2 that prevent outliers of H-fluxes and perform internal calibration. In the SEBAL implementation, the difference between T_{rad} and $T_{aero,}$ becomes less important if dT is derived by inverting the H-flux equation rather than deriving dT from independent T_{rad} and T_a measurements and kB^{-1} adjustments (Bastiaanssen et al., 1998). Computing dT from the inversion of Eq. [2.33] incorporates all biases in T_{rad} and r_{ah}. Thus, the empirical Eq. [2.37] meets the third quality stated by Campbell and Norman (1998) that one should rely on differences in radiometric surface temperature over space rather than absolute surface temperatures to minimize the influence of atmospheric corrections and uncertainties in surface emissivity.

2.2.3.2. Dual source approach

Dual source models were developed to partition radiative and turbulent energies into separate fluxes originating from soil surface and vegetation especially in sparsely vegetated areas. Some models consider energy exchange between soil and vegetation (Shuttleworth and Wallace, 1985; Choudhury and Monteith, 1988) and others assume only vertical fluxes without any interaction between soil and vegetation (Blyth and Harding, 1995; Lhomme and Chehbouni, 1999). Dual source models using remote sensing imagery have been widely applied and validated under various environmental conditions (Anderson et al., 1997; Kustas and Norman, 1997; Mecikalski et al., 1999; French et al., 2002; Li et al., 2005; Sánchez et al., 2007).

The dual source model use radiometric temperature observations to estimate the components of the surface energy balance from soil and vegetation. Here is the common formula used in dual-source models to estimate the sensible heat flux (Anderson et al., 1997; Mecikalski et al., 1999; Timmermans et al., 2007).

$$H = H_s + H_c = \rho C_p \frac{(T_s - T_a)}{r_s + r_a} + \rho C_p \frac{(T_c - T_a)}{r_{ah}} \qquad [2.38]$$

where the subscripts s and c represent soil and canopy components, respectively. r_a is the aerodynamic resistance of the canopy air layer [sm^{-1}], r_s is the resistance of the soil surface [sm^{-1}], r_{ah} is the bulk resistance [sm^{-1}] and T_a, T_c and T_s are the temperature [K] of the air within the canopy and canopy itself and the soil surface, respectively. Air

temperature can be obtained either from local weather station or a nested modeling

approach (Norman et al., 2003; Anderson et al., 2004). The use of this model requires

radiometric temperatures measured from both the soil and the canopy from remote

sensing. Anderson et al. (1997), Mecikalski et al. (1999) and Timmermans et al. (2007)

estimated these temperatures by:

$$T_{rad} \approx f_c(\phi)T_c + [1 - f_c(\phi)]T_s \qquad\qquad [2.39]$$

$$T_c = T_a + \left(\frac{H_c r_{ah}}{\rho C_p} \right) \qquad\qquad [2.40]$$

$$f_c(\phi) = 1 - exp\left(\frac{-0.5 LAI}{cos\,\phi} \right) \qquad\qquad [2.41]$$

where $f_c(\phi)$ is the apparent fractional coverage viewed as seen by the radiometer, ϕ is the

view angle and *LAI* is the leaf area index [-]. To estimate the latent fluxes (LE) from soil

and vegetation, a simple Priestley-Taylor approximation (Priestley and Taylor, 1972) was

used. Soil heat flux (G) is estimated from equation suggested by Choudbury et al. (1987).

$$LE_c = \alpha_{PT} f_g \frac{\Delta}{\Delta + \gamma} R_{nc} \qquad\qquad [2.42]$$

$$LE_s = R_{n\,s} - G - H_s \qquad\qquad [2.43]$$

$$G = 0.3 R_{ns} \qquad\qquad [2.44]$$

$$f_g = 1 - \left(\frac{NDVI_{max} - NDVI}{NDVI_{max} - NDVI_{min}} \right)^{1/\xi} \qquad\qquad [2.45]$$

where *LE_s, LE_c, R_ns, R_nc* are the latent heat and net radiation fluxes from the soil

(subscript s) and the canopy (subscript c), G is the soil heat flux, α_{PT} is the Priestley-Taylor parameter (1.3), Δ is the slope of the saturation vapor pressure-temperature curve at canopy temperature, γ is the psychrometric constant (0.066) [kPaK^{-1}], f_g is the fraction of green vegetation, $NDVI_{max}$ is $NDVI$ for complete vegetation cover, $NDVI_{min}$ is $NDVI$ for bare soil, ξ is a function of leaf orientation (0.8 for planophile canopy and >1.4 for erectophile canopy) (Choudhury et al., 1994; French, 2001).

Kustas and Norman (1997), Anderson et al. (1997) and Timmermans et al (2007) applied a dual-source model, TSEB, in various environments and computed surface energy balance components. Results from the dual-source model were validated against the Bowen ratio or eddy covariance measurements. The estimated total fluxes from combined soil and vegetation data all showed a reasonable accordance (< 20%) with ground measurements.

2.2.4. Numerical Hydrologic Models

Numerical/hydrologic models solve the equations describing the energy and mass flow processes in the soil-vegetation-atmosphere system. Although compared to the simple water bucket model, numerical/hydrologic hydrological models can deal with spatial heterogeneities and describe complex hydrological processes (Houser et al., 1998; Immerzeel and Droogers, 2008). However there is still a difficulty in accurately modeling hydrological cycles due to dynamic spatial and temporal variations of hydrological processes. Major problems in applying sophisticated hydrological models are high demand of input parameters describing soil, vegetation and atmosphere properties and

computation resources (Camillo et al., 1986; Carlson et al., 1995; Chen et al., 2005). In reality, such detailed hydrological data sets are rarely available on regional scale, therefore these models are less suitable for most large scale hydrology studies unless remote sensing information is used.

The use of remote sensing as the input variables to the hydrological models is relatively new research area (Kite and Pietroniro, 1996; Shuttleworth, 1998; Boegh et al., 2004). Here are several research examples successfully implemented hydrological models with remote sensing information. Droogers and Bastiaanssen (2002) applied SEBAL and the soil-water-atmosphere-plant environment (SWAP) model to evaluate an irrigation project in Western Turkey. The authors noted that the combination of a high temporal resolution hydrological model and high spatial resolution remote sensing will generate model products of high resolution in both space and time. Rivalland et al. (2005) used a soil-vegetation-atmosphere transfer (SVAT) method combining weather data and satellite imagery to estimate surface energy balance of the South-East of France. They applied SVAT model with a land use map derived from SPOT satellite imagery and fraction of vegetation cover (LAI) and surface albedo obtained from airborne measurements. The authors present a result showing a good agreement between SVAT estimated fluxes and ground measurements. Chen et al. (2005) applied a distributed hydrological model to estimate the ET and soil moisture of a forested watershed at high spatial resolution (30m) using vegetation index and type from Landsat imagery. Their study shows that spatial and temporal distributions of modeled ET and soil moisture are highly correlated with soil type and rainfall events.

So far, the main remote sensing information used in distributed hydrological modeling studies is high resolution precipitation, soil moisture, vegetation index and land cover data (Graetz, 1990; Band et al., 1993; Wallace, 1995; Kite and Pietroniro, 1996; Sellers et al., 1996; Kim and Barros, 2002). The most common interaction between remote sensing and distributed models is using remotely sensed data as model input variables (Plummer, 2000). However, there are more issues besides high demand of input parameters and computation resources, which are including spatial scale disparity between remote sensing data and a hydrological model (Wood, 1995) and selection of the most suitable remote sensing information (Engman, 1996). Nevertheless, with development of sensor technology and data processing, remote sensing will continue to be an important data source for hydrological models in terms of model validation and calibration.

REFERENCES

Aboukhaled, A., A. Alfaro, and M. Smith. 1982. Lysimeters. FAO Irrigation and Drainage Paper No. 39:1-68.

Allen, R.G., M. Smith, L.S. Pereira, and A. Perrier. 1994. An update for the calculation of reference evapotranspiration. ICID Bulletin 43:35-92.

Allen, R.G., W.O. Pruitt, J.A. Businger, L.J. Fritschen, M.E. Jensen, and F.H. Quinn. 1996. Chapter 4: Evaporation and Transpiration. American Society of Civil Engineering, NY.

Allen, R.G., L.S. Pereira, D. Raes, and M. Smith. 1998. Crop evapotranspiration. FAO Irrigation and drainage paper 56, FAO. Rome.

Allen, R.G., W.G.M. Bastiaanssen, M. Tasumi, and A. Morse. 2001. Evapotranspiration on the watershed scale using the SEBAL model and LandSat Images Paper Number 01-2224, ASAE, Annual International Meeting, Sacramento, California.

Allen, R.G., M. Tasumi, and R. Trezza. 2005. M E T R I C^{tm} Mapping Evapotranspiration at High Resolution. Applications Manual for Landsat Satellite Imagery. Version 2.0, Kimberly, Idaho, University of Idaho.

Allen, R.G., M. Tasumi, and R. Trezza. 2007. Satellite-based Energy Balance for Mapping Evapotranspiration with Internalized Calibration (METRIC) – Model. Journal of Irrigation and Drainage Engineering 133:380-394.

Alley, W.M. 1984. On The Treatment Of Evapotranspiration, Soil Moisture Accounting, And Aquifer Recharge In Monthly Water Balance Models. Water Resources Research 20:1137-1149.

Anderson, M.C., J.M. Norman, G.R. Diak, W.P. Kustas, and J.R. Mecikalski. 1997. A two-source time-integrated model for estimating surface fluxes using thermal infrared remote sensing. Remote Sensing of Environment 60:195-216.

Anderson, M.C., J.M. Norman, J.R. Mecikalski, R.D. Torn, W.P. Kustas, and J.B. Basara. 2004. A multiscale remote sensing model for disaggregating regional fluxes to micrometeorological scales. Journal of Hydrometeorology 5:343-363.

Angus, D.E., and P.J. Watts. 1984. Evapotranspiration - how good is the Bowen ratio method? Agricultural Water Management 8:133-150.

Asanuma, J., and K. Lemoto. 2006. Measurements of regional sensible heat flux over Mongolian grassland using large aperture scintillometer. Journal of Hydrology 333:58-67.

Baldocchi, D.D., B.B. Hicks, and T.P. Meyers. 1988. Measuring biosphere-atmosphere exchanges of biologically related gases with micrometeorological methods Ecology 69:1331-1340.

Band, L.E., P. Patterson, R. Nemani, and S.W. Running. 1993. Forest ecosystem processes at the watershed scale: incorporating hilslope hydrology. Agricultural and Forest Meteorology 63:93-126.

Bastiaanssen, W.G.M. 1995. Regionalization of surface flux densities and moisture indicators in composite terrain, Wageningen Agricultural University, Wageningen, Netherlands.

Bastiaanssen, W.G.M., M. Menenti, R.A. Feddes, and A.A.M. Holtslag. 1998. A remote sensing surface energy balance algorithm for land (SEBAL). Part 1: Formulation. Journal of Hydrology 212-213:198-212.

Bastiaanssen, W.G.M., E.J.M. Noordman, H. Pelgrum, G. Davids, B.P. Thoreson, and R.G. Allen. 2005. SEBAL model with remotely sensed data to improve water-resources management under actual field conditions. Journal of Irrigation and Drainage Engineering 131:85-93.

Beyrich, F., H.A.R. De Bruin, W.M.L. Meijninger, J.W. Schipper, and H. Lohse. 2002. Results from one-year continuous operation of a large aperture scintillometer over heterogeneous land surface. Boundary Layer Meteorology 105:85-97.

Blanc, T.V. 1987. Accuracy of bulk-method-determined flux, stability, and sea surface roughness. Journal of Geophysical Research 92:3867-3876.

Blyth, E.M., and R.J. Harding. 1995. Application of aggregation models to surface heat flux from the Sahelian tiger bush. Agricultural and Forest Meteorology 72:213−235.

Boegh, E., M. Thorsen, M.B. Butts, S. Hansen, J.S. Christiansen, P. Abrahamsen, C.B. Hasager, N. Jensen, P. Van der Keur, J.C. Refsgaard, K. Schelde, H. Soegaard, and A. Thomsen. 2004. Incorporating remote sensing data in physically based distributed agro-hydrological modeling. Journal of Hydrology 287:279–299.

Bowen, I.S. 1926. The ratio of heat losses by conduction and by evaporation from any water surface. Physical Review 27:779-787.

Brutsaert, W. 1991. Evaporation into the Atmosphere - Theory, History and Applications Netherlands, Kkluwer Academic Publishers.

Businger, J.A., J.C. Wyngaard, Y. Izumi, and E.F. Bradley. 1971. Flux profile relationships in the atmospheric surface layer. Journal of Atmospheric Science 28:181-189.

Camillo, P.J., P.E. O'Neill, and R.J. Gurney. 1986. Estimating soil hydraulic parameters using passive microwave data. IEEE Transactions on Geoscience and Remote Sensing GE-24:930-936.

Campbell, G.S., and J.M. Norman. 1998. An introduction to environmental biophysics. Second Edition Springer, New York, NY.

Caparinni, F., and F. Castelli. 2002. Remote sensing used to estimate land surface evaporation. EOS Transactions 83:290-291.

Carlson, T., and R. Buffum. 1989. On estimating total daily evapotranspiration from remote surface temperature measurements. Remote Sensing of Environment 29:197-207.

Carlson, T.N., R.R. Gillies, and T.J. Shmugge. 1995. An interpretation of methodologies for indirect measurement of soil water content. Agricultural and Forest Meteorology 77:191−205.

Cellier, P., and Y. Brunet. 1992. Flux-gradient relationships above tall plant canopies. Agricultural and Forest Meteorology 58:93-117.

Chebouni, A., D.L. Seen, E.G. Njoku, and B.M. Monteney. 1996. Examination of the difference between radiative and aerodynamic surface temperatures over sparsely vegetated surfaces. Remote Sensing of Environment 58:177-186.

Chehbouni, A., C. Watts, Y.H. Kerr, and F. Santiago. 2000. Methods to aggregate turbulent fluxes over heterogeneous surfaces: applications to SALSA data set in Mexico. Agricultural and Forest Meteorology 105:133-144.

Chen, J.M., X. Chen, W. Ju, and X. Geng. 2005. Distributed hydrological model for mapping evapotranspiration using remote sensing inputs. Journal of Hydrology 305:15-39.

Choudhury, B., and J.L. Monteith. 1988. A four-layer model for the heat budget of homogeneous land surfaces. Journal of the Royal Meteorological Society 114:373-398.

Choudhury, B., N. Ahmed, S. Idso, R. Reginato, and S. Daughtry. 1994. Relations between evaporation coefficients and vegetation indices studied by model simulations. Remote Sensing of Environment 50:1-17.

Choudhury, B. 1997. Global pattern of potential evaporation calculated from the Penman-Monteith equation using satellite and assimilated data. Remote Sensing of the Environment 61:64-81.

Choudhury, B.J., S.B. Idso, and R.J. Reginato. 1987. Analysis of an empirical model for soil heat flux under a growing wheat crop for estimating evaporation by an

infrared-temperature-based energy balance equation. Agriculture and Forest Meteorology 39:283-297.

Choudhury, B.J. 1989. Estimating evaporation and carbon assimilation using infrared temperature data: vistas in modeling Wiley, New York.

Compaore, H., J.M.H. Hendrickx, S.-H. Hong, J. Friesen, N.C.v.d. Giesen, C. Rodgers, J. Szarzynski, and P.L.G. Vlek. 2008. Evaporation mapping at two scales using optical imagery in the White Volta Basin, Upper East Ghana. Physics and Chemistry of the Earth 33:127-140.

Cosgrove, B.A., D. Lohmann, K.E. Mitchell, P.R. Houser, E.F. Wood, J. Schaake, A. Robock, C. Marshall, J. Sheffield, L. Luo, Q. Duan, R.T. Pinker, J.D. Tarpley, R.W. Higgins, and J. Meng. 2003. Real-time and retrospective forcing in the North American Land Data Assimilation System (NLDAS) project. Journal of Geophysical Research 108. doi:10.1029/2002JD003118.

Courault, D., B. Seguin, and A. Olioso. 2005. Review on estimation of evapotranspiration from remote sensing data: From empirical to numerical modeling approaches. Irrigation and Drainage Systems 19:223-249.

De Bruin, H.A.R., W. Kohsiek, and B.J.J.M. van den Hurk. 1993. A verification of some methods to determine the fluxes of momentum, sensible heat and water vapour using standard deviation and structure parameter of scalar meteorological quantities. Boundary-Layer Meteorology 76:25-40.

De Bruin, H.A.R., B.J.M. van de Hurk, and W. Kohsiek. 1995. The scintillation method tested over a dry vineyard area. Boundary-Layer Meteorology 76:25-40.

Droogers, P., and W.G.M. Bastiaanssen. 2002. Irrigation performance using hydrological and remote sensing modeling. Journal of Irrigation and Drainage Engineering 128:11-18.

Engman, E.T. 1996. Remote sensing applications to hydrology: future impact. Hydrological Sciences 41:637-647.

Farah, H.O., and W.G.M. Bastiaanssen. 2001. Spatial variations of surface parameters and related evaporation in the Lake Naivasha Basin estimated from remote sensing measurements. Hydrological Processes 15:1585-1607.

Franks, S.W., and K.J. Beven. 1997. Estimation of evapotranspiration at the landscape scale: a fuzzy disaggregation approach. Water Resources Research 33:2929-2938.

French, A.N. 2001. Scaling of surface energy fluxes using remotely sensed data. PhD Thesis, University of Maryland, College Park.

French, A.N., T.J. Schmugge, and W.P. Kustas. 2002. Estimating evapotranspiration over

El Reno, Oklahoma with ASTER imagery. Agronomie 22:105-106.

Fritschen, L.J. 1965. Accuracy of evapotranspiration determinations by the Bowen ratio method. Bulletin of the International Association of Scientific Hydrology 2:38-48.

Fritschen, L.J., and L.W. Gay. 1979. Environmental Instrumentation Springer-Verlag, New York.

Fuchs, M., and C.B. Tanner. 1970. Error analysis of Bowen ratios measured by differential psychrometry. Agricultural Meteorology 7:329-334.

Garatuza-Payan, J., and C. Watts. 2005. The use of remote sensing for estimating ET of irrigated wheat and cotton in Northwest Mexico Irrigation and Drainage Systems 19:301-320.

Garratt, J.R. 1978. Flux-profile relations above tall vegetation. Quarterly Journal of the Royal Meteorological Society 104:199-211.

Garratt, J.R. 1992. The Atmospheric Boundary Layer Cambridge, UK, Cambridge University Press.

Gash, J.H.C. 1986. A note on estimating the effect of a limited fetch on micrometeorological evaporation measurements. Boundary-Layer Meteorology 35:409-413.

Graetz, R.D. 1990. Remote sensing of terrestrial ecosystem structure: An ecologist's pragmatic view Springer–Verlag, New York.

Granger, R.J. 2000. Satellite-derived estimates of evapotranspiration in the Gediz basin. Journal of Hydrology 229:70-76.

Green, A.E., B.E. Clothier, J.P. Kerr, and D.R. Scotter. 1984. Evapotranspiration from Pasture: A Comparison of Lysimeter and Bowen Ratio Measurements with Priestley-Taylor Estimates New Zealand Journal of Agricultural Research 27:321-327.

Green, A.E., K.J. McAneney, and M.S. Astill. 1994. Surface layer scintillation measurements of daytime time heat and momentum fluxes. Boundary-Layer Meteorology 68:357-373.

Green, A.E., M.S. Astill, K.J. McAneney, and J.P. Nieveen. 2001. Path averaged surface fluxes determined from infrared and microwave scintillometers. Agricultural and Forest Meteorology 109:233-247.

Hafeez, M., M. Andreini, J. Liebe, J. Friesen, A. Marx, and N.v.d. Giesen. 2006. Hydrological parameterization through remote sensing in Volta Basin, West Africa. International Journal of River Basin Management 4:1-8.

Hatton, T.J., and R.A. Vertessy. 1990. Transpiration of plantation Pinus radiata estimated by the heat pulse method and the Bowen ratio. Hydrological Processes 4:289-298.

Hemakumara, H., L. Chandrapala, and A. Moene. 2003. Evapotranspiration fluxes over mixed vegetation areas measured from a large aperture scintillometer. Agricultural Water Management 58:109–122.

Hendrickx, J.M.H., and S.-H. Hong. 2005. Mapping sensible and latent heat fluxes in arid areas using optical imagery. Proceedings of International Society for Optical Engineering, SPIE 5811:138-146.

Hendrickx, J.M.H., J. Kleissl, J. Gomez-Vlez, S.-H. Hong, J. Fbrega-Duque, D. Vega, H. Moreno-Ramrez, and F. Ogden. 2007. Scintillometer networks for calibration and validation of energy balance and soil moisture remote sensing algorithms. Proceedings of International Society for Optical Engineering, SPIE 6565:(in press).

Hill, R., S. Clifford, and R. Lawrence. 1980. Refractive-index and absorption fluctuation in the infrared caused by temperature, humidity, and pressure fluctuations. Journal of the Optical Society of America 70:1192-1205.

Hill, R.J., R.A. Bohlander, S.F. Clifford, R.W. McMillan, J.T. Priestley, and W.P. Schoenfeld. 1988. Turbulence-induced millimetre-wave scintillation compared with micrometeorological measurements. IEEE Transactions on Geoscience and Remote Sensing 26:330-341.

Hill, R.J. 1992. Review of optical scintillation methods of measuring the refractive— index spectrum, inner scale, and surface fluxes. Waves in Random Media 2:179-201.

Horst, T.W., and J.C. Weil. 1992. Footprint Estimation for Scalar Flux Measurements in the Atmospheric Surface Layer. Boundary-Layer Meteorology 59:279-296.

Houser, P.R., W.J. Shuttleworth, J.S. Famiglietti, H.V. Gupta, K.H. Syed, and D.C. Goodrich. 1998. Integration of soil moisture remote sensing and hydrological modeling using data assimilation. Water Resources Research 34:3405-3420.

Hsieh, C.-I., G.G. Katul, and T.-W. Chi. 2000. An approximate analytical model for footprint estimation of scalar fluxes in thermally stratified atmospheric flows. Advances in Water Resources 23:765-772.

Immerzeel, W.W., and P. Droogers. 2008. Calibration of a distributed hydrological model based on satellite evapotranspiration. Journal of Hydrology 349:411-424.

Irmak, S., R.G. Allen, and E.B. Whitty. 2003. Daily grass and alfalfa-reference evapotranspiration estimates and alfalfa-to-grass evapotranspiration ratios in Florida. Journal of Irrigation and Drainage Engineering 129:360-370.

Itenfisu, D., R.L. Elliot, R.G. Allen, and I.A. Walter. 2003. Comparison of reference evapotranspiration calculations as part of the ASCE standardization effort. Journal of Irrigation and Drain Engineering 129:440-448.

Itier, B. 1981. Une me´thode simple pour la me´sure de l'evapotranspiration re´elle a` l'e´chelle de la parcelle. Agronomie 1:869-876.

Jackson, R.D., R.J. Reginato, and S.B. Idso. 1977. Wheat canopy temperatures: A practical tool for evaluating water requirements. Water Resources Research 13:651-656.

Jackson, T.J., T.J. Schumgge, and E.T. Engman. 1997. Remote sensing applications to hydrology: soil moisture. Hydrological Sciences Journal 41:517-530.

Janssen, H., J. Carmeliet, and H. Hens. 2004. The influence of soil moisture transfer on building heat loss via the ground. Building and Environment 39:825 - 836.

Jensen, M.E., R.D. Burman, and R.G. Allen. 1990. Evapotranspiration and irrigation water requirements. ASCE Manuals and Rep. on Engineering Practice No. 70, New York.

Jia, L., Z. Su, B.v.d. Hurk, M. Menenti, A. Moene, H.A.R. De Bruin, J.J.B. Yrisarry, M. Ibanez, and A. Cuesta. 2003. Estimation of sensible heat flux using the Surface Energy Balance System (SEBS) and ATSR measurements. Physics and Chemistry of the Earth 28:75-88.

Jiang, L., and S. Islam. 2001. Estimation of surface evaporation map over southern Great Plains using remote sensing data. Water Resources Research 37:329-340.

Kanemasu, E.T., S.B. Verma, E.A. Smith, L.G. Fritschen, M. Wesely, R.T. Field, W.P. Kustas, H. Weaver, J.B. Stewart, R. Gurney, G. Panin, and J.B. Moncrieff. 1992. Surface flux measurement in FIFE: An overview. Journal of Geophysical Research 97:15,547-15,555.

Kerr, H., J. Imbernon, G. Dedieu, O. Hautecoeur, J.P. Lagouarde, and B. Seguin. 1989. NOAA AVHRR and its uses for rainfall and evapotranspiration monitoring. International Journal of Remote Sensing 10:847-854.

Kim, G., and A.P. Barros. 2002. Space-time characterization of soil moisture from passive microwave remotely sensed imagery and ancillary data. Remote Sensing of Environment 81:393-403.

Kite, G.W., and A. Pietroniro. 1996. Remote sensing application in hydrological modeling. Hydrological Sciences 41:563-591.

Kizer, M.A., and R.L. Elliott. 1991. Eddy correlation systems for measuring evapotranspiration. Transactions of American Society of Agricultural Engineers

34:387-392.

Kleissl, J., S.-H. Hong, J.D. Gomez, and J.M.H. Hendrickx. 2008. New Mexico
Scintillometer Network in Support of Remote Sensing, and Hydrologic and
Meteorological Models. Boundary Layer Meteorology (submitted).

Kohsiek, W., W.M.L. Meijninger, A.F. Moene, B.G. Heusinkveld, O.K. Hartogensis,
W.C.A.M. Hillen, and H.A.R. De Bruin. 2002. An extra large aperture
scintillometer (XLAS) with a 9.8km path length. Boundary-Layer Meteorology
105:119-127.

Kondo, J. 1975. Air-sea bulk transfer coefficients in diabatic conditions. Boundary-Layer
Meteorology 9:91-112.

Kustas, W.P., B.J. Choudhury, M.S. Moran, R.J. Reginato, and R.D. Jackson. 1989.
Determination of sensible heat flux over sparse canopy using thermal infrared
data. Agricultural and Forest Meteorology 44:197-216.

Kustas, W.P., M.S. Moran, K.S. Humes, D.I. Stannard, J.P.J. Pinter, L.E. Hipps, E.
Swiatek, and D.C. Goodrich. 1994. Surface energy balance estimates at local and
regional scales using optical remote sensing from an aircraft platform and
atmospheric data collected over semiarid rangelands. Water Resources Research
30:1241-1259.

Kustas, W.P., and J.M. Norman. 1996. Use of remote sensing for evapotranspiration
monitoring over land surfaces. Hydrological Sciences 41:495-516.

Kustas, W.P., and J.M. Norman. 1997. A two-source approach for estimating turbulent
fluxes using multiple angle thermal infrared observations. Water Resources
Research 33:1495-1508.

Laubach, J., and U. Teichmann. 1999. Surface energy budget variability: A case study
over glass with special regard to minor inhomogeneities in the source area.
Theoretical Applied Climatology 62:9-24.

Legg, B.J., I.F. Long, and P.J. Zemroch. 1981. Aerodynamic properties of field bean and
potato crops. Agricultural Meteorology 23-43.

Lhomme, J.-P., B. Monteny, and M. Amadou. 1994. Estimating sensible heat flux from
radiometric temperature over sparse millet. Agricultural and Forest Meteorology
68:77–91.

Lhomme, J.-P., D. Troufleau, B. Monteny, and A. Vidal. 1997. Estimation of sensible
heat flux over sparsely vegetated surfaces. Journal of Hydrology 188-189:839-
855.

Lhomme, J.-P., and A. Chehbouni. 1999. Comments on dual-source

vegetation±atmosphere transfer models. Agricultural and Forest Meteorology 94:269-273.

Lhomme, J.-P., A. Chehbouni, and B. Monteny. 2000. Sensible heat flux-radiometric surface temperature relationship over sparse vegetation parameterizing B^{-1}. Boundary-Layer Meteorology 97:431-457.

Li, F., W.P. Kustas, J.H. Prueger, C.M.U. Neale, and J.J. Jackson. 2005. Utility of remote sensing based two-source energy balance model under low and high vegetation cover conditions. Journal of Hydrometeorology 6:878−891.

Liu, X.Y., and E. Lin. 2005. Performance of the Priestley-Taylor equation in the semiarid climate of North China. Agricultural Water Management 71:1-17.

Lo, S.C.D., E. Mougin, and J.P. Gastellu-Etchegorry. 1993. Relating the global vegetation index to net primary productivity and actual evapotranspiration over Africa. International Journal of Remote Sensing 14:1517-1546.

Loescher, H., T. Ocheltree, B. Tanner, E. Swiatek, B. Dano, J. Wong, G. Zimmerman, J. Campbell, C. Stock, L. Jacobsen, Y. Shiga, J. Kollas, J. Liburdy, and B. Law. 2005. Comparison of temperature and wind statistics in contrasting environments among different sonic anemometer-thermometers. Agricultural Forest Meteorology 133:119-139.

Ma, Y., M. Menenti, O. Tsukamoto, H. Ishikawa, J. Wang, and Q. Gao. 2004. Remote sensing parameterization of regional land surface heat fluxes over arid area in northwestern China. J. Arid Environ. 57:257-273.

Ma, Y., L. Zhong, Z. Su, H. Ishikawa, M. Menenti, and T. Koike. 2006. Determination of regional distributions and seasonal variations of land surface heat fluxes from Landsat-7 Enhanced Thematic Mapper data over the central Tibetan Plateau area. Journal of Geophysical Research 111:D10305, doi:10.1029/2005JD006742.

Massman, W.J. 1999. A model study of kB-1 for vegetated surfaces using 'localized nearfield' Lagrangian theory. Journal of Hydrology 223:27-43.

Massman, W.J., and X. Lee. 2002. Eddy covariance flux corrections and uncertainties in long-term studies of carbon and energy exchanges. Agricultural and Forest Meteorology 113:121-144.

Mather, J.R. 1972. The Climatic Water Budget Lexington Books,.

McAneney, K.J., A.E. Green, and M.S. Astill. 1995. Large-aperture scintillometry: the homogeneous case. Agricultural and Forest Meteorology 76:149–162.

McAneney, K.J., and B. Itier. 1996. Operational limits to the Priestley-Taylor formula. Irrigation Science 17:37–43.

Mecikalski, J.R., G.R. Diak, M.C. Anderson, and J.M. Norman. 1999. Estimating fluxes on continental scales using remotely-sensed data in an atmospheric-land exchange model. Journal of Applied Meteorology 38:1352-1369.

Meijninger, W.M.L., and H.A.R. De Bruin. 2000. The sensible heat fluxes over irrigated areas in western Turkey determined with a large aperture scintillometer. Journal of Hydrology 229:42-49.

Meijninger, W.M.L., O.K. Hartogensis, W. Kohsiek, J.C.B. Hoedjes, R.M. Zuurbier, and H.A.R. De Bruin. 2002. The determination of the area-averaged sensible heat flux with a large aperture scintillometer over a heterogeneous surface-the Flevoland field experiment. Boundary-Layer Meteorology 105:37-62.

Mekonnen, M., and W.G.M. Bastiaanseen. 2000. A new simple method to determine crop coefficients for water allocation planning from satellites: results from Kenya. Irrigation and Drainage Systems 14:237-256.

Menenti, M., S. Azzali, W. Verhoef, and R. van Swol. 1993. Mapping agroecological zones and time lag in vegetation growth by means of Fourier Analysis of time series of NDVI images. Advances in Space Research 13:233-237.

Miller, D.H. 1977. Water at the surface of the Earth Academic Press, New York.

Mintz, Y., and G.K. Walker. 1993. Global Fields of Soil Moisture and Land Surface Evapotranspiration Derived from Observed Precipitation and Surface Air Temperature. Journal of Applied Meteorology 32:1305-1334.

Mohan, S., and N. Arumugam. 1996. Relative importance of meteorological variables in evapotranspiration: Factor analysis approach. Water Resources Management 10:1-20.

Monin, A.S., and A.M. Obukhov. 1954. Basic laws of turbulent mixing in the atmosphere near the ground. Trudy Geofizicheskogo Instituta, Akademiya Nauk SSSR 24:163-187.

Monteith, J.L., and M.H. Unsworth. 1990. Principles of Environmental Physics, Edward Arnold, London.

Moran, M.S., and R.B. Jackson. 1991. Assessing the spatial distribution of evapotranspiration using remotely sensed inputs. Journal of Environmental Quality 20:725-735.

Neale, C., W. Bausch, and D. Heermann. 1989. Development of reflectance-based crop coefficients for corn. Transactions of American Society of Agricultural Engineers 32:1891-1899.

Nie, D., E.T. Kanemasu, L.J. Fritschen, H.L. Weaver, E.A. Smith, S.B. Verma, R.T. Field,

W.P. Kustas, and J.B. Stewart. 1992. An intercomparison of surface flux measurement systems used during FIFE 1987. Journal of Geophysical Research 97:18,715-18,724.

Nieuwenhuis, G., E. Schmidt, and H. Tunnissen. 1985. Estimation of regional evapotranspiration of arable crops from thermal infrared images. International Journal of Remote Sensing 6:1319–1334.

Nieveen, J.G., A.E. Green, and W. Kohsiek. 1998. Using a large-aperture scintillometer to measure absorption and refractive index fluctuations. Boundary-Layer Meteorology 87:101-116.

Nishida, K., R.R. Nemani, S.W. Running, and J.M. Glassy. 2003. An operational remote sensing algorithm of land surface evaporation. Journal of Geophysical Research 108 (D9):doi:10.1029/2002JD002062.

Norman, J.M., W.P. Kustas, and K.S. Humes. 1995. A two-source approach for estimating soil and vegetation energy fluxes from observations of directional radiometric surface temperature. Agricultural and Forest Meteorology 77:163-293.

Norman, J.M., M.C. Anderson, W.P. Kustas, A.N. French, J. Mecikalski, R. Torn, G.R. Diak, T.J. Schmugge, and B.C.W. Tanner. 2003. Remote sensing of surface energy fluxes at 10 1-m pixel resolutions. Water Resources Research 39:1221. doi:10.1029/2002WR001775.

Panofsky, H.A., and J.A. Dutton. 1984. Atmospheric Turbulence: Models and Methods for Engineering Applications Wiley, New York.

Pelgrum, H., and W.G.M. Bastiaanssen. 1996. An intercomparison of techniques to determine the area-averaged latent heat flux from individual in situ observations: a remote sensing approach using the European Field Experiment in a Desertification-Threatened Area data. Water Resources Research 32:2775-2786.

Perez, P.J., F. Castellvi, M. Ibañez, and J.I. Rosell. 1999. Assessment of reliability of Bowen ratio method for partitioning fluxes. Agricultural and Forest Meteorology 97:141-150.

Peters Lidard, C.D., S. Kumar, Y. Tian, J.L. Eastman, and P. Houser. 2004. Global urban-scale land-atmosphere modeling with the land information system. 84th AMS Annual Meeting 11-15 January 2004, Symposium on Planning, Nowcasting, and Forecasting in the Urban Zone.

Plummer, S.E. 2000. Perspectives on combining ecological process models and remotely sensed data. Ecological Modelling 129:169–186.

Polonio, D., and M.R. Soler. 2000. Surface flux estimation over agricultural areas: Comparison of methods and the effects of land surface inhomogeneity.

Theoretical Applied Climatology 67:65-79.

Priestley, C.H.B., and R.J. Taylor. 1972. On the assessment of surface heat flux and evaporation using large-scale parameters. Monthly Weather Review 100:81-92.

Qualls, R., and W. Brutsaert. 1996. Effect of vegetation density on the parameterization of scalar roughness to estimate spatially distributed sensible heat fluxes. Water Resources Research 32:645-652.

Qualls, R., and T. Hopson. 1998. Combined use of vegetation density, friction velocity, and solar elevation to parameterize the scalar roughness for sensible heat. Journal of Atmospheric Sciences 55:1198-1208.

Rana, G., and N. Katerji. 1996. Evapotranspiration measurement for tall plant canopies: the sweet sorghum case. Theoretical Applied Climatology 54:187-200.

Rana, G., and N. Katerji. 2000. Measurement and estimation of actual evapotranspiration in the field under Mediterranean climate: a review. European Journal of Agronomy 13:125-153.

Reginato, R.J., R.D. Jackson, and J. Pinter. 1985. Evapotranspiration calculated from remote sensing and ground station meteorological data. Remote Sensing of Environment 18:75-89.

Rivalland, V., J. Demarty, A. Olioso, M. Weiss, P. Rossello, J. F., Y. Inoue, and F. Baret. 2005. Evapotranspiration monitoring using remote sensing measurements assimilated in a SVAT model. Geophysical Research Abstracts 7.

Sánchez, J.M., W.P. Kustas, V. Caselles, and M.C. Anderson. 2007. Modelling surface energy fluxes over maize using a two-source patch model and radiometric soil and canopy temperature observations. Remote Sensing of Environment accepted.

Schmid, H.P., and T.R. Oke. 1990. A model to estimation the source area contributing to turbulent exchange in the surface layer over patchy terrain. Quarterly Journal of The Royal Meteorological Society 116:965-988.

Schuepp, P.H., M.Y. Leclerc, J.I. MacPherson, and R.L. Desjardins. 1990. Footprint prediction of scalar fluxes from analytical solutions of the diffusion equation. Boundary-Layer Meteorology 50:355-373.

Schüttemeyer, D., C. Schillings, A.F. Moene, and H.A.R. De Bruin. 2007. Satellite-based actual evapotranspiration over drying semiarid terrain in West Africa. Journal of Applied Meteorology and Climatology 46:97-111 DOI: 10.1175/JAM2444.1.

Seevers, P.M., and R.W. Ottmann. 1994. Evapotranspiration estimation using a normalized difference vegetation index transformation of satellite data. Hydrological Sciences:333-345.

Seguin, B., D. Courault, and M. Guerif. 1994. Surface temperature and evapotranspiration: applications of local scale methods to regional scales using satellite data. Remote Sensing of Environment 49:287-295.

Seguin, B.D., and B. Itier. 1983. Using midday surface temperature to estimate daily evapotranspiration from satellite thermal IR data. International Journal of Remote Sensing 4:371-383.

Sellers, P.J., D.A. Randall, G.J. Collatz, J.A. Berry, C.B. Field, D.A. Dazlich, C. Zhang, G.D. Collelo, and L. Bounoua. 1996. A revised land surface parameterization (SiB2) for atmospheric GCMs. Part I. Model formulation. Journal of Climate 9:676–705.

Shouse, P., W.A. Jury, and L.H. Stolzy. 1980. Use of Deterministic and Empirical Models to Predict Potential Evapotranspiration in an Advective Environment Agronomy Journal 72:994-998.

Shuttleworth, J. 1998. Combining remotely sensed data using aggregation algorithms. Hydrology and Earth System Sciences 2:149-158.

Shuttleworth, J. 2007. Putting the 'vap' into evaporation. Hydrology and Earth System Sciences 11:210-244.

Shuttleworth, W.J., and J.S. Wallace. 1985. Evaporation from sparse crops-an energy combination theory. Quarterly Journal of The Royal Meteorological Society 111:839-855.

Silberstein, R.P., M. Sivapalan, and A. Wyllie. 1999. On the validation of a coupled water and energy balance model at small catchment scales. Journal of Hydrology 220:149-160.

Sinclair, T.R., L.H. Allen Jr, and E.R. Lemon. 1975. An analysis of errors in the calculation of energy flux densities above vegetation by a Bowen-ratio profile method. Boundary-Layer Meteorology 8:129-139.

Singh, V.P., and C.-Y. Xu. 1997. Sensitivity of mass transfer-based evaporation equations to errors in daily and monthly input data. Hydrological Processes 11:1465-1473.

Srivastava, S.K., V. Jayaraman, P.P.N. Rao, B. Manikiam, and M.G. Chandrasekhar. 1997. Interlinkages of NOAA/AVHRR derived integrated NDVI to seasonal precipitation and transpiration in dryland tropics. International Journal of Remote Sensing 18:2931-2952.

Stannard, D.I. 1997. A theoretically based determination of Bowen-ratio fetch requirements. Boundary-Layer Meteorology 83:375-406.

Su, Z. 2002. The Surface Energy Balance System (SEBS) for estimation of turbulent heat

fluxes. Hydrology and Earth System Sciences 6:85-99.

Swinbank, W.C. 1951. The measurement of vertical transfer of heat and water vapour and momentum in the lower atmosphere with some results. Journal of Meteorology 8:135-145.

Tanner, B. 1960. Energy balance approach to evapotranspiration from crops. Soil Science Society of America Journal 24:1-9.

Tanner, B. 1988. Use requirements for Bowen ratio and eddy correlation determination of evapotranspiration ASCE, NY.

Tanner, C.B. 1967. Measurement of evapotranspiration American Society of Agronomists, Madison, Wisconsin.

Thom, A.S., J.B. Stewart, H.R. Oliver, and J.H.C. Gash. 1975. Comparison of aerodynamic and energy budget estimates of fluxes over a pine forest. Quarterly Journal of the Royal Meteorological Society 101:93–105.

Thornthwaite, C.W., and B. Holzman. 1942. Measurement of Evaporation from Land and Water Surfaces. U.S. Department of Agriculture Technical Bulletin No. 817. pp. 75.

Thornthwaite, C.W. 1948. An Approach Toward a Rational Classification of Climate. Geographical Review 38:55-94.

Thunnissen, H.A., and J.A. Nieuwenhuis. 1990. A simplified method to estimate regional 24-h evapotranspiration from thermal infrared data. Remote Sensing of Environmental Modelling & Software 31:211-220.

Timmermans, W.J., W.P. Kustas, M.C. Anderson, and A.N. French. 2007. An intercomparison of the Surface Energy Balance Algorithm for Land (SEBAL) and the Two-Source Energy Balance (TSEB) modeling schemes Remote Sensing of Environment 108:369-384

Troufleau, D., J.P. Lhomme, B. Monteny, and A. Vidal. 1997. Sensible heat flux and radiometric surface temperature over sparse Sahelian vegetation. I. An experimental analysis of the kB-1 parameter. Journal of Hydrology 188-189:815-838.

Twine, T.E., W.P. Kustas, J.M. Norman, D.R. Cook, P.R. Houser, T.P. Meyers, J.H. Prueger, P.J. Starks, and M.L. Wesely. 2000. Correcting eddy-covariance flux underestimates over a grassland. Agricultural and Forest Meteorology 103:279-300.

Unland, H.E., P.R. Houser, W.J. Shuttleworth, and Z.L. Yang. 1996. Surface flux measurement and modelling at a semi-arid Sonoran Desert Site. Agricultural and

Forest Meteorology 82:119-153.

Van Der Keur, P., S. Hansen, and K. Svhelde. 2001. Modification of the DAISY SVAT model for potential use of remotely sensed data. Agricultural and Forest Meteorology 106:215-231.

Verhoef, A., H.A.R. De Bruin, and J.M.V.D. Hurk. 1997. Some practical notes on the parameter kB-1 for sparse vegetation. Journal of Applied Meteorology 36:560-577.

Vidal, A., and A. Perrier. 1989. Analysis of a simplified relation for estimating daily evapotranspiration from satellite thermal IR data. International Journal of Remote Sensing 10:1327-1337.

Villagra, M.M., O.O.S. Bacchi, R.L. Tuon, and K. Reichardt. 1995. Difficulties of estimating evapotranspiration from the water balance equation Agricultural and Forest Meteorology 72:317-325.

Wallace, J.S. 1995. Calculating evaporation: resistance to factors. Agricultural and Forest Meteorology 73:353-366.

Wang, J., W.G.M. Bastiaanssen, Y. Ma, and H. Pelgrum. 1998. Aggregation of land surface parameters in the oasis-desert systems of Northwest China. Hydrological Sciences 12:2133-2147.

Watts, C.J., A. Chehbouni, J.-C. Rodriguez, Y.H. Kerr, O. Hartogensis, and H.A.R. De Bruin. 2000. Comparison of sensible heat flux estimates using AVHRR with scintillometer measurements over semi-arid grassland in northwest Mexico. Agricultural and Forest Meteorology 105:81–89.

Wesely, M.L. 1976. A comparison of two optical methods for measuring line-averages of thermal exchanges above warm water surfaces. Journal of Applied Meteorology 16:1177-1188.

Wieringa, J. 1993. Representative roughness parameters for homogeneous terrain. Boundary-Layer Meteorology 63:323–363.

Willmott, C.J., C.M. Rowe, and Y. Mintz. 1985. Climatology of the Terrestrial Seasonal Water Cycle. Journal of Climatology 5:589-606.

Wilson, K.B., P.J. Hanson, P.J. Mulholland, D.D. Baldocchi, and S.D. Wullschleger. 2001. A comparison of methods for determining forest evapotranspiration and its components: sap-flow, soil water budget, eddy covariance and catchment water balance. Agricultural and Forest Meteorology 106:153-168.

Wood, E.F. 1995. Scaling behaviour of hydrological fluxes and variables: empirical studies using a hydrological model and remote sensing data. Hydrological

Processes 9:331–346.

Wright, J.L. 1991. Using weighing lysimeters to developed evapotranspiration crop coefficients. Proceeding of the International Symposium on Lysimetry, Honolulu, Hawaii, ASAE.

Xing, Z., L. Chow, F.-R. Meng, H.W. Rees, L. Stevens, and J. Monteith. 2008. Validating Evapotranspiration Equations Using Bowen Ratio in New Brunswick, Maritime, Canada. Sensors 8:412-428.

Xu, Q., and C.J. Qiu. 1997. A variation method for computing surface heat fluxes from ARM surface energy and radiation balance systems. Journal of Applied Meteorology 36:3-11.

Yaglom, A.M. 1977. Comments on wind and temperature flux-profile relationships. Boundary-Layer Meteorology 11:89-102.

Yoder, R.E., L.O. Odhiambo, and W.C. Wright. 2005. Evaluation of methods for estimating daily reference crop evapotranspiration at a site in the humid Southeast United states. Applied Engineering in Agriculture 21:197–202.

CHAPTER 3

SURFACE ENERGY BALANCE ALGORITHM FOR LAND (SEBAL)

SEBAL is a remote sensing flux algorithm that evaluates the components of the energy balance and determines the ET rate as the residual:

$$LE = R_n - G - H \qquad\qquad [3.1]$$

where R_n is the net radiation flux density [Wm^{-2}], G is the soil heat flux density [Wm^{-2}], H is the sensible heat flux density [Wm^{-2}], and LE (= λET) is the latent heat flux density [Wm^{-2}], which can be converted to the ET rate [mmd^{-1}] using the latent heat of vaporization of water λ [Jkg^{-1}]. Figure 3.1 shows the surface energy balance components for a land surface. In this study, the flux of net radiation (R_n) is considered positive when it is directed toward the surface, latent heat (LE) and sensible heat (H) fluxes are considered positive when coming from the surface toward the atmosphere, and soil heat flux (G) is taken as positive when going away from the surface to deeper depths in the soil.

To implement SEBAL, images are needed with information on reflectance in the
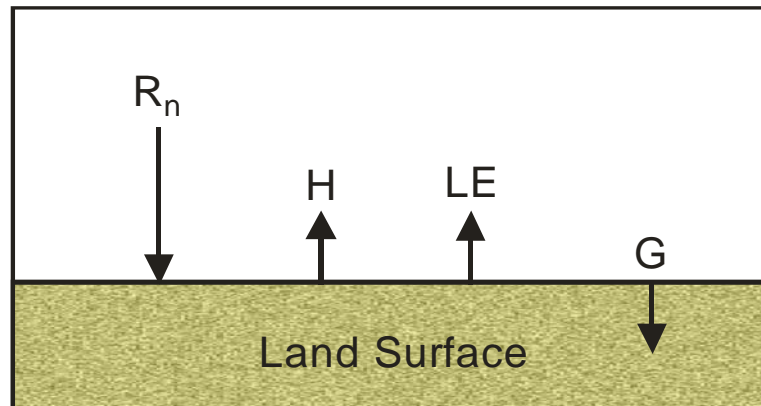
Figure 3.1 Surface energy balance for a vegetated surface. The arrows indicate the direction of positive fluxes.

visible, near-infrared and mid-infrared bands as well as emission in the thermal infrared band. A schematic of the general computational process of SEBAL algorithm is shown in Figure 3.2.

3.1. NET RADIATION

The net radiation R_n under cloud-free conditions is obtained from the radiation balance between net shortwave and net longwave radiation at the land surface.

$$R_n = R_{ns} + R_{nL} \qquad [3.2]$$

where

$$R_{ns} = R_{s\downarrow} - R_{s\uparrow} = R_{s\downarrow} - \alpha \cdot R_{s\downarrow} \qquad [3.3]$$

and

$$R_{nL} = R_{L\downarrow} - R_{L\uparrow} - (1 - \varepsilon_0) \cdot R_{L\downarrow} \qquad [3.4]$$

Here R_{ns} is the net shortwave radiation [Wm^{-2}], R_{nL} is the net longwave radiation [Wm^{-2}], $R_{s\downarrow}$ is the incoming shortwave radiation [Wm^{-2}], $R_{s\uparrow}$ is the outgoing shortwave radiation [Wm^{-2}], $R_{L\downarrow}$ is the incoming longwave radiation emitted from the atmosphere [Wm^{-2}], $R_{L\uparrow}$ is the outgoing longwave radiation emitted from the land surface [Wm^{-2}], α is the albedo of the surface for shortwave radiation [-], and ε_0 is the thermal emissivity of the surface [-]. Kirchoff's law states that for a grey body (such as the earth's surface) the absorptivity at a given wavelength equals the emissivity at the same wavelength. Then
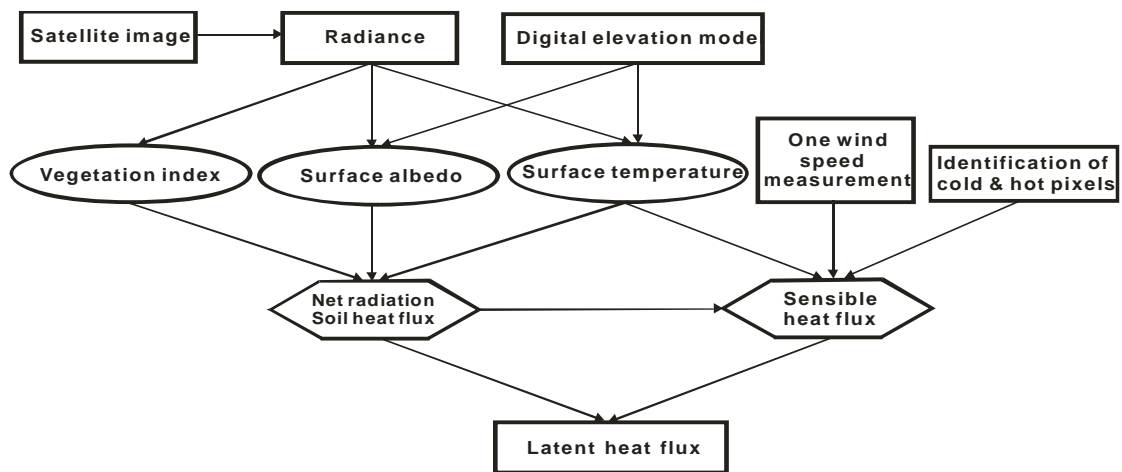
Figure 3.2 Schematic of the general computational process for determining evapotranspiration using SEBAL.

the sum of transmissivity, emissivity, and reflectivity or albedo equals one, the albedo for the sum of transmissivity, emissivity, and reflectivity or albedo equals one. When transmissivity is negligibly small, the albedo for longwave radiation at the earth's surface equals $(1 - \varepsilon_0)$ and $(1 - \varepsilon_0) \cdot R_{L\downarrow}$ represents the reflected longwave radiation. Figure 3.3 illustrates the surface radiative balance components included in Eq. [3.5] for calculation of the net radiation

$$R_n = R_{s\downarrow} - \alpha \cdot R_{s\downarrow} + R_{L\downarrow} - R_{L\uparrow} - (1 - \varepsilon_0) \cdot R_{L\downarrow} \qquad [3.5]$$

3.1.1. Incoming Shortwave Radiation

$R_{s\downarrow}$ is composed of both the direct solar radiation and the diffuse radiation with a strong diurnal variation. It is estimated from the amount of radiation received at the top of the atmosphere (R_a) [Wm^{-2}] and the one-way shortwave transmittance for the atmosphere (τ_{sw}) [-]. The term τ_{sw} accounts for the reduction of the radiation received at the top of the atmosphere due to absorption and scattering effects by the atmosphere.

$$R_{S\downarrow} = R_a \cdot \tau_{sw} \qquad [3.6]$$

where

$$R_a = G_{SC} \cdot \cos\theta \cdot d_r \qquad [3.7]$$

Therefore,

$$R_{S\downarrow} = G_{SC} \cdot \cos\theta \cdot d_r \cdot \tau_{sw} \qquad [3.8]$$
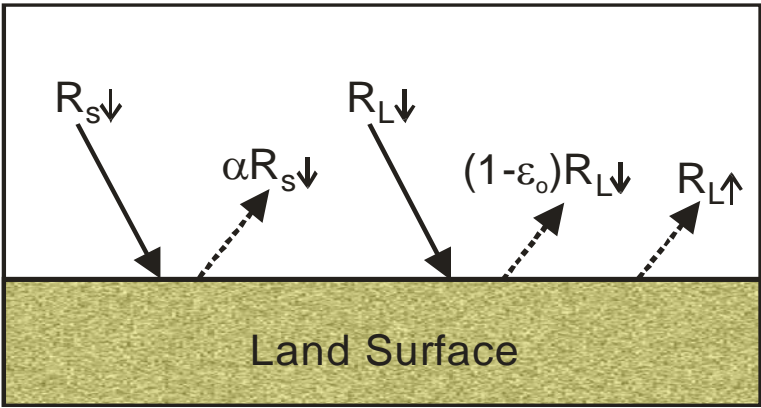
Figure 3.3 Surface radiation balance for a vegetated surface

where G_{sc} is the solar constant (1367) [Wm^{-2}], θ is solar incident angle [radians], d_r is the inverse squared normalized earth-sun distance [-] and τ_{sw} is the shortwave atmospheric transmittance [-].

The value of d_r is calculated following Duffie and Beckman (1980) as:

$$d_r = 1 + 0.033 \cos\left(DOY \frac{2\pi}{365} \right) \qquad [3.9]$$

where DOY is the sequential day of the year (1– 366).

τ_{sw} is estimated in this study by an empirical relationship with elevation (z) from (Allen et al., 1998):

$$\tau_{sw} = 0.75 + 2 \cdot 10^{-5} \cdot z \qquad [3.10]$$

where z is the elevation above sea level [m].

Recent by Allen et al. (2007) present a more sophisticated equation for τ_{sw} that includes the impact of sun angle and water vapor and takes into account beam and diffuse radiation.

$$\tau_{sw} = 0.35 + 0.627 \exp\left[\frac{-0.00146P}{K_t \cos\theta_{hor}} - 0.075 \left(\frac{W}{\cos\theta_{hor}} \right)^{0.4} \right] \qquad [3.11]$$

$$P = 101.3 \left(\frac{293 - 0.0065z}{293} \right)^{5.25}$$

[3.12]

$$W = 0.14 \cdot e_a \cdot P + 2.1$$

[3.13]

where P is the atmospheric pressure [kPa], W is the water in the atmosphere [mm], θ_{hor} is the solar zenith angle over a horizontal surface, K_t is the turbidity coefficient [-], e_a is the near-surface vapor pressure [kPa] and z is the elevation [m]. Eq. [3.11] is more accurate than Eq. [3.10] but requires ground measurements of e_a and an estimate of K_t.

The solar incident angle (θ) is the angle between the solar beam and an imaginary line perpendicular to a surface. For a flat surface, the cosine of the solar incident angle is calculated from the solar elevation angle as:

$$\cos(\theta) = \cos\left(\frac{\pi}{2} - \phi \right)$$

[3.14]

where, θ is the solar incident angle [radians] and ϕ is the sun elevation angle [radians] (Figure 3.4). However for a sloped surface, the solar incident angle (θ) changes with the surface slope and the aspect (Figure 3.5). Duffie and Beckman (1980) computed the cosine of the solar incident angle (θ) on a sloped surface as follows:
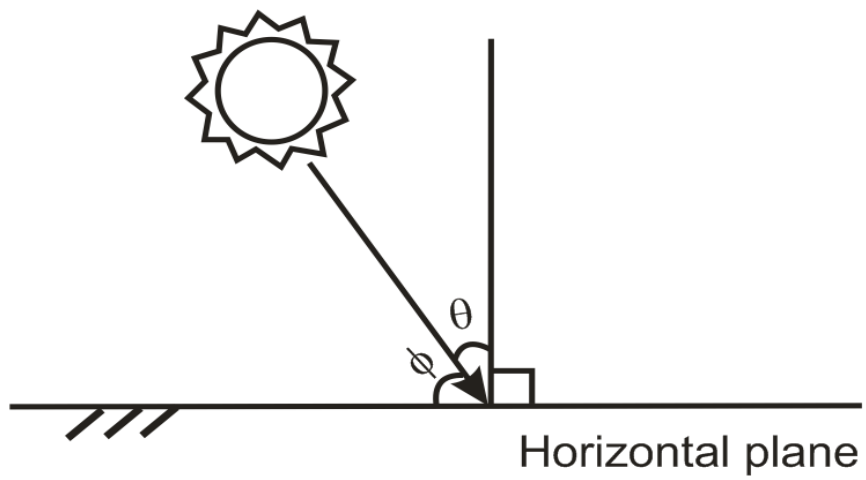
Figure 3.4 Definition of the solar incident angle (θ). ϕ is the sun elevation angle
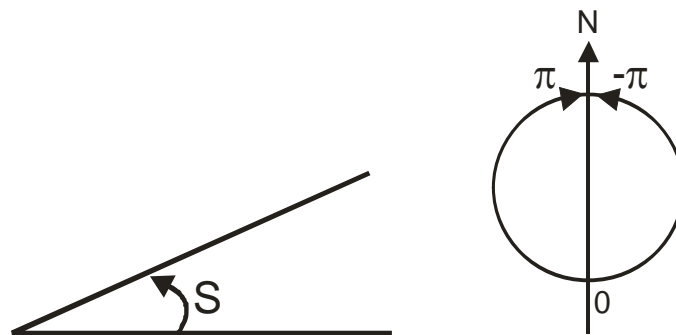
Figure 3.5 Definition of the slope (left) and aspect (right) used in SEBAL

$$\cos\theta_{slope} = \sin(\delta)\sin(\phi)\cos(s) - \sin(\delta)\cos(\phi)\sin(s)\cos(\gamma)$$
$$+ \cos(\delta)\cos(\phi)\cos(s)\cos(\omega)$$
$$+ \cos(\delta)\sin(\phi)\sin(s)\cos(\gamma)\cos(\omega) \qquad [3.15]$$
$$+ \cos(\delta)\sin(\gamma)\sin(s)\sin(\omega)$$

where $\cos\theta_{slope}$ is the cosine of the solar incident angle [radians] for sloped land surfaces,

δ is the solar declination (positive in summer in the northern hemisphere) [radians], ϕ is

the latitude of the pixel (positive for northern hemisphere) [radians], s is the slope

[radians], where "$s = 0$" for a horizontal surface and "$s = \pi/2$" for a vertical surface (s is

always positive and represents a upward/downward slope in any direction), γ is the

surface aspect angle [radians], where "$\gamma = 0$" for surfaces facing south, γ is negative for

east and positive for western aspect, "$\gamma = -\pi/2$" represents an east facing slope and "$\gamma =$

$+\pi/2$" represents a west facing slope. "$\gamma = -\pi$" or "$\gamma = \pi$" represents a north facing slope,

and ω is the hour angle [radians]. The value of ω is equal to 0 at solar noon, ω is negative

in the morning and positive in the afternoon.

SEBAL reprojects the $R_s\!\downarrow$ calculated for slopes to its horizontal equivalent

(Figure 3.6). This conversion can by done by dividing the cosine of the incident solar

angle [$\cos\theta_{slope}$] by the cosine of the slope [$\cos(s)$].

$$\cos\theta = \cos\theta_{slope}/\cos(s) \qquad [3.16]$$
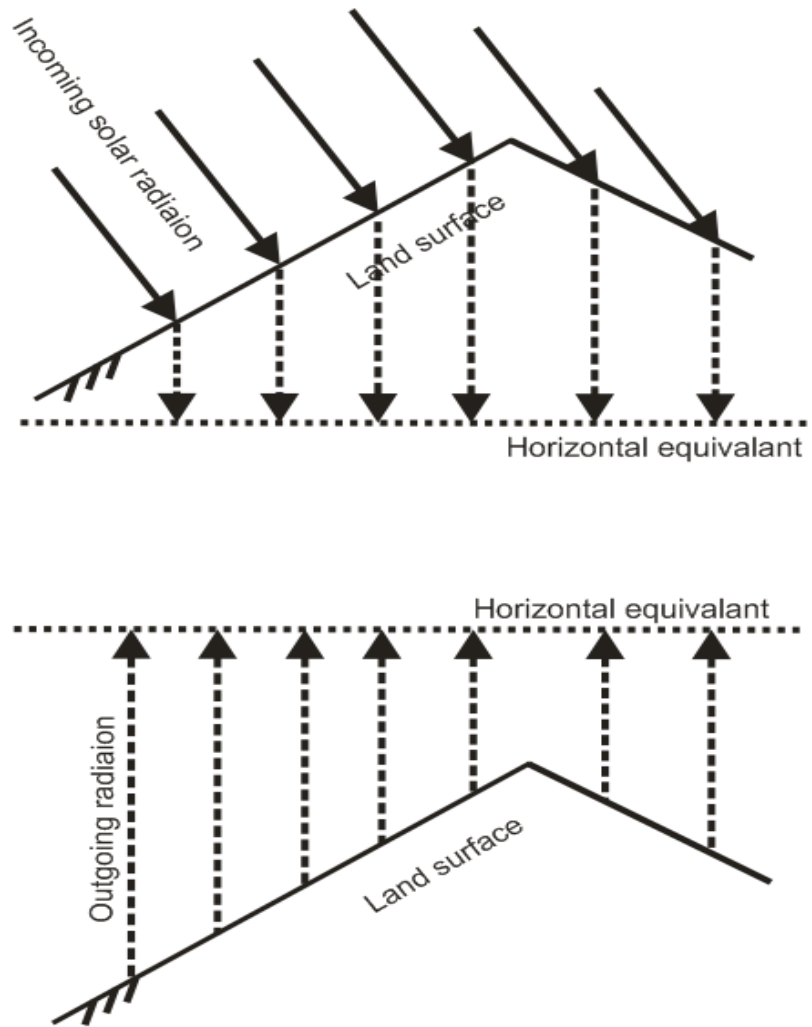
Figure 3.6 Unit area implications in SEBAL

where cos*(s)* is the cosine of the land surface slope. The $\cos\theta$ was used to obtain the horizontal-equivalent value of incoming solar radiation in Eq. [3.8].

The surface slope and aspect for each pixel were obtained from the digital elevation model of the area using ERDAS Imagine software (ERDAS, 2002). The parameters δ and ω were calculated by the following equations (Allen et al., 1998):

$$\delta = 0.409\sin\left(\frac{2\pi}{365}DOY - 1.39\right) \tag{3.17}$$

and

$$\omega = \frac{\pi}{12}\left[\left(t + \frac{L_z - L_m}{15} + S_c\right) - 12\right] \tag{3.18}$$

where t is the standard local time for the satellite overpass (without considering daylight saving time) [h], L_z is the longitude of the center of the local time zone (degrees west of the Greenwich) [deg], L_m is the longitude of the area of interest (degrees west of the Greenwich) [deg], and S_c is the seasonal correction for solar time [h] calculated as follows (Allen et al., 1998):

$$Sc = 0.1645\sin\left(\frac{4\pi(DOY - 81)}{364}\right) - 0.1255\cos\left(\frac{2\pi(DOY - 81)}{364}\right)$$
$$- 0.025\sin\left(\frac{2\pi(DOY - 81)}{364}\right) \tag{3.19}$$

3.1.2. Outgoing Shortwave Radiation

To estimate the outgoing shortwave radiation, $\alpha \cdot R_{s\uparrow}$, the land surface albedo needs to be determined. Surface albedo (α) [-] is the ratio of reflected to incoming solar radiation at the land surface. Albedo values for different surfaces are presented in Table 3.1:

$$\alpha = \frac{R_{s\uparrow}}{R_{s\downarrow}} \qquad [3.20]$$

where $R_{s\downarrow}$ is the incoming shortwave radiation [Wm^{-2}] and $R_{s\uparrow}$ is the outgoing shortwave radiation [Wm^{-2}].

In the SEBAL procedure, the hemispherical surface albedo (α) is obtained from the albedo at the top of the atmosphere (α_{toa}) with the following semi-empirical relationship (Menenti et al., 1989):

$$\alpha = \frac{\alpha_{toa} - \alpha_{path\_radiance}}{\tau_{sw}^{2}} \qquad [3.21]$$

where α is the surface albedo [-], α_{toa} is the clear-sky shortwave albedo at the top of the atmosphere [-] and $\alpha_{path\_radiance}$ is the albedo path radiance [-]. Tasumi and Allen (2000) found that $\alpha_{path\_radiance}$ has a value between 0.025 and 0.04, 0.03 is a reasonable value.

Table 3.1 Albedo values for different surfaces (Brutsaert, 1982).

Surface	Albedo [-]
Green grass and other short vegetation	0.15 – 0.25
Coniferous forest	0.10 – 0.15
Gray soils; bare fields	0.20 – 0.35
Dry soils; deserts	0.15 – 0.25
White sands; lime	0.30 – 0.40
Moist dark soils	0.05 – 0.15
Deep water	0.04 – 0.08
Fresh dry snow	0.80 – 0.90

The albedo at the top of the atmosphere, α_{toa}, is computed by performing an integration over all reflectance bands.

$$\alpha_{toa} = \sum_{i=1}^{n} w_\lambda \rho_{\lambda i} \qquad [3.22]$$

where n represents the total number of spectral bands used in the SEBAL algorithm, w_λ is a weighting factor [-] that accounts for the uneven distribution of the extraterrestrial radiation for each narrow band region of the spectrum [Table 3.2], and $\rho_{\lambda i}$ [-] is the narrow band spectral reflectance (ρ) corresponding to band i.

Tasumi et al. (2008) consider the surface albedo algorithm used in SEBAL overly simplified, since this algorithm (Bastiaanssen et al, 1998a) overestimates the surface albedo for bright-colored bare soils. They suggest the following equation, especially for land surfaces with high surface albedos (> 0.23).

$$\alpha = \sum_{b=1}^{n} \left[\rho_{s,b} \cdot w_b \right] \qquad [3.23]$$

where

$$\rho_{s,b} = \frac{R_{out,s,b}}{R_{in,s,b}} = \frac{\rho_{t,b} - \rho_{a,b}}{\tau_{in,b} \cdot \tau_{out,b}}, \qquad [3.24]$$

w_b is the weighting coefficient, $\rho_{s,b}$ is the surface reflectance for band b, $R_{in,s,b}$ and $R_{out,s,b}$ are the mean at-surface incoming and reflected radiances, respectively, $\tau_{in,b}$ and

Table 3.2 Weighting Coefficients w_λ for Landsat 5, 7 and MODIS

	Band1	Band2	Band3	Band4	Band5	Band6	Band7
Landsat 5	0.293	0.274	0.233	0.157	0.033	*	0.011
Landsat 7	0.293	0.274	0.231	0.156	0.034	*	0.012
MODIS	0.238	0.147	0.291	0.277	†	0.034	0.014

*Not available for thermal infrared band
†Band 5 of MODIS is not used in SEBAL due to sensor error

$\tau_{out,b}$ are the effective transmittances for incoming solar radiation and reflected short wave radiation, respectively, $\rho_{t,b}$ is the reflectance for band b at the top of the atmosphere and $\rho_{a,b}$ is the atmospheric path reflectance for band *b*. Various land surface albedo values calculated from Tasumi et al. (2008) were compared to albedo values estimated using the validated method by Liang (2000). The estimated albedo values from the two studies are almost identical (Tasumi et al., 2008). In this dissertation Eq. [3.21] has been used since Eq. [3.23] was not available during this processing of the images. Because the albedo difference affects only pixels with albedos exceeding 0.23, i.e. dry or almost dry pixels, the use of Eq. [3.21] had only a minor impact on the predicted ET rates of riparian areas.

The weighting coefficients are calculated as the radio of the solar constant for a particular band and the sum of the solar constant for all the bands:

$$w_\lambda = \frac{ESUN_\lambda}{\sum ESUN_\lambda} \qquad [3.25]$$

The reflectance for each band is computed following Markham and Barker (1987) and NASA (2002):

$$\rho_\lambda = \frac{\pi \cdot L_\lambda \cdot d^2}{ESUN_\lambda \cdot \cos\theta} \qquad [3.26]$$

where ρ is the at-satellite spectral planetary reflectance [-] for band λ, L_λ is the at-satellite spectral radiance [$Wm^{-2}ster^{-1}\mu m^{-1}$], which is the outgoing radiation energy of the band observed at the top of atmosphere by the satellite, d is the normalized Earth-Sun distance [-], $\cos\theta$ is the cosine of the solar incident angle, and $ESUN_\lambda$ is mean solar irradiances [$Wm^{-2}ster^{-1}\mu m^{-1}$] for each band λ. Values of $ESUN_\lambda$ are given in Table 3.3.

Since the inverse of d^2 is equal to d_r, Eq. [3.21] can be rewritten as:

$$\rho_\lambda = \frac{\pi \cdot L_\lambda}{ESUN_\lambda \cdot \cos\theta \cdot d_r} \qquad [3.27]$$

where d_r was calculated from Eq. [3.9]. The values of at-satellite spectral radiance (L_λ) for Landsat 5 TM are calculated as follows:

$$L_\lambda = \left(\frac{L_{MAX} - L_{MIN}}{255}\right) \cdot DN + L_{MIN} \qquad [3.28]$$

where, L_λ is sensor observed radiance [$Wm^{-2}ster^{-1}\mu m^{-1}$] for band λ, L_{MAX} [$Wm^{-2}ster^{-1}\mu m^{-1}$] and L_{MIN} [$Wm^{-2}ster^{-1}\mu m^{-1}$] are constants and DN [-] is the digital number recorded in the satellite image. The values of L_{MIN} and L_{MAX} vary over time as the Landsat 5 TM detectors age and begin to deteriorate. Recent updated values for L_{MIN} and L_{MAX} from Chander et al. (2007) are given in Table 3.4.

Table 3.3 $ESUN_\lambda$ [$Wm^{-2}\mu m^{-1}$] for Landsat 5 TM (Markham and Barker, 1986), Landsat 7 ETM+ (NASA, 2002) and MODIS (http://modis.gsfc.nasa.gov/).

	Band 1	Band 2	Band 3	Band 4	Band 5	Band 6	Band 7
Landsat 5	1957	1829	1557	1047	219.3	*	74.5
Landsat 7	1969	1840	1551	1044	225.7	*	82.1
MODIS	1631	1005	1997	1903	†	232.3	92.9

*Not available for thermal infrared band
†Band 5 of MODIS is not used in SEBAL due to sensor error

Table 3.4 L_{MIN} and L_{MAX} values for Landsat 5 TM (Chander et al., 2007)

Processing Date: From April 2, 2007

Band	Acquisition Date	L_{MIN} $(Wm^{-2}ster^{-1}\mu m\text{-}1)$	L_{MAX} $(Wm^{-2}ster^{-1}\mu m\text{-}1)$
1	Mar 1, 1984 – Dec 31, 1991	-1.52	169
	Jan 1, 1992 - Present	-1.52	193
2	Mar 1, 1984 – Dec 31, 1991	-2.84	333
	Jan 1, 1992 - Present	-2.84	365
3	Mar 1, 1984 – Present	-1.17	264
4	Mar 1, 1984 – Present	-1.51	221
5	Mar 1, 1984 – Present	-0.37	30.2
6	Mar 1, 1984 – Present	1.24	15.3
7	Mar 1, 1984 – Present	-0.15	16.5

Landsat 7 ETM+ and MODIS images provide calibration constants in the header files of each satellite image. The spectral radiance for each band is calculated by the following equation from NASA (2002):

$$L_{\lambda} = gain \cdot DN + offset \qquad [3.29]$$

where, L_{λ} is sensor observed radiance for band λ in $Wm^{-2}ster^{-1}\mu m^{-1}$, and "*gain*" and "*offset*" correspond to the "*gain*" and "*bias*" and "*scale*" and "*offset*" values provided in the header file of Landsat 7 and MODIS images, respectively. The values for *gain* [$Wm^{-2}ster^{-1}\mu m^{-1}$] and *offset* [$Wm^{-2}ster^{-1}\mu m^{-1}$] of each band are specific for each individual scene. Examples of values for *gain* [$Wm^{-2}ster^{-1}\mu m^{-1}$] and *offset* [$Wm^{-2}ster^{-1}\mu m^{-1}$] are presented in Table 3.5.

3.1.3. Outgoing Longwave Radiation

The total radiation emitted by a body, at a given temperature, is explained by the Stefan-Boltzman law:

$$B = \varepsilon_o \cdot \sigma \cdot T_s^{4} \qquad [3.30]$$

where B is radiation emitted from the body [Wm^{-2}], ε_o is the emissivity of the surface [-], σ is the Stefan Boltzman constant ($5.67 * 10^{-8}$) [$Wm^{-2}K^{-4}$], and T_s is the surface temperature of the body [K]. In SEBAL, longwave radiation from the land surface depends on its temperature and emissivity.

Table 3.5 Example of gain and offset values for band of Landsat 7 [path 33/ row: 35] and MODIS [Lat/Long of center (degree): 35.7/-105.2] on June 16, 2002.

	Gain $(Wm^{-2}ster^{-1}\mu m\text{-}1)$	Offset $(Wm^{-2}ster^{-1}\mu m\text{-}1)$
Landsat 7 (band 1)	1.1761	-6.20
Landsat 7 (band 2)	1.2051	-6.40
Landsat 7 (band 3)	0.9388	-5.00
Landsat 7 (band 4)	0.9655	-5.10
Landsat 7 (band 5)	0.1905	-1.00
Landsat 7 (band 6)	0.0668	0.00
Landsat 7 (band 7)	0.0662	-0.35
MODIS (band 1)	0.0000547	0.00
MODIS (band 2)	0.0000339	0.00
MODIS (band 3)	0.0000318	0.00
MODIS (band 4)	0.0000313	0.00
MODIS (band 6)	0.0000340	0.00
MODIS (band 7)	0.0000277	0.00
MODIS (band 31)	0.0008400	1577.3
MODIS (band 32)	0.0007297	1658.2

$$R_{L\uparrow} = \varepsilon_o \cdot \sigma \cdot T_s^{\,4} \qquad\qquad\qquad [3.31]$$

where ε_0 is the land surface emissivity [-].

In this study ε_0 and T_s are estimated using empirical relationships. NASA (2002) presented the following equation to compute surface brightness temperatures from thermal radiance:

$$T_b = \frac{K_2}{ln\left(\dfrac{K_1}{L_\lambda} + 1\right)} \qquad\qquad\qquad [3.32]$$

where T_b is brightness temperature [K], L_λ is the spectral radiance for thermal band, and K_1 [Wm^{-2}ster^{-1}μm^{-1}] and K_2 [Wm^{-2}ster^{-1}μm^{-1}] are coefficients that were developed considering the amount of radiation from a blackbody. Values of K_1 and K_2 are listed in Table 3.6.

Most of the SEBAL algorithms using MODIS are similar to Landsat algorithms. The major difference exists in the algorithm for surface temperature calculations. Landsat has one thermal band while MODIS has 16 thermal bands (Bands 20-25 and 27-36). The SEBAL algorithm for surface temperature estimation with Landsat was based on its single thermal band while thermal bands 31 and 32 were used for the MODIS application.

Table 3.6 Constants K_1 and K_2 in $Wm^{-2}ster^{-1}\mu m^{-1}$, for Landsat 5 TM (Markham and Barker, 1986) Landsat 7 ETM+ (NASA, 2002) and MODIS (http://modis.gsfc.nasa.gov/).

	K_1	K_2
Landsat 5	607.76	12605.6
Landsat 7	666.09	1282.71
MODIS (band 31)	730.01	1305.84
MODIS (band 32)	474.99	1198.29

To obtain the surface temperature from Landsat imagery, SEBAL uses the following equation to calculate the surface temperature (Tasumi et al., 2000). Several studies indicates relationship between T_s and the surface emissivity (e.g. Price, 1984; Moran et al., 1989).

$$T_s = \frac{T_b}{\varepsilon_0^{0.25}}$$

[3.33]

where ε_0 is the surface emissivity [-]. The emissivity of an object is the ratio of the energy radiated by that object at a given temperature to the energy radiated by a blackbody at the same temperature (according to Plank's Law). Since the thermal radiation of the surface is observed in the thermal band, one can compute the surface temperature from this band if the emissivity of the land surface is estimated.

In SEBAL, surface emissivity is estimated using *NDVI* and an empirically-derived method (Bastiaanssen et al., 1998a):

$$\varepsilon_o = 1.009 + 0.47 \cdot \ln(NDVI)$$

[3.34]

where *NDVI* is the normalized difference vegetation index [-] (Jensen, 2000), which is calculated as follows:

$$NDVI = \frac{\rho_{NIR} - \rho_{red}}{\rho_{NIR} + \rho_{red}}$$

[3.35]

where ρ_{NIR} is near-infrared reflectance [-] and ρ_{red} is the reflectance [-] in the red region of the visible spectrum.

Allen et al. (2007) present slightly different equations for the surface temperature calculation that utilize 'standardized' coefficients that tend to provide atmospheric correction.

$$T_s = \frac{K_2}{\ln\left(\dfrac{\varepsilon_{NNB} K_1}{R_c} + 1\right)} \qquad [3.36]$$

$$R_c = \frac{L_{t,b} - R_p}{\tau_{NB}} - \left(1 - \varepsilon_{NB}\right) R_{sky} \qquad [3.37]$$

where ε_{NB} is the narrow band surface emissivity [-], R_c is the corrected thermal radiance from the surface [Wm^{-2}ster^{-1}μm^{-1}], $L_{t,b}$ is the spectral radiance [Wm^{-2}ster^{-1}μm^{-1}], R_p is the path radiance [Wm^{-2}ster^{-1}μm^{-1}], R_{sky} is the thermal radiation from a clear sky [Wm^{-2}ster^{-1}μm^{-1}] and τ_{NB} is the narrow band transmissivity of air [-]. The difference in surface temperatures calculated with Eqs. [3.33] and [3.36] is rather small for colder pixels with high ET but can increase to 3 – 4 K at T_s around 315 K. However, the bias is relatively linear with T_s and therefore will be compensated for with the dT functions of Eq. [3.61].

Since MODIS imagery includes multiple thermal bands, split window algorithms take advantage of the differential absorption in two close thermal bands to account for the effects of absorption by atmospheric gases. Several split window algorithms are currently available to derive surface temperature from brightness temperature when multiple thermal bands are available. In this study the algorithm developed by Ulivieri et al. (1992) was applied that has been validated in natural grassland with patches of bare soil during various seasons with a wide range of T_s. There, the algorithm agreed quite well with ground data (Vazquez et al., 1997).

$$T_s = T_{31} + 1.8(T_{31} - T_{32}) + 48(1 - \varepsilon) - 75\Delta\varepsilon \qquad \text{[3.38]}$$

where

$$\varepsilon = (\varepsilon_{31} + \varepsilon_{32})/2 \qquad \text{[3.39]}$$

and

$$\Delta\varepsilon = \varepsilon_{31} - \varepsilon_{32} \ . \qquad \text{[3.40]}$$

Here T_{31} is the brightness temperature obtained from band 31 [K], T_{32} is the brightness temperature obtained from band 32 [K], ε_{31} is the surface emissivity [-] in band 31 and ε_{32} is the surface emissivity in band 32. The brightness temperature of MODIS bands 31 and 32 are estimated by using Eq. [3.32]. The dimension of the empirical constants 48 and 75 is degree K. These constants are hardly influenced by the values of surface emissivity or total vapor content of the atmosphere as long as it is less than 3 g/cm^2. The latter value is unlikely for most New Mexico conditions.

For the surface emissivity estimation, an empirical approach with NDVI is often used in remote sensing study, since it is simple and the lack of proved techniques for estimating emissivity of large pixels with a partially covered soil surface. The relation between emissivity and *NDVI* is also observed from various experimental studies (Becker and Li, 1991; Van de Griend and Owe, 1993). This study uses the equation developed by Cihlar et al. (1997). The equation by Cihlar et al. (1997) is similar to the one proposed by Van de Griend and Owe (1993) and uses data from various studies (Wan and Dozier, 1989; Nerry et al., 1990; Salisbury and D'Aria, 1992; Van de Griend and Owe, 1993) to bound the emissivity to reasonable range (0.955 - 0.985).

$$\Delta \varepsilon = \varepsilon_{31} - \varepsilon_{32} = 0.01019 + 0.01344 \ln(NDVI) \qquad [3.41]$$

where

$$\varepsilon_{31} = 0.9897 + 0.029 \ln(NDVI) \qquad [3.42]$$

The relations are mainly based upon measurements on natural surfaces (bare soils and different vegetation types) in semi-arid Botswana (Van de Griend and Owe, 1993). Therefore, their application to the Southwestern USA is justified. The absolute estimate of T_s is not critical for the accuracy of the final SEBAL result (latent heat flux). SEBAL relies on an internal calibration by "anchoring" *H* and *LE* at the cold and hot pixels which reduces or cancels biases in the calculation of albedo, net radiation, and surface temperature as well as errors in narrow band emissivity, atmospheric correction, satellite sensor, aerodynamic resistance, and soil heat flux function.

3.1.4. Incoming Longwave Radiation

Incoming longwave radiation, $R_{L\downarrow}$, emitted by the atmosphere can be calculated theoretically with the Stephan-Boltzman equation:

$$R_{L\downarrow} = \varepsilon_a \cdot \sigma \cdot T_a^{\,4} \qquad\qquad [3.43]$$

where ε_a is the atmospheric emissivity [-], σ is the Stefan-Boltzmann [$Wm^{-2}K^{-4}$] constant and T_a is the air temperature [K].

To utilize Eq. [3.43] both emissivity and temperature for each layer of the atmosphere are required. Since direct use of this equation is extremely complicated, SEBAL uses an empirical equation to estimate the effective atmospheric emissivity as a function of atmospheric transmissivity (Allen et al., 2000).

$$R_{L\downarrow} = \varepsilon_a \cdot \sigma \cdot T_{s\_cold}^{\,4} \qquad\qquad [3.44]$$

$$\varepsilon_a = 0.85 \cdot \left(-\ln \tau_{sw}\right)^{0.09} \qquad\qquad [3.45]$$

where T_{s_cold} is the surface temperature at a reference point (cold pixel). The cold pixel is generally selected from a well-watered agricultural field where surface and air temperatures are assumed to be similar. Air temperature change due to elevation is accounted for by the lapse rate in this study. Note that since $R_{L\downarrow}$ is from the entire

atmosphere not from the near surface atmosphere only, ε_a is an 'effective' atmospheric emissivity rather than the actual emissivity. Coefficient 0.09 in Eq. [3.35] was calibrated using air temperature observed over a well-watered agricultural field in southern Idaho (Allen, 2000). In a recent study by Allen et al. (2007) the radiometric surface temperature of each pixel is used as a surrogate for T_a in Eq. [3.43].

3.2. SOIL HEAT FLUX

The soil heat flux density (G) is driven by the vertical temperature gradient between surface and soil and is positive for downward flux into the ground. Soil heat flux at any depth z can be expressed by (Oke, 1987):

$$G = K_{TS} \frac{\partial T_{soil}}{\partial z}$$
[3.46]

where G is the soil heat flux [Wm^{-2}], T_{soil} is the temperature of the soil [K], K_{TS} is the thermal conductivity of the soil [Jm^{-1}s^{-1}K^{-1}], and z is the depth [m].

However, since it is impossible to estimate the term $\partial T_{soil}/\partial z$ in Eq. [3.46] from satellite observations, soil heat flux cannot be obtained directly. Therefore, in satellite applications, the soil heat flux is often estimated as a fraction of R_n (Choudhury et al.,

1987; Norman et al., 1995; Anderson et al., 1997; Bastiaanssen, 2000). Choudhury et al.

(1987) proposed the following conceptual model:

$$G/R_n = \Gamma' \cdot \Gamma''$$
[3.47]

where Γ' is a proportionality factor [-] that describes the conductive heat transfer in soil

and Γ'' is an extinction factor [-] that represents the attenuation of radiation through the

vegetation.

The soil heat flux is determined using the semi-empirical equation suggested by

Bastiaanssen (1995) in which G is related to R_n, surface albedo (α), surface temperature

(T_s) and normalized difference vegetation index ($NDVI$). The soil heat flux equation used

in this study has been validated extensively (Clothier et al., 1986; Choudhury et al., 1987;

Daughtry et al., 1990; Bastiaanssen, 2000).

$$G/R_n = \left[\frac{T_S(t)}{\alpha(t)}\left(0.0038\alpha^{avg} + 0.0074\alpha^{avg2}\right)\right]\left[1 - 0.98NDVI^4\right]$$
[3.48]

where $\alpha(t)$ is the surface albedo at certain time t and α^{avg} is the day time averaged

surface albedo. Since SEBAL assumes surface albedo at the time of satellite over pass is

equal to daytime average ($\alpha(t) = \alpha^{avg}$). In Eq. [3.48] the term

$$\frac{T_S(t)}{\alpha(t)}\left(0.0038\alpha^{avg} + 0.0074\alpha^{avg2}\right)$$ represents the factor Γ' and the term $\left(1 - 0.98NDVI^4\right)$

represents the term Γ'' of Eq. [3.47].

For water and snow surfaces, it is not recommended to apply Eq. [3.48]. Several studies have shown that G/R_n ratio for water surfaces is quite large because the ratio is dependent upon the turbidity and the depth of the water body and the ratio is very different from other land surfaces (Yamartino, 1984; Amayreh, 1995; Burba et al., 1999). Tasumi (2003) and Trezza (2002) suggested the following fixed expression to estimate G for water and snow surfaces, because no other better estimates yet exist.

$$G_{water} = G_{snow} = 0.5R_n \qquad [3.49]$$

3.3. SENSIBLE HEAT FLUX

The aerodynamic sensible heat flux is predicted using the following equation (Brutsaert, 1982).

$$H = \rho \cdot C_P \cdot \frac{T_{aero} - T_a}{r_{ah}} = \rho \cdot C_p \cdot \frac{dT}{r_{ah}} \qquad [3.50]$$

where ρ_a is the density of air [kgm^{-3}], C_p is the specific heat capacity of air [Jkg^{-1} K^{-1}], T_{aero} is the aerodynamic surface temperature [K], T_a is the air temperature measured at a

standard screen height [K], r_{ah} is the aerodynamic resistance to heat transfer [sm^{-1}], and

dT [K] is the difference between T_{aero} and T_a. As is explained below, T_{aero} and T_a can not

be estimated from remote sensing images. Therefore, SEBAL uses an internal calibration

method to estimate dT instead.

The simplicity of Eq. [3.50] is deceptive since T_{aero} cannot be measured by remote

sensing. Remote sensing techniques measure the radiometric surface temperature, T_s,

which is not the same as T_{aero}. Brutsaert (1982) and Choudhury et al., (1986) argued that

T_s and T_{aero} are almost identical for near-neutral conditions. However, T_s is higher than

T_{aero} for stable conditions and lower for unstable conditions. The two temperatures can

differ by 1 to 5 K. Unfortunately, an error of 1 K in $T_{aero} - T_a$ can result in a 50 Wm^{-2}

error in H (Hall et al., 1992; Campbell and Norman, 1998) that may result in an error in

the daily evaporation rate of as much as 2 mm per day. Although many investigators have

tried to obtain T_{aero} from T_s by adjusting r_{ah} or by using an additional resistance term, so

far no generally applicable solution to this problem has been developed (Kustas and

Norman, 1996). Thus, the most complex issue in SEBAL is how to estimate the

parameters needed for estimation of the sensible heat flux. The SEBAL sensible heat flux

calculations are based on the Monin-Obukov similarity theory that takes into account the

effects of atmospheric stability and aerodynamic resistance for heat transport (r_{ah}).

The step by step procedures for H calculation in SEBAL are as follows:
1) SEBAL needs a ground measurement (or atmospheric model estimation) of wind

speed at the time of satellite pass over, the height of the wind speed measurement and

information about the surface conditions around the weather station. The friction velocity [ms^{-1}] for the location of the weather station x at the time of satellite overpass (u_{x*}) is calculated assuming neutral atmospheric conditions (Panofsky and Dutton, 1984).

$$u_{x*} = \frac{u_x \cdot k}{\ln\left(\dfrac{z_x}{z_{om}}\right)} \tag{3.51}$$

where u_x is the wind speed [ms^{-1}] measured at height z_x at the weather station [m], k is the von Karman's constant (0.41) [-], and z_{om} is the surface roughness length for momentum transport [m] which is estimated from the average vegetation height around the weather station by (Brutsaert, 1982):

$$z_{om} = 0.123 \cdot h \tag{3.52}$$

where h is the vegetation height [m].

2) SEBAL calculates the wind speed at a "blending" height of 200 m above the weather station assuming a constant friction velocity with height. At the "blending" height the wind speed is assumed to be unaffected by surface roughness.

$$u_{200} = \frac{u_{x*}}{k} \ln\left(\frac{200}{z_{om}}\right) \tag{3.53}$$

3) SEBAL calculates a friction velocity (u_*) for each pixel by downward extrapolation of the spatially constant wind speed at the blending height (u_{200}) using the specific value of z_{om} for each pixel.

$$u_* = \frac{u_{200} \cdot k}{\ln\left(\dfrac{z_{200}}{z_{om}}\right)}$$ [3.54]

The values of z_{om} for each pixel are derived either by using estimates about vegetation height from a landuse map or from an empirical relationship between z_{om} and $NDVI$ and α (Morse et al., 2000; Tasumi and Allen, 2000)

$$z_{om} = exp\left[\left(\frac{c_1 \cdot NDVI}{\alpha}\right) + c_2\right]$$ [3.55]

where, c_1 and c_2 are constants that need to be determined for each image. For each image parameters c_1 and c_2 were obtained from linear regression between $ln(z_{om})$ and $NDVI/\alpha$ of known landuse pixels including surface water and riparian vegetations. Tasumi et al. (2000) indicate that using the ratio $NDVI/\alpha$, rather than using only α (Bastiaanssen et al., 1998a), is more effective in predicting differences in z_{0m} between tall and short vegetation, because tall vegetation generally has lower albedo values than short vegetation due to shading from tall vegetation.

Terrain elevation and slope affect how wind speed and surface roughness length are used for calculation of momentum transport (Oke, 1987; Tasumi, 2003). To adjust for elevation and slope in mountainous regions, the empirical equations suggested by Tasumi (2003) can be used;

$$u_{200\_adjusted} = C_{wind} \cdot u_{200} \qquad [3.56]$$

where

$$C_{wind} = 1 + 0.1 \cdot \frac{(z - z_x)}{1000} \qquad [3.57]$$

and $u_{200\_adjusted}$ is the adjusted wind speed at 200 m height [ms^{-1}] taking into account elevation effects, u_{200} is the wind speed at height of 200 m [ms^{-1}] unadjusted by elevation, C_{wind} is an adjustment coefficient [-], z_x is the elevation of weather station location [m], and z is the elevation [m].

The adjusted surface roughness length for momentum transport is calculated as:

$$z_{om\_adjusted} = C_{zom} \cdot z_{om} \qquad [3.58]$$

where

$$C_{zom} = 1 + \frac{S - 5}{20} \qquad [3.59]$$

where, $z_{om\_adjusted}$ [m] is the adjusted value of z_{om}, C_{zom} is a z_{om} correction coefficient [-], and S is the surface slope [deg]. The z_{om} adjustment is necessary only when the slope is greater than 5°.

4) SEBAL calculates initial values of the aerodynamic resistance for heat transport (r_{ah}) for each pixel assuming neutral atmospheric conditions:

$$ r_{ah} = \frac{\ln\left(\dfrac{z_2}{z_1}\right)}{u^* \cdot k} \qquad [3.60]$$

where z_1 is 0.1 m and z_2 is 2.0 m above the zero plane displacement d (Figure 3.7)

5) As shown in Eq. [3.50] SEBAL calculates the sensible heat flux for each pixel using the air temperature difference (dT) between heights z_1 and z_2. A common field observation is that land surfaces with a high dT are associated with high radiometric temperatures (T_s) and those with a low dT with low radiometric temperatures. Field measurements in Egypt and Niger (Bastiaanssen et al., 1998b), China (Wang et al., 1998), USA (Franks and Beven, 1997), and Kenya (Farah and Bastiaanssen, 2001) have shown that the relationship between T_s and dT is approximately positively linear for different field conditions including irrigated fields, deserts, and mountains. Therefore, SEBAL uses a linear relationship between dT and surface temperature (T_s) (Figure 3.8) for the calculation of dT for each pixel in an image.
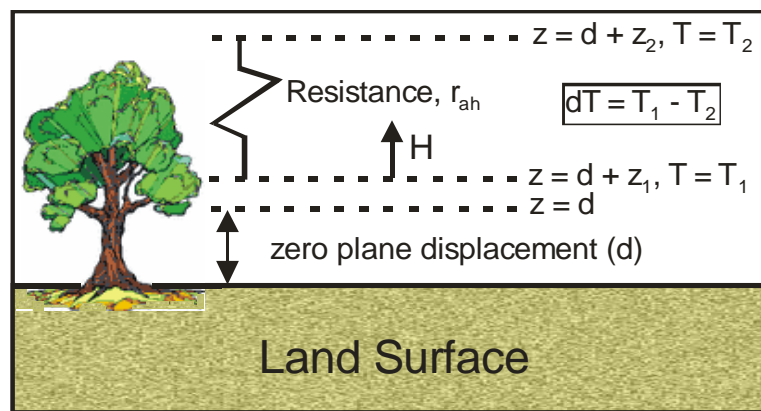
Figure 3.7 Definition of aerodynamic resistance for heat transfer (Tasumi, 2003)
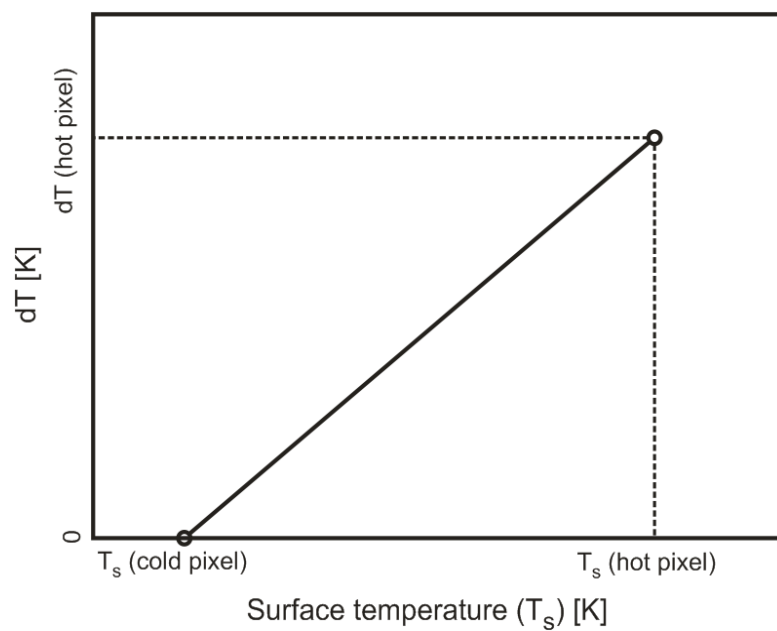
Figure 3.8 SEBAL definition of the relationship between *dT* and *T_s*

$$dT = a \cdot T_s + b \qquad\qquad [3.61]$$

To define the coefficients "*a*" and "*b*" in Eq. [3.61], the SEBAL approach involves the selection of two "anchor" pixels, where the value of dT can be reasonably assumed. The temperature difference (dT) for a dry surface without evaporation (hot pixel) is obtained from the inversion of the energy balance equation Eq. [3.1] with LE set to zero so that $H = R_n - G$. Then, dT is calculated by inversion of Eq. [3.60]. On the other hand, for a wet surface (cold pixel) all available energy $R_n - G$ is used for evapotranspiration so that $H = 0$ and $dT = 0$ (Bastiaanssen et al., 1998a; Bastiaanssen, 2000; Hendrickx and Hong, 2005).

The values of dT and T_s for the cold and hot pixel are used to find the regression coefficients a and b which will prevent outliers of H-fluxes. In particular, the empirical equation Eq. [3.61] relies on spatial differences of the radiometric surface temperature rather than absolute surface temperatures to derive maps of the sensible heat flux. This procedure minimizes the influence of atmospheric conditions and uncertainties in surface emissivity on H estimates (Allen et al., 2007). However, if regional and local advection of heat are present, the sensible heat fluxes over the area will be decreased due to a decrease in temperature gradient. Therefore it is possible that H at the cold pixel has a negative value. If this happens, SEBAL will overestimate H, and thus underestimate LE.

In areas with elevation changes exceeding a few hundred of meters, the surface temperature (T_s) needs to be adjusted to take into account air temperature changes since

on the average the air temperature decreases by about 6.5 K in the lower troposphere

when elevation increases by 1 km (Andrews, 2000). Typically, land surface temperatures

are in equilibrium with air temperature so that similar decreases are expected in surface

temperatures. Therefore, dry areas at high elevations appear to be "cool" which could be

misinterpreted as having a high ET. Therefore, the lapse rate effect on surface

temperature has to be accounted for in the dT estimation in SEBAL. To correct for the

error introduced by elevation changes, the surface temperature is adjusted using the lapse

rate (6.5 K per 1 km) as

$$T_{s\_adjusted} = T_s + 0.0065 \cdot \Delta z \qquad [3.62]$$

where $T_{s\_adjusted}$ is the adjusted surface temperature [K] using the lapse rate (6.5 K per 1

km) and Δz [m] is the difference between elevation of each pixel minus the average

elevation in the image. $T_{s\_adjusted}$ rather than T_s should be used for derivation of

coefficients a and b in Eq. [3.61].

6) The initial estimate of sensible heat flux is obtained by assuming neutral atmospheric

conditions in the calculation of r_{ah} in step 4. To account for the buoyancy effects that

surface heating generates in the lower atmosphere, SEBAL uses the Monin-Obukov

similarity theory through the following iterative process. The Monin-Obukhov length

parameter (L) is used to define the stability conditions of the atmosphere (Monteith and

Unsworth, 1990).

$$L = -\frac{\rho c_p u_*^{3} T_s}{kgH} \qquad [3.63]$$

where, g is the gravitational acceleration constant (9.81) [ms^{-2}]. Theoretically, the

absolute value of L [m] represents the thickness of the layer where wind shear effects

dominate over buoyancy forces in the production of turbulence. For that reason, when H

= 0 (no buoyancy forces), L is infinite. On the other hand, when H is positive L tends to

be numerically smaller as H increases.

Based on the value of L, the stability correction factors for momentum and heat transport

(Ψ_m and Ψ_h) can be obtained from the following equations (Allen et al., 1996).

If $L<0$: unstable atmosphere:

$$\Psi_{m(200m)} = 2\ln\left(\frac{1+x_{(200m)}}{2}\right) + \ln\left(\frac{1+x_{(200m)}^{2}}{2}\right) - 2ARCTAN\left(x_{(200m)}\right) + 0.5\pi \qquad [3.64]$$

$$\Psi_{h(2m)} = 2\ln\left(\frac{1+x_{(2m)}^{2}}{2}\right) \qquad [3.65]$$

$$\Psi_{h(0.1m)} = 2\ln\left(\frac{1+x_{(0.1m)}^{2}}{2}\right) \qquad [3.66]$$

where

$$x_{(200m)} = \left(1-16\cdot\frac{200}{L}\right)^{0.25} \qquad [3.67]$$

$$x_{(2m)} = \left(1 - 16 \cdot \frac{2}{L}\right)^{0.25} \qquad\qquad [3.68]$$

$$x_{(0.1m)} = \left(1 - 16 \cdot \frac{0.1}{L}\right)^{0.25} \qquad\qquad [3.69]$$

If $L > 0$: stable atmosphere:

$$\Psi_{m(200m)} = -5 \cdot \left(\frac{2}{L}\right) \qquad\qquad [3.70]$$

$$\Psi_{h(2m)} = -5 \cdot \left(\frac{2}{L}\right) \qquad\qquad [3.71]$$

$$\Psi_{h(0.1m)} = -5 \cdot \left(\frac{0.1}{L}\right) \qquad\qquad [3.72]$$

Eq [3.70] uses 2 m rather than 200 m since the boundary layer under stable atmospheric conditions will not extend above at most a few tens of meters. The use of 2m guarantees a stable numerical solution (Allen et al., 2005).

If $L = 0$; neutral atmosphere:

$$\Psi_m \text{ and } \Psi_h = 0 \qquad\qquad [3.73]$$

Next, new values of the friction velocity (u_*) and aerodynamic resistance (r_{ah}) for each

pixel are calculated as:

$$u_* = \frac{k \cdot u_{200}}{\ln\left(\dfrac{200}{z_{om}}\right) - \Psi_{m(200m)}}$$ [3.74]

and

$$r_{ah} = \frac{\ln\left(\dfrac{z_2}{z_1}\right) - \Psi_{h(z2)} + \Psi_{h(z1)}}{u_* \cdot k}$$ [3.75]

7) Because of the new value of r_{ah} corresponding to the hot pixel, the value of dT has to

be re-calculated for the hot pixel by inverting Eq. [3.50] as $dT_{hotpixel} = \dfrac{H \cdot r_{ah}}{\rho \cdot C_P}$. This new

value of $dT_{hotpixel}$ changes the linear equation that defines the dT versus T_s relationship in

Eq. [3.61] and requires a new calculation of the value of sensible heat flux for each pixel.

The iterative process for r_{ah}, dT and H for the hot pixel continues until values of hot

pixel's r_{ah} become stable. Figure 3.9 shows the iterative process used in SEBAL to obtain

the sensible heat flux for each pixel.

3.4. LATENT HEAT FLUX

At last, the latent heat flux (LE) is obtained for each pixel after inserting the

numerically stable sensible heat flux (H) as well as net radiation (R_n) and ground
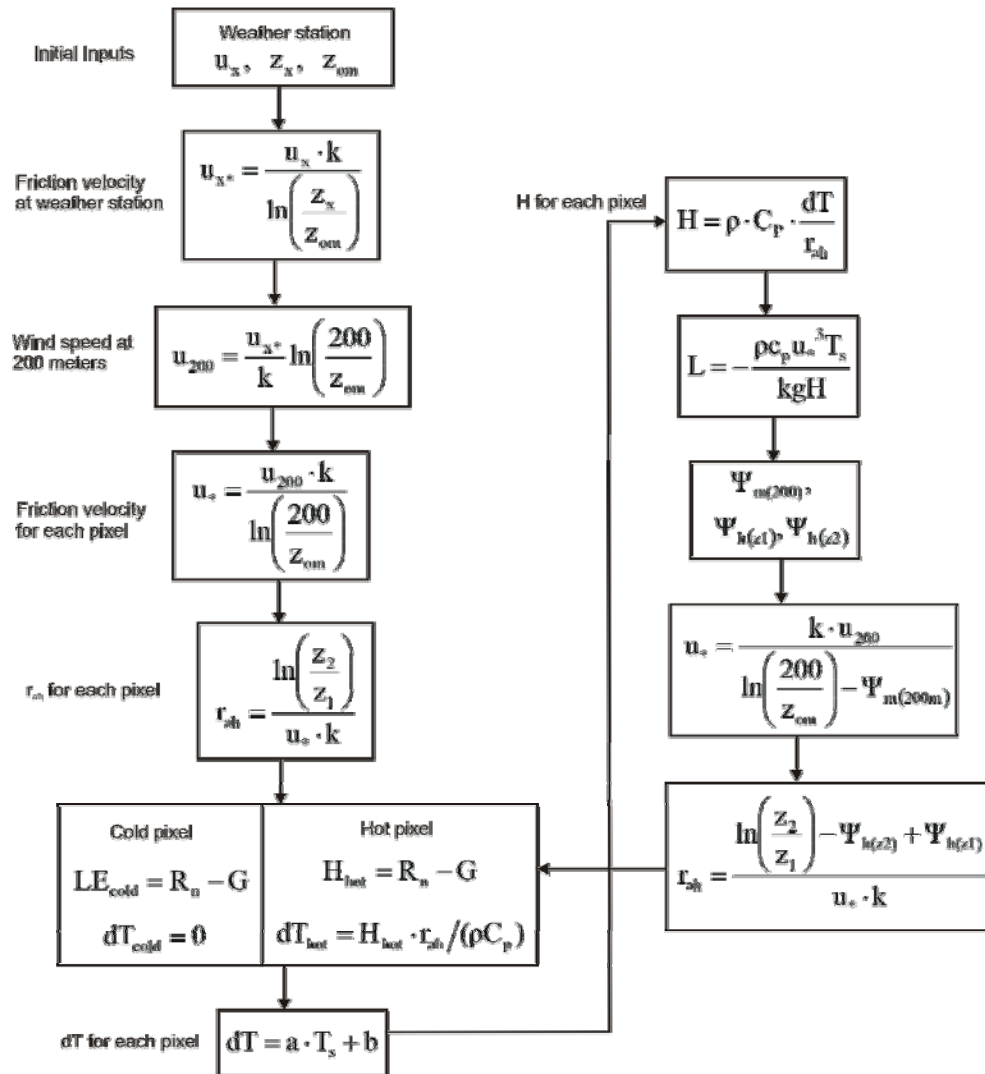
Figure 3.9 Schematic of iterative procedures to calculate sensible heat flux in SEBAL.

heat flux (G) into Eq. [3.1]. This value of LE represents the instantaneous flux [Wm^{-2}] at the time of the satellite overpass.

3.5. DAILY ENERGY BALANCE FLUXES

SEBAL yields an estimate of LE [Wm^{-2}] at the time of the Landsat overpass. However, for most hydrological applications the daily total LE (daily ET) is needed; so the instantaneous LE needs to be extrapolated to the daily LE. The extrapolation is done using the evaporative fraction (EF) [-] which has been shown to be approximately constant during the day (Shuttleworth et al., 1989; Brutsaert and Sugita, 1992; Crago, 1996; Farah et al., 2004; Gentine et al., 2007).

$$EF_{inst} = \frac{R_n - G - H}{R_n - G} = \frac{LE_{inst}}{LE_{inst} + H_{inst}} \approx EF_{24} \qquad [3.76]$$

Therefore, multiplication of the instantaneous EF (EF_{inst}) determined from SEBAL with the total daily available energy yields the daily ET rate in mm per day (Bastiaanssen et al., 1998a).

$$LE_{24} = EF_{inst} \cdot \left(R_{n24} - G_{24}\right) \qquad [3.77]$$

and

$$ET_{24} = \frac{EF_{inst} \cdot \left(R_{n24} - G_{24}\right)}{\lambda} \qquad [3.78]$$

where

$$\lambda = [2.501 - 0.00236 \cdot (T_s - 273.1)] \cdot 10^6 .$$ [3.79]

Here LE_{24} is daily latent heat flux [MJm^{-2}day^{-1}], ET_{24} is daily ET [mmd^{-1}], G_{24} is daily

soil heat flux [MJm^{-2}d^{-1}], EF_{inst} is the evaporative fraction [$(R_n - G - H)/(R_n - G)$] at the

time of satellite overpass, λ is the latent heat of vaporization [Jkg^{-1}] and R_{n24} is daily net

radiation [MJm^{-2}d^{-1}]. R_{n24} is obtained by an semi-empirical expression (De Bruin, 1987).

$$R_{n24} = 0.0864 \cdot [(1 - \alpha) \cdot R_{a24}/cos(s) \cdot \tau_{sw} - 110\tau_{sw}]$$ [3.80]

$$R_{a24} = G_{SC} \cdot d_r \cdot \int_{\omega 1}^{\omega 2} cos(\theta) \cdot d\omega$$ [3.81]

where 0.0864 is the conversion parameter from Wm^{-2} to MJm^{-2}day^{-1}. Eq. [3.80] was

developed by de Bruin (1987) and recommended by Bastiaanssen et al (1998a) only for

all-day clear sky condition. If the day of the satellite image is known to have had some

cloudiness during periods preceding or following the time of the image, then one should

use a ground measured value for 24-h solar radiation (R_s) in place of $R_{a24} \cdot \tau_{sw}$. The

constant -100 depends somewhat on the type of surface. For example, Tasumi et al.

(2000) suggested -140 for irrigated fields in Idaho. In this study for the riparian vegetated

areas, the coefficient -110 is used since it yields R_{n24} estimates that agree quite well with

ground measurements (MRD < 3%). R_{a24} is the daily-averaged extraterrestrial shortwave

radiation [Wm^{-2}] which is calculated using information on location, day of year, slope

and aspect for each pixel. Detailed information on the R_{a24} computation and SEBAL

implementation using ERDAS Imagine are found in Tasumi et al. (2000).

With the information of daily total LE (LE_{24}), daily H (H_{24}) is estimated from the

energy balance equation by assuming daily G (G_{24}) is negligibly small, i.e. zero (Kustas

et al., 1993).

$$H_{24} = R_{n24} - G_{24} - LE_{24} \approx R_{n24} - LE_{24} \qquad [3.82]$$

Note that H_{24} is not derived from the instantaneous H. Instead it is calculated as the

difference between R_{n24} and LE_{24}. The R_{n24} is directly derived independently from

SEBAL results using Eq. [3.80]. The LE_{24} depends on the EF_{inst} which is dependent upon

the instantaneous R_n, G and H obtained from SEBAL.

REFERENCES

Allen, R.G., W.O. Pruitt, J.A. Businger, L.J. Fritschen, M.E. Jensen, and F.H. Quinn. 1996. Chapter 4: Evaporation and Transpiration. American Society of Civil Engineering, NY.

Allen, R.G., L.S. Pereira, D. Raes, and M. Smith. 1998. Crop evapotranspiration. FAO Irrigation and drainage paper 56, FAO. Rome.

Allen, R.G., H.D. Bruin, O. Hartogensis, B. Tanner, and C. Neale. 2000. Regional Advection Perturbations in an Irrigated Desert (RAPID)-Impacts on Evapotranspiration. University of Idaho, Kimberly.

Allen, R.G., M. Tasumi, and R. Trezza. 2005. M E T R I C^{tm} Mapping Evapotranspiration at High Resolution. Applications Manual for Landsat Satellite Imagery. Version 2.0. University of Idaho, Kimberly, Idaho.

Allen, R.G., M. Tasumi, and R. Trezza. 2007. Satellite-based Energy Balance for Mapping Evapotranspiration with Internalized Calibration (METRIC) – Model. Journal of Irrigation and Drainage Engineering 133:380-394.

Amayreh, J.A. 1995. Lake evaporation: a model study, Utah State University, Logan, UT.

Anderson, M.C., J.M. Norman, G.R. Diak, W.P. Kustas, and J.R. Mecikalski. 1997. A two-source time-integrated model for estimating surface fluxes using thermal infrared remote sensing. Remote Sensing of Environment 60:195-216.

Andrews, D.G. 2000. An Introduction to Atmospheric Physics Cambridge University Press.

Bastiaanssen, W.G.M. 1995. Regionalization of surface flux densities and moisture indicators in composite terrain, Wageningen Agricultural University, Wageningen, Netherlands.

Bastiaanssen, W.G.M., M. Menenti, R.A. Feddes, and A.A.M. Holtslag. 1998a. A remote sensing surface energy balance algorithm for land (SEBAL). Part 1: Formulation. Journal of Hydrology 212-213:198-212.

Bastiaanssen, W.G.M., H. Pelgrum, J. Wang, Y. Ma, J.F. Moreno, G.J. Roerink, R.A. Roebeling, and T.v.d. Wal. 1998b. A remote sensing surface energy balance algorithm for land (SEBAL). Part 2: Validation. Journal of Hydrology 212-213:213-229.

Bastiaanssen, W.G.M. 2000. SEBAL-based sensible and latent heat fluxes in the Irrigated Gediz Basin, Turkey. Journal of Hydrology 229:87-100.

Becker, F., and Z.L. Li. 1991. Complementarity of temperature independent Thermal Infrared Spectral Indices (TISI) and NDVI: Compared properties and combined use for soil and vegetation discrimination Physical Measurements and Signatures in Remote Sensing 2:475-480.

Brutsaert, W. 1982. Evaporation into the atmosphere D. Reidel Pub. Co., Dordrecht, The Netherlands.

Brutsaert, W., and M. Sugita. 1992. Application of self-preservation in the diurnal evolution of the surface energy budget to determine daily evaporation. Journal of Geophysical Research 97:18,377-18,382.

Burba, G.G., S.B. Verma, and J. Kim. 1999. Surface energy fluxes of Phragmites australis in prairie wetlands. Journal of Agricultural and Forest Meteorology 93:31-51.

Campbell, G.S., and J.M. Norman. 1998. An introduction to environmental biophysics. Second Edition Springer, New York, NY.

Chander, G., B.L. Markham, and A.B. J. 2007. Revised Landsat-5 Thematic Mapper Radiometric Calibration. IEEE Transactions on Geoscience and Remote Sensing 4:490-494.

Choudhury, B.J., R.J. Reginato, and S.B. Idso. 1986. An analysis of infrared temperature observations over wheat and calculation of latent heat flux. Agricultural and Forest Meteorology 37:75-88.

Choudhury, B.J., S.B. Idso, and R.J. Reginato. 1987. Analysis of an empirical model for soil heat flux under a growing wheat crop for estimating evaporation by an infrared-temperature-based energy balance equation. Agriculture and Forest Meteorology 39:283-297.

Clothier, B.E., K.L. Clawson, J. P.J. Pinter, M.S. Moran, R.J. Reginato, and R.D. Jackson. 1986. Estimation of soil heat flux from net radiation during growth of alfalfa. Agricultural and Forest Meteorology 37:319-329,.

Crago, R.D. 1996. Conservation and variability of the evaporative fraction during the daytime. Journal of Hydrology 180:173-194.

Daughtry, C.S., W.P. Kustas, M.S. Moran, R.D. Jackson, and J. Pinter. 1990. Spectral estimates of net radiation and soil heat flux. Remote Sensing of Environment 32:111-124.

De Bruin, H.A.R. 1987. From Penman to Makkink Proceedings and Information No. 39, TNO Committee on Hydrological Research, The Hague.

Duffie, J.A., and W.A. Beckman. 1991. Solar engineering of thermal processes John Wiley and Sons, NY.

ERDAS. 2002. Field Guide 6th ed. Atlanta, Georgia, ERDAS Inc.

Farah, H.O., and W.G.M. Bastiaanssen. 2001. Spatial variations of surface parameters and related evaporation in the Lake Naivasha Basin estimated from remote sensing measurements. Hydrological Processes 15:1585-1607.

Farah, H.O., W.G.M. Bastiaanssen, and R.A. Feddes. 2004. Evaluation of the temporal variability of the evaporative fraction in a tropical watershed. International Journal of Applied Earth Observation and Geoinformation 5:129-140.

Franks, S.W., and K.J. Beven. 1997. Estimation of evapotranspiration at the landscape scale: a fuzzy disaggregation approach. Water Resources Research 33:2929-2938.

Gentine, P., D. Entekhabi, A. Chehbouni, G. Boulet, and B. Duchemin. 2007. Analysis of evaporative fraction diurnal behaviour. Agricultural and Forest Meteorology 143:13-29.

Hall, F.G., K.F. Huemmrich, S.J. Goetz, P.J. Sellers, and J.E. Nickeson. 1992. Satellite remote sensing of surface energy balance: sucesses, failures, and unresolved issues in FIFE. Journal of Geophysical Research 97:19,061-19,089.

Hendrickx, J.M.H., and S.-H. Hong. 2005. Mapping sensible and latent heat fluxes in arid areas using optical imagery. Proceedings of International Society for Optical Engineering, SPIE 5811:138-146.

Jensen, J.R. 2000. Remote sensing of the environment: An earth resource perspective Prentice-Hall, Inc., New Jersey.

Kustas, W.P., C.S.T. Daughtry, and P.J.V. Oevelen. 1993. Analytical treatment of the relationships between soil heat flux/net radiation ratio and vegetation indices. Remote Sensing and Environment 46:319-330.

Kustas, W.P., and J.M. Norman. 1996. Use of remote sensing for evapotranspiration monitoring over land surfaces. Hydrological Sciences 41:495-516.

Markham, B.L., and J.L. Barker. 1987. Thematic Mapper. bandpass solar exoatmospheric irradiances. International Journal of Remote Sensing 8:517-523.

Menenti, M., W.G.M. Bastiaanssen, and D. Van Eick. 1989. Determination of hemispheric reflectance with thematic mapper data. Remote Sensing of the Environment 28:327-337.

Monteith, J.L., and M.H. Unsworth. 1990. Principles of Environmental Physics, Edward Arnold, London.

Moran, M.S., R.B. Jackson, L.H. Raymond, L.W. Gay, and P.N. Slater. 1989. Mapping surface energy balance components by combing Landsat Thematic Mapper and ground-based meteorological data. Remote Sensing of Environment 30:77-87.

Morse, A., M. Tasumi, R.G. Allen, and W.J. Kramer. 2000. Application of the SEBAL methodology for estimating consumptive use of water and streamflow depletion in the Bear river basin of Idaho through remote sensing. Final report submitted to the Raytheon Systems Company, Earth Observation System Data and Information System Project, by Idaho Department of Water Resources and University of Idaho.

NASA. 2002. The Landsat-7 Science Data User's Handbook.

Nerry, F., J. Labed, and M.P. Stoll. 1990. Spectral properties of land surfaces in the thermal infrared 1. Laboratory measurements of absolute spectral emissivity signatures. Journal of Geophysical Research 95:7027-7044.

Norman, J.M., W.P. Kustas, and K.S. Humes. 1995. A two-source approach for estimating soil and vegetation energy fluxes from observations of directional radiometric surface temperature. Agriculture and Forest Meteorology 77:263-293.

Oke, T.R. 1987. Boundary Layer Climates Routledge, NY.

Panofsky, H.A., and J.A. Dutton. 1984. Atmospheric Turbulence: Models and Methods for Engineering Applications Wiley, New York.

Price, J.C. 1984. Land surface temperature measurements from the split window channel of the NOAA 7 Advanced Very High Resolution Radiometer. Journal of Geophysical Research 89:7231-7237.

Salisbury, J.W., and D.M. D'Aria. 1992. Emissivity of terrestrial materials in the 8-14 um atmospheric window. Remote Sensing of Environment 42:83-106.

Shuttleworth, W.J., R.J. Gurney, A.Y. Hsu, and J.P. Ormsby. 1989. The variation in energy partition at surface flux sites. Proceedings of the IAHS Third International Assembly, Baltimore, MD. 186:67-74.

Tasumi, M., and R.G. Allen. 2000. Application of the SEBAL methodology for estimating consumptive use of water and stream flow depletion in the Bear River Basin of Idaho through remote sensing. Appendix A: The theoretical basis of SEBAL. Final report submitted to the Raytheon Systems Company, Earth Observation System Data and Information System Project.

Tasumi, M., R.G. Allen, and W.G.M. Bastiaanssen. 2000. The theoretical basis of SEBAL. Appendix A of Morse et al. (2000). Idaho Department of Water Resources, Idaho.

Tasumi, M. 2003. Progress in operational estimation of regional evapotranspiration using satellite imagery, Ph.D. Thesis, University of Idaho, Moscow, Idaho.

Tasumi, M., R.G. Allen, and R. Trezza. 2008. At-surface reflectance and albedo from satellite for operational calculation of land surface energy balance. Journal of Hydrologic Engineering 13:51-63.

Trezza, R. 2002. Evapotranspiration using a satellite-based surface energy balance with standardized ground control. Ph.D. Thesis, Utah State University: Logan, Utah.

Van de Griend, A.A., and M. Owe. 1993. On the relationship between thermal emissivity and the normalized difference vegetation index for natural surfaces. International Joural of Remote Sensing 14:1119-1131.

Vazquez, D.P., F.J. Olmo Reyes, and L.A. Arboledas. 1997. A comparative study of algorithms for estimating land surface temperature from AVHRR data. Remote Sensing of Environment 62:215-222.

Wan, Z., and J. Dozier. 1989. Land-surface temperature measurement from space: Physical principles and inverse modeling. IEEE Transactions on Geoscience and Remote Sensing 27:268-278.

Wang, J., W.G.M. Bastiaanssen, Y. Ma, and H. Pelgrum. 1998. Aggregation of land surface parameters in the oasis-desert systems of Northwest China. Hydrological Sciences 12:2133-2147.

Yamartino, R.J. 1984. A comparison of several "Single-Pass" estimators of the standard deviation of wind direction. Journal of Climate and Applied Meteorology 23:1362-1366.

CHAPTER 4

EVALUTION OF AN EXTREME-CONDITION-INVERSE-CALIBRATION REMOTE SENSING MODEL FOR MAPPING ENERGY BALANCE FLUXES IN ARID RIPARIAN AREAS

ABSTRACT

Accurate information on the distribution of the surface energy balance components in arid riparian areas is needed for sustainable management of water resources as well as for a better understanding of water and heat exchange processes between the land surface and the atmosphere. Since the spatial and temporal distributions of these fluxes over large areas are difficult to determine from ground measurements alone, their prediction from remote sensing data is very attractive as it enables large area coverage and a high repetition rate. In this study the Surface Energy Balance Algorithm for Land (SEBAL) was selected to estimate all the energy balance components in the arid/semi-arid riparian areas of the Middle Rio Grande Basin (New Mexico), San Pedro River (Arizona), and Owens Valley (California). We compare instantaneous and daily SEBAL fluxes derived from Landsat TM images to surface-based measurements with

eddy covariance flux towers. This study shows the potential for SEBAL to yield reliable estimates for energy balance components in riparian areas in the southwestern United States. The great strength of the SEBAL method is its internal calibration procedure that eliminates most of the bias in latent heat flux at the expense of increased bias in sensible heat flux.

4.1.   INTRODUCTION

The regional distribution of the energy balance components, net surface radiation (R_n), soil heat flux (G), sensible heat flux (H) and latent heat flux (LE) in arid riparian areas is critical knowledge for agricultural, hydrological and climatological investigations. However, R_n, G, H and LE are complex functions of atmospheric conditions, land use, vegetation, soils, and topography which cause these fluxes to vary in space and time. Therefore, it is difficult to estimate or representatively measure them at the regional scale (Parlange et al., 1995). Measurement approaches for LE from the land surface including eddy covariance (Kizer and Elliott, 1991), Bowen ratio (Scott et al., 2000) and weighing lysimeters (Wright, 1982) are too expensive and time consuming for continuous application at sufficient spatial density at the regional scale. These techniques produce LE measurements over small footprints (m^2 to ha) which are difficult to extrapolate to the regional scale, especially over heterogeneous land surfaces (Moran and Jackson, 1991). For example, in the heterogeneous landscape of the central plateau of Spain as many as 13 ground measurements of evapotranspiration in a relatively small area of 5000 km^2

were not sufficient to predict accurately the area-averaged evapotranspiration rate (Pelgrum and Bastiaanssen, 1996).

Since larger scale estimates of *LE* require alternative measurement and estimation approaches, the potential of satellite image-based remote sensing for examining spatial patterns or regional estimates of *H* and *LE* has been investigated by a number of investigators (Caparinni and Castelli, 2002; Choudhury, 1989; Granger, 2000; Kustas and Norman, 1996; Mecikalski et al., 1999; Menenti et al., 1993; Moran and Jackson, 1991; Nishida et al., 2003). These efforts have resulted in the development of remote sensing algorithms that are quite different in their spatial and temporal scales: 30 m to 1/8th degree (about 13 km in New Mexico), daily to monthly. Examples of algorithms used in hydrological investigations that have produced *H* and *LE* maps on local, regional, or national scales are: the North American Land Data Assimilation Systems (NLDAS) (Cosgrove et al., 2003), the Land Information Systems (LIS) (Peters Lidard et al., 2004), the Atmosphere-Land Exchange Inverse (ALEXI) (Anderson et al., 1997; Norman et al., 2003), the disaggregated ALEXI model (DisALEXI) (Norman et al., 2003), the Surface Energy Balance System (SEBS) (Han and Yang, 2004; Jia et al., 2003; Su, 2002), the Surface Energy Balance Algorithm for Land (SEBAL) (Bastiaanssen et al., 1998; Bastiaanssen et al., 2005), Mapping EvapoTranspiration at high spatial Resolution with Internalized Calibration (METRIC) (Allen et al., 2005; Allen et al., 2007a; Allen et al., 2007b), as well as algorithms without distinct acronyms (Jiang and Islam, 2001; Ma et al., 2004; Ma et al., 2006; Schüttemeyer et al., 2007).

SEBAL has been developed and pioneered by Bastiaanssen and his colleagues in
The Netherlands during the 1990s (Bastiaanssen, 1995; Bastiaanssen et al., 1994).
METRIC has been developed by Allen and his research team in Idaho using SEBAL as
its foundation (Allen et al., 2007a; Allen et al., 2007b). Unlike ALEXI and DisALEXI,
SEBAL and METRIC do not require spatial fields of air temperature and atmospheric
temperature soundings interpolated across the region of interest; unlike NLDAS and LIS,
SEBAL and METRIC do not require land cover maps. However, applications of SEBAL
and METRIC are restricted to clear days over areas of unvarying weather, and require
some supervised calibration for each image, preventing application at the continental
scale such as done by ALEXI, DisALEXI, NLDAS and LIS.

SEBAL and METRIC calculate the energy balance using extreme thermal and
vegetation conditions within an image using a "cold" and "hot" pixel. These procedures
index H from the land surface (one of the major energy balance components) to satellite
measured surface temperatures at specific surface boundary conditions. The main
difference between SEBAL and METRIC is that the latter makes use of the reference
evapotranspiration (ET_r) calculated using high-quality ground measurements from
weather stations (Allen et al., 1998) while the former can be applied without using
ground measurements. Since many areas of the world have no adequate ground
measurements there is a need for algorithms such as SEBAL, on the other hand METRIC
allows assimilation of ground measurements which can improve the quality of the H and
LE maps. The SEBAL approach has demonstrated a high accuracy for evaporation
mapping worldwide with typical accuracies of about ±15% and ±5% for, respectively,

daily and seasonal evaporation estimates (Bastiaanssen et al., 2005). Validation of METRIC evaporation in Idaho using precision lysimeter measurements (considered the best standard) has shown METRIC evaporation estimates to be within ±10% at the sub-field scale for daily, monthly and annual time scales (Allen et al., 2003; Allen et al., 2007b; Morse et al., 2000).

In this study we have selected SEBAL to estimate H and LE over arid riparian areas for the following reasons: (i) SEBAL consists of physically-based image analysis algorithms using standard satellite imagery and requires a minimum of ancillary meteorological information from surface measurements or atmospheric models; (ii) SEBAL deals with a large number of environmental variables and does not assume variables to be constant over space as do many other methods. For example, some methods assume all variables besides surface and air temperatures to be spatially constant (Jackson et al., 1996; Seguin and Itier, 1983); (iii) In SEBAL, the need for atmospheric correction of short-wave and thermal information in images is reduced (Tasumi, 2003) because SEBAL H and LE estimates depend only on radiometric temperature differences in the scene rather than on the absolute value of the surface temperature. This greatly enhances the applicability of SEBAL since the measurements needed for atmospheric corrections are often not available (Allen et al., 2007a); (iv) SEBAL uses Landsat images with high spatial resolution which allows to capture the small scale spatial heterogeneity that is typical for riparian areas in the southwestern United States.

Previous validation studies have mainly been conducted in relatively homogeneous agricultural areas and have focused on comparison of daily ET rates estimated from SEBAL and METRIC with ground measurements using lysimeters (Tasumi, 2003; Trezza, 2002), Bowen ratio and eddy covariance methods (Bastiaanssen et al., 2002; Droogers and Bastiaanssen, 2002) and scintillometer technique (Hemakumara et al., 2003; Kite and Droogers, 2000). The overall goal of this study is to conduct a thorough evaluation of the performance of SEBAL in arid riparian areas in New Mexico, Arizona and California. Here, vast deserts are transected by narrow river valleys covered by a mosaic of irrigated agricultural fields and riparian vegetation (cottonwood, saltcedar, Russian-willow and salt grasses) which creates a very heterogeneous landscape with a short patch length scale. If SEBAL performs well under these challenging conditions, it is likely to perform well in most arid and semi-arid regions. Another difference with previous studies is our focus on all components of the energy balance during the instant of satellite overpass as well as on a daily basis. We can accomplish this since we have available a quality controlled data set consisting of R_n, G, H and LE measurements in the riparian areas of the Middle Rio Grande Basin (New Mexico), San Pedro River Valley (Arizona) and the Owens River Valley (California).

4.2.   SURFACE ENERGY BALANCE ALGORITHM FOR LAND (SEBAL)

SEBAL is a remote sensing algorithm that evaluates the fluxes of the energy balance and determines *LE* as the residual

$$LE = R_n - G - H \qquad\qquad [4.1]$$

where R_n is the net radiation flux density [Wm^{-2}], G is the soil heat flux density [Wm^{-2}], H is the sensible heat flux density [Wm^{-2}], and *LE* (= λET) is the latent heat flux density [Wm^{-2}], which can be converted to the ET rate [mmday^{-1}] using the latent heat of vaporization of water λ [Jkg^{-1}] and the density of water ρ_w [kgm^{-3}].

To implement SEBAL, images are needed with information on reflectance in the visible, near-infrared and mid-infrared bands as well as emission in the thermal infrared band. Such images are offered by a number of satellites such as Land Satellite (Landsat), Moderate Resolution Imaging Spectroradiometer (MODIS), Advanced Very High Resolution Radiometer (AVHRR), Advanced Spaceborne Thermal Emission and Reflection Radiometer (ASTER), ENVISAT-Advanced Along Track Scanning Radiometer (AATSR) and China-Brazil Earth Resources Satellite (CBERS). In this study, we use Landsat images for their high spatial resolution. In undulated landscapes and mountains, a Digital Elevation Model (DEM) is also needed to take into account terrain slope and aspect of each pixel (Allen et al., 2007a; Tasumi and Allen, 2000). Extensive descriptions of SEBAL and METRIC and their implementations have been presented by

(Allen et al., 2007a; Allen et al., 2007b; Bastiaanssen et al., 1998; Bastiaanssen et al., 2005; Koloskov et al., 2007). In this section, we aim to present in a succinct manner all relevant SEBAL equations with emphasis on the semi-empirical and empirical equations.

4.2.1. Net Radiation

The net radiation R_n is obtained from the radiation budget under cloud-free conditions as

$$R_n = R_{s\downarrow} - \alpha \cdot R_{s\downarrow} + R_{L\downarrow} - R_{L\uparrow} - (1 - \varepsilon_0) \cdot R_{L\downarrow}$$ [4.2]

where $R_{S\downarrow}$ is the incoming shortwave radiation [Wm^{-2}], $R_{L\downarrow}$ is the incoming longwave radiation [W m^{-2}], $R_{L\uparrow}$ is the outgoing longwave radiation [Wm^{-2}], α is the surface albedo [-], and ε_0 is the surface emissivity [-].

The incoming shortwave radiation $R_{s\downarrow}$ is composed of both the direct solar radiation and the diffuse radiation. It is estimated as

$$R_{S\downarrow} = G_{sc} \cdot \cos\theta \cdot d_r \cdot \tau_{sw}$$ [4.3]

where G_{sc} is the solar constant (1367) [Wm^{-2}], θ is solar incident angle, d_r is the inverse squared relative Earth-sun distance [-], and τ_{sw} is the transmissivity of air [-]. In this study, we use DEMs (30 x 30m) to take into account (1) the effects of slope and aspect on the radiation balance and (2) the effects of elevation on pixel surface temperature as

explained in section [4.2.3]. The DEMs were obtained from United States Geological Survey (http://seamless.usgs.gov).

The cosine of the solar incidence angle (θ) is calculated as (Duffie and Beckman, 1991)

$$
\begin{aligned}
\cos\theta = {} & \sin(\delta)\sin(\phi)\cos(s) - \sin(\delta)\cos(\phi)\sin(s)\cos(\gamma) \\
& + \cos(\delta)\cos(\phi)\cos(s)\cos(\omega) \\
& + \cos(\delta)\sin(\phi)\sin(s)\cos(\gamma)\cos(\omega) \\
& + \cos(\delta)\sin(\gamma)\sin(s)\sin(\omega)
\end{aligned}
\qquad [4.4]
$$

where δ is the declination of the Earth [rad], ϕ is the latitude of the pixel [rad], s is the slope [rad], γ is the aspect ($\gamma = 0$ represents a south-facing slope, and $\gamma = -\pi$ or $\gamma = \pi$ represents a north-facing slope, $\gamma = -\pi/2$ is an east-facing slope and $\gamma = \pi/2$ represents an west-facing slope) and ω is the hour angle [rad]. Incoming solar and long wave radiation fluxes on slopes are converted to their horizontal equivalents by dividing the cosine of the incident solar angle [cos θ] by the cosine of the slope.

τ_{sw} in most SEBAL applications is estimated by an empirical relationship with elevation (z) (Allen et al., 1998):

$$
\tau_{sw} = 0.75 + 2\cdot10^{-5}\cdot z
\qquad [4.5]
$$

In METRIC, a band-by-band transmissivity is computed following Tasumi et al. (2008), based on sun and satellite view angle, elevation and precipitable water (Allen et al. 2007a). Reflected shortwave radiation $\alpha \cdot R_{s\uparrow}$ is dependent upon the surface albedo which is reflectivity in shortwave radiation. The albedo at the top of the atmosphere (α_{toa}) is computed using a standard method by NASA (Handbook, 2002). The surface albedo (α) is calculated in classical SEBAL applications using a semi-empirical relationship (Menenti et al., 1989):

$$\alpha = \frac{\alpha_{toa} - \alpha_{path\_radiance}}{\tau_{sw}^2}$$
[4.6]

where $\alpha_{path\_radiance}$ is the albedo path radiance [-], $\alpha_{path\_radiance}$ has a value between 0.025 to 0.04 and 0.03 is used in this study (Bastiaanssen, 2000). In METRIC, band-by-band corrections are made and integrated (Allen et al., 2007b). The latter method produces estimates for the albedo that are similar to those from Eq. [4.6] for most types of vegetation, but tends to estimate a lower albedo for bare soil (Tasumi et al., 2008)

Longwave radiation from atmosphere and surface depend on their temperatures and emissivities.

$$R_{L\downarrow} = \varepsilon_a \cdot \sigma \cdot T_{s\_cold}^4$$
[4.7]

$$R_{L\uparrow} = \varepsilon_o \cdot \sigma \cdot T_s^{\,4} \tag{4.8}$$

where ε_a is the emissivity of air [-], ε_0 is the surface emissivity [-], σ is the Stefan-Boltzmann constant (5.67 x 10^{-8}) [Wm^{-2}K^{-4}], T_{s_cold} is the surface temperature of a well-watered pixel in agricultural field [K] which is assumed to be equal to air temperature, and T_s is the surface temperature [K]. In a well-watered area, surface and air temperatures are assumed to be similar and the air temperature is relatively constant over a large area. Air temperature change due to elevation is accounted by lapse rate in this study. Note that since $R_{L\downarrow}$ is from the entire atmosphere not from the near surface atmosphere only, ε_a is really an 'effective' atmospheric emissivity rather than the actual emissivity derived from the near surface air temperature. In a recent study by Allen et al. (2007) the radiometric surface temperature of each pixel is used as a surrogate for T_a in Eq. [4.7] since ground measurements at American Falls Reservoir in SE Idaho during 2004 show that the surface temperature generates better estimate of the incoming longwave radiation.

In this study ε_a, ε_0 and T_s are estimated using empirical relationships by (Bastiaanssen et al., 1998; Tasumi and Allen, 2000) as

$$\varepsilon_0 = 1.009 + 0.047 \ln(NDVI) \tag{4.9}$$

$$\varepsilon_a = 0.85(-\ln \tau_{sw})^{0.09} \tag{4.10}$$

$$T_s = \frac{T_b}{\varepsilon_0^{0.25}} \qquad\qquad\qquad [4.11]$$

$$T_b = \frac{K_2}{\ln\left(\dfrac{K_1}{L_6} + 1\right)} \qquad\qquad\qquad [4.12]$$

where *NDVI* is normalized difference vegetation index, L_6 is the spectral radiance of thermal band 6 [Wm^{-2}sr^{-1}μm^{-1}], T_b is the brightness temperature [K] and K_1 and K_2 are constants [Wm^{-2}ster^{-1}μm^{-1}] (Landsat 7: $K_1 = 666.09$, $K_2 = 1282.71$; Landsat 5: $K_1 = 60.776$, $K_2 = 1260.56$). Coefficient 0.09 in Eq. [4.10] was calibrated using air temperature observed over a well-watered agricultural field in southern Idaho (Allen et al., 2000). Recent study by Allen et al. (2007a) uses radiometric surface temperature as a surrogate for T_a in Eq. [4.7].

4.2.2. Soil Heat Flux

The soil heat flux density *G* is positive for downward flux into the ground. Since *G* cannot be directly obtained from satellite observations, it is often estimated as a fraction of R_n (Anderson et al., 1997; Bastiaanssen, 2000; Choudhury et al., 1987; Norman et al., 1995). In this study, the soil heat flux is determined using a semi-empirical equation (Bastiaanssen, 2000) in which *G* is related to R_n, surface albedo α, surface temperature T_s and normalized difference vegetation index *NDVI*:

$$G = \left[(T_S - 273.1)(0.0038 + 0.0074\alpha)(1 - 0.98NDVI^4)\right]R \qquad\qquad [4.13]$$

4.2.3. Sensible and Latent Heat Fluxes

The most difficult issue in remote sensing algorithms is to solve the equation for the sensible heat flux density (Brutsaert et al., 1993)

$$H = \frac{\rho_a \cdot c_p \cdot (T_{aero} - T_a)}{r_{ah}}$$ [4.14]

where ρ_a is the density of air [kgm^{-3}], c_p is the specific heat capacity of air [Jkg^{-1}K^{-1}], T_{aero} is the aerodynamic surface temperature, T_a is the air temperature measured at a standard screen height, and r_{ah} is the aerodynamic resistance to heat transfer [sm^{-1}]. The simplicity of Eq. [4.14] is deceptive since T_{aero} cannot be measured by remote sensing. Remote sensing techniques measure the radiometric surface temperature, T_s, which is not the same as T_{aero}. T_s and T_{aero} are almost identical for near-neutral conditions, but T_s is higher than T_{aero} for stable conditions and lower for unstable conditions (Choudhury et al., 1986). The two temperatures can differ by 1 to 5 °C. Unfortunately, an error of 1 °C in $T_{aero} - T_a$ can result in a 50 Wm^{-2} error in H (Campbell and Norman, 1998; Hall et al., 1992) that may result in an error in the daily evaporation rate of as much as 2 mm per day. Although many investigators have tried to obtain T_{aero} from T_s by adjusting r_{ah} or by using an additional resistance term, so far no generally applicable solution to this problem has been developed (Kustas and Norman, 1996).

The aerodynamic resistance to heat transfer between levels z_1 and z_2, r_{ah12} [sm^{-1}] is affected by wind speed, atmospheric stability, and surface roughness (Brutsaert and

Sugita, 1992) and determined by:

$$r_{ah12} = \frac{ln\left(\frac{z_2}{z_1}\right) - \Psi_{h(z2)} + \Psi_{h(z1)}}{u^* \cdot k}$$ [4.15]

where

$$u^* = \frac{k \cdot u_{200}}{\ln\left(\frac{200}{z_{om}}\right) - \Psi_{m(200m)}}$$ [4.16]

where

$$u_{200} = \frac{u_x^*}{k} \ln\left(\frac{200}{z_{om}}\right)$$ [4.17]

where

$$u_x^* = \frac{u_x \cdot k}{\ln\left(\frac{z_x}{z_{om}}\right)},$$ [4.18]

z_1 and z_2 are two arbitrary heights, Ψ_h and Ψ_m are the stability correction factors for heat and momentum transport, respectively, u^* is the friction velocity [ms^{-1}], k is the von Karman's constant (0.41), u_{200} is the wind velocity at height 200 m, u_x^* is the friction velocity at weather station, u_x is the wind velocity [ms^{-1}] at weather station at height , z_x [m] and z_{0m} is the momentum roughness length [m].

In this study, z_{0m} is either estimated directly from the landuse map, if available, by assigning a typical z_{0m} for each land use/land cover class. When no land use map is

available we use an empirical relationship between z_{0m}, *NDVI* and α (Tasumi and Allen, 2000):

$$z_{om} = \exp[(a \times NDVI / \alpha) + b] \qquad\qquad [4.19]$$

where *a* is the slope and *b* is the intercept. Using the ratio *NDVI/α* (Tasumi et al., 2000) rather than using only α (Bastiaanssen et al., 1998), is more effective in predicting differences in z_{0m} between tall and short vegetation, because tall vegetation generally has lower albedo values than short vegetation due to shading from tall vegetation.

In the Middle Rio Grande Basin the image of September 14, 2000 was analyzed using land use maps prepared by Paul Neville at the Earth Data Analysis Center of the University of New Mexico. For all other dates, we used selected locations on each image with known land use and assigned z_{0m} to determine the *a* and *b* coefficients in Eq. [4.19] using regression analysis.

The Monin-Obukhov length parameter (*L*) is used to define the stability conditions of the atmosphere (Monteith and Unsworth, 1990).

$$L = -\frac{\rho c_p u_*^3 T_s}{kgH} \qquad\qquad [4.20]$$

where, *g* is the gravitational constant [9.81 ms^{-2}]

The stability correction factors for momentum and heat transport (Ψ_m and Ψ_h) can be obtained from the following equations (Allen et al., 2007a; Allen et al., 1996).

If $L < 0$: unstable atmosphere:

$$\Psi_{m(200m)} = 2\ln\left(\frac{1+x_{(200m)}}{2}\right) + \ln\left(\frac{1+x_{(200m)}^2}{2}\right) - 2\,ARCTAN\left(x_{(200m)}\right) + 0.5\pi \quad [4.21]$$

$$\Psi_{h(2m)} = 2\ln\left(\frac{1+x_{(2m)}^2}{2}\right) \quad [4.22]$$

$$\Psi_{h(0.1m)} = 2\ln\left(\frac{1+x_{(0.1m)}^2}{2}\right) \quad [4.23]$$

where

$$x_{(200m)} = \left(1 - 16 \cdot \frac{200}{L}\right)^{0.25} \quad [4.24]$$

$$x_{(2m)} = \left(1 - 16 \cdot \frac{2}{L}\right)^{0.25} \quad [4.25]$$

$$x_{(0.1m)} = \left(1 - 16 \cdot \frac{0.1}{L}\right)^{0.25} \quad [4.26]$$

If $L > 0$: stable atmosphere:

$$\Psi_{m(200m)} = -5 \cdot \left(\frac{2}{L}\right) \quad [4.27]$$

$$\Psi_{h(2m)} = -5 \cdot \left(\frac{2}{L}\right) \quad [4.28]$$

$$\Psi_{h(0.1m)} = -5 \cdot \left(\frac{0.1}{L} \right)$$

[4.29]

Eq [4.27] uses 2 m rather than 200 m since the boundary layer under stable atmospheric conditions will not extend above a few tens of meters at most. The use of 2m guarantees a stable numerical solution (Allen et al., 2005).

If $L = 0$; neutral atmosphere:

$$\Psi_m \text{ and } \Psi_h = 0$$

[4.30]

SEBAL overcomes the problem of inferring the aerodynamic surface temperature from the radiometric surface temperature and the need for near-surface air temperature measurements by directly estimating the temperature difference ΔT between T_1 and T_2 taken at two levels z_1 (0.10 m) and z_2 (2 m) above the canopy or soil surface without explicitly solving for the absolute temperature at a given height.

$$T_1 - T_2 = \Delta T = \frac{H \cdot r_{ah12}}{\rho_a \cdot c_p}$$

[4.31]

$$H = \frac{\rho_a \cdot c_p \cdot \Delta T}{r_{ah12}}$$

[4.32]

where r_{ah12} is the aerodynamic resistance between levels z_1 and z_2. The ΔT gradient

essentially 'floats' over the surface and eliminates the need to estimate the roughness length for sensible heat transport (z_{0h}). In addition, the floating gradient may reduce complications in applying the energy balance to conditions of sparse vegetation, where some argue for applying a two-source model.

The temperature difference for a dry surface without evaporation (the "hot" pixel) is obtained from the energy balance equation (Eq. [4.1]) with LE set to zero so that $H = R_n - G$ followed by the inversion of Eq. [4.14] to $\Delta T = H\, r_{ah12}/(\rho_a\, c_p)$. On the other hand, for a wet surface (the "cold" pixel) all available energy $R_n - G$ is assumed in traditional applications of SEBAL to be used for evapotranspiration so that $H = 0$ and $\Delta T = 0$ (Bastiaanssen, 2000; Bastiaanssen et al., 1998). As discussed in more detail later, this assumption suggests that no advection of energy from outside sources exists that would cause $H + LE$ to exceed $R_n - G$. METRIC uses a weather data-based reference (potential) ET to estimate the influence of advection (Allen et al., 2007a). The implicit assumption in extreme-condition-inverted-calibration processes such as SEBAL is that land surfaces with a high ΔT are associated with high radiometric temperatures and those with a low ΔT with low radiometric temperatures. Field measurements in Egypt and Niger (Bastiaanssen et al., 1998), China (Wang et al., 1998), USA (Franks and Beven, 1997), and Kenya (Farah and Bastiaanssen, 2001) have shown that the relationship between T_s and ΔT is approximately positively linear for different field conditions including irrigated fields, deserts and mountains.

$$\Delta T = c_1 \cdot T_s + c_2, \qquad\qquad [4.33]$$

where c_1 and c_2 are the linear regression coefficients valid for one particular moment (the time and date the image is taken) and landscape. By using the values of ΔT calculated for the cold and hot pixel (see section [4.3.5]) the regression coefficients c_1 and c_2 can be determined so that the extremes of H are constrained which will prevent outliers of H-fluxes. Occasionally, T_s of dry desert areas can exceed that of dry, bare agricultural soils. The impact of this is discussed in a later section. In summary, the empirical Eq. [4.33] relies on spatial differences of the radiometric surface temperature rather than absolute surface temperatures to derive maps of the sensible heat flux. This procedure minimizes the influence of atmospheric corrections, uncertainties in surface emissivity, surface roughness and differences in T_{aero} and T_s on H estimates (Allen et al., 2007a).

Generally, in the lower troposphere air temperature decreases by about 6.5 to 10 degree K for saturated and dry air, respectively, when elevation increases by 1 km (Allen et al., 1998; Andrews, 2000). The lapse rate effect on surface temperature has to be accounted for in the ΔT estimation in SEBAL because high elevations that appear to be "cool" due to the temperature decreases with elevation would be misinterpreted as having high ET. To correct for the error introduced by elevation changes in this study, the surface temperature is adjusted using the standard saturated air lapse rate (6.5 K / km), before Eq. [4.33] is applied by assuming that surface temperature expects similar decreases in air temperature with elevation change. Instead of using T_s determined with Eq. [4.11], we adjust the surface temperature for elevation as

$$T_{s\_adjusted} = T_s + 0.0065\Delta z \hspace{5cm} [4.34]$$

where Δz is the elevation of each pixel minus the elevation of an arbitrary datum [m] in the image where $T_{s\_adjusted}$ is specified to equal T_s. The term Δz is positive where the elevation of the pixel is higher than the datum. In our study area, the maximum Δz between ground measurements of the sensible and latent heat fluxes is 130 m or less (Table 4.2). Therefore, the maximum surface temperature difference caused by elevation is approximately 0.0065 x 130 = 0.8 K which is about 4 % or less of the temperature differences between the hot and cold pixels in the images used in this study. Thus, errors introduced by assuming an average lapse rate of 6.5 K/1000 m for each of the images analyzed will be negligible. When SEBAL is applied over larger elevation differences, it will be necessary to determine for each image the appropriate lapse rate.

Besides ΔT the other unknown in Eq. [4.32] is the aerodynamic resistance to heat transfer r_{ah12} (Eq. [4.15]) which is affected by wind speed, atmospheric stability, and surface roughness. Several algorithms take a few field measurements of wind speed and consider it spatially constant over representative parts of the landscape (Hall et al., 1992; Kalman and Jupp, 1990; Rosema, 1990). This assumption is only valid over homogeneous surfaces. For heterogeneous landscapes a wind speed near the ground surface is required for each pixel. One way to overcome this problem is to consider the wind speed spatially constant at a height of 200 m above ground level. This is a reasonable assumption since this height is usually above the blending height, where the wind speed is not affected by local changes in surface roughness. The wind speed at 200

m is obtained by an upward extrapolation of a wind speed measurement at the surface assuming a logarithmic, stability corrected, surface-layer wind profile (Holtslag, 1984). The wind speed distribution for each pixel is then obtained by a downward extrapolation using the local surface roughness, which is determined for each pixel using empirical Eq. [4.19] or a land cover map.

Finally, knowing r_{ah12} and ΔT, H can be determined for each pixel using Eq. [4.32]. However, as is seen in Eqs. [4.14] – [4.15] and [4.20] – [4.29], r_{ah12} is needed to calculate H while H is required to calculate r_{ah12}. Therefore, an iterative process is required to solve for H and r_{ah12}. The iteration starts with the assumption of neutral stability, i.e. Ψ_h and Ψ_m are zero, so that the first estimate for r_{ah12} can be calculated directly. The iterative process continues until the values of r_{ah12} and H become stable. Then, after inserting R_n, G and H into Eq. [4.1] the latent heat flux LE is obtained for each pixel. Finally, by dividing LE by the latent heat of vaporization of water we derive the instantaneous ET (mmhour^{-1}) at the time of the Landsat overpass around 10:30 am.

4.2.4. Daily Energy Balance Fluxes

SEBAL yields an estimate of the instantaneous LE at the time of the Landsat overpass. However, for most hydrological applications the daily LE is needed; so the instantaneous LE needs to be extrapolated to the daily LE which is done using the evaporative fraction (*EF*). Where soil moisture does not significantly change and advection does not occur, the evaporative fraction has been shown to be approximately

constant during the day (Brutsaert and Sugita, 1992; Crago, 1996; Farah and Bastiaanssen, 2001; Farah et al., 2004; Shuttleworth et al., 1989). However, analysis of field measurements by other investigators (Anderson et al., 1997; Sugita and Brutsaert, 1991; Teixeira et al., 2008) indicates that the instantaneous evaporative fraction on clear days at satellite overpass time (around 11:00 am) tends to be approximately 10 – 18 % smaller than the daytime average. Therefore, a correction coefficient c_{EF} is introduced to take into account differences between instantaneous and daily evaporative fractions. Some investigators use c_{EF} of 1.00 (Bastiaanssen et al., 1998; Bastiaanssen et al., 2005) while others suggest c_{EF} of 1.10 (Anderson et al., 1997) or c_{EF} of 1.18 (Teixeira et al., 2008). The value for c_{EF} should depend on the relative amount of advection of heat, which in turn is a function of regional evaporation, wind speed and relative humidity.

$$EF_{inst} \cdot c_{EF} = \frac{R_n - G - H}{R_n - G} \cdot c_{EF} = \frac{LE_{inst}}{LE_{inst} + H_{inst}} \cdot c_{EF} \approx EF_{24} \qquad [4.35]$$

Allen et al. (2007a) suggest using the fraction of reference ET (ET_rF) to extrapolate from instantaneous ET to daily ET, rather than EF, where the reference ET basis accounts for impacts of advection on the energy balance processes. Advection can be stronger during afternoon periods than at the time of the 10:30 am Landsat overpasses.

Assuming c_{EF} of 1.0, multiplication of the instantaneous EF_{inst} determined from SEBAL with the total daily available energy yields the daily ET rate in mm per day (Bastiaanssen et al., 1998; Bastiaanssen et al., 2005) as

$$LE_{24} = EF_{inst} \cdot \left(R_{n24} - G_{24}\right) \qquad [4.36]$$

and since the daily soil heat flux G_{24} [MJm^{-2}day^{-1}] is close to zero

$$ET_{24} = \frac{EF_{inst} \cdot (R_{n24} - G_{24})}{\lambda \cdot \rho_w} \approx \frac{EF_{inst} \cdot R_{n24}}{\lambda \cdot \rho_w} \qquad [4.37]$$

where LE_{24} is daily latent heat flux [MJm^{-2}day^{-1}], ET_{24} is daily ET [mmday^{-1}], EF_{inst} is the evaporative fraction [$(R_n - G - H)/(R_n - G)$] at the time of satellite overpass, λ is the latent heat of vaporization [Jkg^{-1}], ρ_w is the density of water [kgm^{-3}] and R_{n24} is daily net radiation [MJm^{-2}day^{-1}]. R_{n24} is obtained by an semi-empirical expression (De Bruin, 1987).

$$R_{n24} = 0.0864 \cdot \left[(1-\alpha) \cdot R_{a24} \cdot \tau_{sw} - 110\tau_{sw}\right] \qquad [4.38]$$

where

$$R_{a24} = G_{SC} \cdot d_r \cdot \int_{\omega 1}^{\omega 2} \cos(\theta) d\omega \qquad [4.39]$$

and 0.0864 is the conversion parameter from Wm^{-2} to MJm^{-2}day^{-1}. Eq. [4.38] was developed by de Bruin (1987) and recommended by Bastiaanssen et al (1998a) only for all-day clear sky condition. If the day of the satellite image is known to have had some cloudiness during periods preceding or following the time of the image, then one should

use a ground measured value for 24-h solar radiation (R_s) in place of $R_{a24} \cdot \tau_{sw}$. The

constant -110 depends somewhat on the type of surface. For example, Tasumi et al. (2000)

suggested -140 for irrigated fields in Idaho. In this study for riparian vegetated areas, the

coefficient -110 is used since it yields R_{n24} estimates that agree quite well with ground

measurements (MRD < 3%). R_{a24} is the daily-averaged extraterrestrial shortwave

radiation [Wm^{-2}] which is calculated by using information on location, day of year, slope

and aspect for each pixel (Tasumi and Allen, 2000).

In this study we compare the daily H derived from SEBAL with those measured

on the ground assuming that the daily G is negligibly small, i.e. zero (Kustas et al., 1993).

The daily H is calculated as

$$H_{24} = R_{n24} - G_{24} - LE_{24} \approx R_{n24} - LE_{24}.$$ [4.40]

Thus, H_{24} is not derived from the instantaneous H. Instead it is calculated as the

difference between R_{n24} and LE_{24}. The R_{n24} is derived independently from SEBAL results

using Eq. [4.38]. The LE_{24} depends on the EF_{inst} which is dependent upon the

instantaneous R_n, G, H and LE obtained from SEBAL.

4.3.   METHOD AND MATERIALS

4.3.1. Study Areas

The components of the energy balance (R_n, G, H and LE) are determined by SEBAL from sixteen Landsat images for three typical riparian areas in the southwestern United States: the Middle Rio Grande Valley (NM), the Owens Valley (CA) and the San Pedro Valley (AZ) (Figure 4.1 and Table 4.1).

The Middle Rio Grande Valley extends through central New Mexico and is defined as the reach of the Rio Grande between Cochiti Dam and Elephant Butte Reservoir. The Middle Rio Grande riparian vegetation consists of native vegetation such as cottonwood and salt grasses as well as various non-native species including saltcedar and russian olive. In the Middle Rio Grande Valley, the average annual air temperature is 15 °C. Daily summer temperatures range from 20 to 40 °C, while daily winter temperatures range from -12 to 10 °C. Mean annual precipitation is about 25 cm and mean annual potential evapotranspiration is approximately 170 cm.

The Owens Valley is a long, narrow valley on the eastern slope of the Sierra Nevada in Inyo County, California. It is a closed basin drained by the Owens River which terminates at saline Owens Lake. The Owens Valley has a mild high-desert climate: in summer (June, July and Aug) the lowest average daily minimum temperature is 7 °C and the highest average daily maximum temperature temperatures is 37 °C, and in winter (Nov, Dec, Jan and Feb) from -7 to 21 °C. Since, the Owens Valley is located in the "rain
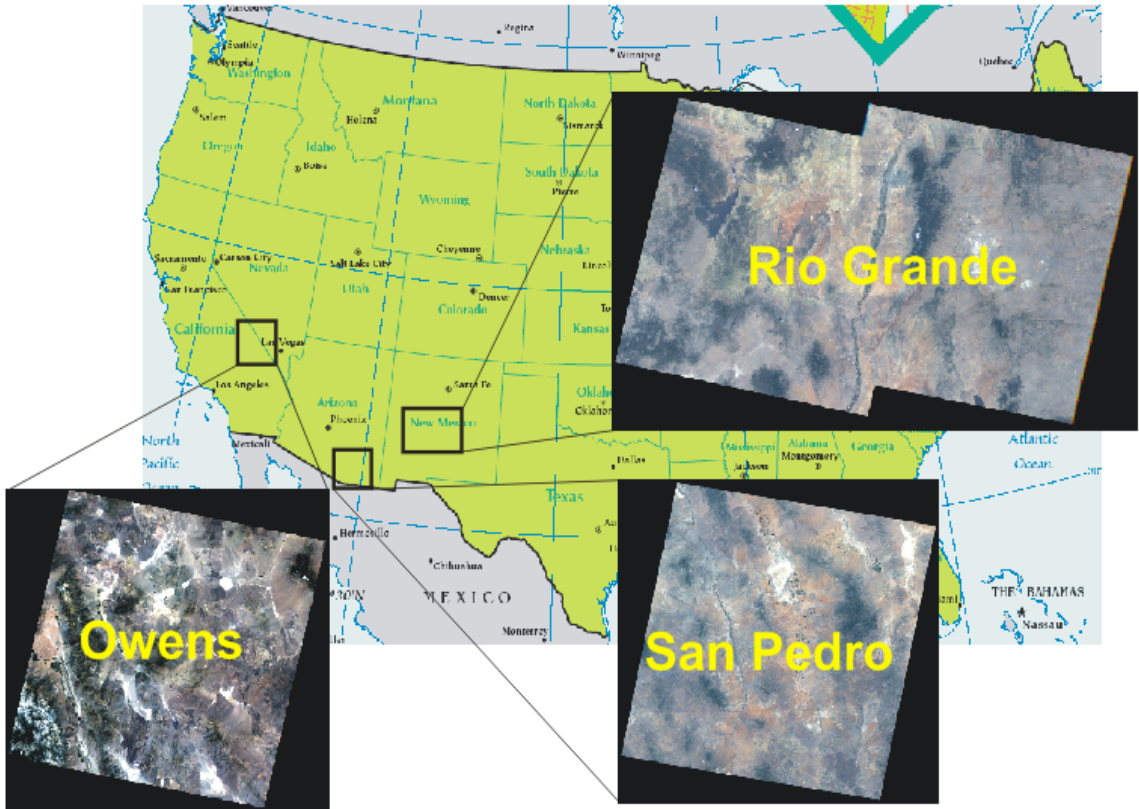
Figure 4.1 Landsat7 scenes of the study areas in New Mexico, Arizona and California

Table 4.1 List of Landsat TM images used in this study (overpass around 10:30 am).

Satellite	Area	Path/Row	Date
Landsat7	Rio Grande	33/36	04/07/2000
Landsat7	Rio Grande	33/36	07/28/2000
Landsat7	Rio Grande	33/36	09/14/2000
Landsat7	Rio Grande	33/36	09/30/2000
Landsat7	Rio Grande	33/36	05/09/2000
Landsat7	Rio Grande	34/36	06/04/2001
Landsat7	Rio Grande	34/36	05/06/2002
Landsat7	Rio Grande	33/36	05/31/2002
Landsat7	Rio Grande	33/37	05/31/2002
Landsat7	Rio Grande	33/36	06/16/2002
Landsat7	Rio Grande	33/36	08/19/2002
Landsat7	Owens Valley	41/34	07/10/2002
Landsat7	Owens Valley	41/34	08/11/2002
Landsat7	Owens Valley	41/34	09/12/2002
Landsat7	San Pedro	35/38	05/16/2003
Landsat7	San Pedro	35/38	08/12/2003

shadow" of the Sierra Nevada, the average annual precipitation in the Owens Valley is only about 12 cm and mean annual potential evapotranspiration is about 150 cm. Snowmelt runoff from the Sierra Nevada creates a shallow water table underneath the valley floor which supports approximately 28,000 hectares of native shrubs and grasses in riparian areas.

The San Pedro River flows north from the mountains of Sonora, Mexico, to the Gila River in southern Arizona. It is surrounded by vegetation consisting of cottonwood, willow, mesquite and sacaton grass. The mean air temperature of the Upper San Pedro valley is around 18 °C. Daily summer temperatures range from 22 to 44 °C, while daily winter temperatures range from 9 to 24 °C. Mean annual precipitation is about 36 cm and mean annual potential evapotranspiration is approximately 200 cm.

Although, the regional climate of all three areas is classified as arid/semiarid, there exists a difference in precipitation pattern. In the Owens Valley, precipitation occurs primarily in winter and spring, while in the San Pedro and the Middle Rio Grande Valleys, the annual precipitation distribution is bimodal, with more than half of the rainfall being monsoonal in summer, although the proportion varies considerably from year to year (Cleverly et al., 2002; Costigan et al., 2000; Elmore et al., 2002; Scott et al., 2000; Stromberg, 1998). Table 4.2 presents main characteristics of the study areas: vegetation type, elevation above sea level, height of vegetation canopy and the height of flux sensors above ground level. The average elevations are 1440, 1230 and 1220 m

Table 4.2 Site characteristics and sensor heights on the eddy covariance towers.

Site	Vegetation type	Elevation (m)	Vegetation height (m)	Sensor height (m)
Rio Grande – BDAS	saltcedar	1370	6.2	8.2
Rio Grande – BLN	cottonwood	1460	25.1	27.2
Rio Grande – SEV	saltcedar	1430	4.9	6.5
Rio Grande – SHK	cottonwood	1500	23.7	26.3
Owens – FSL138	alkali meadow	1280	0.2	2.5
Owens – PLC018	rabbitbrush scrub	1250	0.5	2.5
Owens – PLC074	saltbush meadow	1240	1.0	2.5
Owens – PLC185	desert sink scrub	1220	0.5	2.5
Owens – BLK100	alkali meadow	1170	0.2	2.5
San Pedro – CM	mesquite	1190	7.0	14
San Pedro – LSS	Sacaton	1230	1.0	3.5
San Pedro – LSM	mesquite	1240	3.5	6.5

above sea level for, respectively, the Middle Rio Grande Basin, Owens Valley and San Pedro Valley.

4.3.2. Eddy Covariance Measurements and Closure Forcing

SEBAL estimates of LE, H, G, and R_n are compared to ground-based eddy covariance and energy balance measurements. At each site, the turbulent heat fluxes were measured using the eddy covariance (EC) method. EC can theoretically provide direct and reliable measurements of H and LE (Arya, 2001). Although the method is relatively simple, EC measurements require expensive instrumentation that must be installed with great care. Any mistake with instrument leveling, orientation, calibration, and maintenance will lead to less accurate measurements. Some measurement errors such as instrument tilt, and reduced correlation due to spatial displacement between the EC sensors can be partially corrected during post-processing.

At all of the ground measurement sites, a three-dimensional sonic anemometer-thermometer that measures the three-dimensional wind vector and virtual temperature, was collocated with a Krypton hygrometer that measures water vapor density [gm^{-3}] with a sampling rate of 10 Hz (Cleverly et al., 2002; Scott et al., 2004; Steinwand et al., 2006). The covariances between the vertical wind speed and, respectively, water vapor density and virtual air temperature are used for the computation of, respectively, 30 minutes averages of the latent heat flux LE and the kinematic sensible heat flux H. The installed eddy covariance systems are oriented toward the predominant wind direction, thereby reducing data loss due to winds blocked by the tower and instrumentation. All eddy

covariance data were quality controlled and corrected for tilt by coordinate rotations, frequency response, oxygen absorption of the Krypton hygrometer, and flux effects on air density. The coordinate rotation, however, can not correct for effects of changing wind direction during 30-minute average periods that can cause mean 'vertical' wind speeds to deviate from 0, thereby inducing error in the H and LE measurements. This problem is common to EC measurements in tall vegetation such as trees where the sensors are placed too close to tree branches or canopy. Soil heat fluxes in the San Pedro Valley and Owens Valley were obtained from measurements using a soil heat flux plate that were corrected for soil heat storage above the plate using collocated soil temperature and soil moisture measurements.

At the Middle Rio Grande sites, soil heat storage could not be calculated due to the absence of soil moisture measurements. Therefore, the soil heat flux measurements in the Middle Rio Grande Valley have not been compared with those estimated by SEBAL. The net radiation was obtained from REBS Q7 net radiometers. In some of the installations, the R_n sensors may have been mounted too close to the towers and may have been impacted by reflection from the local structure. For the comparison of the 30 minutes averaged ground measurements with the instantaneous energy fluxes estimated using SEBAL, an 'instantaneous' ground measurement was determined by linear interpolation between the two 30 minutes averaged, ground measurements before and after the satellite overpass. To compute daily values of LE, H, G and R_n the 30 minutes flux data were summed over the day (00 – 24 hours).

We use the energy balance closure as a criterion for the selection of high-quality R_n, G, H, and LE ground measurements for comparison with SEBAL estimates. The relative closure (RC) is defined as (Twine et al., 2000).

$$RC = \frac{H + LE}{R_n - G} * 100 \qquad [4.41]$$

Figure 4.2 presents the relative closures at one location-day occurring on a satellite overpass day for all sites as provided by the investigators operating the EC towers in the Owens and San Pedro River Valleys. Since no soil heat flux measurements were available in the Middle Rio Grande Valley, we calculated the instantaneous relative closure [%] as

$$RC = \frac{H + LE}{R_n - G_{SEBAL}} * 100 \qquad [4.42]$$

where G_{SEBAL} is the instantaneous soil heat flux derived by SEBAL. This approach is justified on the basis of the reasonable agreement found between SEBAL derived instantaneous soil heat fluxes and those measured on the ground in the Owens and San Pedro River Valleys (see Table 4.8). If the sum of H and LE, before correction, was less than 65 % or greater than 110 % of the available energy ($R_n - G$), the data were not used in our analysis. This criterion leads to the exclusion of 45 % of instantaneous fluxes and 39 % of the daily fluxes of the data from the Middle Rio Grande Valley, 79 % (instantaneous) and 43 % (daily) from the Owens River Valley and 17 % (instantaneous) and zero % (daily) from the San Pedro River Valley.
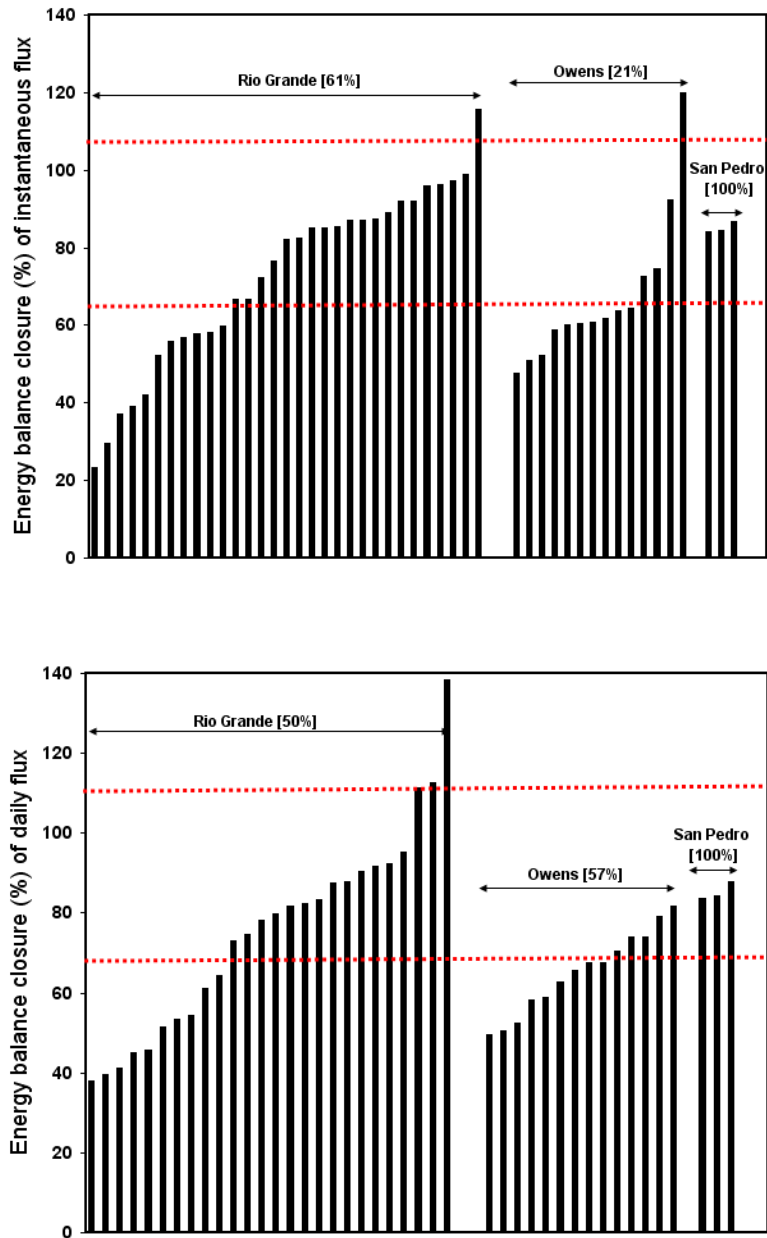
Figure 4.2 Distribution of energy balance relative closure $(H+LE)/(R_n-G)$ of instantaneous (top panel) and total daily (bottom panel) fluxes from eddy covariance towers. Each 'bar' represents one location-day occurring on a satellite overpass day. The dotted lines show criteria of acceptable closure [65 and 110 %] and percentage of the data having acceptable closure is shown in bracket.

Reviews of the EC method (Anderson and Farrar, 2001; Laubach and Teichmann, 1999; Paw et al., 2004; Richardson et al., 2006; Twine et al., 2000; Wilson et al., 2002) revealed that even if EC measurements are corrected for measurement errors as described above, the sum of the turbulent heat fluxes ($H+LE$) is typically 10 – 30 % less than $R_n - G$. One way to improve the turbulent heat flux estimates is to force the closure of the energy balance by increasing LE and H by the Bowen ratio (Twine et al., 2000). The adjusted H and LE are computed as

$$LE_{adj} = \frac{R_n - G}{\beta + 1} \qquad\qquad [4.43]$$

$$H_{adj} = R_n - G - LE_{adj} \qquad\qquad [4.44]$$

where H_{adj} and LE_{adj} are the adjusted H and LE by energy balance closure and β is the Bowen-ratio (H/LE), where H and LE were the original estimates from the EC system after correction for frequency response, oxygen absorption, and air density. A relative closure of 70 % is generally accepted to be of sufficient quality to use the data with confidence. However, some investigators go as low as 40 % (Anderson et al., 2004). In this SEBAL validation study we need high quality ground measurements and, therefore, we use only those measurements with relative closures exceeding 65 % after they have been adjusted using Eqs. [4.43] and [4.44].

We have not found in the literature any discussions of relative closures exceeding 100 %, yet some of our data have relative closure between 110 – 120 %. Relative closure

exceeding 100 % can be explained by a time shift in the flux time series, e.g. a sudden

decrease in R_n will take some time to be detectable as a smaller H and, thus, yield a

relative closure exceeding 100 % (see Eq. [4.42]). However, since we expect relative

closure around 70 – 90 % (Twine et al., 2000) any value exceeding 110 % is considered a

large outlier. Especially, since all our EC measurements reflect clear sky conditions

without clouds, i.e. without sudden R_n decreases. Therefore, we removed all

measurements with relative closures exceeding 110 %.

After elimination of EC measurements on the basis of unacceptable closures, we

eliminated three more EC measurements taken on May 16, 2003 in the San Pedro River

Valley at the Mesquite (CM) site. On this day the wind direction was approximately 90

degrees different from the prevailing wind direction which resulted in fetch distances

considerably shorter than the recommended 100 times the sensor height above the canopy

(Stannard, 1993; Sumner and Jacobs, 2005). The problem was exacerbated by the

relatively high placement (7 m) of the sensors above the canopy (Table 4.2) since the heat

fluxes can vary significantly with height under such conditions (De Bruin et al., 1991).

4.3.3. Comparison of SEBAL Predictions of Energy Balance Fluxes to Ground Measurements.

Comparison of SEBAL derived estimates of R_n, G, H and LE with ground

measurements is not a straightforward operation because the spatial and temporal scales

of the SEBAL predictions and ground measurements are quite different. In this section

we will discuss these scale issues for each flux in the energy balance.

4.3.3.1. Net radiation

R_n is measured with a net radiometer at a height of about 2 – 3 m above the canopy that covers typically a ground area on the order of 10 m^2. The measurements are taken every second and made available as 30 minutes averages for this study. The SEBAL R_n prediction is derived from reflectances in the visible, near-infrared and mid-infrared bands from a 900 m^2 pixel as well as the emittance in the thermal band from a 3600 m^2 pixel. Thus, the R_n ground observation is based on a measurement area at least two orders of magnitude smaller than the SEBAL R_n prediction. For homogeneous areas this difference will not matter much but for heterogeneous areas it may cause serious bias, since the satellite based R_n samples a larger area and is therefore more representative of the EC footprint. In arid riparian areas heterogeneity is the rule rather than exception. Radiometers are typically placed over the canopy of interest which may cause under-representation of surrounding bare soil or ground cover in the angle of view. Therefore, ground measured R_n is expected to be biased towards the R_n of the vegetation of interest in heterogeneous arid riparian areas.

4.3.3.2. Soil heat flux

G is measured by soil heat flux plates combined with the determination of changes in heat storage above the plate using soil temperature and soil water content measurements. If G is not corrected for heat storage above the plate, large errors will result (Sauer, 2002). This is the case for the measurements at the Middle Rio Grande sites and, therefore, these G measurements have not been used for the comparison. The

measurement area of a soil heat flux plate is about 0.001 m^2 which is almost six orders of magnitude less than a 900 m^2 Landsat pixel. G is spatially variable due to heterogeneity in soil moisture and vegetation cover, so that numerous flux measurements would be needed to estimate the average pixel G with the desired accuracy (Humes et al., 1994; Kustas et al., 2000). Therefore, we expect the instantaneous G ground measurements to be a rather crude estimation of the true instantaneous G of a pixel. The instantaneous G can vary widely depending on soil condition (20 – 300 Wm^{-2}) (Sauer et al., 2003). Since G is positive during the day and negative during the night the daily G is rather small compared to the other components of the energy balance (Seguin and Itier, 1983). G is measured in the field every second; we used 30 minutes averages for this study.

4.3.3.3. Sensible and latent heat fluxes

H and LE are measured using a three-dimensional sonic anemometer-thermometer and Krypton hygrometer, respectively. For these components of the energy balance the relationship between ground measurement area and pixel size is the opposite of the one discussed for R_n and G: the area of ground measurements is several times larger than a Landsat pixel. As discussed below a typical footprint for H and LE under the micrometeorological conditions of this clear-sky study covers about 5 pixels or about 4500 m^2. The location of the footprint is upwind of the EC tower and its size and distance from the tower are dependent upon atmospheric stability conditions. For the comparison of H and LE SEBAL estimates with ground measurements, first the footprint area must be determined and then, the weighted average is taken of the SEBAL estimated H and LE values of all pixels within the footprint area. These weighted averages of H and LE are

compared with the ground measured *H* and *LE* at the EC tower. This approach is expected to work reasonably well for comparison of SEBAL instantaneous *H* and *LE* estimates with ground measurements at the time of the satellite overpass.

Comparison of daily *H* and *LE* fluxes is problematic. Every 30 minutes instantaneous *H* and *LE* measurements are available at the EC tower but SEBAL estimates of the instantaneous *H* and *LE* are only available once per day at the time of the satellite overpass. Therefore, it is impossible to compare every 30 minutes the footprint averaged SEBAL estimates with the ground measurements. It is also problematic to compare daily SEBAL estimates of *H* and *LE* at each pixel with daily *H* and *LE* measurements at the EC tower. Daily *H* and *LE* measurements at the EC tower are the daily sum of 30 minutes instantaneous *H* and *LE* measurements originating from different footprints covering a wide area especially on days with highly variable wind directions. Combining the assumption of constant evaporative fraction during the day with the daily footprint using daily-averaged parameters including air temperature, u*, wind speed and direction, it may be possible to compare daily *H* and *LE* measurements at the tower with SEBAL estimates. However, uncertainties would remain and at best a rough comparison can be made since the average daily values are not necessarily a good measure for determination of a daily footprint. Therefore, in this study rather than trying to determine the true location of the "representative" daily foot print, the daily *H* and *LE* ground measurements will be compared with the average SEBAL estimated *H* and *LE* fluxes originating from twenty-five homogeneous pixels surrounding the EC tower. The homogeneity of the pixels surrounding the tower is evaluated by inspecting *NDVI*, albedo,

and surface temperature values as well as the *H* and *LE* values themselves.

4.3.3.4. Quantitative measures to compare SEBAL estimates and ground measurements

The numerical comparison of the energy balance components (R_n, *G*, *H*, and *LE*) estimated by SEBAL with those measured on the ground is conducted by means of quantitative measures proposed by Willmott and others for the validation of atmospheric models (Fox, 1981; Willmott, 1981; Willmott, 1982). We use the coefficient of determination (r^2), mean absolute difference (MAD), root mean square difference (RMSD), and the mean relative difference (MRD) as defined in Table 4.3 (Anderson et al., 1997). The coefficients of determination may be misleading as "high" or statistically significant values of *r* are often unrelated to the sizes of the differences between model estimates and measurements (Willmott and Wicks, 1980). In addition, the distributions of the estimates and measurements will often not conform to the assumptions that are prerequisite to the application of inferential statistics (Willmott, 1982). However, since r^2 is a commonly used correlation measure that reflects the proportion of the "variance explained" by the model, we report this measure. The MAD and RMSD are robust measures as they summarize the mean differences between SEBAL estimates and ground measurements; the MAD is less sensitive to outliers than RMSD. The MRD is often used as an indication how well SEBAL estimates agree with ground measurements (Bastiaanssen et al., 2005).

The quantitative measures provide useful information for the interpretation of the comparisons between ground measurements and SEBAL estimates of the heat fluxes.

Table 4.3 Definition of quantitative measures used to evaluate the performance of SEBAL

Measure	Description	Computational Form
n	Number of observations	
$\overline{G}$	Mean of the ground measurement	$\dfrac{1}{n}\sum\limits_{i=1}^{n} G_i$
$\overline{S}$	Mean of the SEBAL estimate	$\dfrac{1}{n}\sum\limits_{i=1}^{n} S_i$
SD_G	Standard deviation of the ground measurement	$\sqrt{\dfrac{1}{n-1}\sum\limits_{i=1}^{n}\left(G-\overline{G}\right)^2}$
SD_S	Standard deviation of the SEBAL estimates	$\sqrt{\dfrac{1}{n-1}\sum\limits_{i=1}^{n}\left(S-\overline{S}\right)^2}$
r^2	Coefficient of determination	$\left(\dfrac{n\cdot\sum\limits_{i=1}^{n}(G_i\cdot S_i)-\sum\limits_{i=1}^{n}G_i\sum\limits_{i=1}^{n}S_i}{\sqrt{\left[n\cdot\sum\limits_{i=1}^{n}\left(G_i{}^2\right)-\left(\sum\limits_{i=1}^{n}G_i\right)^2\right]\cdot\left[n\cdot\sum\limits_{i=1}^{n}\left(S_i{}^2\right)-\left(\sum\limits_{i=1}^{n}S_i\right)^2\right]}}\right)^2$
MAD	Mean absolute difference	$\dfrac{1}{n}\left[\sum\limits_{i=1}^{n}\left|G_i-S_i\right|\right]$
RMSD	Root mean square difference	$\sqrt{\dfrac{1}{n}\sum\limits_{i=1}^{n}\left(G_i-S_i\right)^2}$
MRD	Mean Relative Difference	$\dfrac{\left(\overline{G}-\overline{S}\right)}{\overline{G}}$

However, in order to detect significant differences among all comparisons under consideration a two-way Analysis of Variance (ANOVA) (McClave and Dietrich II, 1979) was conducted on the original difference values between ground measurement minus SEBAL estimate as well as on the ranks of the difference values. The latter approach does not require the assumption of normally distributed values (Conover and Iman, 1981). The "treatments" in the ANOVA are the different combinations of ground measurements and SEBAL estimates discussed in Section [4.4.4]. The "blocks" are ground measurements of one EC tower on a given day: 25 blocks are used for comparison of instantaneous heat fluxes and 24 blocks for comparison of daily fluxes.

4.3.4. Footprint Model

The location and extent of the footprint depends on surface roughness, atmospheric stability, wind speed, wind direction and may cover many pixels upwind of the eddy covariance tower (e.g. Hsieh et al., 2000; e.g. Schmid and Oke, 1990). There are several types of footprint models. Initially, simple two-dimensional analytical footprint models for neutral atmospheric conditions were developed (e.g. Gash, 1986; Schuepp et al., 1990). Later, the analytical footprint model was improved to account for atmospheric stability conditions (e.g. Horst and Weil, 1992; Hsieh et al., 2000). The footprint flux, $F_{(x,\ Zs)}$ [-], along the upwind direction, x [m], measured at the height z_s [m], suggested by (Hsieh et al., 2000) is used in this study.

$$F_{(x,z_s)} = \frac{1}{k^2 x^2} D z_u^P |L|^{1-P} \exp\left(\frac{-1}{k^2 x} D z_u^P |L|^{1-P}\right)$$
[4.45]

where

$$z_u = z_s \left[\ln \left(z_s / z_{0m} \right) - 1 + z_{0m} / z_s \right]$$ [4.46]

and

$$L = \frac{- \rho_a \cdot u_*^3 \cdot c_p \cdot T_a}{k \cdot g \cdot H}$$ [4.47]

and

$$\begin{cases} D = 0.28; P = 0.59 : unstable[L < 0] \\ D = 2.44; P = 1.33 : stable[L > 0] \end{cases}$$ [4.48]

where k is the von Karman constant (0.4), D and P are similarity constants, z_u is a length scale [m], L is the Obukhov length [m], z_s is the instrument height [m] above the zero-plane displacement, d [m], z_{0m} is the momentum roughness height [m], ρ_a is the density of air [kgm^{-3}], $u*$ is the friction velocity [ms^{-1}], c_p is the specific heat capacity of dry air at constant pressure (1005) [Jkg^{-1}K^{-1}], T_a is the mean air temperature [K], g is the gravitational constant (9.81) [ms^{-2}], and H is the sensible heat flux [Wm^{-2}].

The cumulative footprint scalar flux, $F_{(x, Zs)\_cum}$ [-], along the upwind direction, x, can be calculated by the following equation (Hsieh et al., 2000).

$$F_{(x,z_s)\_cum} = \exp \left(\frac{-1}{k^2 \cdot x} D z_u^P |L|^{1-P} \right)$$ [4.49]

In order to get a three-dimensional view of the footprint, the footprint flux across the main wind direction (y) is assumed to have a Gaussian distribution with an integrated

value equal to $F_{(x,y,z_s)}$. Incorporating equations for lateral plume dispersion the three-dimensional footprint flux at any point x, y and z_s is calculated as (Gryning et al., 1987):

$$F_{(x,y,z_s)} = \frac{F_{(x,z_s)}}{\sqrt{2\pi} \cdot \sigma_y} e^{-\left(y^2/2\sigma_y^2\right)}$$

[4.50]

where y is the distance [m] from the mean wind-axis x. σ_y is the cross wind spread [m] estimated as (Hanna et al., 1977)

$$\sigma_y = \sigma_\theta \cdot x \cdot f_y$$

[4.51]

where σ_θ is the standard deviation of the wind direction in azimuth angle [-], x is the distance along the upwind direction and f_y is an empirical function [-] (Draxler, 1976; Gryning et al., 1987; Irwin, 1983)

$$f_y = 1/\left(1 + \left(t/2T_y\right)\right)^{0.5}$$

[4.52]

where t is the travel time [s] and T_y is the Lagrangian time scale for the lateral dispersion. We used a value of 600s for T_y, irrespective of the atmospheric stability (Irwin, 1983). In this study, σ_θ is calculated using the Yamartino algorithm (Yamartino, 1984) as

$$\sigma_\theta = \sin^{-1}(\varepsilon)\left[1 + 0.1547\varepsilon^3\right]$$

[4.53]

where

$$\varepsilon = \left[1 - \left(\left(U_x\right)^2 + \left(U_y\right)^2\right)\right]^{0.5}$$ [4.54]

where

$$U_x = \left(\sum \sin \theta_i\right)/N$$ [4.55]

and

$$U_Y = \left(\sum \cos \theta_i\right)/N$$ [4.56]

where N is the number of samples and θ_i is the azimuth wind direction [degree] of an individual measurement.

In order to compute the H and LE fluxes from SEBAL which correspond to the eddy covariance measurements, the weighting factor for each pixel W_i within the footprint area needs to be determined according to

$$W_i = \frac{F_{(x,y,z_s)i}}{\sum_1^n F_{(x,y,z_s)i}}$$ [4.57]

The footprint weighted H_{FP} and LE_{FP} (FP stands for footprint) is then calculated by the equations:

$$H_{FP} = \sum_i^n \left(W_i \cdot H_i\right)$$ [4.58]

$$LE_{FP} = \sum_i^n \left(W_i \cdot LE_i\right)$$ [4.59]

where H_i and LE_i are the pixel-scale H and LE estimated from SEBAL.

A typical footprint size and footprint intensity for one 30 minute period on August 19, 2002, at a Rio Grande saltcedar EC tower is presented in Figure 4.3. To verify the quality of the footprint model used in this study, we also calculated x_{max} (peak footprint) for this period with the model by Schuepp et al. (1990). The models by Hsieh et al (2000) and Schuepp et al. (2000) calculate x_{max} as 10 m (Figure 4.3) and 11 m, respectively, which implies that the footprint from Hsieh et al (2000) is indeed close to the tower. At most EC sites, the maximum contribution to the footprint was within 50 m from the tower (wind speeds were generally less than 4 ms^{-1}) and most of the footprint intensity (>90 %) is located within 300 m from the tower. We compute the footprints from meteorological parameters including air temperature, sensible heat flux, wind speed, wind direction and friction velocity. The footprints for H and LE are obtained for the time of the satellite overpass using the 30 minute averaged meteorological parameters. Approximately 80 % of all footprint fluxes cover an area of 5 to 9 pixels, twenty percent cover larger areas. As explained in Section [4.3.3.3] calculation of a representative daily footprint for comparison of SEBAL H and LE estimates and ground measurements is nearly impossible. Therefore, the use the average H and LE values of the 25 pixels surrounding the EC tower pixel is considered to be the best option for the comparison of daily ground measurements and SEBAL estimates.
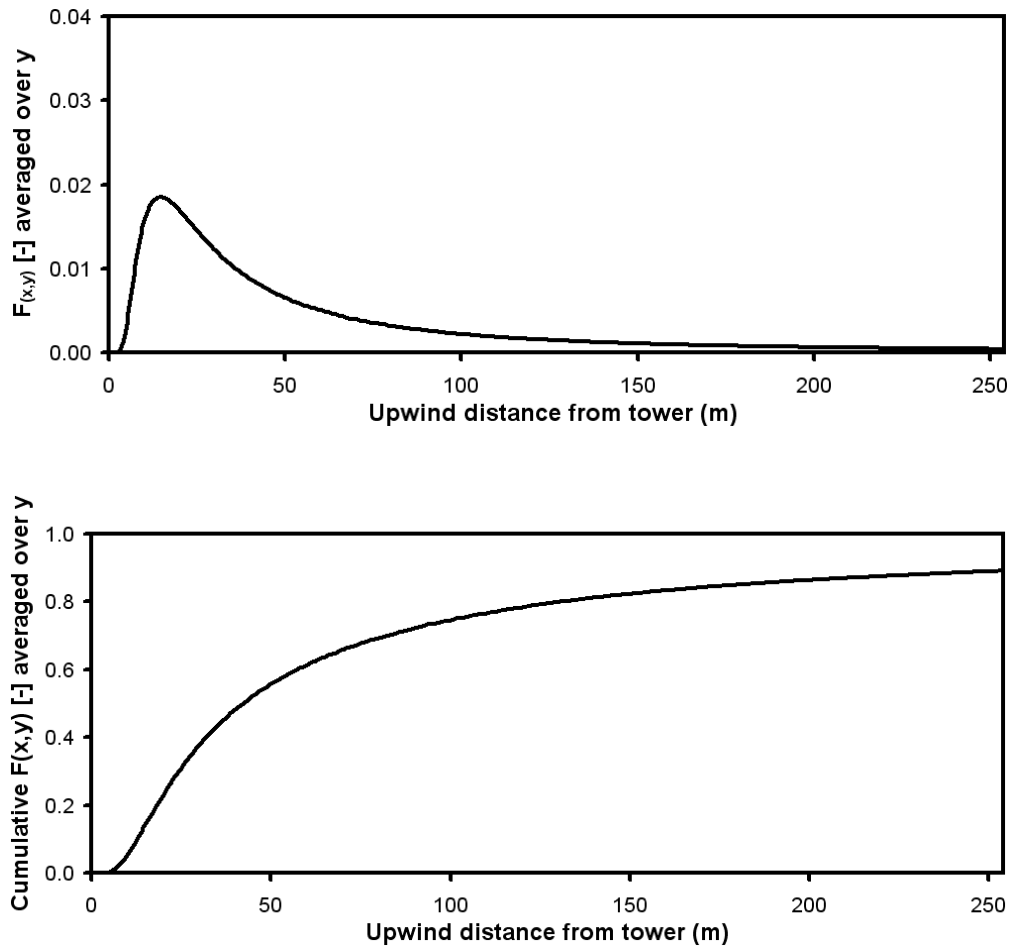
Figure 4.3 Footprint size and footprint intensity from the eddy covariance tower located at SEV (saltcedar) in Rio Grande on August 19, 2002 (10:40 am) (wind speed: 3.4 m/s, vegetation height: 4.9 m and sonic anemometer height from ground: 6.5 m).

4.3.5. Selection of Temperatures for the Hot and Cold pixel

During the course of this study we have found that the correct selection of the temperatures of the cold and hot pixel for the derivation of parameters c_1 and c_2 in Eq. [4.33] is the most critical step in the entire SEBAL process. An error of a few degrees K will cause serious distortion of the distribution of the sensible and latent heat fluxes over an image. The ranking of the heat fluxes from smallest to largest will still be correct but their absolute values can be considerably flawed. The selection of cold and hot pixels requires a thorough understanding of field micrometeorology and is somewhat subjective, i.e. different experts will select slightly different temperature values.

The cold pixel is normally selected in areas with well-watered healthy crops with full soil cover or in shallow water bodies (Bastiaanssen et al., 2005). Over the cold pixel it is assumed that $\Delta T = 0$, which implies that $H = 0$ and $LE = R_n - G$. An alternative manner is to use the reference ET (Allen et al., 1998) for the estimation of H in well-irrigated alfalfa and clipped grass fields (Allen et al., 2007a; Tasumi, 2003). However, during the period of this study a lack of high-quality weather data for calculation of the reference ET in the Middle Rio Grande Valley made implementation of the latter approach is cumbersome. Of course, the absence of high quality weather data is the default condition for many regions worldwide (Droogers and Bastiaanssen, 2002) which leaves the original SEBAL implementation as the only alternative.

The selection of the hot pixel is often difficult since the heterogeneous landscapes of the southwestern U.S. contain many hot pixels with a wide range of temperatures and,

therefore, of ΔT's that fulfill the condition that $LE = 0$ and $H = R_n - G$. In this study, the hot pixel is selected from a dry bare agricultural field with negligible ET. There are hotter pixels in the scene (e.g. a parking lot or sparsely-vegetated desert), but the ET over the cooler dry bare agricultural field is already expected to be zero. Thus, for any pixel cooler than the hot pixel, ET > 0 (if the R_n and G are the same), and for any pixel warmer than the hot pixel, ET = 0. In addition, the estimation equation for G was derived for agricultural conditions and therefore produces more dependable estimates for calibration when applied to a bare, agricultural soil having a tillage history.

We used two different approaches for the selection of the temperatures for the cold and hot pixel: the *EC approach* is based on inspection of the hydrogeological features of the landscape followed by fine-tuning the parameters c_1 (slope) and c_2 (intercept) in Eq. [4.33] using ground measurements of available instantaneous latent heat fluxes at the EC towers. In the EC approaches, cold pixels are selected from a fully covered well-watered agricultural field characterized by $NDVI > 0.7$ or higher and albedo $0.16 - 0.25$. Since there were no fully covered irrigated fields in the image of April 7, 2000 just before the start of the growing season, we selected the cold pixel in a shallow surface water body. All the hot pixels in the EC approach are chosen inside of a bare agricultural field characterized by $NDVI < 0.15$. Since selection of the cold pixel is straightforward in fully covered fields, the temperature of the cold pixel was fixed but the temperature of the hot pixel was varied to best match the instantaneous ground measurements of LE. Steps for hot pixel selection in the EC approach are presented in Figure 4.4. First dT and then LE were calculated from the first set of anchor pixels
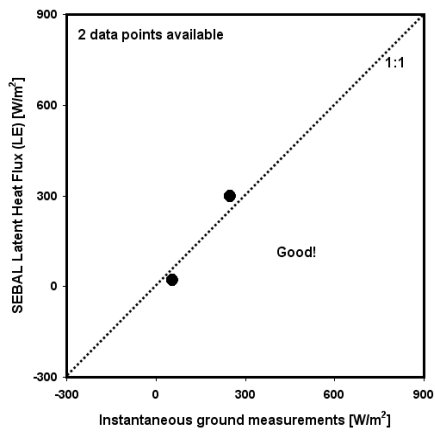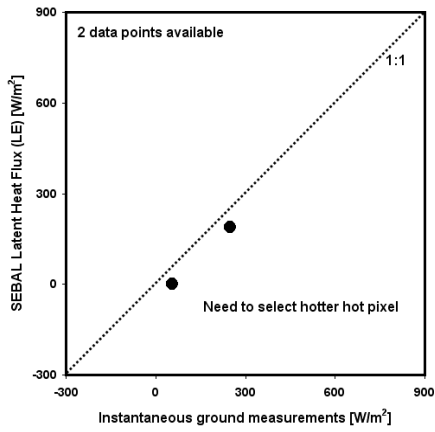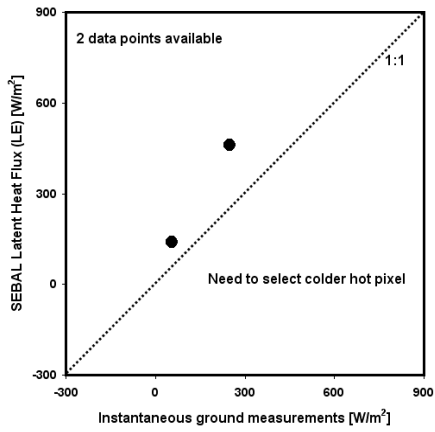
Figure 4.4 Example of steps for hot pixel selection in EC approach.

selected using the guidelines in the METRIC manual (Allen et al., 2005). Next, different

hot temperatures were selected in a bare field close to the first choice for the hot pixel.

Then, the hot temperature that resulted in the best visual agreement with the ground

measurements of LE was selected for determination of coefficients c_1 and c_2 in Eq. [4.33].

However, it is not trivial to obtain a perfect match with 2 to 3 LE ground measurements.

Therefore, there always remains some discrepancy as shown in Figure 4.4. The *Empirical*

(EM) approach is based only on inspection of the hydrogeological features of the

landscape and micrometeorological considerations. The latter approach is typical for most

SEBAL applications since the high density network of EC towers available in this study

is a unique situation. The data in Table 4.4 show that the EM approach results in cold

pixels around $2 - 3$ degree colder than the EC approach and hot pixels about 1 degree

colder. In order to independently evaluate the EC versus the EM approach, I implemented

the EC approach while my advisor, Dr. Hendrickx, implemented the EM approach.

**4.3.6. Scenarios for Comparison of SEBAL Estimates of Sensible and Latent Heat
Fluxes to Ground Measurements.**

      In the previous sections we discussed several different ways to establish energy

balances using either SEBAL or ground measurements. SEBAL has been implemented

using the EC and the EM approaches for selection of the cold and hot pixel (Section

[4.3.5]). In the EC approach, calibration of SEBAL to ground measurements was

implemented either using the average footprint weighted instantaneous heat fluxes

(EC_FP) or using the instantaneous heat fluxes of the pixel where the EC tower is located

Table 4.4 Information of anchor pixel temperatures and dT-T_s relationship parameters.

Date	EC approach (FP)				EC approach (TP)				EM approach			
	T_{s_c}[1]	T_{s_h}[2]	c_1[3]	c_2[4]	T_{s_c}	T_{s_h}	c_1	c_2	T_{s_c}	T_{s_h}	c_1	c_2
4/07/2000	289	313	0.24	-69.7	289	311	0.28	-98.5	289	313	0.24	-69.7
5/06/2002	293	316	0.25	-72.6	293	318	0.22	-64.5	292	320	0.20	-59.0
5/09/2000	296	314	0.36	-107.9	296	316	0.32	-93.7	291	317	0.25	-74.2
5/31/2002[5]	299	326	0.19	-58.2	299	332	0.14	-40.6	298	326	0.18	-54.9
5/31/2002[6]	299	325	0.22	-66.4	299	325	0.23	-68.0	297	326	0.19	-56.0
6/04/2001	299	325	0.19	-57.5	299	321	0.22	-64.5	293	319	0.19	-57.4
6/16/2002	302	331	0.18	-55.9	302	331	0.18	-54.7	296	325	0.18	-53.9
7/28/2000	300	317	0.34	-100.8	300	318	0.32	-96.9	297	317	0.29	-85.4
8/19/2002	297	316	0.27	-81.6	297	318	0.25	-75.9	294	312	0.34	-99.3
9/14/2000	296	313	0.38	-111.4	296	315	0.32	-95.8	294	312	0.33	-96.7
9/30/2000	296	312	0.40	-120.0	296	313	0.36	-108.2	289	309	0.30	-85.8
7/10/2002	303	334	0.14	-41.9	303	335	0.13	-39.5	303	334	0.13	-39.3
8/11/2002	300	326	0.17	-51.2	300	326	0.15	-45.4	299	328	0.13	-39.4
9/12/2002	295	326	0.13	-39.9	295	322	0.17	-50.2	296	324	0.14	-42.1
8/12/2003	298	319	0.31	-92.8	298	319	0.29	-86.9	298	317	0.32	-97.3
Average	297	321	0.3	-75.2	297	321	0.24	-72.2	295	320	0.2	-67.4

[1]Temperature [K] of cold pixel, [2]Temperature [K] of hot pixel, [3]slope in dT-T_s relation, [4]intercept in dT-T_s relation, [5]path/row: 33/36, [6]path/row: 33/37

(EC_TP). The former method is difficult to implement for most practitioners while the latter is practical and fast. In addition, ground energy balances have been established using either net radiation measurements on the ground with a footprint of about 10 m^2 or the net radiation estimated by SEBAL at the pixel scale. For the comparison of these different methods for deriving SEBAL estimated and ground measured heat fluxes, we defined seven different scenarios (Table 4.5). Scenarios S1, S2, and S4 employed the EC approach for selection of the cold and hot pixel, while scenarios S3 and S5 used the EM approach (see Section [4.3.5]). The EM approach is the classical SEBAL approach (Bastiaanssen, 2000; Bastiaanssen et al., 1998) that can be implemented without high quality meteorological data. Scenarios S1, S2, and S3 compared SEBAL based estimates against ground measurements of fluxes where the ground measured R_n was used to adjust H and LE measurements to close the energy balance using Eqs. [4.43] and [4.44]. With the exception of the soil heat flux in the Middle Rio Grande Valley that was taken from SEBAL. Scenarios S4 and S5 established the closure and adjustment of LE and H from the ground based energy balance using SEBAL R_n estimates since those seemed to be more representative for heterogeneous pixels as discussed in Section [4.3.3.1]. Since the differences between S1 and S2 turned out to be relatively minor, the labor intensive footprint (FP) analysis for selection of the anchor pixel temperature was not implemented along with scenarios S4 and S5.

No independent radiation data are available that present absolute proof about the possible higher quality of the SEBAL net radiation estimates at the pixel scale over the ground measurements. The Q7 net radiometers may have been placed preferentially over

Table 4.5 Scenarios of comparison between SEBAL and ground measurements

ID	Scenario	Assumption	Practitioner's assumption
S1	EC Approach (FP)[1]	R_n^5 is correct	R_n is correct
S2	EC Approach (TP)[2]	R_n is correct	R_n is correct
S3	EM Approach[3]	No ground measurements used	
S4	EC Approach (SR_n[4])	SR_n is correct	SR_n is correct
S5	EM Approach (SR_n)	No ground measurements used	
AS2	EC Approach (TP)	SR_n is correct	R_n is correct
AS4	EC Approach (SR_n)	R_n is correct	SR_n is correct

[1]Match between the ground measured instantaneous *LE* (adjusted for closure error) at the satellite overpass and the footprint weighted averaged SEBAL *LE*. [2]Match between the ground measured instantaneous *LE* (adjusted for closure error) at the satellite overpass and the SEBAL *LE* of the tower pixel. [3]Consider the hydrogeological features of the landscape and micrometeorological considerations. [4]SEBAL R_n estimate is used for the determination of the closure adjusted ground measured *H* and *LE*. [5]Ground measured R_n is used for the determination of the closure adjusted ground measured *H* and *LE*.

vegetation and may have some calibration challenges. On the other hand, the radiation subroutines in SEBAL rely on SEBAL's internal calibration that eliminates to some extent the need for atmospheric corrections for estimation of LE (Allen et al., 2007a; Bastiaanssen et al., 2005) but do not necessarily guarantee a perfect estimate of net radiation. Therefore, two more alternative scenarios have been defined (AS2 and AS4 in Table 4.5) for the evaluation of biases that are introduced when practitioners use ground measurements for calibration and validation of SEBAL as we have done in S1, S2 and S4. Scenario AS2 is counterpart to S2 and assumes that the ground energy balance that uses the SEBAL estimated R_n is really the correct one for adjusting H and LE for closure error, while a practitioner unknowingly uses the ground based H and LE where the energy balance closure was done using the ground R_n measurements (S1–S3), without knowledge of satellite based R_n. Scenario AS4 is counterpart to S4 and assumes that the ground energy balance that uses the ground R_n measurements for closure error is correct, while a practitioner unknowingly uses the LE and H, but with the SEBAL R_n. Given the current interest in the use of EC and scintillometer ground measurements for the validation and calibration of remote sensing ET algorithms (Hendrickx et al., 2007; Watts et al., 2000), these scenarios are bound to occur. No alternative scenario counter to S1 has been implemented since S1 and S2 are quite similar.

4.4. RESULTS AND DISCUSSION

4.4.1. Spatio-temporal Distribution of Daily Latent Heat Fluxes

Figure 4.5 presents an example of the ET maps that can be produced by SEBAL for all components of the energy balance as well as other environmental parameters such as albedo, *NDVI*, surface temperature, etc. In Figure 4.5, daily ET rates are mapped in the Middle Rio Grande Valley and surrounding deserts on four different days during the spring, summer and fall. The maps show how the ET rates increase from April 7 (just after the start of the irrigation season) to June 16 at the height of the irrigation season; a decrease of ET is observed during September and October when fields are harvested and lower temperatures are impeding crop growth. On all four days higher ET rates are observed over irrigated fields and in the riparian areas while low to very low rates occur in the surrounding deserts. The high spatial resolution of these maps (30 m) allows water resources managers (i) to follow where, when, and how much water has moved into the atmosphere by evapotranspiration; (ii) to monitor crop performance; (iii) to better evaluate the performance of irrigation systems; and (iv) to estimate water use for water rights adjudication. In this study we evaluate the quality of SEBAL estimated ET maps in riparian areas of the southwestern U.S. through a systematic comparison of SEBAL predicted and ground measured energy balance fluxes.

4.4.2. Comparison of SEBAL Net Radiation with Ground Measurements

Figures 4.6 and 4.7 and Table 4.6 present the comparisons of the instantaneous and daily R_n measured on the ground and estimated by SEBAL. The method used for the
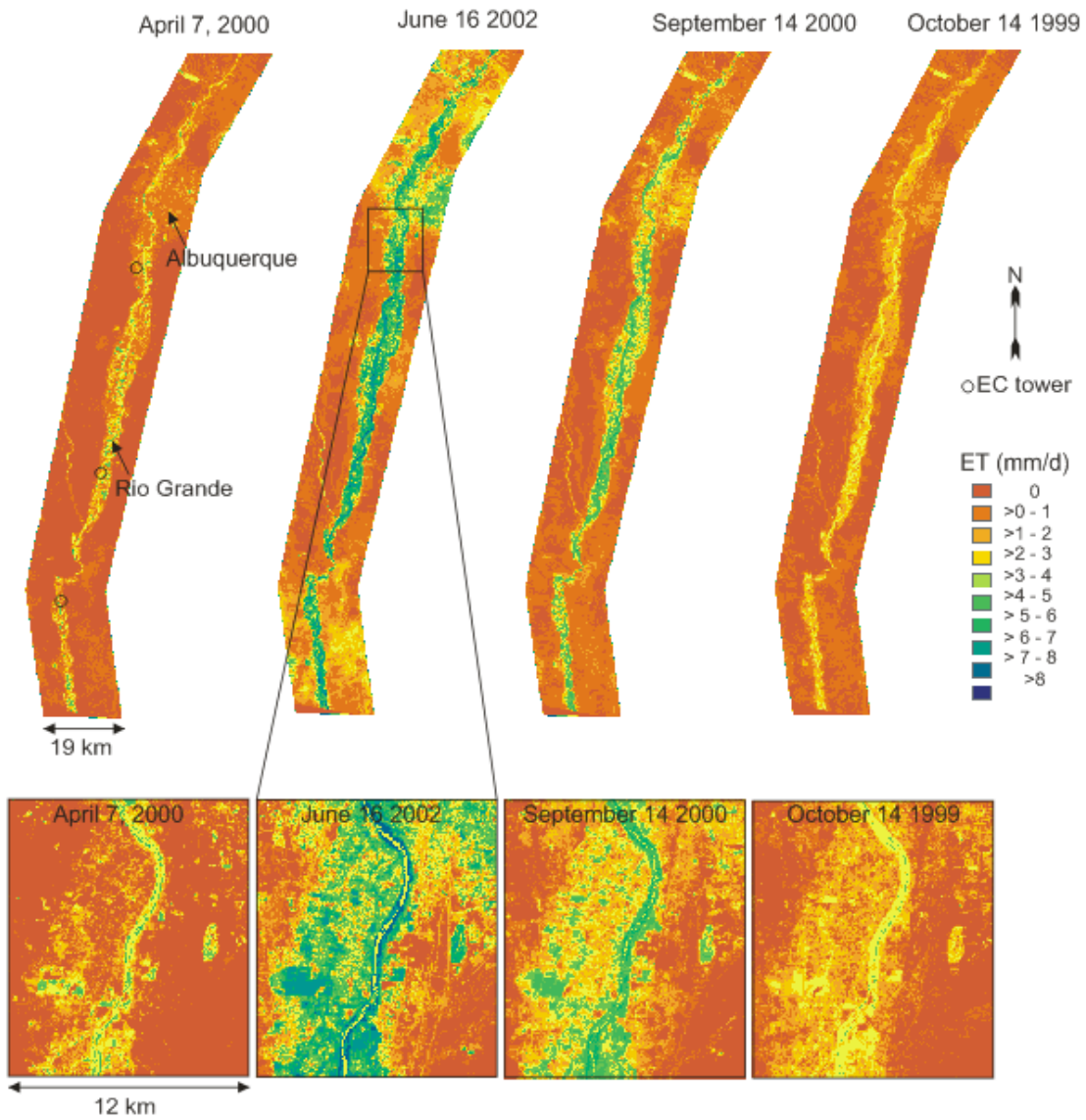
Figure 4.5 SEBAL evapotranspiration (mm/d) maps along the Rio Grande in spring, summer and fall.
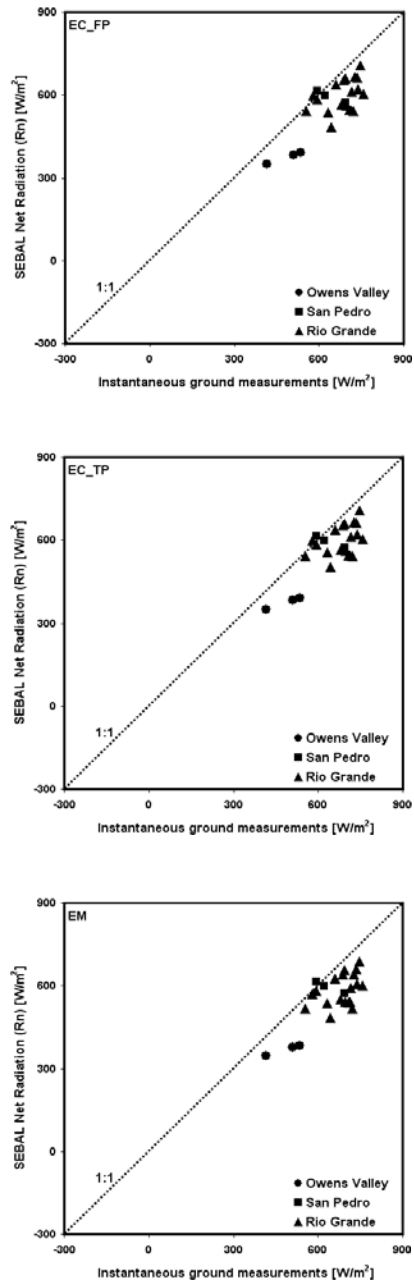
Figure 4.6 Comparison of instantaneous net radiation (R_n) between net radiometer measurements and SEBAL estimates. (EC_FP method selected anchor pixels to match fluxes of the ground measured instantaneous *LE* (adjusted for closure error) at the satellite overpass and the footprint weight averaged SEBAL *LE*. EC_TP method selected anchor pixels to match fluxes of the ground measured instantaneous LE and the flux of the tower pixel. EM method selected the anchor pixels with the hydrogeological features of the landscape and micrometeorological considerations)
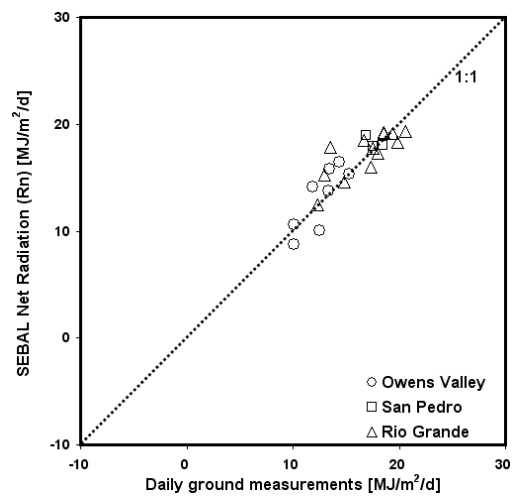
Figure 4.7 Comparison of daily net radiation (R_n) between net radiometer measurements and SEBAL estimates.

Table 4.6 Quantitative measures for comparison of SEBAL instantaneous and daily net radiation estimates ($\overline{S}$) versus ground measurements ($\overline{G}$) using the EC and Empirical Approaches for selection of hot and cold pixels.

Selection Cold and Hot Pixel	n	$\overline{G}$	$\overline{S}$ [4]	SD_G	SD_S	r^2	MAD	RMSD	MRD
Instantaneous R$_n$	(-)	(W/m^2)	(W/m^2)	(W/m^2)	(W/m^2)	(-)	(W/m^2)	(W/m^2)	%
EC Approach (FP[1])	25	654	569	86	90	0.56	88	105	13.0
EC Approach (TP[2])	25	654	571	86	89	0.56	87	103	12.8
Empirical Approach	25	654	559	86	88	0.56	97	113	14.6
Daily R$_n$	(-)	(MJ/m^2/d)	(MJ/m^2/d)	(MJ/m^2/d)	(MJ/m^2/d)	(-)	(MJ/m^2/d)	(MJ/m^2/d)	%
EC Approach[3]	24	15.6	16.0	3.1	3.1	0.75	1.3	1.6	-2.9
Empirical Approach	24	15.6	15.9	3.1	3.0	0.69	1.3	1.8	-2.3

[1]Cold and hot pixels were selected by matching the instantaneous latent heat flux measured at the EC tower with the footprint weighted averaged SEBAL instantaneous latent heat flux.
[2]Cold and hot pixels were selected by matching the instantaneous latent heat flux measured at the EC tower with the SEBAL instantaneous latent heat flux of the EC tower pixel.
[3]The daily net radiation does not depend on the selection of the cold and hot pixels; both EC Approaches yield the same values.
[4]The SEBAL instantaneous net radiation estimate ($\overline{S}$) was obtained by calculating the footprint weighted average for the instantaneous net radiation; the daily net radiation ($\overline{S}$) was obtained as the average SEBAL daily net radiation of the 25 pixels around the EC tower.

selection of the cold pixel (see Eq. [4.7]) slightly affects the significant differences

(paired t-test, p<0.0005) between the averaged measured ground instantaneous net

radiation and the averaged SEBAL estimates due to the influence of the cold pixel

temperature on the R_n estimate. These differences are 87 and 97 W/m^2 for, respectively,

the EC approach and Empirical Approach resulting in MRDs of 12.8 and 14.6%. These

differences are about two to three times larger than those typically reported in the

literature (Allen et al., 2006; Ma et al., 2006). Much of this larger than usual MRD is

attributed to the heterogeneity of the riparian sites, the different footprints of net

radiometer and Landsat pixel, and the directional preference of the net radiometer for the

vegetation studied as described in Section [4.3.3.1]. The higher net radiation measured on

the ground as compared with the SEBAL net radiation supports this argument. A bias

occurs where the net radiometer is placed preferentially above vegetation that has a lower

albedo, lower surface temperature and higher surface emissivity than the patches of bare

soil present next to the vegetation in the Landsat pixel. These arguments are supported

with experimental data from another study where the MRD's between ground measured

R_n's and the one's estimated with SEBS were 1.2, 9.2, and 17.2 %, respectively, for a

homogeneous cotton field, heterogeneous shrub terrain, and heterogeneous grassland (Su,

2002). The MRD of 9.2 and 17.2 % from the heterogeneous pixels are similar to the ones

reported in Table 4.6.

SEBAL calculates the incoming longwave radiation from the atmosphere ($R_{L\downarrow}$)

with the cold pixel surface temperature (T_{s_cold}) instead of the air temperature (T_a)

(section [4.2.1]). Recently Allen et al. (2007) suggest to use the radiometric surface

temperature (T_s) of each pixel as a surrogate for T_a. In order to test the robustness of the

SEBAL estimated $R_L\downarrow$, we calculate three different $R_L\downarrow$ estimates from Eq. [4.7] at the EC

tower sites of Middle Rio Grande: (1) T_a from ground measurement, (2) T_{s_cold} from

SEBAL, and (3) T_s of each pixel from SEBAL. The top panel of the Figure 4.8 presents

$R_L\downarrow$ using T_a from ground measurement versus T_{s_cold} from SEBAL. In Figure 4.8 (middle

and bottom panels), we also compare the SEBAL $R_L\downarrow$ estimates using either T_{s_cold} or T_s

with $R_L\downarrow$ calculated with the equation of Brutsaert (1975). Duarte et al. (2006) and

Lhomme et al (2007) indicate that the equation by Brutsaert (1975) produces a best

estimate of the incoming longwave radiation. However, it requires a ground measured T_a

and actual vapor pressure (e_a). In Figure 4.8, the mean difference between T_{s_cold} and T_a is

2.3 K. The MRD for each method (top, middle and bottom panels in Figure 4.8) is 3.1, -

0.9 and 16.4 %, respectively. Thus, using T_{s_cold} in Eq. [4.7] yields more robust estimates

of $R_L\downarrow$ than use of T_s for each pixel. The top and middle panels in Figure 4.8 show that

T_{s_cold} is a reasonable parameter to calculate $R_L\downarrow$.

The daily net radiations match very well with a MRD of only -2.3 to -2.9 %, i.e.

the SEBAL predicted daily R_n using Eq. [4.38] is $0.3 - 0.4$ MJm^{-2}day^{-1} larger than the

ground measured daily R_n. This is an excellent agreement but it immediately begs the

question "why?" since the instantaneous R_n's differ by more than 12%. The main reason

appears to be that on clear days over sparsely vegetated surfaces the maximum

temperature differences between bare soil and vegetation typically occur around noon;
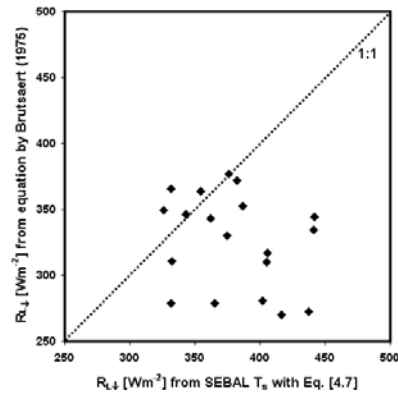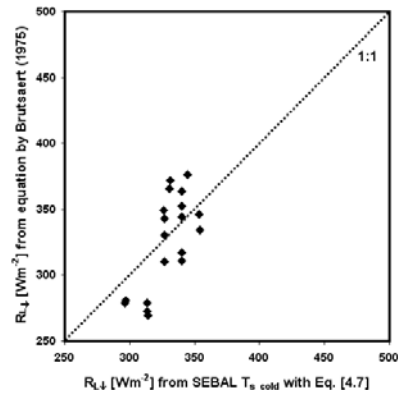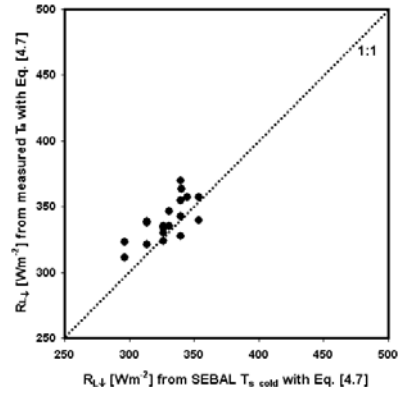
Figure 4.8 Comparison of incoming longwave radiation ($R_L\downarrow$) values calculated using SEBAL estimated cold pixel surface temperature (T_{s_cold}) versus ground measured air temperature (T_a) [top], SEBAL estimated T_{s_cold} versus the equation of Brutsaert (1975) [middle], and SEBAL estimated T_s versus the equation of Brutsaert (1975) [bottom].

temperature differences measured in the Walnut Gulch Experimental Watershed near Tombstone, Arizona, varied between 10 and 25 ºC during that time of the day (Humes et al., 1994). Since the conditions in the arid riparian areas of this study are similar, we expect similar temperature differences to occur when the satellite passes over around 11:00 am. The incoming short and longwave radiation are equal for the bare soil and the vegetation, therefore the net radiation will depend on the outgoing short and long wave radiation. The albedo and surface temperature of dry bare soils around 11:00 am are higher than of vegetation resulting in more reflection of short wave radiation and more emission of long wave radiation which results in a lower R_n during the day for bare soil. During the night the surface temperatures of vegetation and bare soil are similar so that – due to the higher emissivity of vegetation (0.99) as compared to bare soil (0.94) (Humes et al., 1994) – the R_n of vegetation is lower. Using the equations presented in Section [4.2.1] one can roughly calculate that the daily R_n difference between vegetation and soil will be considerably smaller than the instantaneous R_n difference around 11:00 am.

These differences have been quantified by comparing the SEBAL estimated instantaneous and daily net radiation for fully vegetated agricultural fields, saltcedar, and bare soils (Table 4.7). Whereas the measured instantaneous net radiation fluxes of fully cropped agricultural fields and saltcedar stands exceeded those of bare soils by 54 to 77 %, the daily net radiation fluxes were only 20 to 36 percent larger. A typical low Leaf Area Index (LAI) for saltcedar is about 2.5 (Cleverly et al., 2002) which indicates that bare soil is present but vegetation cover is dominant. Now let us assume a typical mixed pixel for the Middle Rio Grande Valley with a 75% soil cover of saltcedar and 25% bare

Table 4.7 Selected instantaneous and daily net radiation fluxes and relevant parameters for adjacent clusters of vegetated and bare soil pixels on June 16, 2002.

Vegetation	Albedo (-)		NDVI[1] (-)		T-surface (degree K)		Instantaneous Net Radiation (W/m^2)			Daily Net Radiation (MJ/(m^2 d))			N[2]
	Veg	Bare	Veg	Bare	Veg	Bare	Veg	Bare	Ratio	Veg	Bare	Ratio	
Alfalfa	0.22	0.32	0.84	0.14	299	325	634	384	1.65	17.9	14.8	1.21	50
Alfalfa	0.21	0.31	0.80	0.24	301	322	627	408	1.54	18.1	15.1	1.20	20
saltcedar	0.16	0.32	0.65	0.14	302	326	670	379	1.77	19.8	14.8	1.34	50
saltcedar	0.14	0.31	0.49	0.24	308	322	657	408	1.61	20.6	15.1	1.36	20

1) NDVI = Normalized Difference Vegetation Index
2) N = number of pixels in each

soil. The data from Table 4.7 for the first saltcedar plot show that the ratios between

100% saltcedar and 100% bare soil for, respectively, instantaneous and daily net radiation

are 1.77 and 1.34. We want to find similar ratios between 100% saltcedar and our mixed

pixel using the values of Table 4.7 for the instantaneous and daily net radiation for

saltcedar and bare soil. Ignoring the effect of thermal radiation from soil that is

intercepted by adjacent vegetation, the instantaneous and daily net radiations for the

mixed pixel are, respectively, $0.75 \times 670 + 0.25 \times 379 = 598$ Wm^{-2} and $0.75 \times 19.8 +$

$0.25 \times 14.8 = 14.9 + 3.7 = 18.6$ MJm^{-2}day^{-1}. So, the net instantaneous and daily radiations

of a fully vegetated saltcedar pixel are $670/598 = 1.12$ and $19.8/18.6 = 1.06$ times those

of our mixed pixel. The 12 percent difference is similar to the MRD's of $13 - 15\%$

presented for the difference in instantaneous net radiation between ground measurements

and SEBAL estimates. The 6 percent difference for daily net radiation falls within error

ranges of radiation measurements (Field et al., 1992; Halldin and Lundroth, 1992). Thus,

the much smaller MRD for daily R_n (-2.3 to 2.9 %) compared to the MRD of

instantaneous R_n (about 13 %) can be explained by environmental radiation physics and

is not necessarily caused by errors or biases in the SEBAL method for instantaneous R_n

or in the sensor itself.

The difference between ground measured instantaneous R_n and the one

determined by SEBAL is quite large. Above we made the case that in heterogeneous

pixels the SEBAL R_n seems more reliable than the ground measured one due to its more

representative footprint. Therefore, we have merged ground and remote sensing

observations for best estimates of the energy balance at the EC towers in Section [4.4.4.1].

We established energy balances using the sensible and latent heat fluxes measured on the EC tower together with SEBAL R_n estimates. In this manner all major components of the energy balance are estimated on the basis of a footprint of one Landsat pixel or larger.

4.4.3. Comparison of SEBAL Soil Heat Flux with Ground Measurements

The magnitude of soil heat flux G depends on surface cover, soil water content, and solar irradiance. For a moist soil beneath a plant canopy or residue layer the instantaneous G will often be less than ±20 Wm^{-2} (Sauer, 2002) while a bare, dry, exposed soil in midsummer could have a day-peak in excess of 300 Wm^{-2} (Fuchs and Tanner, 1970). In the Middle Rio Grande Basin during summer typical midday (10 am through 2 pm) values of G are 104 and 132 Wm^{-2} for, respectively, grassland and shrubs (Kurc and Small, 2004). These examples demonstrate that the instantaneous G can be an important component of the instantaneous energy balance that needs to be taken into account. In most field soils the instantaneous G exhibits not only a temporal variability but also a large spatial variability which makes it very difficult to measure an average G for areas with the size of a typical Landsat pixel (30 x 30 m) (Sauer, 2002).

For this study six soil heat flux measurements were available from the Owens Valley and the San Pedro Valley. The SEBAL determined G approaches the ground measured G reasonably well but the MRD is relatively high with values of 32.2 and 30.8 % for, respectively, the EC and Empirical approaches for determination of the cold and hot pixel (Figure 4.9 and Table 4.8). The overall impact of the relatively high MRD in instantaneous G is minor. Although it is about 30% of the smallest component of the

energy balance, it hovers around 6% percent of the instantaneous net radiation. The daily G is close to zero since heat enters the soil during the day but leaves the soil during the night. The daily G measurements in the field confirm this (Table 4.8). Therefore, it is assumed in SEBAL that the daily heat flux can be neglected, i.e. G is zero.

Given the high spatial and temporal variability of G (Sauer, 2002) within one Landsat pixel, the reasonable agreement between SEBAL predicted instantaneous G and ground measurements (Figure 4.9 and Table 4.8), the relatively minor impact of an error in G on the estimates of ET, and the impossibility to measure a truly representative G for a 900 m^2 heterogeneous riparian pixel using soil heat flux plates with a foot print of only 0.001 m^2, it appears that the SEBAL estimated G often will result in a quite acceptable estimate on the pixel scale.

4.4.4. Comparison of SEBAL Sensible and Latent Heat Fluxes with Ground Measurements

Since there is a strong interplay between sensible and latent heat fluxes we discuss both heat fluxes together in this section. First we inspect the plots of instantaneous and daily SEBAL heat flux estimates versus ground measurements using the S1 (EC_FP) approach for the selection of the cold and hot pixel temperatures and calibration of SEBAL to the ground measurements. The instantaneous and daily sensible and latent heat fluxes are presented in Figure 4.10 which demonstrates several interesting features. Our data set covers a wide range of conditions varying from dry to moist which allows evaluation of SEBAL over a wide range of environmental conditions in the
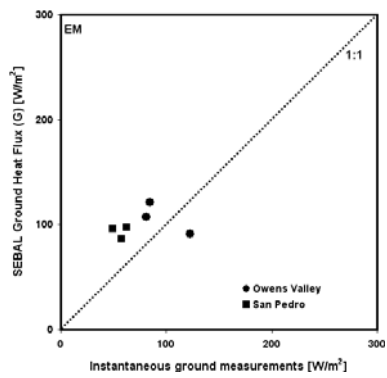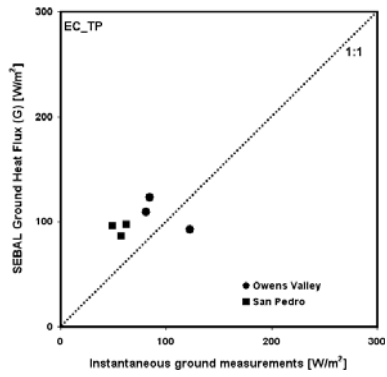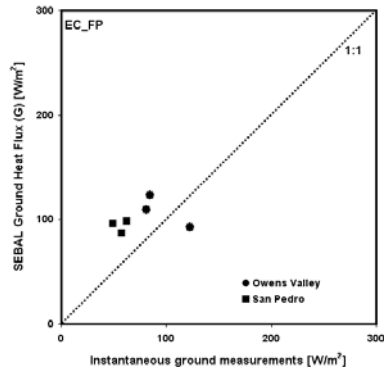
Figure 4.9 Comparison of instantaneous ground heat flux (*G*) between soil heat flux plate measurements and SEBAL estimates.

Table 4.8 Quantitative measures for comparison of instantaneous and daily SEBAL soil heat flux estimates ($\overline{S}$) versus ground measurements ($\overline{G}$) using the EC and Empirical Approaches for selection of hot and cold pixels.

Selection Cold and Hot Pixel	N[4]	$\overline{G}$	$\overline{S}$ [5]	SD_G	SD_S	r^2	MAD	RMSD	MRD
Instantaneous G	(-)	(W/m^2)	(W/m^2)	(W/m^2)	(W/m^2)	(-)	(W/m^2)	(W/m^2)	%
EC Approach (FP[1])	6	76	101	26	13	0.02	35	35	-32.2
EC Approach (TP[2])	6	76	101	26	13	0.02	35	35	-31.9
Empirical Approach	6	76	100	26	13	0.02	34	34	-30.9
Daily G	(-)	(MJ/m^2/d)	(MJ/m^2/d)	(MJ/m^2/d)	(MJ/m^2/d)	(-)	(MJ/m^2/d)	(MJ/m^2/d)	%
EC Approach[3]	24	0.5	0.0	0.4	0.0	-	0.5	0.6	>100
Empirical Approach	24	0.5	0.0	0.4	0.0	-	0.5	0.6	>100

[1] Cold and hot pixels were selected by matching the instantaneous latent heat flux measured at the EC tower with the footprint weighted averaged SEBAL instantaneous latent heat flux.
[2] Cold and hot pixels were selected by matching the instantaneous latent heat flux measured at the EC tower with the SEBAL instantaneous heat flux of the EC tower pixel.
[3] The daily soil heat flux does not depend on the selection of the cold and hot pixels; both EC Approaches yield the same values.
[4] No instantaneous soil heat flux measurements were available in the Middle Rio Grande Basin.
[5] The SEBAL instantaneous soil heat flux estimate ($\overline{S}$) was obtained by calculating the footprint average for the instantaneous soil heat flux; the daily soil heat flux ($\overline{S}$) was obtained as the average SEBAL daily soil heat flux of the 25 pixels around the EC tow

southwestern U.S. The ground measured instantaneous and daily sensible heat fluxes have, respectively, twice and six times a negative value which is an indication of the occurrence of local or regional advection. The corresponding SEBAL estimated instantaneous and daily sensible heat fluxes on the other hand are close to zero since their surface temperature are close to the cold pixel's temperature. When high quality hourly meteorological data are available regional advection can be accounted for in SEBAL by defining an advection enhancement parameter that is a function of soil moisture and weather conditions (Bastiaanssen et al., 2006) or one could implement METRIC (Allen et al., 2007a). However, in this study our aim is to evaluate the performance of SEBAL in heterogeneous arid environments using a minimum of weather data. The data in Figure 4.10 show that ignoring regional advection results in a maximum underestimation of the instantaneous and daily latent heat fluxes by, respectively, about 10 and 20 percent under moist conditions; it becomes considerably less when the soil dries out. For our data analysis we have removed all data related to negative instantaneous and daily sensible heat fluxes so that advection effects will not interfere with our analysis. The advection scenario will be discussed in a future study.

4.4.4.1. Comparison of instantaneous heat fluxes

Figures 4.11 and 4.12 present the plots of, respectively, the adjusted sensible and latent heat fluxes measured at the EC towers versus the SEBAL estimates resulting from scenarios S1 through S5. While there exists a severe mismatch between the SEBAL estimated instantaneous sensible heat fluxes and the ground measurements (S1–S3), once the SEBAL estimated net radiation is used in the "ground measured" energy balance
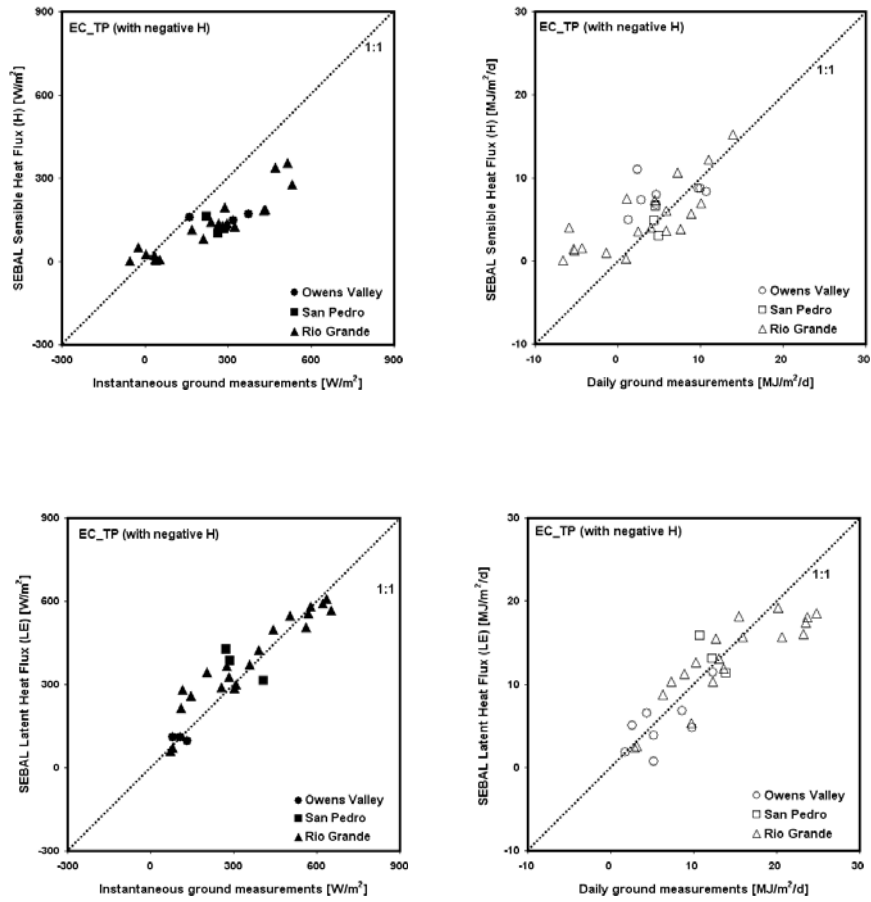
Figure 4.10 Comparison of sensible (H) and latent heat (LE) fluxes between adjusted eddy covariance tower measurements (with negative H data points) and SEBAL estimates from scenario S2 (EC_TP).
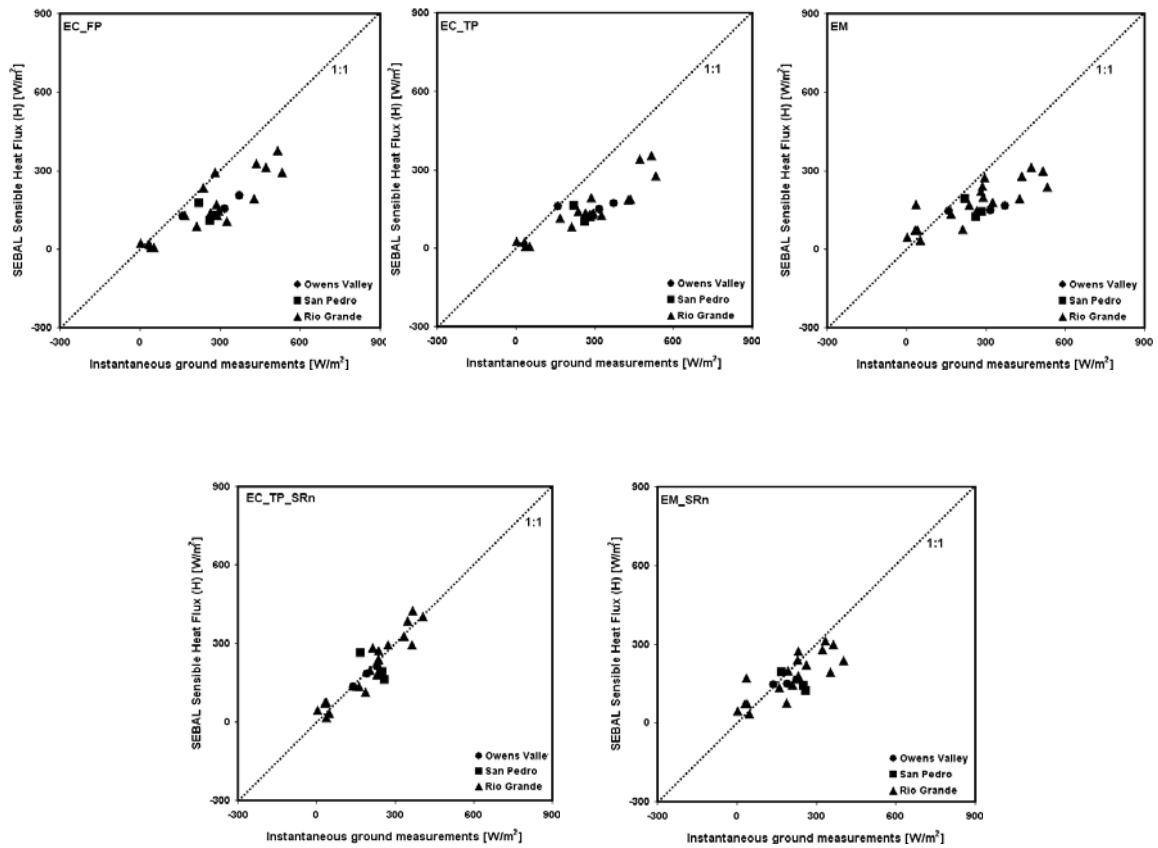
Figure 4.11 Comparison of instantaneous sensible heat flux (*H*) between adjusted eddy covariance tower measurements and SEBAL estimates for scenarios S1–S5.
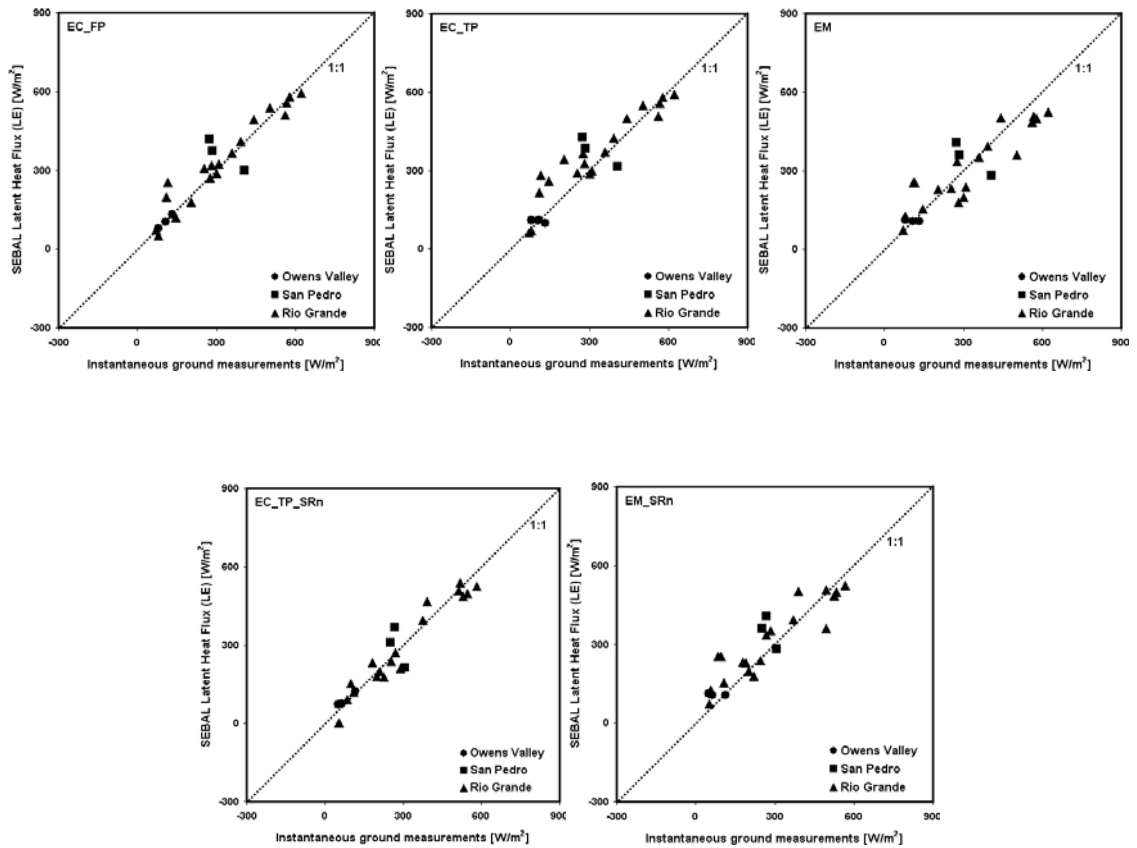
Figure 4.12 Comparison of instantaneous latent heat flux (*LE*) between adjusted eddy covariance tower measurements and SEBAL estimates for scenarios S1–S5.

good agreement is reached (S4 and S5). The agreement between SEBAL estimated instantaneous latent heat fluxes and the ground measurements is good for all five scenarios (S1 – S5). These observations are quantified in Table 4.9 that contains the quantitative comparison measures for these scenarios as well as for scenarios AS2 and AS4. The prediction of latent heat fluxes is very good for scenarios S1–S5 and consistently less than the average 14% instantaneous deviation reported for SEBAL applications worldwide (Bastiaanssen et al., 2005), except for AS2 where the MRD for *LE* is -27%. This mismatch will be discussed below.

Table 4.10 compares the differences between the ground measured and SEBAL estimated *H* and *LE* using the numerical statistics of a two-way ANOVA. However, our data do not obey all the assumptions needed for significance testing of the ANOVA results. The biggest violation is the fact that the ground measurements and SEBAL estimates are not independent. The SEBAL LE estimates in S1, S2, S4, AS2 and AS4 have been calibrated using ground measurements of the instantaneous latent heat flux while the "ground measured" soil heat flux for Middle Rio Grande sites in all scenarios (S1 – S5, AS2 and AS4) was estimated using the SEBAL determined soil heat flux due to lack of ground measurements (see section [4.4.3]). Nevertheless, we have classes that are distinctly different by using a comparison of means at a significance level of p < 0.01. This classification is more qualitative than quantitative but gives an appreciation for the differences between the "means of the differences between ground measurements and SEBAL estimates" (Tables 4.10 and 4.12). In S1 and S2, the ground measured and SEBAL estimated sensible and latent heat fluxes are not distinctly different. Thus,

Table 4.9 Quantitative measures for comparison of SEBAL derived instantaneous sensible (H) and latent (LE) heat fluxes estimates ($\overline{S}$) versus ground measurements ($\overline{G}$). Scenarios S1–S5 assume that all ground measurements ($\overline{G}$) are correct; scenarios AS2 and AS4 assume that the ground measurements of, respectively, S4–S5 and S2–S3 are the correct ones.

Scenario	Selection Anchor Pixel	Comments		n	$\overline{G}$ [6]	$\overline{S}$ [7]	SD_G	SD_S	r^2	MAD	RMSD	MRD
				(-)	(W/m^2)	(W/m^2)	(W/m^2)	(W/m^2)	(-)	(W/m^2)	(W/m^2)	%
S1	EC Approach (FP) [1]	-	H	25	262	156	151	105	0.76	108	131	40.4
			LE	25	299	314	174	170	0.90	39	57	-5.0
S2	EC Approach (TP) [2]	-	H	25	262	138	151	91	0.81	126	147	47.2
			LE	25	299	333	174	162	0.85	56	74	-11.5
S3	EM Approach	-	H	25	262	171	151	77	0.64	111	135	35.0
			LE	25	299	291	174	143	0.78	66	81	2.7
S4	EC Approach (TP) [3]	SEBAL R$_n$ replaces ground R$_n$ [4]	H	25	209	207	112	114	0.83	36	46	0.8
			LE	25	262	258	171	170	0.92	39	48	1.7
S5	EM Approach	SEBAL R$_n$ replaces ground R$_n$ [5]	H	25	205	171	110	77	0.59	61	77	16.6
			LE	25	257	291	167	143	0.82	61	77	-13.2
AS2	EC Approach (TP) [2]	SEBAL R$_n$ replaces ground R$_n$ [4]	H	25	209	138	112	91	0.74	74	90	33.7
			LE	25	262	333	171	162	0.89	74	91	-26.9
AS4	EC Approach (TP) [3]	-	H	25	262	207	151	114	0.84	70	84	21.1
			LE	25	299	258	174	170	0.87	58	75	13.6

[1] Anchor pixels were selected by matching the instantaneous LE at the satellite overpass measured at the EC tower and the footprint weighted averaged SEBAL flux. [2] Anchor pixels were selected by matching the instantaneous LE at the satellite overpass measured at the EC tower and the SEBAL flux of the tower pixel. [3] Anchor pixels were selected by matching the instantaneous LE at the satellite overpass measured at the EC tower and the SEBAL flux of the tower pixel. In S4 the SEBAL estimated R$_n$ replaces the R$_n$ measured on the ground for adjustment of the latent heat flux using Eq. [4.43]. [4] Instead of using the R$_n$ measurements made on the ground, the SEBAL derived R$_n$ in Scenario 2 is used for the determination of the ground measured energy balance and in adjusting the H and LE from the EC for closure error (using Bowen ratio). [5] Instead of using the R$_n$ measurements made on the ground, the SEBAL derived R$_n$ in Scenario 3 is used for the determination of the ground measured energy balance and in adjusting the H and LE from the EC for closure error (using Bowen ratio). [6] The heat fluxes have been calculated from the EC measurements using Eqs. [4.43] and [4.44]. Since no soil heat flux measurements were available for the Middle Rio Grande Basin, the SEBAL soil heat flux was used to establish the ground measured energy balance (see Eq. [4.42]). [7] The SEBAL estimates of the instantaneous H and LE were obtained by calculating the footprint weighted averaged SEBAL heat fluxes.

Table 4.10 Comparison of means of differences between ground measurements and SEBAL estimates of instantaneous sensible (DH) and latent heat (DLE) fluxes.

ID	Scenario	Comments	Mean DH (W/m^2)	Grouping[5]	Mean DLE (W/m^2)	Grouping
				Means of Differences Instantaneous Ground Measurements minus SEBAL Estimates			
S1	EC Approach (FP)[1]	-	106	A B	-15	B C
S2	EC Approach (TP)[2]	-	124	A	-34	C
S3	EM Approach	-	92	B C	8	B
S4	EC Approach (TP)[2]	SEBAL R$_n$ replaces ground R$_n$[3]	2	F	4	B
S5	EM Approach	SEBAL R$_n$ replaces ground R$_n$[4]	34	E	-34	C
AS2	EC Approach (TP)[2]	SEBAL R$_n$ replaces ground R$_n$[3]	70	C D	-71	D
AS4	EC Approach (TP)[2]	-	55	D E	41	A

[1] Anchor pixels were selected by matching the instantaneous LE at the satellite overpass measured at the EC tower and the footprint weighted averaged SEBAL flux. [2] Anchor pixels were selected by matching the instantaneous LE at the satellite overpass measured at the EC tower and the SEBAL flux of the tower pixel. [3] Instead of using the R$_n$ measurements made on the ground, the SEBAL derived R$_n$ in Scenario 2 is used for the determination of the ground measured energy balance. [4] Instead of using the R$_n$ measurements made on the ground, the SEBAL derived R$_n$ in Scenario 3 is used for the determination of the ground measured energy balance. [5] Means with different letters are distinctly different.

SEBAL calibrations based on the instantaneous latent heat flux of the tower pixels (EC_TP) or on the latent heat flux of the instantaneous foot prints during the satellite's overpass (EC_FP) yield very similar results. This finding is relevant for practitioners who need to calibrate SEBAL on a routine basis and/or in nearly real-time: using only the tower pixels is much faster and easier to implement automatically than determination of a footprint weighted average. It also justifies the omission of S1 from further consideration in the other scenarios (S4–S5, AS2 and AS4). However, for *posterior* SEBAL analyses and research applications use of the footprint is still recommended since (1) it results in somewhat smaller comparison measures (Tables 4.9 and 4.10) and (2) footprint analyses are effective for the detection of unusual environmental conditions.

The ground measured H and LE are identical in S1– S3 but differ slightly from each other in S4 and S5. SEBAL estimated net radiation fluxes in S2 and S3 are slightly different due to a slight difference in the temperature of the cold pixel that is used in Eq. [4.7] as an approximation of the air temperature for estimation of the incoming long wave radiation (see Table 4.4). However, a large difference exists between the ground measured H and LE in S1–S3 versus those in S4–S5. This is caused by the hypothesized large bias in instantaneous net radiation of the ground measurements versus the net radiation determined with SEBAL (Table 4.6). The H and LE SEBAL estimates for the Empirical approach (S3 and S5) are identical since this approach does not use the EC measured instantaneous LE for calibration; one set of cold and hot pixels are used for both scenarios in SEBAL. However, in S1, S2 and S4 a different set of cold and hot pixels are determined for each scenario by forcing the constants c_1 and c_2 in Eq. [4.33] to

fit the *LE* measurements at the EC towers. This leads to quite different *H* and *LE* SEBAL estimates in S1, S2 and S4.

A striking feature in S1–S3 is the very poor prediction of the sensible heat flux with MRD's between 35 and 47 %. Especially, for S1 and S2 that have been calibrated against ground measured instantaneous latent heat fluxes, this result had not been expected. The discrepancy is not caused by any obvious error in the SEBAL procedure but by the hypothesized apparent bias in the ground measurements of the net radiation that was reported earlier (see Section [4.4.2]). When the ground measured net radiation is replaced with the arguably more accurate SEBAL estimate of net radiation, the SEBAL estimates of sensible heat fluxes improve dramatically with MRD's in S4 and S5 of, respectively, 1 and 17 %. Despite the poor MRD's of *H* (35 to 47 %) in S1 – S3 the SEBAL *LE* estimates exhibit good MRD's (3 to -12 %). Therefore, these numbers provide an unexpectedly clear demonstration of the power of SEBAL's internal calibration. Through the "anchoring" of *H* and *LE* at the cold and hot pixels SEBAL reduces or cancels biases introduced in the calculation of albedo, net radiation, and surface temperature as well as errors in narrow band emissivity, atmospheric correction, satellite sensor, aerodynamic resistance, and soil heat flux function. This may result in a reduction of total bias in ET of as much as 30 % compared to other models that are not routinely internally calibrated (Allen et al., 2006). Allen et al. (2006, 2007a) describe how METRIC, through the use of weather based reference ET, is able to eliminate most internal energy balance component biases at both the cold and hot extreme conditions. SEBAL, on the other hand, eliminates biases at the hot extreme, but necessarily retains a

bias at the cold extreme where it is assumed that $LE = R_n - G$. The cost for the improved

estimates for LE is a deterioration of the SEBAL and METRIC H estimates since the

sensible heat flux, as an intermediate parameter, absorbs most of the aforementioned

biases as a result of the internal calibration process. As shown in Table 4.10 the mean

difference in sensible heat fluxes measured on the ground and estimated with SEBAL

varies from 92 to 124 W/m^2 in S1–S3 but reduces dramatically to 2 and 34 W/m^2 in S4–

S5 while the mean difference in latent heat fluxes is very similar in S1–S5. Also, while

the mean differences of the latent heat fluxes are hardly different between S1–S5, the

mean differences in sensible heat fluxes between these scenarios is distinctly different.

The mean differences of S1–S3 are much larger and distinctly different from the ones of

S4–S5. Also, the mean difference of S4 (the EC_TP calibrated implantation of SEBAL)

is distinctly less than S5 which suggests that calibrating SEBAL with reliable ground

measurements at the pixel scale will indeed improve its estimates of both, sensible and

latent heat fluxes. We can reasonably assume that the effect of SEBAL estimated

instantaneous soil heat fluxes for the ground measured LE can be ignored. Therefore, the

relatively small MRD's for LE of 2.7 and -13.% in S3 and S5 are strong evidence that

SEBAL yields robust estimates of LE similar to those measured with EC systems since

LE's in S3 and S5 has been derived independently from the ground measurements. The

rather small MRD's for LE of -5, -11.5 and 1.7 % in S1, S2 and S4 are expected since the

ground measurements have been used to calibrate SEBAL. However, the significance of

these low MRD's is that ground measurements can be used successfully for the

calibration of SEBAL.

The data presented in scenarios AS2 and AS4 allow us to evaluate the not uncommon scenario AS2 where a practitioner would rely entirely on the (biased) ground measurements of S1–S3 to calibrate a SEBAL application. Assuming that the ground measurements AS2 are unbiased, the misplaced trust in S1–S3 ground measurements will cause quite large MRD's of 34 % for H and -27 % for LE in AS2 due to the large differences between R_n of SEBAL vs. that measured at the ground. Thus, calibration with biased ground measurements can do much more harm than good if the ground energy balance components are not all unbiased. Of course, the practitioner would have been warned about potential problems by the high MRS's for H found under S1 and S2. Of course –since we don't have unbiased net radiation measurements at the pixel scale on the ground– one could make an argument that the ground measured net radiation of S1–S3 could be unbiased and not fully representative. Then, when a practitioner would use the ground measurements of S4 and S5 to calibrate a SEBAL application MRD's for H and LE of, respectively, 21 and 14 % would result. Also differences in MRD of 21 and 14 % indicate that it is not trivial to have a perfect match between SEBAL LE and ground measurement by calibrating dT in EC method as shown in Figure 4.4. In this case (S4 and S5), since unbiased ground measurements have been used the SEBAL LE converges to its "true" value while H absorbs the bias caused by the mismatch between unbiased and biased ground measurements. The data presented under scenarios S3 and S5 indicate that the Empirical approach for selection of the cold and hot pixel –if implemented by an experienced SEBAL expert– is a powerful tool for detection of severe biases in procedures that use ground measurements for calibration of Eq. [4.33] in SEBAL.

The data presented in Figures 4.11 and 4.12 and Tables 4.9 and 4.10 lead to three important conclusions. The first one is that ground measurements of sensible heat fluxes should be used cautiously and carefully for the calibration and validation of SEBAL, since the SEBAL sensible heat flux is biased necessarily to compensate for bias in R_n, G and aerodynamics, and deviates from the ground measured sensible heat flux (even if the ground based H is correct) in order to arrive at unbiased estimates of LE. The second conclusion is that SEBAL's internal calibration procedure is its greatest strength since it endeavors to eliminate total bias in LE albeit at the expense of increased bias in H. The third conclusion is that the empirical calibration approach implemented by a SEBAL expert is a powerful tool for detection of severe biases in the ground measurements.

4.4.4.2. Instantaneous and daily evaporative fraction

In Figure 4.13 the ground measured daily evaporative fraction (EF_{24}) is plotted against the instantaneous evaporative fraction (EF_{inst}). It is clear that the two evaporative fractions are not identical: the daily evaporative fraction is larger than the instantaneous one. Due to the large variability in the data as well as the fact that both the instantaneous and daily evaporative fractions are random variables a straightforward linear regression forced through the origin is not recommended. A simple linear regression with a 5% significance level yields a small intercept of 0.04 that is not significantly different from zero with a slope of 1.19 with a 95 % confidence interval from 0.99 to 1.36. This demonstrates that there is about 20 % difference between instant EF and daily EF. While recognizing that 1.18 is much closer to 1.1 than to 1.0, we employed two different coefficients c_{EF} for the conversion from instantaneous latent heat flux to daily latent heat
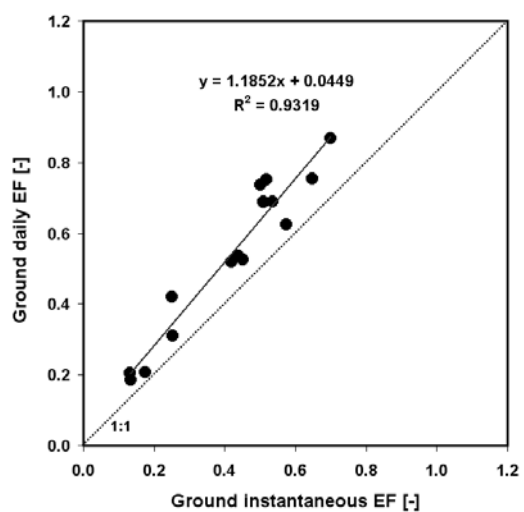
Figure 4.13 Comparison of satellite overpass instantaneous evaporative fraction (*EF*) with daytime average measured on the ground.

flux (see Eqs. [4.35] and [4.36]): 1.0 as assumed in the classical SEBAL application (Bastiaanssen et al., 1998) and 1.1 as found by some researchers on the basis of field measurements (Anderson et al., 1997).

4.4.4.3. Comparison of daily sensible and latent heat fluxes

Figures 4.14 – 4.17 present the plots of, respectively, the adjusted sensible and latent daily heat fluxes measured at the EC towers versus the SEBAL estimates resulting from scenarios S1–S5 assuming c_{EF} equals 1.0 (Figures 4.14 and 4.16) or 1.1 (Figures 4.15 and 4.17). Visual inspection of these figures reveals that generally there is good agreement between the daily ground measurements and the daily SEBAL estimates. Exceptions are the sensible daily heat fluxes for S4 and S5 that show SEBAL overestimated as well as the latent daily heat flux for S4 where SEBAL underestimated the ground measurement. These observations are confirmed by the MRD's in Table 4.11. Before inspecting the quantitative measures in Table 4.11, we examine which means of differences between ground measurements and SEBAL estimates are distinctly different from each other in Table 4.12. In S1 and S2 –as before with the instantaneous heat fluxes– there exists no distinct difference between the means of differences between ground measured and SEBAL estimated sensible and latent daily heat fluxes for both evaporative fractions. Thus, no distinct difference occurs between SEBAL calibrations based on the instantaneous latent heat flux of the tower pixels (EC_TP) or on the latent heat flux of the instantaneous foot prints during the satellite's overpass (EC_FP). This finding is relevant for practitioners who need to calibrate SEBAL on a routine basis and/or in nearly real-time. Also, there are no major distinct differences between the
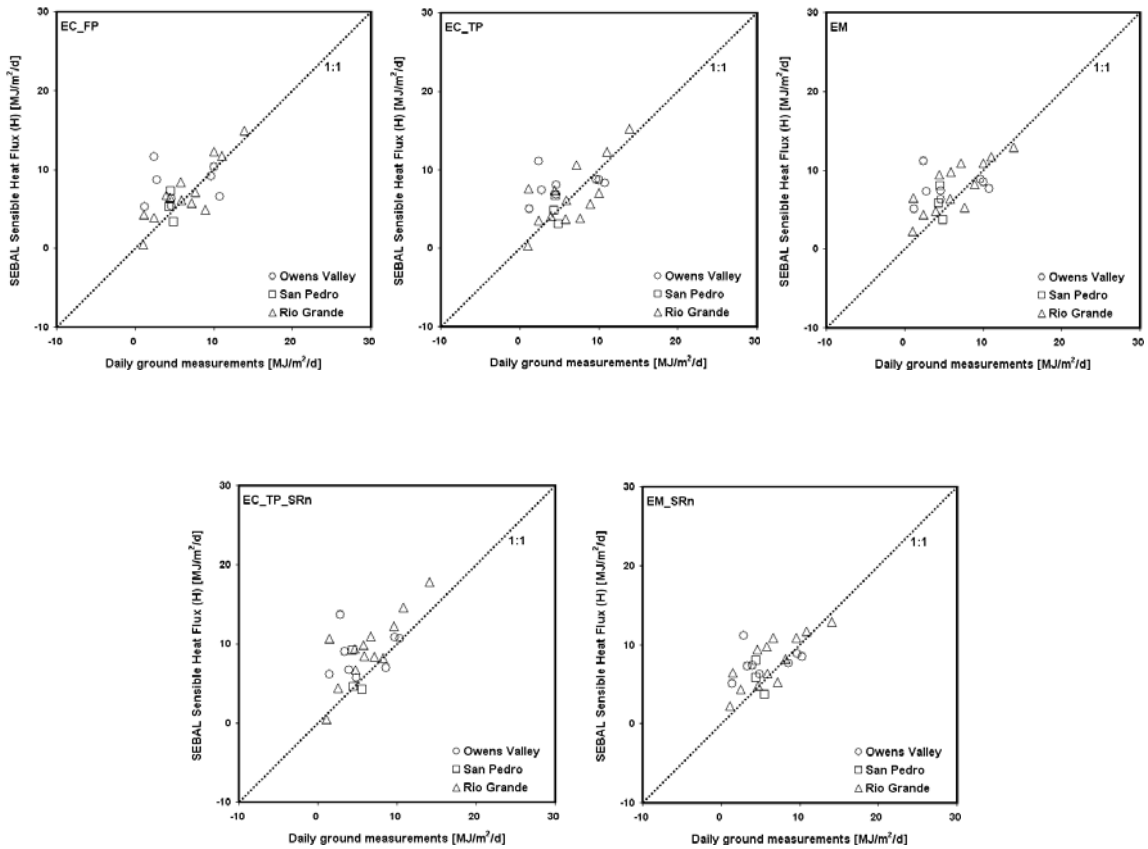
Figure 4.14 Comparison of daily sensible heat flux (*H*) between adjusted eddy covariance tower measurements and SEBAL estimates. ($EF_{24} = 1.0*EF_{inst}$)
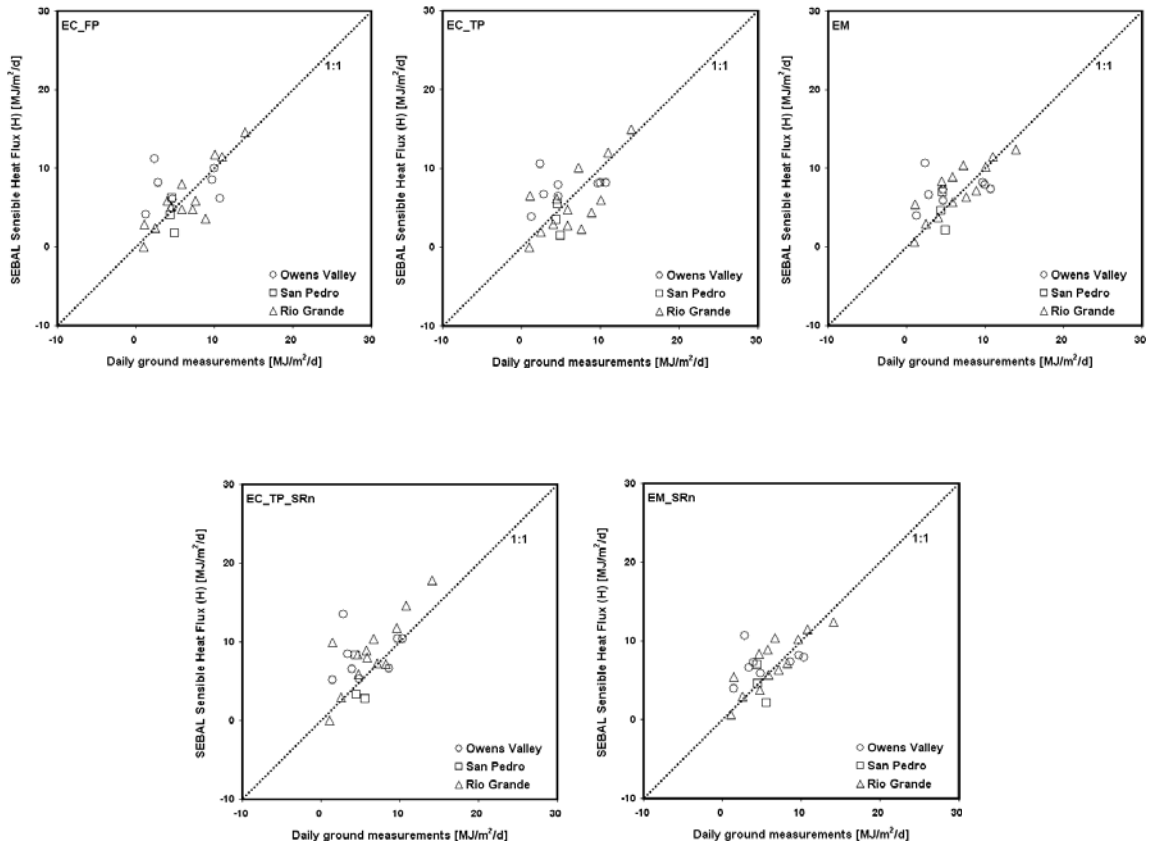
Figure 4.15 Comparison of daily sensible heat flux (*H*) between adjusted eddy covariance tower measurements and SEBAL estimates. ($EF_{24} = 1.1 * EF_{inst}$)
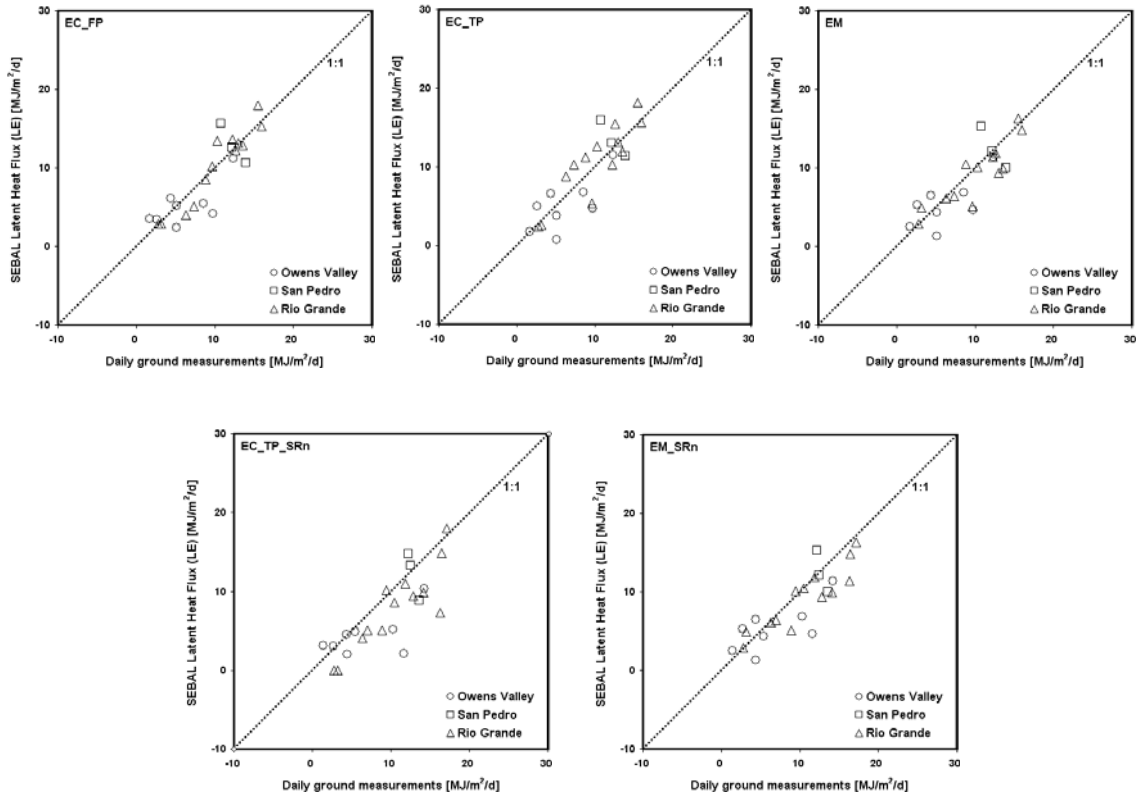
Figure 4.16 Comparison of daily latent heat flux (*LE*) between adjusted eddy covariance tower measurements and SEBAL estimates. ($EF_{24} = 1.0* EF_{inst}$)
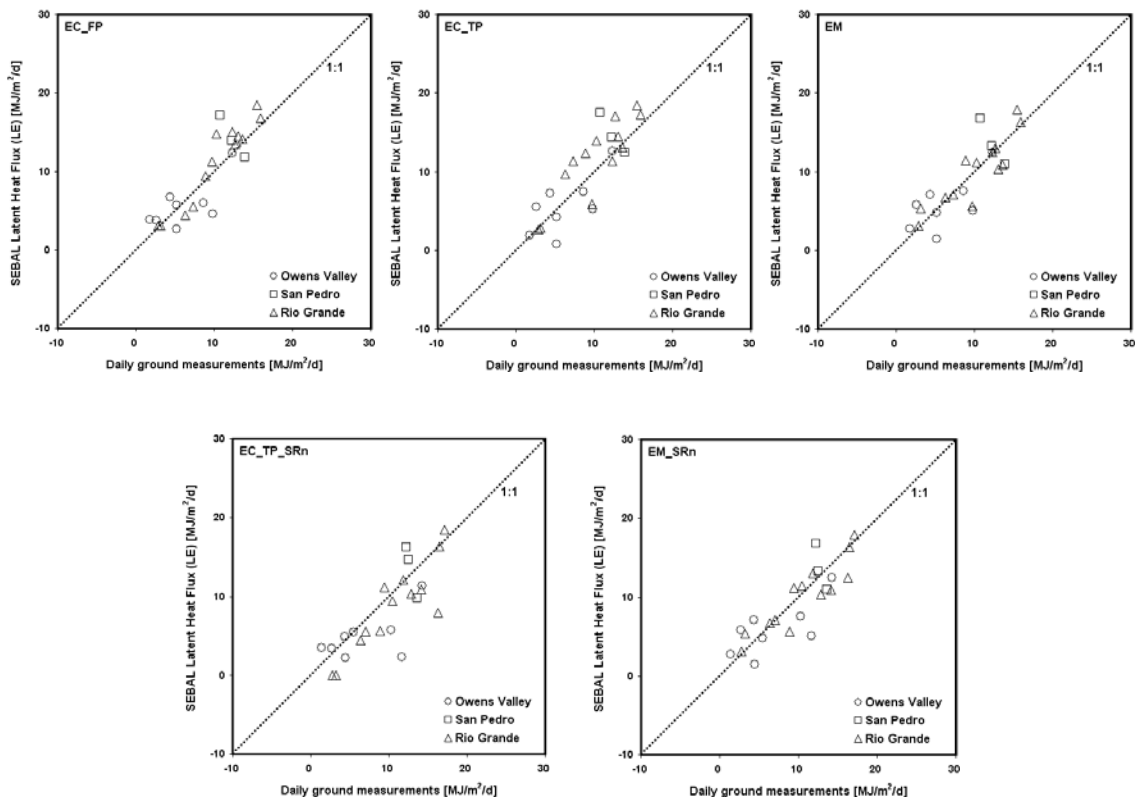
Figure 4.17 Comparison of daily latent heat flux (*LE*) between adjusted eddy covariance tower measurements and SEBAL estimates. ($EF_{24} = 1.1* EF_{inst}$)

Table 4.11 Quantitative measures for comparison of SEBAL derived daily sensible (*H*) and latent (*LE*) heat fluxes estimates ($\overline{S}$) versus ground measurements ($\overline{G}$). Scenarios S1–S5 assume that all ground measurements ($\overline{G}$) are correct; scenarios AS2 and AS4 assume that the ground measurements of, respectively, S4–S5 and S2–S3 are the correct ones.

$EF_{24} = 1.0 \times EF_{inst}$

Scenario	Selection Anchor Pixel	Comments		n	$\overline{G}$ [6]	$\overline{S}$ [7]	SD_G	SD_S	r^2	MAD	RMSD	MRD
				(-)	MJ/(m²d)	MJ/(m²d)	MJ/(m²d)	MJ/(m²d)	(-)	MJ/(m²d)	MJ/(m²d)	%
S1	EC Approach (FP) [1]	-	H	24	6.0	7.2	3.7	3.2	0.41	2.3	3.1	-19.4
			LE	24	9.1	8.9	4.4	4.9	0.78	1.7	2.2	2.9
S2	EC Approach (TP) [2]	-	H	24	6.0	6.9	3.7	3.3	0.32	2.6	3.3	-14.9
			LE	24	9.1	9.1	4.4	5.0	0.72	2.2	2.6	0.0
S3	EM Approach	-	H	24	6.0	7.6	3.7	2.7	0.37	2.6	3.3	-27.0
			LE	24	9.1	8.3	4.4	4.2	0.69	1.9	2.6	8.9
S4	EC Approach (TP) [3]	SEBAL R_n replaces ground R_n [4]	H	24	6.0	8.7	3.4	3.8	0.40	3.1	4.1	-46.4
			LE	24	9.5	7.3	4.9	4.9	0.64	2.8	3.7	22.8
S5	EM Approach	SEBAL R_n replaces ground R_n [5]	H	24	6.0	7.7	3.4	2.7	0.41	2.4	3.1	-27.9
			LE	24	9.5	8.3	4.9	4.2	0.70	2.2	2.9	12.1
AS2	EC Approach (TP) [2]	SEBAL R_n replaces ground R_n [4]	H	24	6.0	6.9	3.4	3.3	0.34	2.5	3.1	-15.7
			LE	24	9.5	9.1	4.9	5.0	0.66	2.4	3.0	3.5
AS4	EC Approach (TP) [3]	-	H	24	6.0	8.7	3.7	3.8	0.34	3.2	4.3	-45.5
			LE	24	9.1	7.3	4.4	4.9	0.70	2.6	3.2	20.0

$$EF_{24} = 1.1 \times EF_{inst}$$

Scenario	Selection Anchor Pixel	Comments		n	$\bar{G}$ [6]	$\bar{S}$ [7]	SD_G	SD_S	r^2	MAD	RMSD	MRD
				(-)	MJ/(m²d)	MJ/(m²d)	MJ/(m²d)	MJ/(m²d)	(-)	MJ/(m²d)	MJ/(m²d)	%
S1	EC Approach (FP) [1]	-	H	24	6.0	6.3	3.7	3.5	0.41	2.1	3.0	-5.6
			LE	24	9.1	9.7	4.4	5.3	0.78	1.9	2.5	-6.3
S2	EC Approach (TP) [2]	-	H	24	6.0	6.0	3.7	3.6	0.32	2.7	3.3	-0.8
			LE	24	9.1	10.0	4.4	5.4	0.71	2.4	3.0	-9.3
S3	EM Approach	-	H	24	6.0	6.9	3.7	3.0	0.42	2.3	2.9	-14.8
			LE	24	9.1	9.2	4.4	4.6	0.69	2.0	2.5	-0.3
S4	EC Approach (TP) [3]	SEBAL R_n replaces ground R_n [4]	H	24	6.0	8.1	3.4	4.0	0.40	2.8	3.8	-35.2
			LE	24	9.5	8.0	4.9	5.2	0.64	2.6	3.5	15.6
S5	EM Approach	SEBAL R_n replaces ground R_n [5]	H	24	6.0	6.9	3.4	3.0	0.44	2.1	2.8	-15.6
			LE	24	9.5	9.2	4.9	4.6	0.70	2.1	2.7	3.2
AS2	EC Approach (TP) [2]	SEBAL R_n replaces ground R_n [4]	H	24	6.0	6.0	3.4	3.6	0.33	2.6	3.2	-1.5
			LE	24	9.5	10.0	4.9	5.4	0.66	2.6	3.2	-5.5
AS4	EC Approach (TP) [3]	-	H	24	6.0	8.1	3.7	4.0	0.35	3.0	4.0	-34.2
			LE	24	9.1	8.0	4.4	5.2	0.71	2.4	3.0	12.6

[1] Anchor pixels were selected by matching the instantaneous LE at the satellite overpass measured at the EC tower and the footprint weighted averaged SEBAL flux. [2] Anchor pixels were selected by matching the instantaneous LE at the satellite overpass measured at the EC tower and the SEBAL flux of the tower pixel. [3] Anchor pixels were selected by matching the instantaneous LE at the satellite overpass measured at the EC tower and the SEBAL flux of the tower pixel. In S4 the SEBAL estimated R_n replaces the R_n measured on the ground for adjustment of the latent heat flux using Eq. [4.43]. [4] Instead of using the R_n measurements made on the ground, the SEBAL derived R_n in Scenario 2 is used for the determination of the ground measured energy balance. [5] Instead of using the R_n measurements made on the ground, the SEBAL derived R_n in Scenario 3 is used for the determination of the ground measured energy balance. [6] The heat fluxes have been calculated from the EC measurements using Eqs. [4.43] and [4.44]. Since no soil heat flux measurements were available for the Middle Rio Grande Basin, the SEBAL soil heat flux was used to establish the ground measured energy balance (see Eq. [4.42]).
[7] The SEBAL estimates of the instantaneous H and LE were obtained by calculating the footprint weighted averaged SEBAL heat fluxes.

Table 4.12 Comparison of means of differences between ground measurements and SEBAL estimates of daily sensible (DH) and latent heat (DLE) fluxes.

$$EF_{24} = 1.0 \times EF_{inst}$$

ID	Scenario	Comments	Means of Differences Daily Ground Measurements minus SEBAL Estimates			
			Mean DH MJ/(m^2 d)	Grouping[5]	Mean DLE MJ/(m^2 d)	Grouping
S1	EC Approach (FP)[1]	-	-1.16	A	0.27	C D
S2	EC Approach (TP)[2]	-	-0.90	A	0.00	D
S3	EM Approach	-	-1.62	A	0.81	C D
S4	EC Approach (TP)[2]	SEBAL R_n replaces ground R_n[3]	-2.77	B	2.15	A
S5	EM Approach	SEBAL R_n replaces ground R_n[4]	-1.66	A	1.15	B C
AS2	EC Approach (TP)[2]	SEBAL R_n replaces ground R_n[3]	-0.94	A	0.33	C D
AS4	EC Approach (TP)[2]	-	-2.73	B	1.82	A B

$$EF_{24} = 1.1 \times EF_{inst}$$

ID	Scenario	Comments	Means of Differences Instantaneous Ground Measurements minus SEBAL Estimates			
			Mean DH MJ/(m² d)	Grouping[5]	Mean DLE MJ/(m² d)	Grouping
S1	EC Approach (FP) [1]	-	-0.33	A	-0.57	C D
S2	EC Approach (TP) [2]	-	-0.05	A	-0.85	D
S3	EM Approach	-	-0.89	A	-0.03	C D
S4	EC Approach (TP) [2]	SEBAL R_n replaces ground R_n [3]	-2.10	B	1.48	A
S5	EM Approach	SEBAL R_n replaces ground R_n [4]	-0.93	A	0.30	B C
AS2	EC Approach (TP) [2]	SEBAL R_n replaces ground R_n [3]	-0.09	A	-0.52	C D
AS4	EC Approach (TP) [2]	-	-2.05	B	1.15	A B

[1] Anchor pixels were selected by matching the instantaneous LE at the satellite overpass measured at the EC tower and the footprint weighted averaged SEBAL flux. [2] Anchor pixels were selected by matching the instantaneous LE at the satellite overpass measured at the EC tower and the SEBAL flux of the tower pixel. [3] Instead of using the R_n measurements made on the ground, the SEBAL derived R_n in Scenario 2 is used for the determination of the ground measured energy balance. [4] Instead of using the R_n measurements made on the ground, the SEBAL derived R_n in Scenario 3 is used for the determination of the ground measured energy balance. [5] Means with different letters are distinctly different.

means of differences between ground measured and SEBAL estimated latent daily heat fluxes of S1, S2, S3, and S5 but the mean of differences of S4 is distinctly different from those in S1, S2, S3, and S5 for both evaporative fractions. The same pattern is observed for the sensible daily heat fluxes for both evaporative fractions. Thus, the relative ranking of the means and the location of distinct differences is identical for c_{EF} of 1.0 and 1.1.

We conducted a two-way ANOVA for detection of distinct differences between the means of the differences of the same scenario under c_{EF} of 1.0 and 1.1. None of the means of differences between ground measurements and SEBAL estimates of daily sensible and latent heat fluxes turned out to be distinctly different when using c_{EF} of 1.0 or 1.1. For example, the MRD of H in S1 under c_{EF} of 1.0 is -19.4% which is not distinctly different of -5.5% found under c_{EF} of 1.1. Therefore, we cannot determine with certainty which of the c_{EF}'s yields more accurate estimates of H and LE. Inspection of Table 4.11 suggests that the use of 1.1 yields better overall values for both sensible and latent heat fluxes. Our conclusion is that the use of 1.1 in our study (non-advective conditions during months April to September) is preferred given the regression analysis conducted in section [4.4.4.2], data reported in the literature, and the MRD's in Table 4.11 but a conclusive determination cannot be made on the basis of our data.

In addition, Table 4.11 reveals that SEBAL also tends to absorb biases in the daily sensible heat flux in order to yield the best possible estimate of the daily latent heat flux. For c_{EF} of 1.0, the MRD's for sensible daily heat flux vary from -46 to -15 % while those for latent heat flux vary from 0 to 20%; for c_{EF} of 1.1, the respective numbers are -35 to -

1% and -9 to 16%. These numbers indicate that using the daily sensible heat flux for calibration of SEBAL applications has a high risk of introducing severe bias. Therefore, on the basis of this study we conclude that only reliable measurements of the latent heat flux, either instantaneous or daily, should be used to calibrate SEBAL.

A comparison between ground measurements and SEBAL estimates of daily evapotranspiration is made in Figure 4.18 where the unadjusted EC measurements of ET are compared with SEBAL estimates of ET with c_{EF} of 1.1. For scenarios S1 (EC_FP), S2 (EC_TP), and S3 (EC_EM) the slopes between unadjusted ET measured at the EC tower and the SEBAL estimates are, respectively, 1.30, 1.32, and 1.08 which averages to 1.23. Thus, SEBAL ET estimates are about 21% higher than the unadjusted ET measurements at the EC towers. This discrepancy is expected since it has been reported in the literature that the systematic underestimation of heat fluxes by the eddy covariance method can be as high as 10 to 30 % (Paw et al., 2004; Twine et al., 2000). Given the inherent uncertainties of the SEBAL approach and the eddy covariance method the agreement between the two methods is surprisingly good. Especially, considering that we compare sensible and latent heat fluxes measured in heterogeneous arid riparian areas. Therefore, this study confirms other recent studies (Allen et al., 2007b; Bastiaanssen et al., 2005) that SEBAL is a powerful tool for high resolution mapping of evapotranspiration.
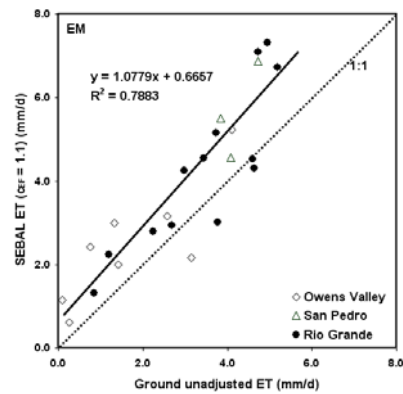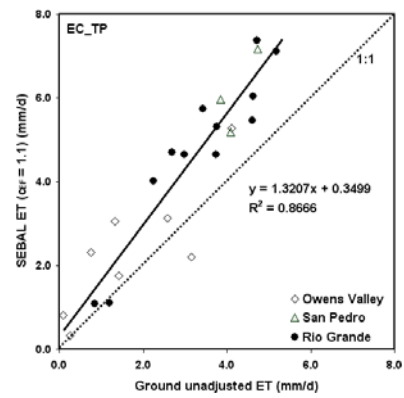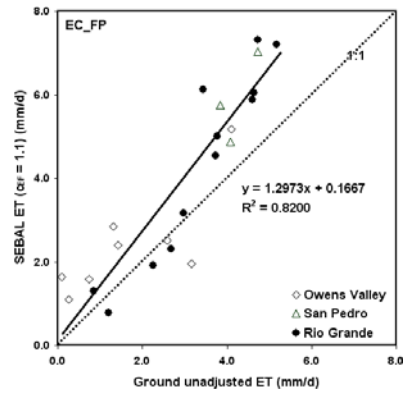
Figure 4.18 Comparison of ET rates determined from SEBAL with c_{EF} of 1.1 to eddy covariance ground measurements in riparian areas of the Rio Grande Valley (NM), San Pedro Valley (AZ), and Owens Valley (CA).

4.5. CONCLUSIONS

In this paper we report the results of a study to compare sensible and latent heat fluxes of riparian and desert systems measured on the ground with the eddy covariance method and those based on SEBAL using only Landsat satellite images with few to no ground measurements. The comparison of these heat fluxes in arid heterogeneous riparian areas in the southwestern United States clearly demonstrates that SEBAL can be applied for mapping sensible and latent heat fluxes at high spatial resolutions.

Analyses indicate that when ground based eddy covariance data were used to calibrate SEBAL, no distinct difference occurred between SEBAL calibrations based on the instantaneous latent heat flux of the tower pixel itself or on the latent heat flux of the instantaneous foot print during the satellite overpass. This finding is relevant for practitioners who need to calibrate SEBAL on a routine basis since using only the tower pixel is quicker and easier to implement automatically than determination of a footprint weighted average flux. However, for research applications use of the footprint is still recommended since it results in slightly smaller comparison differences (Tables 4.9 and 4.11).

An analysis of differences in instantaneous R_n during late morning (Landsat overpass time) between vegetation and exposed soil emphasizes the large impact of soil in the R_n view, and the importance of proper vegetative mixture viewed by the R_n sensor. We hypothesize that tower R_n is generally biased toward vegetation, resulting in higher

R_n values. Instantaneous R_n from SEBAL, representing a larger area for heterogeneous vegetation, gives lower R_n values. When these are used to close the eddy covariance energy balance, LE and H from SEBAL and LE and H from the ground based EC are much more similar.

An important conclusion of the comparisons between various calibration strategies for SEBAL is that ground measurements of sensible heat fluxes should be used with caution for the calibration and validation of SEBAL, since the SEBAL sensible heat flux is intentionally biased during calibration (to produce an unbiased LE) and will deviate from the ground measured sensible heat flux in order to arrive at unbiased estimates of LE.

The true strength and the effectiveness of the internal calibration procedure for SEBAL LE estimation is demonstrated where despite a poor quality ground measured energy balance, SEBAL LE estimates tend to converge to the ground measured LE (after correction of EC for closure error). The comparison measures in S1–S5 are strong evidence that the great strength of the SEBAL method is its internal calibration procedure that eliminates most of the total bias in LE at the expense of increased bias in H. We conclude that the empirical approach implemented by a SEBAL expert is a powerful tool for detection of severe biases in the ground measurements.

The use of a multiplier on the instantaneous evaporative fraction of 1.1 to convert the instantaneous ET to daily ET is preferred for the non-advective conditions during the months April to September that were covered during this study.

ACKNOWLEDGEMENT

REFERENCES

Allen, R.G., A. Morse, and M. Tasumi. 2003. Application of SEBAL for western US water rights regulation and planning Proceedings of the International Workshop on Remote Sensing of Crop Evapotranspiration for Large Regions. 54th IEC Meeting of the International Commission on Irrigation and Drainage (ICID), Montpellier, France.

Allen, R.G., M. Tasumi, and R. Trezza. 2005. M E T R I C^{tm} Mapping Evapotranspiration at High Resolution. Applications Manual for Landsat Satellite Imagery. Version 2.0. University of Idaho, Kimberly, Idaho.

Allen, R.G., M. Tasumi, and R. Trezza. 2006. Benefits from tying satellite-based energy balance to reference evapotranspiration. Earth Observation for Vegetation Monitoring and Water Management. AIP Conference Proceedings 852:127-137.

Allen, R.G., M. Tasumi, and R. Trezza. 2007a. Satellite-based Energy Balance for Mapping Evapotranspiration with Internalized Calibration (METRIC) – Model. Journal of Irrigation and Drainage Engineering 133:380-394.

Allen, R.G., L.S. Pereira, D. Raes, and M. Smith. 1998. Crop evapotranspiration. FAO Irrigation and drainage paper 56, FAO. Rome.

Allen, R.G., H.D. Bruin, O. Hartogensis, B. Tanner, and C. Neale. 2000. Regional Advection Perturbations in an Irrigated Desert (RAPID)-Impacts on Evapotranspiration. University of Idaho, Kimberly.

Allen, R.G., W.O. Pruitt, J.A. Businger, L.J. Fritschen, M.E. Jensen, and F.H. Quinn. 1996. Chapter 4: Evaporation and Transpiration. American Society of Civil Engineering, NY.

Allen, R.G., M. Tasumi, A. Morse, R. Trezza, J.L. Wright, W. Bastiaanssen, W. Kramber, I. Lorite, and C.W. Robison. 2007b. Satellite-based Energy Balance for Mapping Evapotranspiration with Internalized Calibration (METRIC) – Applications. Journal of Irrigation and Drainage Engineering 133:395-406.

Anderson, D.E., and C.D. Farrar. 2001. Eddy covariance measurement of CO^2 flux to the atmosphere from an area of high volcanogenic emissions, Mammoth Mountain, California. Chemical Geology 177:31-42.

Anderson, M.C., J.M. Norman, G.R. Diak, W.P. Kustas, and J.R. Mecikalski. 1997. A two-source time-integrated model for estimating surface fluxes using thermal infrared remote sensing. Remote Sensing of Environment 60:195-216.

Anderson, M.C., J.M. Norman, J.R. Mecikalski, R.D. Torn, W.P. Kustas, and J.B. Basara. 2004. A multiscale remote sensing model for disaggregating regional fluxes to

micrometeorological scales. Journal of Hydrometeorology 5:343-363.

Andrews, D.G. 2000. An Introduction to Atmospheric Physics Cambridge University Press.

Arya, S.P. 2001. Introduction to micrometeorology. Second ed. International Geophysics Series, ed. R. Dmowska, J.R. Holton, and H.T. Rossby. Vol. 79, San Diego: Academic Press. 420.

Bastiaanssen, W.G.M. 1995. Regionalization of surface flux densities and moisture indicators in composite terrain, Wageningen Agricultural University, Wageningen, Netherlands.

Bastiaanssen, W.G.M. 2000. SEBAL-based sensible and latent heat fluxes in the Irrigated Gediz Basin, Turkey. Journal of Hydrology 229:87-100.

Bastiaanssen, W.G.M., D.H. Hoekman, and R.A. Roebeling. 1994. A methodology for the assessment of surface resistance and soil water storage variability at mesoscale based on remote sensing measurements. IAHS Special Publications, No. 2, IAHS Press, Institute of Hydrology, Wallingford, UK: pp. 63.

Bastiaanssen, W.G.M., M.-D. Ahmad, and Y. Chemin. 2002. Satellite surveillance of evaporative depletion across the Indus Basin. Water Resources Research 38:1273, doi:10.1029/2001WR000386.

Bastiaanssen, W.G.M., M. Menenti, R.A. Feddes, and A.A.M. Holtslag. 1998. A remote sensing surface energy balance algorithm for land (SEBAL). Part 1: Formulation. Journal of Hydrology 212-213:198-212.

Bastiaanssen, W.G.M., A. Klaasse, S. Zwart, W. Immerzeel, and P. Droogers. 2006. The hydrological flow path and options for sustainable water resources management in the overexploited Rio Bravo Basin. A world bank project, Final report:102p.

Bastiaanssen, W.G.M., E.J.M. Noordman, H. Pelgrum, G. Davids, B.P. Thoreson, and R.G. Allen. 2005. SEBAL model with remotely sensed data to improve water-resources management under actual field conditions. Journal of Irrigation and Drainage Engineering 131:85-93.

Brutsaert, W. 1975. On a derivable formula for long-wave radiation from clear skies. Water Resources Research 11:742-744.

Brutsaert, W., and M. Sugita. 1992. Application of self-preservation in the diurnal evolution of the surface energy budget to determine daily evaporation. Journal of Geophysical Research 97:18,377-18,382.

Brutsaert, W., A.Y. Hsu, and T.J. Schmugge. 1993. Parameterization of surface heat fluxes above a forest with satellite thermal sensing and boundary layer soundings. Journal of Applied Meteorology 32:909-917.

Campbell, G.S., and J.M. Norman. 1998. An introduction to environmental biophysics. Second Edition Springer, New York, NY.

Caparinni, F., and F. Castelli. 2002. Remote sensing used to estimate land surface evaporation. EOS Transactions 83:290-291.

Choudhury, B.J. 1989. Estimating evaporation and carbon assimilation using infrared temperature data: vistas in modeling Wiley, New York.

Choudhury, B.J., R.J. Reginato, and S.B. Idso. 1986. An analysis of infrared temperature observations over wheat and calculation of latent heat flux. Agricultural and Forest Meteorology 37:75-88.

Choudhury, B.J., S.B. Idso, and R.J. Reginato. 1987. Analysis of an empirical model for soil heat flux under a growing wheat crop for estimating evaporation by an infrared-temperature-based energy balance equation. Agriculture and Forest Meteorology 39:283-297.

Cleverly, J.R., C.N. Dahm, J.R. Thibault, D.J. Gilroy, and J.E.A. Coonrod. 2002. Seasonal estimates of actual evapotranspiration from Tamarix ramosissima stands using 3-dimensional eddy covariance. Journal of Arid Environments 52:181-197.

Conover, W.J., and R.L. Iman. 1981. Rank transformations as a bridge between parametric and nonparametric statistics. The Amer. Stat. 35:124.

Cosgrove, B.A., D. Lohmann, K.E. Mitchell, P.R. Houser, E.F. Wood, J. Schaake, A. Robock, C. Marshall, J. Sheffield, L. Luo, Q. Duan, R.T. Pinker, J.D. Tarpley, R.W. Higgins, and J. Meng. 2003. Real-time and retrospective forcing in the North American Land Data Assimilation System (NLDAS) project. Journal of Geophysical Research 108. doi:10.1029/2002JD003118.

Costigan, K.R., J.E. Bossert, and D.L. Langley. 2000. Atmospheric/hydrologic models for the Rio Grande Basin: simulations of precipitation variability. Global and Planetary Change 25:83-110.

Crago, R.D. 1996. Conservation and variability of the evaporative fraction during the daytime. Journal of Hydrology 180:173-194.

De Bruin, H.A.R. 1987. In: J.C Hooghart (Ed.), From Penman to Makkink, Evaporation and weather. Proceedings and Information No. 39, TNO Committee on Hydrological Research, The Hague, pp. 5-31.

De Bruin, H.A.R., N.J. Bink, and L.J.M. Kroon. 1991. Fluxes in the surface layer under advective conditions Springer-Verlag New York, Inc.

Draxler, R.R. 1976. Determination of atmospheric diffusion parameters. Atmospheric Environment 10:99-105.

Droogers, P., and W.G.M. Bastiaanssen. 2002. Irrigation performance using hydrological and remote sensing modeling. Journal of Irrigation and Drainage Engineering 128:11-18.

Duarte, H.F., N.L. Dias, and S.R. Maggiotto. 2006. Assessing daytime downward longwave radiation estimates for clear and cloudy skies in Southern Brazil Agricultural and Forest Meteorology 139:171-181

Duffie, J.A., and W.A. Beckman. 1991. Solar engineering of thermal processes John Wiley and Sons, NY.

Elmore, A.J., J.F. Mustard, and S.J. Manning. 2002. Regional patterns of plant community response to changes in water: Owens Valley, California. Ecological Applications 13:443-460.

Farah, H.O., and W.G.M. Bastiaanssen. 2001. Spatial variations of surface parameters and related evaporation in the Lake Naivasha Basin estimated from remote sensing measurements. Hydrological Processes 15:1585-1607.

Farah, H.O., W.G.M. Bastiaanssen, and R.A. Feddes. 2004. Evaluation of the temporal variability of the evaporative fraction in a tropical watershed. International Journal of Applied Earth Observation and Geoinformation 5:129-140.

Field, R.T., L.J. Fritschen, E.T. Kanemasu, E.A. Smith, J.B. Stewart, S.B. Verma, and W.B. Kustas. 1992. Calibration, comparison and correction of net radiation instruments used during FIFE. Journal of Geophysical Research 97:18,681 – 18,695.

Fox, D.G. 1981. Judging air quality model performance: A summary of the AMS Workshop on Dispersion Model Performance. Bulletin of the American Meteorological Society 62:599-609.

Franks, S.W., and K.J. Beven. 1997. Estimation of evapotranspiration at the landscape scale: a fuzzy disaggregation approach. Water Resources Research 33:2929-2938.

Fuchs, M., and C.B. Tanner. 1970. Error analysis of Bowen ratios measured by differential psychrometry. Agricultural Meteorology 7:329-334.

Gash, J.H.C. 1986. A note on estimating the effect of a limited fetch on micrometeorological evaporation measurements. Boundary-Layer Meteorology 35:409-413.

Granger, R.J. 2000. Satellite-derived estimates of evapotranspiration in the Gediz basin. Journal of Hydrology 229:70-76.

Gryning, S.E., A.A.M. Holtslag, J.S. Irwin, and B. Siverstsen. 1987. Applied dispersion modeling based on meteorological scaling parameters. Atmospheric Environment 21:79-89.

Hall, F.G., K.F. Huemmrich, S.J. Goetz, P.J. Sellers, and J.E. Nickeson. 1992. Satellite remote sensing of surface energy balance: sucesses, failures, and unresolved issues in FIFE. Journal of Geophysical Research 97:19,061-19,089.

Halldin, S., and A. Lundroth. 1992. Errors in net radiometry: comparison and evaluation of six radiometer designs. Journal of Atmospheric and Oceanic Technology 6:762-783.

Han, H., and L. Yang. 2004. Evaluation of regional scale evapotranspiration using SEBS model in western Chinese Loess Plateau. Geoscience and Remote Sensing Symposium 2:1339-1342.

Handbook, L.S.D.U. 2002. Landsat Project Science Office, NASA Goddard Space Flight Center in Greenbelt, Maryland, http://Itpwww.gsfc.nasa.gov/IAS/handbook/handbook_toc.html.

Hanna, S.R., G.A. Briggs, J.W. Deardorff, B.A. Egan, F.A. Gifford, and F. Pasquill. 1977. AMS workshop on stability classification schemes and sigma curves-Summary of recommendations. Bulletin of the American Meteorological Society 58:1305-1309.

Hemakumara, H., L. Chandrapala, and A. Moene. 2003. Evapotranspiration fluxes over mixed vegetation areas measured from a large aperture scintillometer. Agricultural Water Management 58:109–122.

Hendrickx, J.M.H., J. Kleissl, J. Gomez-Vlez, S.-H. Hong, J. Fbrega-Duque, D. Vega, H. Moreno-Ramrez, and F. Ogden. 2007. Scintillometer networks for calibration and validation of energy balance and soil moisture remote sensing algorithms. Proceedings of International Society for Optical Engineering, SPIE 6565:in press.

Holtslag, A.A.M. 1984. Estimation of diabatic wind speed profiles from near-surface weather observations. Boundary-Layer Meteorology 29:225–250.

Horst, T.W., and J.C. Weil. 1992. Footprint Estimation for Scalar Flux Measurements in the Atmospheric Surface Layer. Boundary-Layer Meteorology 59:279-296.

Hsieh, C.-I., G.G. Katul, and T.-W. Chi. 2000. An approximate analytical model for footprint estimation of scalar fluxes in thermally stratified atmospheric flows. Advances in Water Resources 23:765-772.

Humes, K.S., W.P. Kustas, M.S. Moran, W.D. Nichols, and M.A. Weltz. 1994. Variability of emissivity and surface temperature over a sparsely vegetated surface. Water Resources Research 30:1299 - 1310.

Irwin, J.S. 1983. Estimating plume dispersion - a comparison of several sigma schemes. Journal of Climate and Applied Meteorology 22:92 - 114.

Jackson, T.J., J. Schmugge, and E.T. Engman. 1996. Remote sensing applications to hydrology: soil moisture. Hydrological Sciences Journal 41:517-530.

Jia, L., Z. Su, B.v.d. Hurk, M. Menenti, A. Moene, H.A.R. De Bruin, J.J.B. Yrisarry, M. Ibanez, and A. Cuesta. 2003. Estimation of sensible heat flux using the Surface Energy Balance System (SEBS) and ATSR measurements. Physics and Chemistry of the Earth 28:75-88.

Jiang, L., and S. Islam. 2001. Estimation of surface evaporation map over southern Great Plains using remote sensing data. Water Resources Research 37:329-340.

Kalman, J.D., and D.L.B. Jupp. 1990. Estimating evaporation from pasture using infrared thermography: evaluation of a one-layer resistance model Agricultural and Forest Meteorology 51:223-246.

Kite, G.W., and P. Droogers. 2000. Comparing evapotranspiration estimates from satellites, hydological models and field data. Journal of Hydrology 229:3-18.

Kizer, M.A., and R.L. Elliott. 1991. Eddy correlation systems for measuring evapotranspiration. Transactions of American Society of Agricultural Engineers 34:387-392.

Koloskov, G., K. Mukhamejanov, and T.W. Tanton. 2007. Monin-Obukhov length as a cornerstone of the SEBAL calculations of evapotranspiration. Journal of Hydrology 335:170-179.

Kurc, S.A., and E.E. Small. 2004. Dynamics of evapotranspiration in semiarid grassland and shrubland ecosystems during the summer monsoon season, central New Mexico. Water Resources Research 40:W09305, doi:10.1029/2004WR003068.

Kustas, W.P., and J.M. Norman. 1996. Use of remote sensing for evapotranspiration monitoring over land surfaces. Hydrological Sciences Journal 41:495-516.

Kustas, W.P., C.S.T. Daughtry, and P.J.V. Oevelen. 1993. Analytical treatment of the relationships between soil heat flux/net radiation ratio and vegetation indices. Remote Sensing and Environment 46:319-330.

Kustas, W.P., J.H. Prueger, J.L. Hatfield, K. Ramalingam, and L.E. Hipps. 2000. Variability in soil heat flux from a mesquite dune site. Agricultural and Forest Meteorology 103:249– 264.

Laubach, J., and U. Teichmann. 1999. Surface energy budget variability: A case study over glass with special regard to minor inhomogeneities in the source area. Theoretical Applied Climatology 62:9-24.

Lhomme, J.P., J.J. Vacher, and A. Rocheteau. 2007. Estimating downward long-wave radiation on the Andean Altiplano Agricultural and Forest Meteorology 145:139-148

Ma, Y., M. Menenti, O. Tsukamoto, H. Ishikawa, J. Wang, and Q. Gao. 2004. Remote sensing parameterization of regional land surface heat fluxes over arid area in

northwestern China. Journal of Arid Environments 57:257-273.

Ma, Y., L. Zhong, Z. Su, H. Ishikawa, M. Menenti, and T. Koike. 2006. Determination of regional distributions and seasonal variations of land surface heat fluxes from Landsat-7 Enhanced Thematic Mapper data over the central Tibetan Plateau area. Journal of Geophysical Research 111:D10305, doi:10.1029/2005JD006742.

McClave, J.T., and F.H. Dietrich II. 1979. Statistics Dellen Publishing Company, San Francisco, California.

Mecikalski, J.R., G.R. Diak, M.C. Anderson, and J.M. Norman. 1999. Estimating fluxes on continental scales using remotely-sensed data in an atmospheric-land exchange model. Journal of Applied Meteorology 38:1352-1369.

Menenti, M., W.G.M. Bastiaanssen, and D. Van Eick. 1989. Determination of hemispheric reflectance with thematic mapper data. Remote Sensing of the Environment 28:327-337.

Menenti, M., S. Azzali, W. Verhoef, and R. van Swol. 1993. Mapping agroecological zones and time lag in vegetation growth by means of Fourier Analysis of time series of NDVI images. Advances in Space Research 13:233-237.

Monteith, J.L., and M.H. Unsworth. 1990. Principles of Environmental Physics, Edward Arnold, London.

Moran, M.S., and R.B. Jackson. 1991. Assessing the spatial distribution of evapotranspiration using remotely sensed inputs. Journal of Environmental Quality 20:725-735.

Morse, A., M. Tasumi, R.G. Allen, and W.J. Kramer. 2000. Application of the SEBAL methodology for estimating consumptive use of water and streamflow depletion in the Bear river basin of Idaho through remote sensing. Final report submitted to the Raytheon Systems Company, Earth Observation System Data and Information System Project, by Idaho Department of Water Resources and University of Idaho.

Nishida, K., R.R. Nemani, S.W. Running, and J.M. Glassy. 2003. An operational remote sensing algorithm of land surface evaporation. Journal of Geophysical Research 108 (D9):doi:10.1029/2002JD002062.

Norman, J.M., W.P. Kustas, and K.S. Humes. 1995. A two-source approach for estimating soil and vegetation energy fluxes from observations of directional radiometric surface temperature. Agriculture and Forest Meteorology 77:263-293.

Norman, J.M., M.C. Anderson, W.P. Kustas, A.N. French, J. Mecikalski, R. Torn, G.R. Diak, T.J. Schmugge, and B.C.W. Tanner. 2003. Remote sensing of surface energy fluxes at 10 1-m pixel resolutions. Water Resources Research 39:1221. doi:10.1029/2002WR001775.

Parlange, M.B., W.E. Eichinger, and J.D. Albertson. 1995. Regional scale evaporation and the atmosphere boundary layer. Reviews of Geophysics 33:99-124.

Paw, K.T., S. Wharton, L. Xu, M. Falk, M. Schroeder, and E. Gonzales. 2004. Zen and the art of energy balance closure Symposium "Progress in Radiation and Energy Balance Closure", 68th Annual Meeting Soil Science Society of America, Seattle, Washington.

Pelgrum, H., and W.G.M. Bastiaanssen. 1996. An intercomparison of techniques to determine the area-averaged latent heat flux from individual in situ observations: a remote sensing approach using the European Field Experiment in a Desertification-Threatened Area data. Water Resources Research 32:2775–2786.

Peters Lidard, C.D., S. Kumar, Y. Tian, J.L. Eastman, and P. Houser. 2004. Global urban-scale land-atmosphere modeling with the land information system. 84th AMS Annual Meeting 11-15 January 2004, Symposium on Planning, Nowcasting, and Forecasting in the Urban Zone.

Richardson, A.D., D.Y. Hollinger, G.G. Burba, K.J. Davis, L.B. Flanagan, G.G. Katul, J.W. Munger, D.M. Ricciuto, P.C. Stoy, A.E. Suyker, S.B. Verma, and S.C. Wofsy. 2006. A multi-site analysis of random error in tower-based measurements of carbon and energy fluxes. Agricultural and Forest Meteorology 136:1-18.

Rosema, A. 1990. Comparison of meteosat-based rainfall and evapotranspiration mapping of Sahel region. Remote Sensing of Environment 46:27-44.

Sauer, T.J. 2002. Soil Heat Flux. Encyclopedia of Soil Science Marcel Dekker, INC., New York, NY.

Sauer, T.J., D.W. Meek, T.E. Ochsner, A.R. Harris, and R. Horton. 2003. Errors in heat flux measurement by flux plates of contrasting design and thermal conductivity. Vadose Zone Journal 2:580-588.

Schmid, H.P., and T.R. Oke. 1990. A model to estimation the source area contributing to turbulent exchange in the surface layer over patchy terrain. Quarterly Journal of The Royal Meteorological Society 116:965-988.

Schuepp, P.H., M.Y. Leclerc, J.I. MacPherson, and R.L. Desjardins. 1990. Footprint prediction of scalar fluxes from analytical solutions of the diffusion equation. Boundary-Layer Meteorology 50:355-373.

Schüttemeyer, D., C. Schillings, A.F. Moene, and H.A.R. De Bruin. 2007. Satellite-based actual evapotranspiration over drying semiarid terrain in West Africa. Journal of Applied Meteorology and Climatology 46:97-111 DOI: 10.1175/JAM2444.1.

Scott, R.L., J.W. Shuttleworth, G. D.C., and M.I. T. 2000. The water use of two dominant vegetation communities in a semiarid riparian ecosystem. Agricultural and Forest Meteorology 105:241-256.

Scott, R.L., E.A. Edwards, W.J. Shuttleworth, T.E. Huxman, C.Watts, and D.C. Goodrich. 2004. Interannual and seasonal variation in fluxes of water and carbon dioxide from a riparian woodland ecosystem. Agricultural and Forest Meteorology 122 65–84.

Seguin, B.D., and B. Itier. 1983. Using midday surface temperature to estimate daily evapotranspiration from satellite thermal IR data. International Journal of Remote Sensing 4:371-383.

Shuttleworth, W.J., R.J. Gurney, A.Y. Hsu, and J.P. Ormsby. 1989. The variation in energy partition at surface flux sites. Proceedings of the IAHS Third International Assembly, Baltimore, MD. 186:67-74.

Stannard, D.I. 1993. Comparison of Penman-Monteith, Shuttleworth-Wallace, and Modified Priestley-Tayor evapotranspiration models for wildland vegetation in Semiarid rangeland. Water Resources Research 29:1379-1392.

Steinwand, A.L., R.F. Harrington, and D. Or. 2006. Water balance for Great Basin phreatophytes derived from eddy covariance, soil water, and water table measurements. Journal of Hydrology 329:595-605.

Stromberg, J.C. 1998. Dynamics of Fremont cottonwood (Populus fremontii) and saltcedar (Tamarix chinensis) populations along the San Pedro River, Arizona. Journal of Arid Environments 40:133-155.

Su, Z. 2002. The Surface Energy Balance System (SEBS) for estimation of turbulent heat fluxes. Hydrology and Earth System Sciences 6:85-99.

Sugita, M., and W. Brutsaert. 1991. Daily evaporation over a region from lower boundary layer profiles measured with radiosondes. Water Resources Research 27:747-752.

Sumner, D.M., and J.M. Jacobs. 2005. Utility of Penman–Monteith, Priestley–Taylor, reference evapotranspiration, and pan evaporation methods to estimate pasture evapotranspiration. Journal of Hydrology 308:81-104.

Tasumi, M. 2003. Progress in operational estimation of regional evapotranspiration using satellite imagery, Ph.D. Thesis, University of Idaho, Moscow, Idaho.

Tasumi, M., and R.G. Allen. 2000. Application of the SEBAL methodology for estimating consumptive use of water and stream flow depletion in the Bear River Basin of Idaho through remote sensing. Appendix A: The theoretical basis of SEBAL. Final report submitted to the Raytheon Systems Company, Earth Observation System Data and Information System Project.

Tasumi, M., R.G. Allen, and R. Trezza. 2008. At-surface reflectance and albedo from satellite for operational calculation of land surface energy balance. Journal of Hydrologic Engineering 13:51-63.

Teixeira, A.H.d.C., W.G.M. Bastiaanssen, M.D. Ahmad, and M.G. Bos. 2008. Inspecting SEBAL model parameters and application in São Francisco River basin to assess evapotranspiration and water productivity. Part 1: Calibration and validation. Remote Sensing Environment (submitted).

Trezza, R. 2002. Evapotranspiration using a satellite-based surface energy balance with standardized ground control. Ph.D. Thesis, Utah State University: Logan, Utah.

Twine, T.E., W.P. Kustas, J.M. Norman, D.R. Cook, P.R. Houser, T.P. Meyers, J.H. Prueger, P.J. Starks, and M.L. Wesely. 2000. Correcting eddy-covariance flux underestimates over a grassland. Agricultural and Forest Meteorology 103:279-300.

Wang, J., W.G.M. Bastiaanssen, Y. Ma, and H. Pelgrum. 1998. Aggregation of land surface parameters in the oasis-desert systems of Northwest China. Hydrological Sciences 12:2133-2147.

Watts, C.J., A. Chehbouni, J.-C. Rodriguez, Y.H. Kerr, O. Hartogensis, and H.A.R. De Bruin. 2000. Comparison of sensible heat flux estimates using AVHRR with scintillometer measurements over semi-arid grassland in northwest Mexico. Agricultural and Forest Meteorology 105:81–89.

Willmott, C.J. 1981. On the validation of models. Physical Geography 2:184-194.

Willmott, C.J. 1982. Some comments on the evaluation of model performance. Bulletin of the American Meteorological Society 63:1309–1313.

Willmott, C.J., and D.E. Wicks. 1980. An empirical method for the spatial interpolation of monthly precipitation within California. Physical Geography 1:59-73.

Wilson, K., A. Goldstein, E. Falge, M. Aubinet, D. Baldocchi, P. Berbigier, C. Bernhofer, R. Ceulemans, H. Dolman, C. Field, A. Grelle, A. Ibrom, B.E. Law, A. Kowalski, T. Meyers, J. Moncrieff, R. Monson, W. Oechel, J. Tenhunen, R. Valentini, and S. Verma. 2002. Energy balance closure at FLUXNET sites. Agricultural and Forest Meteorology 113 223-243.

Wright, J.L. 1982. New evapotranspiration crop coefficients. Journal of Irrigation and Drainage Engineering 108:57-74.

Yamartino, R.J. 1984. A comparison of several "Single-Pass" estimators of the standard deviation of wind direction. Journal of Climate and Applied Meteorology 23:1362-1366.

CHAPTER 5

UP-SCALING OF SEBAL DERIVED EVAPOTRANSPIRATION MAPS FROM LANDSAT (30m) TO MODIS (250m) SCALE

ABSTRACT

Remotely sensed imagery of the Earth's surface via satellite sensors provides information to estimate the spatial distribution of evapotranspiration. The spatial resolution of evapotranspiration predictions depends on the sensor type and varies from the 30 – 60 m Landsat scale to the 250 – 1000 m MODIS scale. Therefore, for an accurate characterization of the regional distribution of evapotranspiration, scaling transfer between images of different resolutions is important. Scaling transfer includes both up-scaling (aggregation) and down-scaling (disaggregation). In this paper, we address the up-scaling problem.

The Surface Energy Balance Algorithm for Land (SEBAL) was used to derive evapotranspiration maps from Landsat 7 Enhanced Thematic Mapper Plus (ETM+) and Moderate Resolution Imaging Spectroradiometer (MODIS) images. Landsat 7 bands have spatial resolutions of 30 to 60 m, while MODIS bands have resolutions of 250, 500 and 1000 m. Evaluations were conducted for both "output" and "input" up-scaling procedures, with aggregation accomplished by both simple averaging and nearest neighboring resampling techniques. Output up-scaling consisted of first applying SEBAL and then aggregating the output variable (daily evapotranspiration). Input up-scaling consisted of aggregating 30 m Landsat pixels of the input variable (radiance) to obtain pixels at 60, 120, 250, 500 and 1000 m before SEBAL was applied. The objectives of this study were first to test the consistency of SEBAL algorithm for Landsat and MODIS satellite images and second to investigate the effect of the four different up-scaling processes on the spatial distribution of evapotranspiration.

We conclude that good agreement exists between SEBAL estimated ET maps directly derived from Landsat 7 and MODIS images. Among the four up-scaling methods compared, the output simple averaging method produced aggregated data and aggregated differences with the most statistically and spatially predictable behavior. The input nearest neighbor method was the least predictable but was still acceptable. Overall, the daily evapotranspiration maps over the Middle Rio Grande Basin aggregated from Landsat images were in good agreement with evapotranspiration maps directly derived from MODIS images.

5.1. INTRODUCTION

Remote sensing data from satellite-based sensors have the potential to provide detailed information on land surface properties and parameters at local to regional scales. Perhaps one of the most important land surface parameters that can be derived from remote sensing is actual evapotranspiration (ET). The spatio-temporal distribution of ET is needed for sustainable management of water resources as well as for a better understanding of water exchange processes between the land surface and the atmosphere. However, ground measurements of ET over a range of space and time scales are very difficult to obtain due to the time and cost involved. Remotely sensed imagery with numerous spatial and temporal resolutions is therefore an ideal solution for determination of the spatio-temporal distribution of ET.

Today, large amounts of remotely sensed data with variable spatial, temporal, and spectral resolutions are available. A number of studies have attempted to estimate ET from different satellite sensors, including the Land remote sensing satellite Enhanced Thematic Mapper Plus (Landsat ETM+) (Bastiaanssen et al., 2005; Hendrickx and Hong, 2005; Allen et al., 2007), the Advanced Spaceborne Thermal Emission and Reflection Radiometer (ASTER) (French et al., 2002), the Advanced Very High Resolution Radiometer (AVHRR) (Seguin et al., 1991), the Moderate Resolution Imaging Spectroradiometer (MODIS) (Nishida et al., 2003; Hong et al., 2005) and the Geostationary Orbiting Environmental Satellite (GOES) (Mecikalski et al., 1999).

We employ the Surface Energy Balance Algorithm for Land (SEBAL) that is one of several remote sensing algorithms used to extract information from raw satellite data. It estimates various land surface parameters, including surface albedo, normalized difference vegetation index (*NDVI*), surface temperature, and energy balance parameters from the remotely sensed radiance values obtained from satellite sensors. Since satellite sensors have different spatial, spectral and radiometric resolutions, the consistency of ET estimates from different satellites by SEBAL needs to be certified. We have successfully used SEBAL for ET mapping in New Mexico, Arizona, and California (Hendrickx and Hong, 2005), the Panama Canal watershed (Hendrickx et al., 2005), and the Volta Basin in West Africa (Hendrickx et al., 2006; Compaore et al., 2008). We have validated our implementation of SEBAL by comparing its results with eddy covariance ground measurements of ET in riparian areas of the southwestern USA (Hendrickx and Hong, 2005).

The validation of products of remote sensing algorithms is dependent upon the spatial resolution (Liang, 2004). Fine resolution products (< 100 m) such as Landsat can be validated with ground measurements. However, validating coarse resolution products, such as MODIS (1000 m in thermal band), using ground measurements is very difficult because of the scale disparity between ground "point" measurements and the coarse spatial resolution imagery. Therefore, for validation of MODIS products, the products of high resolution remotely sensed imagery such as Landsat 7 (30 to 60 m resolution) need to be first validated with ground point measurements. MODIS products can then be compared against up-scaled (aggregated) Landsat product.

Many studies regarding the effect of up-scaling data sets have been reported (Nellis and Briggs, 1989; Turner et al., 1989; Lam and Quattrochi, 1992; Stoms, 1992; Brown et al., 1993; Vieux, 1993; De Cola, 1994; Mark and Aronson, 1994; Wolock and Price, 1994; Zhang and Montgomery, 1994; Bian et al., 1999). During an aggregation process, the raster spatial data are reduced to a smaller number of data pixels covering the same spatial extent. It is generally recognized that data aggregation modifies the statistical and spatial characteristics of the data (Bian et al., 1999). Since the total number of pixels is reduced, the variance and frequency distribution of the sampled data may deviate from the original data set and tends to reduce spatial autocorrelation at coarser resolutions (Bian, 1997). Some studies have pointed out that data accuracy is enhanced significantly by reduction of spatial resolution (Townshend et al., 1992; Dai and Khorram, 1998; Van Rompaey et al., 1999; Carmel, 2004). Several studies have also argued that aggregation to a coarser resolution reveals certain spatial patterns which are not shown until the data are presented at a coarser scale (Zhang and Montgomery, 1994; Seyfried and Wilcox, 1995). On the other hand, the decrease in spatial resolution possibly results in a loss of information that may be valuable for particular applications (Carmel et al., 2001).

The methodology for aggregating simple rectangular grid data is well developed (Bian, 1997; Bian et al., 1999; Mengelkamp et al., 2006). In this study, the simple averaging and nearest neighbor resampling methods were selected for the data aggregation scheme, since these methods have been the most popular and convenient to

use (Atkinson, 1985; Liang, 2004). The simple averaging method calculates the average value over an area of interest to produce a new coarser resolution data set. Nearest neighbor sampling produces a subset of the original data; the extremes and subtleties of the data values are therefore preserved.

For the up-scaling scheme, numerous studies have used the assumption that surface fluxes can be expressed as direct area averages of the surface fluxes (Shuttleworth, 1991; Lhomme, 1992; Li and Avissar, 1994). Liang (2000) simply averaged the remotely sensed reflectance values from 30 m to 1 km and explored the aggregation effect. He concluded that the spectral reflectance was basically linear from 30 m resolution to 1000 m resolution. More recently, Mengelkamp et al (2006) mentioned that area averaged small scale ET calculated from local measurements was in good agreement with the area represented regional values. Nevertheless, few papers have examined the effect of different up-scaling schemes on the relative accuracy of the aggregated data despite its practical importance. A spatial resolution gap exists between the data requirements of regional-scale models and the output data from remote sensing energy balance algorithms such as SEBAL. For example, general global circulation models or regional weather prediction models need input data with a spatial resolution of hundreds of kilometers which is much larger than the spatial resolution of most satellite sensors (Liang, 2004). Therefore, an up-scaling (data aggregation) procedure is needed to fill the scale gap between satellite measurements and input requirements for large scale models. Increasing spatial resolution by data aggregation has shown the potential to

generate observed or modeled surface flux estimates over a range of different spatial resolutions (Gupta et al., 1986; Lhomme, 1992; Ebleringer and Field, 1993).

In this study, high quality scenes of two different dates of Landsat 7 Enhanced Thematic Mapper Plus (ETM+) and Moderate Resolution Imaging Spectroradiometer (MODIS) imagery were selected and SEBAL was applied to estimate daily ET. Landsat scale pixels (30 m) were aggregated to larger scale (60, 120, 250, 500 and 1000 m). The objectives of this study were first to test the consistency of the SEBAL algorithm for Landsat 7 and MODIS images, and second to investigate the effects of four different up-scaling processes on the spatial distribution of ET, especially how the relative accuracy of ET changes with different up-scaling processes.

5.2.   METHOD AND MATERIALS

5.2.1. Study Area and Satellite Imagery

Landsat 7 and MODIS images on two different dates during the growing season (September 14, 2000 and June 16, 2002) (Figures 5.1 and 5.2) were used to examine the effect of aggregation processes. Four satellite images used in this study were georeferenced to match the spatial coordinates as closely as possible. This was done by identifying the several accurate Ground Control Points (e.g. road intersections and agricultural field boundaries) on the images and aligning them to fit on between images. The image used in this study is the subset of the Middle Rio Grande Basin that

MODIS
(Temporal resolution: daily; Spatial resolution: 250, 500, 1000m)
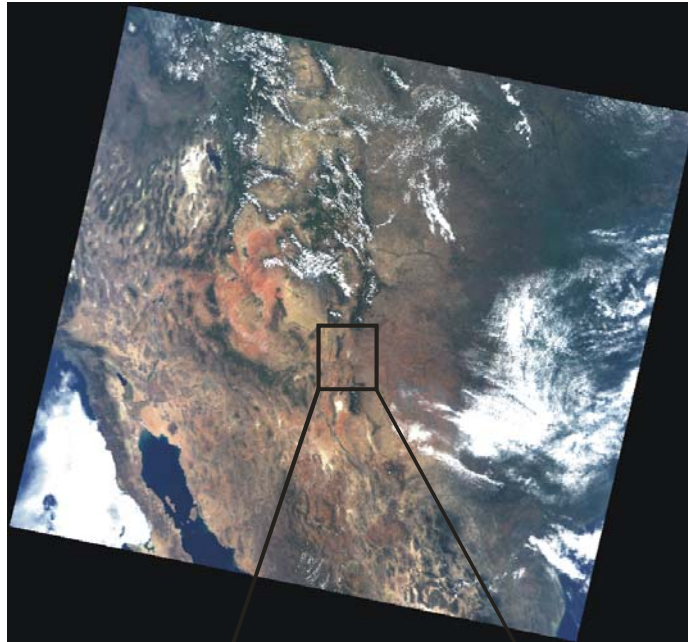
Landsat7
(Temporal resolution: 16 days; Spatial resolution: 30, 60m)
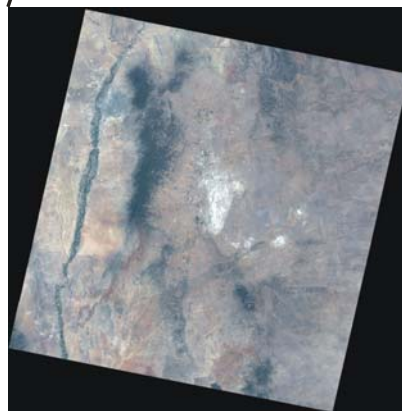
Figure 5.1. Landsat and MODIS satellite imagery on June 16, 2002
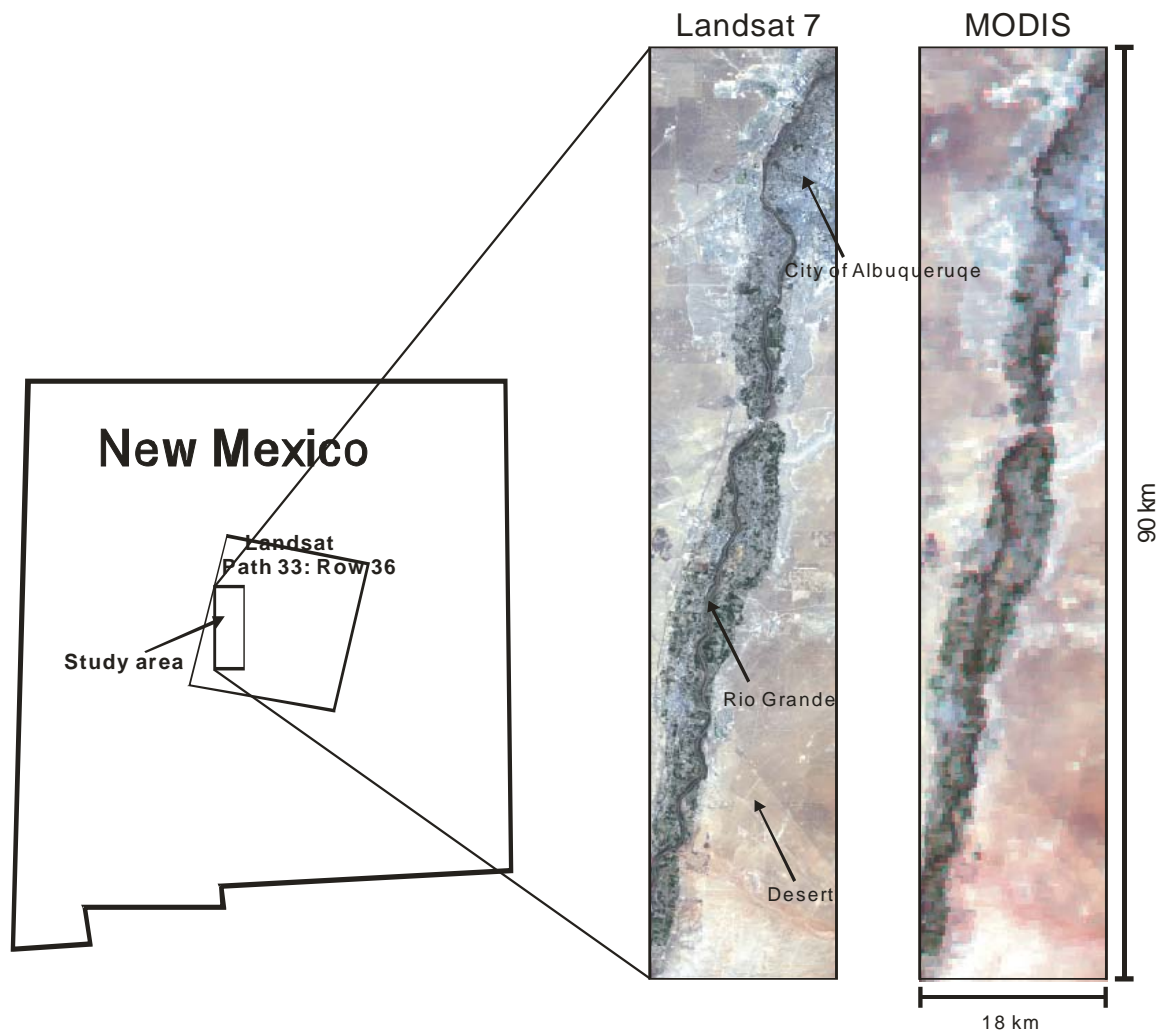
Figure 5.2. Location of the study area (18km by 90km). True color Landsat 7 (30 m by 30 m resolution) and MODIS (250 m by 250 m resolution) images on June 16, 2002.

covers an area of 18 by 90km. The Middle Rio Grande setting is mainly composed of

agricultural fields, riparian forests and surrounding desert areas (Figures 5.3 and 5.4).

5.2.2. Surface Energy Balance Algorithm for Land (SEBAL)

SEBAL is a physically based analytical image processing method that evaluates

the components of the energy balance and determines the ET rate as the residual. SEBAL

is based on the computation of energy balance parameters from multi spectral satellite

data (Bastiaanssen et al., 1998; Morse et al., 2000; Allen et al., 2007). To implement

SEBAL, images are needed with information on reflectance in the visible, near-infrared

and mid-infrared bands, as well as emission in the thermal infrared band. To account for

the influence of topographical variations on the energy balance components, a digital

elevation model (DEM) with the same spatial resolution as the satellite imagery is also

required. The slope and aspect were calculated from DEM using models provided in

ERDAS IMAGINE software (ERDAS, 2002).

The energy balance equation is

$$R_n - G - H = \lambda ET \qquad\qquad [5.1]$$

where R_n is the net incoming radiation flux density [Wm^{-2}], G is the ground heat flux

density [Wm^{-2}], H is the sensible heat flux density [Wm^{-2}], λET is the latent heat flux

density [Wm^{-2}], and parameter λ is the latent heat of vaporization of water [Jkg^{-1}].

Landsat7 spectral band resolution
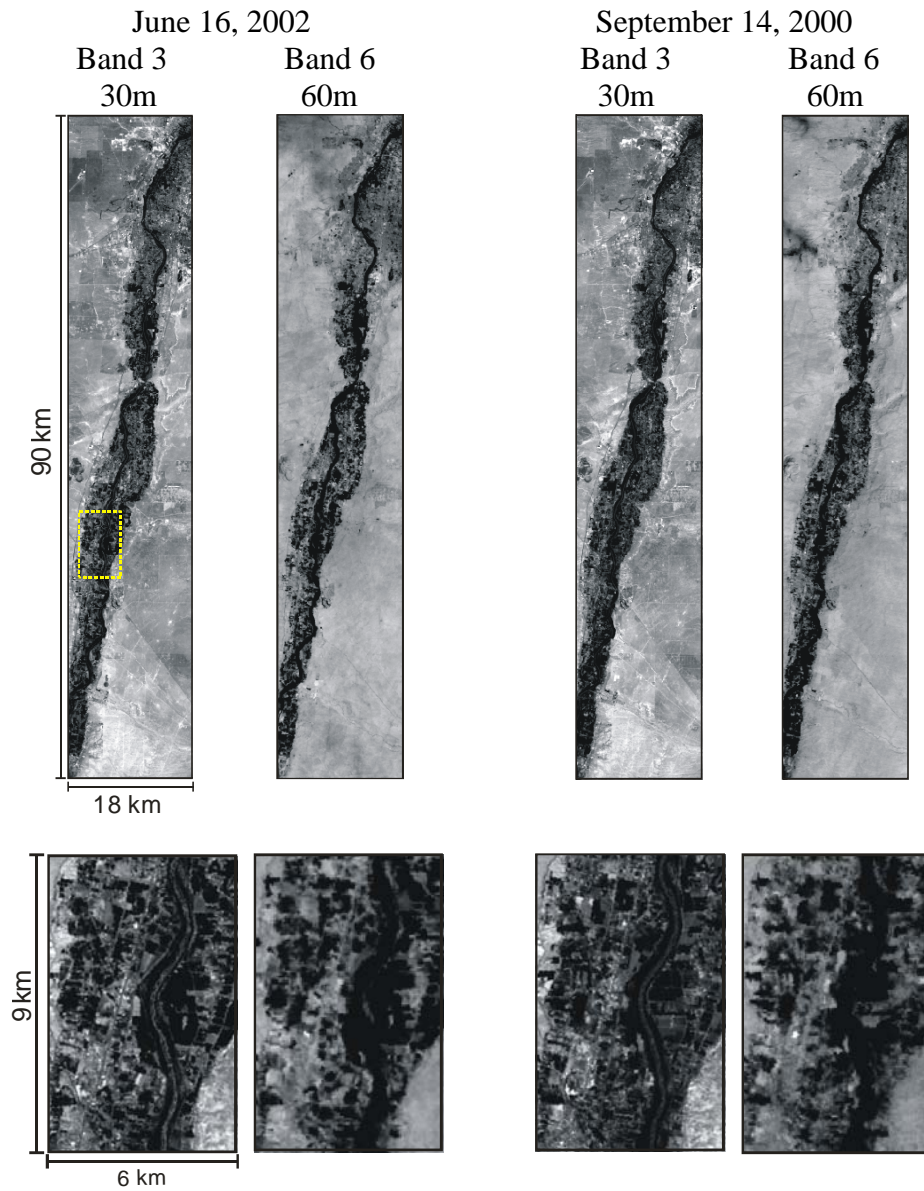
Figure 5.3. Landsat 7 images on June 16, 2002 and September 14, 2000. [Band 3: visible band (30 m by 30 m resolution), Band 6: thermal infrared band (60 m by 60 m resolution)]. Enlarged areas (6 by 9 km) shown at the bottom correspond to the dotted square of the upper images.

MODIS spectral band resolution

June 16, 2002

Band 1
250m

Band 31
1000m

September 14, 2000

Band 1
250m
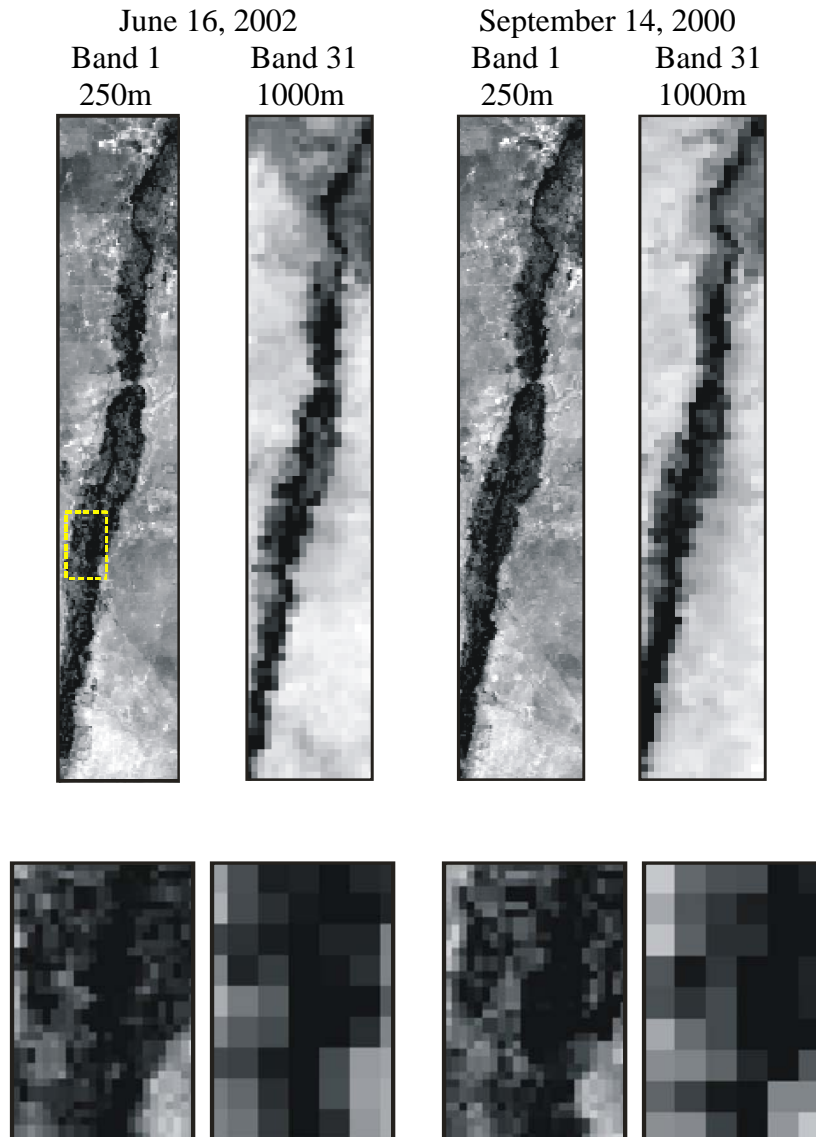
Band 31
1000m

Figure 5.4. MODIS images on June 16, 2002 and September 14, 2000. [Band 1: visible band (250 m by 250 m resolution), Band 31: thermal infrared band (1000 m by 1000 m resolution)]. Enlarged areas (6 by 9 km) shown at the bottom correspond to the dotted square of the upper images.

The net radiation (R_n) was computed for each pixel from the radiation balance using surface albedo obtained from short-wave radiation and using emissivity estimated from the long-wave radiation (Allen et al., 1998; Bastiaanssen et al., 1998; Morse et al., 2000). Soil heat flux (G) was estimated from net radiation together with other parameters such as normalized difference vegetation index ($NDVI$), surface temperature and surface albedo (Clothier et al., 1986; Choudhury et al., 1987; Daughtry et al., 1990; Bastiaanssen, 2000). Sensible heat flux (H) was calculated from wind speed, estimated surface roughness for momentum transport, and air temperature differences between two heights (0.1 and 2 m) using an iterative process based on the Monin-Obukhov similarity theory (Brutsaert, 1982; Morse et al., 2000; Tasumi, 2003).

The spatial resolutions of the Landsat 7 bands are 30 and 60 m, compared with 250, 500 and 1000m for the MODIS bands (Table 5.1). Besides the difference in the spatial resolution between Landsat 7 and MODIS, a difference in radiance measurements between the two sensors is expected as a result of slightly different band widths for each sensor. Table 5.1 also shows the spectral bands of Landsat 7 and MODIS in the visible, near infrared and thermal infrared wavelength regions used for SEBAL application. MODIS bands 1, 2, 3, 4, 6 and 7 are compatible with Landsat 7 bands 3, 4, 1, 2, 5 and 7, respectively. The band widths of MODIS in the visible and near infrared, with the exception of Band 3, are narrower than those of Landsat. This results in different responses from the surface, which in turn may alter the computed surface albedo and vegetation index.

Table 5.1. Band spatial resolutions (m) and wavelengths (μm) of Landsat 7 and MODIS sensors.

Sensors		Band number								
		1	2	3	4	5[#]	6	7	31	32
Landsat 7	Pixel size [m]	30	30	30	30	30	60	30	NA*	NA*
	Band width [μm]	0.45 – 0.51	0.52 – 0.60	0.63 – 0.69	0.75 – 0.9	1.55 – 1.75	10.4 – 12.5	2.09 – 2.35	NA*	NA
MODIS	Pixel size [m]	250	250	500	500	500	500	500	1000	1000
	Band width [μm]	0.62 – 0.67	0.84 – 0.87	0.46 – 0.48	0.54 – 0.56	1.23 – 1.25	1.63 – 1.65	2.11 – 2.15	10.8 – 11.3	11.8 – 12.3

[#]MODIS band5 is not used in this study because of streaking noise,
*Not available

5.2.2.1. Brightness temperature

The major difference in the ET derivation from Landsat and MODIS images was in the surface temperature calculations. SEBAL used one thermal band for surface temperature estimation for Landsat 7 data while two thermal bands were used with MODIS data. The temperature detected by a thermal sensor is called the brightness temperature. Radiance data from Landsat 7 and MODIS thermal infrared bands were first converted to brightness temperatures with an inversion of Planck's equation:

$$T_b = \frac{hc/k\lambda}{\ln\left(\dfrac{2hc^2\lambda^{-5}}{L_\lambda}+1\right)} = \frac{K_2}{\ln\left(\dfrac{K_1}{L_\lambda}+1\right)} \qquad [5.2]$$

where T_b is the brightness temperature in Kelvin [K], c is the speed of light (2.998 x 10^8) [ms^{-1}], h is the Planck's Constant (6.626 x 10^{-34}) [Js], k is the Boltzmann constant (1.3807 x 10^{-23}) [JK^{-1}], L_λ is the spectral radiance [Wm^{-2}μm^{-1}sr^{-1}], λ is the band effective center wavelength [μm] and K_1 and K_2 are calibration coefficients [Wm^{-2}sr^{-1}μm^{-1}] (Table 5.2).

5.2.2.2. Surface temperature

For Landsat images the surface temperature (T_s) is estimated using T_b and ε_0 with the following empirical relationship (Tasumi et al., 2000). Several studies reported similar relationship between T_s and ε_0 (e.g. Price, 1984; e.g. Moran et al., 1989).

$$T_s = \frac{T_b}{\varepsilon_0^{0.25}} \qquad [5.3]$$

where

Table 5.2. Constants K_1 and K_2 [$Wm^{-2}ster^{-1}\mu m^{-1}$] for Landsat 7 ETM+ (NASA, 2002) and MODIS (http://modis.gsfc.nasa.gov/).

	K_1	K_2
Landsat 7	666.09	1282.71
MODIS (band 31)	730.01	1305.84
MODIS (band 32)	474.99	1198.29

$$\varepsilon_0 = 1.009 + 0.47 \, ln(NDVI). \hspace{4cm} [5.4]$$

For MODIS images the split window technique is used. Split window algorithms take advantage of the differential absorption in two close infrared bands to account for the effects of absorption by atmospheric gases. Several split window algorithms are currently available to derive surface temperature from brightness temperature when multiple thermal bands are available. In this study the algorithm developed by Ulivieri et al. (1992) was applied. Vazquez et al. (1997) validated the algorithm at the area of natural grassland with patches of bare soil covering various seasons and a wide range of T_s and the algorithm present a great level of accordance with ground data (Ulivieri et al., 1992; Vazquez et al., 1997).

$$T_s = T_{31} + 1.8(T_{31} - T_{32}) + 48(1 - \varepsilon) - 75\Delta\varepsilon \hspace{3cm} [5.5]$$

where T_{31} is the brightness temperature obtained from band31 [K], T_{32} is the brightness temperature obtained from band 32 [K], $\varepsilon = (\varepsilon_{31} + \varepsilon_{32})/2$, $\Delta\varepsilon = \varepsilon_{31} - \varepsilon_{32}$, ε_{31} is the surface emissivity in band 31 and ε_{32} is the surface emissivity in band 32.

Cihlar et al. (1997) developed an algorithm to calculate the surface emissivity from *NDVI*.

$$\Delta\varepsilon = \varepsilon_{31} - \varepsilon_{32} = 0.01019 + 0.01344\ln(NDVI) \hspace{2.5cm} [5.6]$$

where

$$\varepsilon_{31} = 0.9897 + 0.029 \ln(NDVI) .$$
[5.7]

5.2.2.3. Daily evapotranspiration

In SEBAL, daily ET was interpolated by assuming the instantaneous evaporative fraction (*EF*) when the satellite was passing over is approximately equal to the daily mean value (Shuttleworth et al., 1989; Brutsaert and Sugita, 1992; Crago, 1996; Farah et al., 2004; Gentine et al., 2007). The soil heat flux is assumed to be zero on a daily basis (Kustas et al., 1993). Based on the known value of the instantaneous EF, the daily-averaged net radiation flux, and the soil heat flux over a daily period, daily ET (ET_{24}) can be computed by (Bastiaanssen et al., 1998):

$$ET_{24} = \frac{86400 \cdot EF \cdot (R_{n24} - G_{24})}{\lambda \cdot \rho_w}$$
[5.8]

where $EF = \lambda E / (\lambda E + H)$, *86400* is a constant for time scale conversion, ET_{24} is daily ET [mmd^{-1}], R_{n24} is daily-averaged net radiation [Wm^{-2}], G_{24} is daily-averaged soil heat flux [Wm^{-2}], *EF* is the evaporative fraction and ρ_w is the density of water [kgm^{-3}].

5.2.3. Up-scaling (Aggregation) Process

In the up-scaling process, two different procedures were evaluated. The first consisted of applying SEBAL first and then aggregating the output variable (daily ET). The second consisted of aggregating Landsat pixels of input variable (radiance) to obtain pixels at the MODIS scale before SEBAL was applied (Figure 5.5). If the model is insensitive to an input parameter, aggregating the value with increasing scale will have
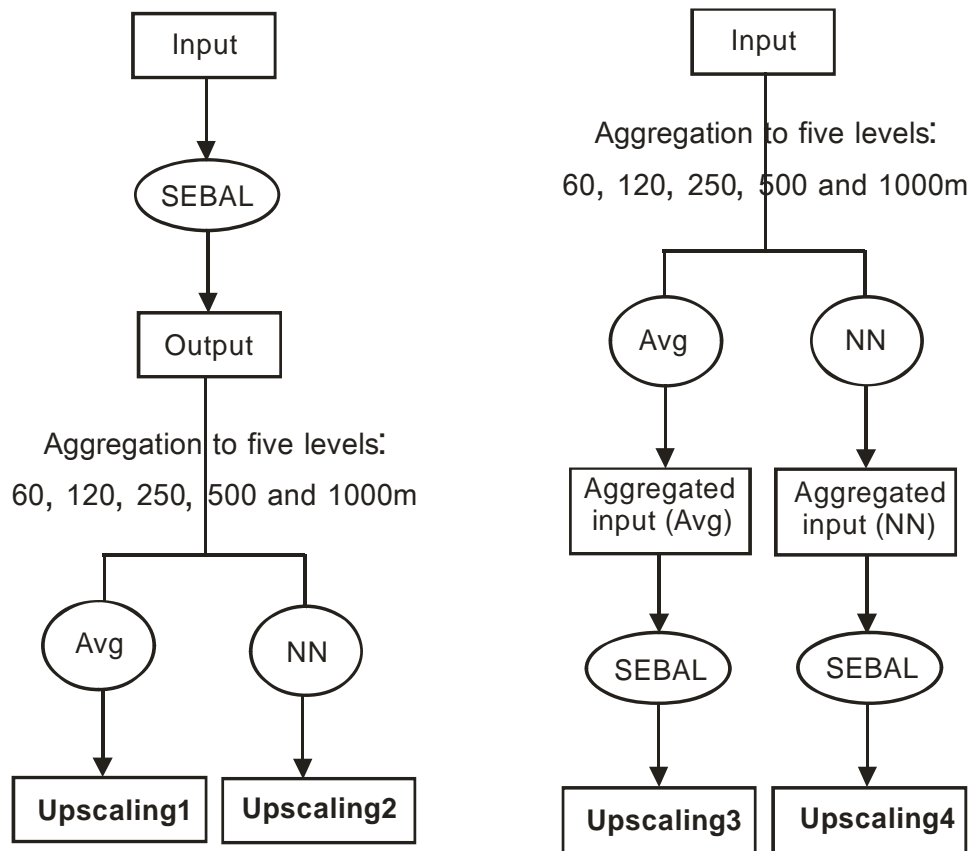
Figure 5.5. Schematic of up-scaling schemes applied in this study. (Upscaling1: output up-scaling with simple averaging, Upscaling2: output up-scaling with nearest neighbor, Upscaling3: input up-scaling with simple-averaging and Upscaling4: input-up-scaling with nearest neighbor).

little influence on model predictions. However, when the model does not operate linearly, the change in data aggregation could increase or decrease model predictions (Quattrochi and Goodchild, 1997; French, 2001; Liang, 2004).

Aggregation imagery was obtained by simple averaging and by nearest neighbor selection, and done with ERDAS IMAGINE (Leica Geosystems LLC). The simple averaging resampling method calculated the arithmetic mean over an n by n window. Since a pixel value of satellite imagery is considered to be the integrated value over the corresponding area on the ground, simple averaging is considered appropriate for aggregating remotely sensed images. The simple averaging method smoothes the original data values and therefore produces a "tighter" histogram than the original data set. Furthermore, aggregating a data set by simple averaging generally decreases the variance and also increases the spatial autocorrelation (Anselin and Getis, 1993).

The nearest neighbor approach uses the value of the input pixel closest to the center of the output pixel. To determine the nearest neighbor, the algorithm uses the inverse of the transformation matrix to calculate the image file coordinates of the desired geographic coordinate. The pixel value occupying the closest image file coordinate to the estimated coordinate will be used for the output pixel value in the georeferenced image. Unlike simple averaging, nearest neighbor is appropriate for thematic files having data file values based on a qualitative system. One advantage of the nearest neighbor method is that, unlike the simple averaging resampling method, its output values are original input values. The other advantage is that it is easy to compute and therefore fastest to use. However, the disadvantage is that nearest neighbor generates a choppy, "stair-stepped"

effect. The image tends to have a rough appearance relative to the original data (Cover and Hart, 1967; Atkinson, 1985; Dodgson, 1997; Bian et al., 1999).

The aggregation was operated at six levels: 30, 60, 120, 250, 500 and 1000 m pixel sizes. At each level, Landsat scale 30 by 30 m pixels were broken into 10 by 10 m pixels with the same pixel values; the data were then aggregated directly from the 10 m resolution instead of from a previous aggregation. This procedure made it easier to aggregate from the Landsat 30 m pixel size to MODIS 250, 500 and 1000 m pixel sizes.

5.3.   RESULTS AND DISCUSSION

5.3.1. SEBAL Consistency between Landsat and MODIS

The SEBAL algorithm was applied to both Landsat 7 and MODIS images acquired on September 14, 2000 and June 16, 2002 and estimated their daily ET rates. In order to check the consistency of SEBAL performance for the different satellite sensors, SEBAL estimated ET from Landsat and MODIS images were compared each other. Spatial distribution of ET maps for visual verification and histograms and basic statistics for quantitative examination were selected. Two approaches were used to inspect the ET estimation difference between two different satellite sensors: one is a difference image (pixel-by-pixel difference between Landsat and MODIS estimates), while the other was a relative difference image (absolute value of the pixel difference was divided by the MODIS derived pixel value). Basic statistics of the difference and relative difference

images were also computed to quantify the discrepancy between Landsat and MODIS estimates.

5.3.1.1. Comparison between Landsat (30m) and MODIS (250m) estimated ET

Figure 5.6 shows that the June image taken during the summer has significantly higher ET rates than the September image taken in the early fall. All of the ET images clearly show high ET rates in the irrigated fields and riparian areas along the Rio Grande Valley, while low ET rates are shown in the surrounding desert areas and bare soils. The city of Albuquerque has a somewhat higher ET rate than surrounding desert areas due to urban and residential vegetations.

The disparate spatial resolutions of Landsat- and MODIS-based ET images result in some differences in ET distribution, as may be expected. Many small areas (length scale on the order of 10 to 100 m) with high ET rates along the river are captured well in the Landsat-based ET map with a spatial resolution of 30 m. These peak ET rates are averaged out, however, on the MODIS derived ET map with a spatial resolution of 250 m. Figure 5.6 shows that MODIS derived ET distributions have a tighter and taller histogram and fewer pixels have close to zero (0.0 to 0.5) ET than the histogram from Landsat imagery. In the table of basic statistics in Figure 5.6, the ET map derived from the Landsat 7 image shows a higher maximum and standard deviation than the one derived from the MODIS images. However, the mean values of Landsat- and MODIS-based ET images are very similar. The minimum value of ET in each image equals to zero.

June 16, 2002		September 14, 2000	
Landsat 30m	MODIS 250m	Landsat 30m	MODIS 250m

ET [mm/d]
- 0.0
- < 1.0
- < 2.0
- < 3.0
- < 4.0
- < 5.0
- < 6.0
- < 7.0
- < 8.0
- > 8.0

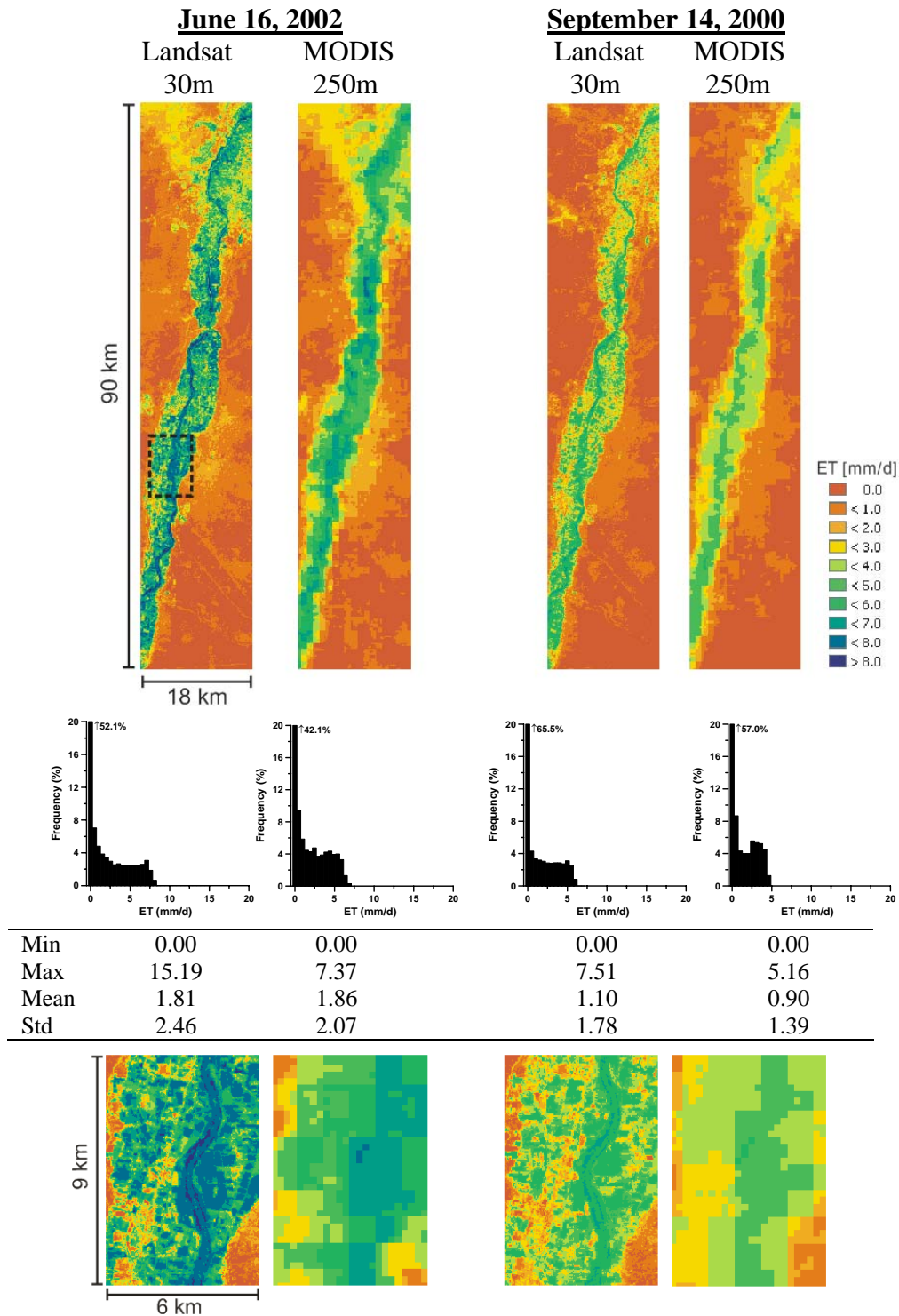|				
Min	0.00	0.00	0.00	0.00
Max	15.19	7.37	7.51	5.16
Mean	1.81	1.86	1.10	0.90
Std	2.46	2.07	1.78	1.39

Figure 5.6. Landsat (30 m) and MODIS (250 m) derived ET by SEBAL of June and September. Bin size of the histogram is 0.5 mm/d and frequency occurrence exceeding 20% marked next to the arrow. The histograms and basic statistics are based on the entire maps (18 km x 90 km). Enlarged areas (9 by 6 km) shown at the bottom correspond to the dotted square of the upper images.

Difference images between the Landsat-based ET at 30m resolution and MODIS-based ET at 250m resolution show how these products are dissimilar to each other (Figure 5.7). Each difference image was produced by subtracting MODIS-based ET from Landsat-based ET [$ET_{Landsat} - ET_{MODIS}$], with brown-colored pixels in the difference map in Figure 5.7 representing points where the MODIS-based ET is significantly higher than Landsat-based ET. Blue-colored pixels represent points where the ET from Landsat is significantly higher than the ET from MODIS imagery. Areas with apparently high ET differences (> +2.0 or < -2.0 mm/d) shown as brown or blue, are observed along the boundary between Rio Grande River riparian areas and surrounding deserts. These high differences are mostly due to (1) disagreement in image georeferencing between the Landsat and MODIS imagery and (2) differences resulting from subtracting the ET value of a large (250m) MODIS based pixel from that of a small (30m) Landsat based pixel.

It is not trivial to generate georeferenced imagery with error of less than one pixel (Eugenio and Marqués, 2003). The georeferencing of two maps with spatial resolutions differing an order of magnitude is especially difficult (Liang et al., 2002). One or two pixels of georeferencing disagreement can cause abrupt ET changes at the boundaries between riparian (high ET) and desert (low ET) areas. The effect of different pixel sizes is clearly demonstrated with the brown and blue pixels located along the sudden transition from riparian area to desert. The brown-colored pixels (ET difference < -2 mm/d) are located in the desert and result from subtracting a large MODIS pixel located partially in the riparian area with relatively high ET from a small Landsat pixel located in the desert with zero ET. The blue-colored pixels (ET difference > 2 mm/d) are located in

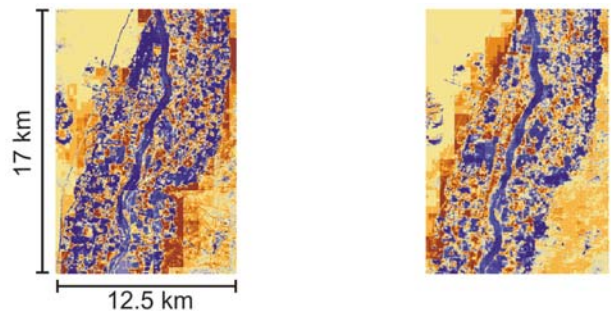**Difference map: [ET$_{Landsat}$ – ET$_{MODIS}$]**
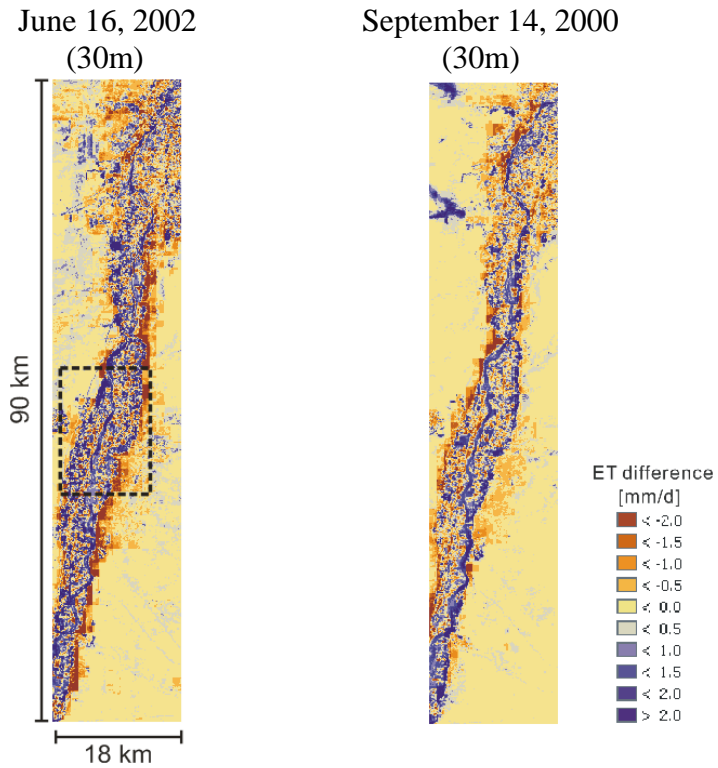
Figure 5.7. ET difference map (30 m) between the Landsat estimated ET (30m) and the MODIS estimate ET (250m). (note: mean and standard deviation (STD) are calculated with the absolute difference). Enlarged areas (12.5 by 17 km) shown at the bottom correspond to the dotted square of the upper images.

the riparian area and result from subtracting a large MODIS pixel located partially in the desert from a riparian area located small Landsat pixel.

Basic statistics (mean and standard deviation) allow a quantitative means of comparison and evaluation. Positive and negative differences due to georeferencing disagreement between two images tend to cancel each other in these calculations since they occur in opposite directions at both sides of the transgression from riparian to desert area. Therefore the mean and standard deviation of each difference image were calculated based on the "absolute" difference between Landsat- and MODIS-based ET images. For both study dates, the mean and standard deviation of difference between the Landsat and MODIS-based ET are within 1.0 mm/day. Basic statistics in Figure 5.7 show that the September images have a slightly lower mean difference and standard deviation than the June images. However, this does not imply that the September Landsat- and MODIS-based ET images agree better than June images. The difference in basic statistics is caused by the smaller values of the mean and standard deviation of ET rates in the September images.

Relative difference images were produced as well by dividing the absolute difference image by the MODIS derived ET image [$|(ET_{Landsat} - ET_{MODIS})| / ET_{MODIS}$] (Figure 5.8). The relative difference value ranges from zero to infinity. The infinity values occur when the MODIS-based ET is much smaller than the Landsat-based ET. The infinity values were constrained to 1.0 and pixels having zero values either in the MODIS-based ET or in the Landsat-based ET image are also assigned to 1.0 as relative

Relative difference between Landsat estimated ET (30m) and MODIS estimate ET (250m): [|(ET$_{Landsat}$ − ET$_{MODIS}$)| / ET$_{MODIS}$]|

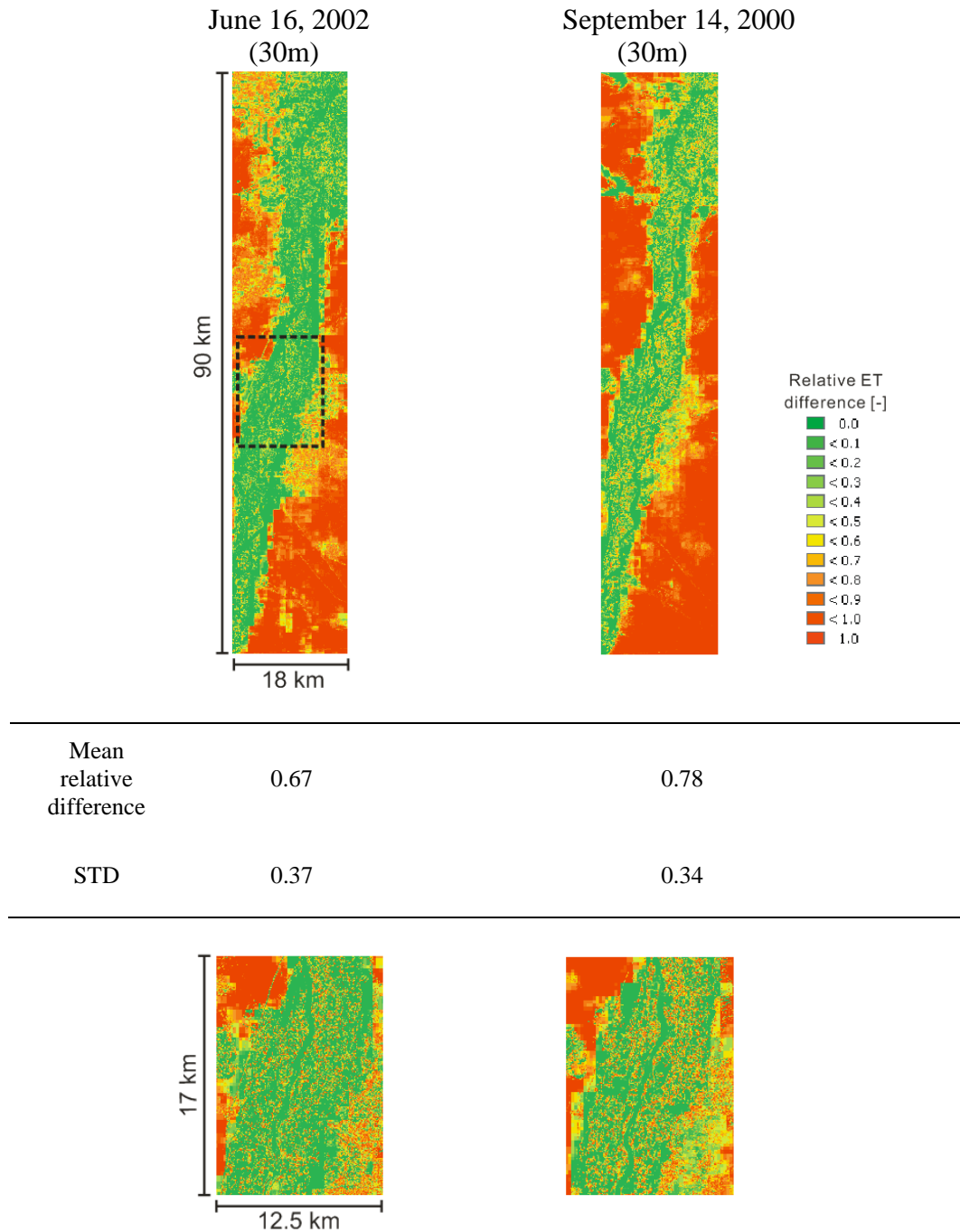|	June 16, 2002 (30m)	September 14, 2000 (30m)
Mean relative difference	0.67	0.78
STD	0.37	0.34

Figure 5.8. Relative difference (30 m) between the Landsat estimated ET (30m) and the MODIS estimate ET (250m) on June 16, 2002. Enlarged areas (12.5 by 17 km) shown at the bottom correspond to the dotted square of the upper images.

difference. Most of the pixels having 1.0 (red-colored) relative difference are located in the desert area. One interesting point is that the quite a few pixels having 1.0 as relative difference are found along the transition zone between riparian and desert areas. Those pixels result from 30 m Landsat pixels having high ET inside 250 m coarse resolution of MODIS pixels having low ET (Figure 5.8).

Figure 5.9 presents three dimensional graphs of the relationship between relative difference and daily ET rate on both June and September images. Both graphs in Figure 5.9 show that large relative difference predominantly occur in areas having low ET while areas having ET such as greater than 3 mm/d exhibit relative differences of about less than 0.4. However, there are some points having 1.0 relative difference with daily ET greater than 2.0 mm/d. These points are resulted from pixels having significant difference between Landsat and MODIS derived ET and mainly due to georeferencing disagreement between Landsat and MODIS satellite images. These questionable points are mostly located in the boundary area between riparian and surrounding desert.

5.3.2. Analysis of Up-scaling Effects

The spatial distribution and its statistical features were evaluated and compared among the four different up-scaling methods across the five aggregation levels. Output up-scaling aggregated the SEBAL estimated daily ET rates either with simple averaging or the nearest neighbor resampling method. The resultant aggregated ET map may represent the best estimate of ET at the coarser resolution, since the aggregated ET was derived directly by aggregation of the fine resolution ET data. For input up-scaling, since
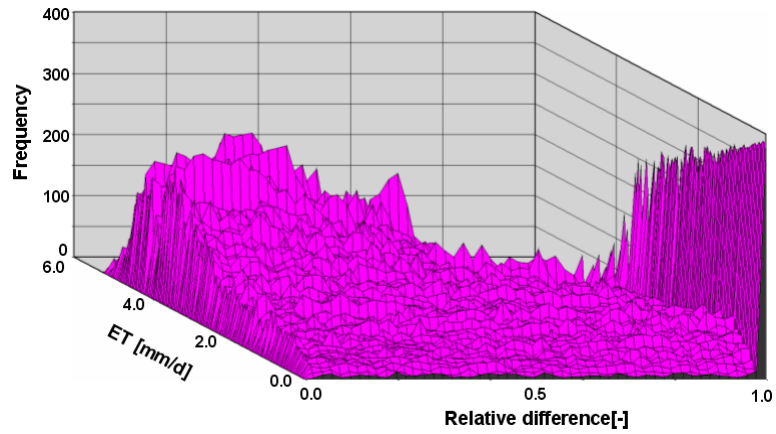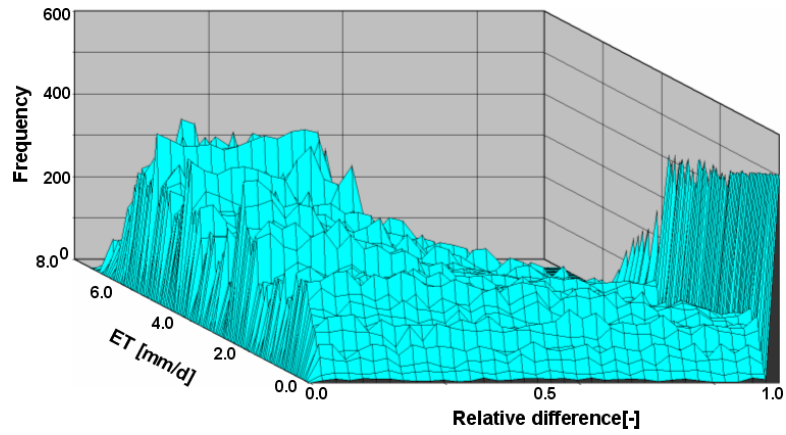
Figure 5.9. 3D frequency plot of the relative difference between Landsat derived ET (30m) and MODIS derived ET (250m) against MODIS derived ET (250m) (top: June 16, 2002 and bottom: September 14, 2000).

the radiometric observations (radiance) or SEBAL model inputs were aggregated, one expects to retrieve the best estimate of a radiometric observation at the coarser resolutions. These aggregated data were used as input to the SEBAL model and calculated daily ET.

The different up-scaling methodologies were evaluated by: (1) spatial distribution of aggregated imagery by four different schemes at each aggregation level to evaluate the changes in spatial pattern after aggregation, and (2) histograms and basic statistics of the aggregated data for different up-scaling schemes at all levels. The spatial details lost during aggregation were considered to be the difference between original image and up-scaled image. In this study difference images were created by subtracting the up-scaled pixels from the original pixels of the Landsat- or MODIS-based ET estimates. While relative difference images were produced by dividing the absolute difference by the original Landsat- and MODIS-based ET images. The statistical and spatial characteristics of differences were evaluated by analyzing the spatial distribution of differences as well as the mean and standard deviation of absolute differences.

5.3.2.1. Effect of aggregation

Spatial and statistical characteristics of up-scaled products from June and September Landsat-based ET maps at 30m resolution to five aggregation levels are presented in Figures 5.10 – 5.13. Figure 5.10 presents ET maps from output up-scaling using simple averaging resampling on June 16, 2002, at spatial resolutions of 60, 120, 250, 500 and 1000m. This method produces the most statistically and spatially

Output up-scaling with simple averaging on June 16, 2002
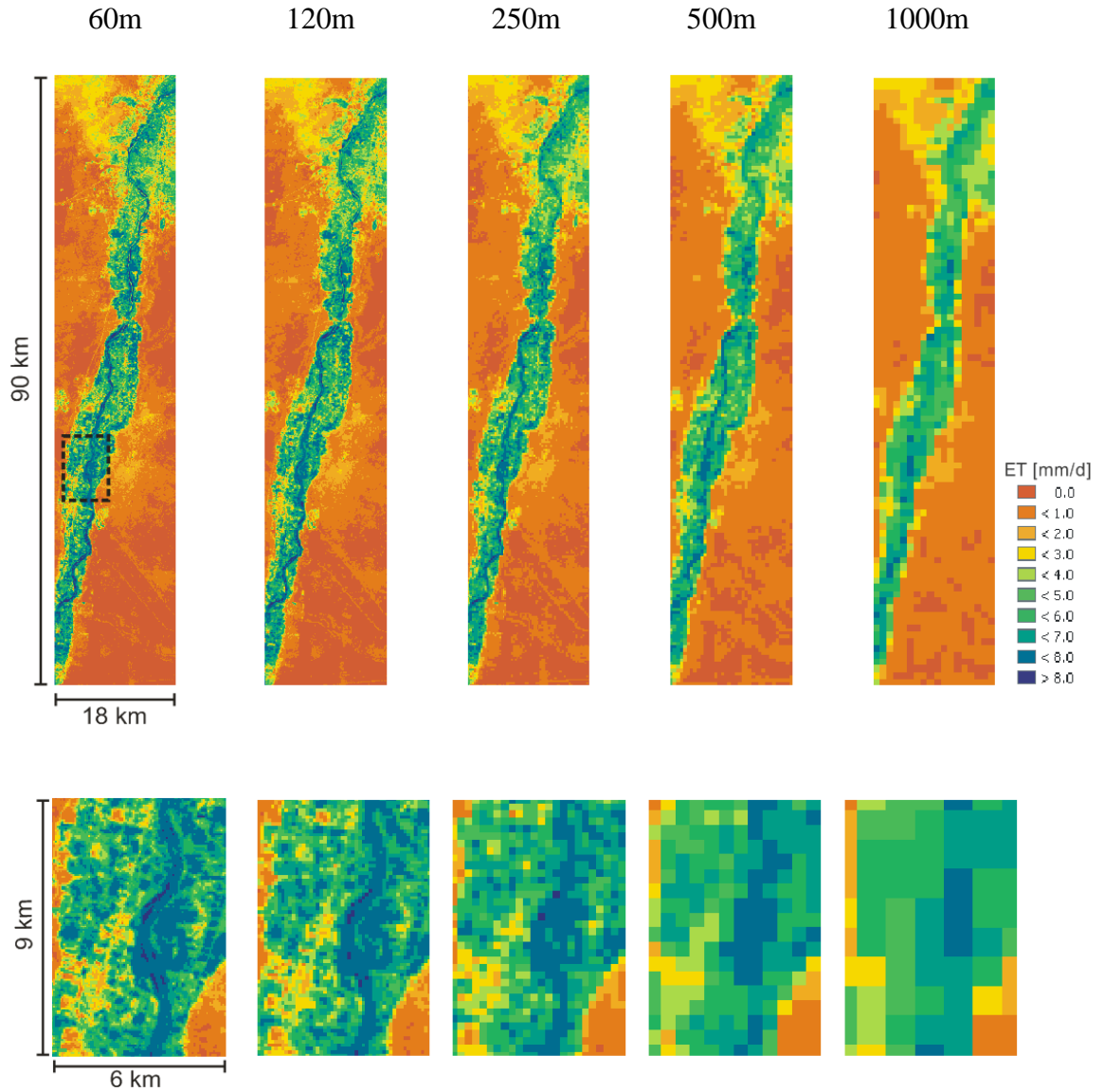
Figure 5.10. ET maps from output up-scaling using simple averaging resampling on June 16, 2002. Spatial resolutions are 60, 120, 250, 500 and 1000 m from the left. This method produces the most statistically and spatially predictable behavior.

Input up-scaling using nearest neighbor on June 16, 2002
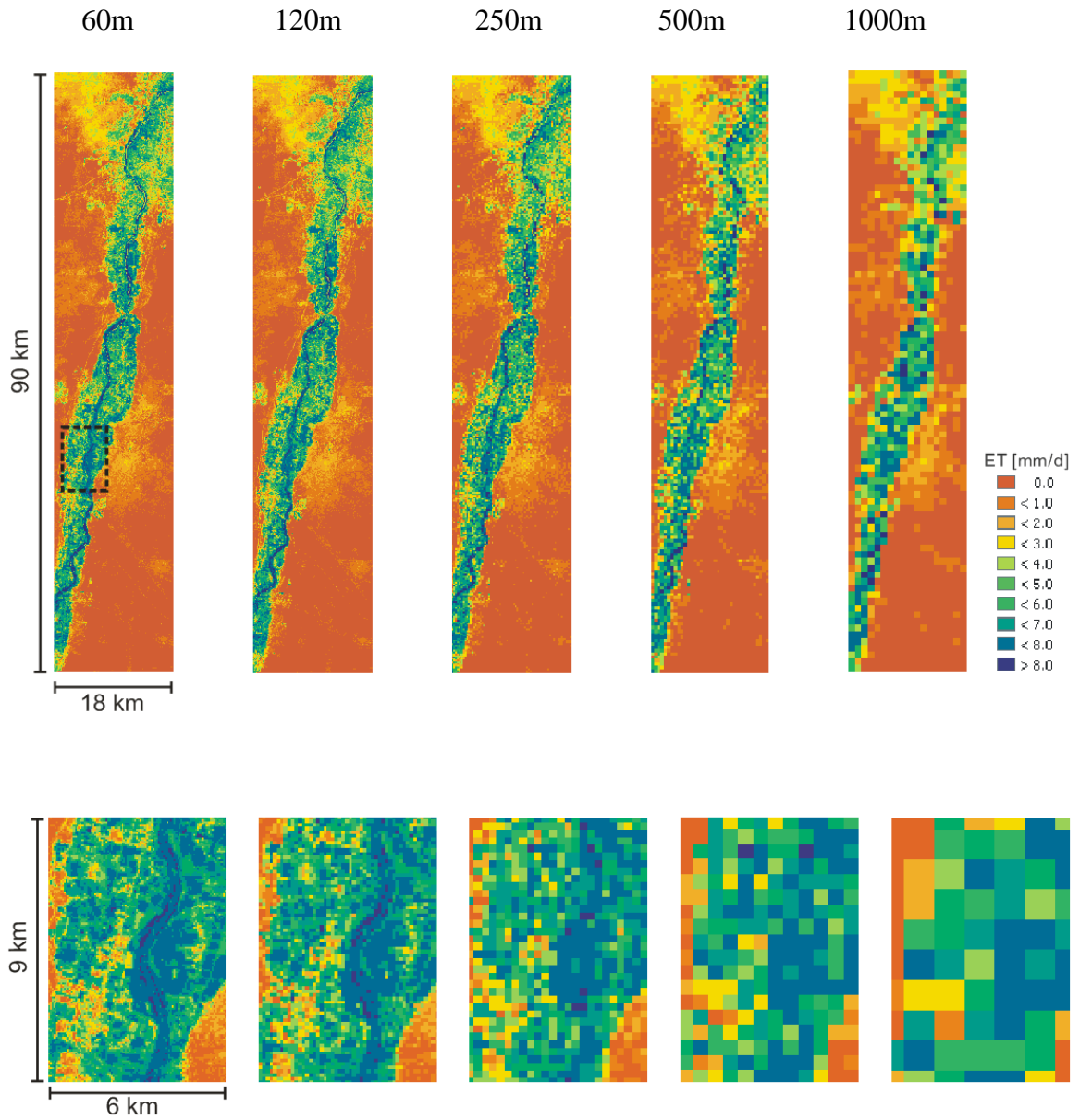
Figure 5.11. ET maps from input up-scaling using nearest neighbor resampling on June 16, 2002. Spatial resolutions are 60, 120, 250, 500 and 1000 m from the left. This method produces the least predictable behavior but is still acceptable.

Output up-scaling with simple averaging on **June 16, 2002**
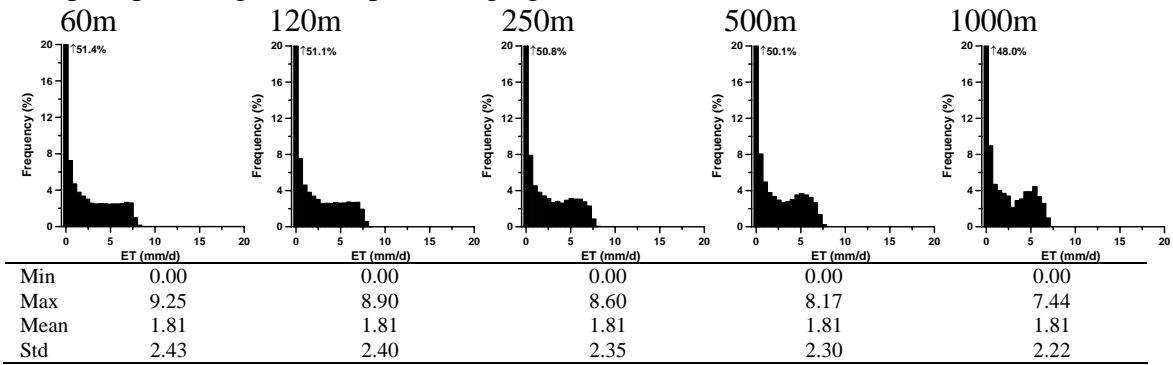
	60m	120m	250m	500m	1000m

Min	0.00	0.00	0.00	0.00	0.00
Max	9.25	8.90	8.60	8.17	7.44
Mean	1.81	1.81	1.81	1.81	1.81
Std	2.43	2.40	2.35	2.30	2.22

Output up-scaling using nearest neighbor

Min	0.00	0.00	0.00	0.00	0.00
Max	9.38	9.02	8.78	8.56	8.53
Mean	1.81	1.81	1.81	1.81	1.79
Std	2.46	2.46	2.46	2.46	2.45

Input up-scaling using simple averaging

Min	0.00	0.00	0.00	0.00	0.00
Max	9.26	8.92	8.57	8.28	7.81
Mean	1.81	1.82	1.84	1.84	1.85
Std	2.47	2.47	2.47	2.46	2.44

Input up-scaling using nearest neighbor

Min	0.00	0.00	0.00	0.00	0.00
Max	9.26	8.92	8.57	8.28	7.81
Mean	1.81	1.82	1.84	1.84	1.85
Std	2.47	2.47	2.47	2.46	2.44
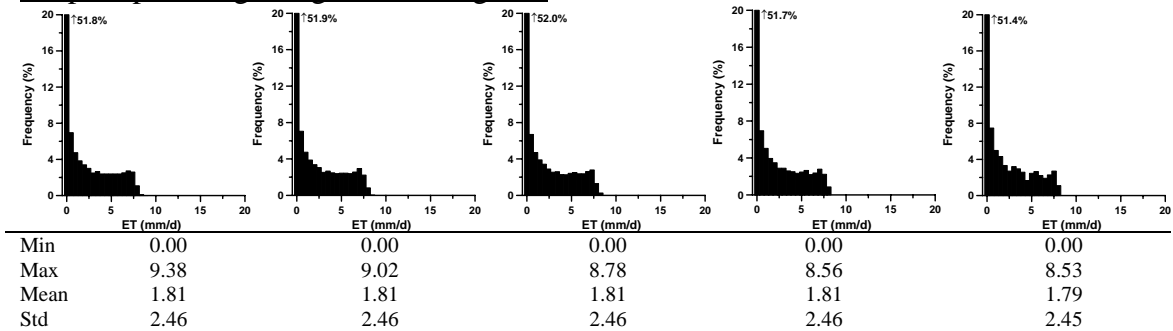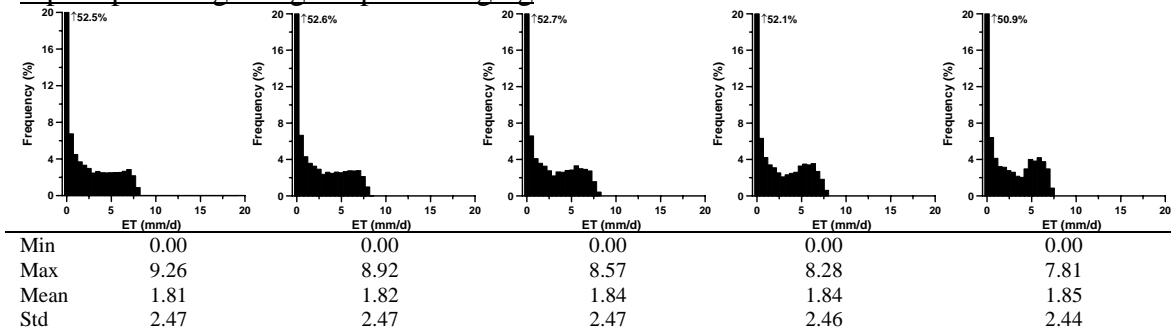
Figure 5.12. Frequency distribution and basic statistics of up-scaled maps on June 16, 2002. Bin size of the histogram is 0.5 mm/d and frequency occurrence exceeding 20% marked next to the arrow.

Output up-scaling using simple averaging on **September 14, 2000**

60m	120m	250m	500m	1000m

	60m	120m	250m	500m	1000m
Min	0.00	0.00	0.00	0.00	0.00
Max	6.43	6.29	6.21	6.05	5.78
Mean	1.10	1.10	1.10	1.10	1.10
Std	1.76	1.74	1.71	1.66	1.60

Output up-scaling using nearest neighbor

Min	0.00	0.00	0.00	0.00	0.00
Max	7.10	6.61	6.48	6.40	6.40
Mean	1.10	1.10	1.10	1.10	1.08
Std	1.78	1.78	1.78	1.78	1.75

Input up-scaling using simple averaging

Min	0.00	0.00	0.00	0.00	0.00
Max	6.40	6.35	6.27	6.19	5.99
Mean	1.10	1.10	1.11	1.11	1.12
Std	1.78	1.77	1.76	1.75	1.71

Input up-scaling using nearest neighbor

Min	0.00	0.00	0.00	0.00	0.00
Max	6.75	6.44	6.43	6.42	6.42
Mean	1.10	1.10	1.09	1.09	1.07
Std	1.78	1.78	1.78	1.78	1.75

Figure 5.13. Frequency distribution and basic statistics of up-scaled maps on September 14, 2000. Bin size of the histogram is 0.5 mm/d and frequency occurrence exceeding 20% marked next to the arrow.

predictable behavior. The least predictable – but still acceptable – behavior is produced
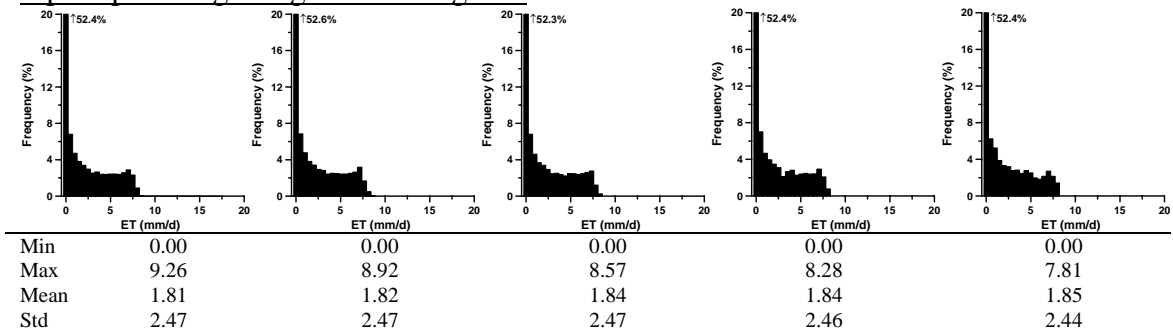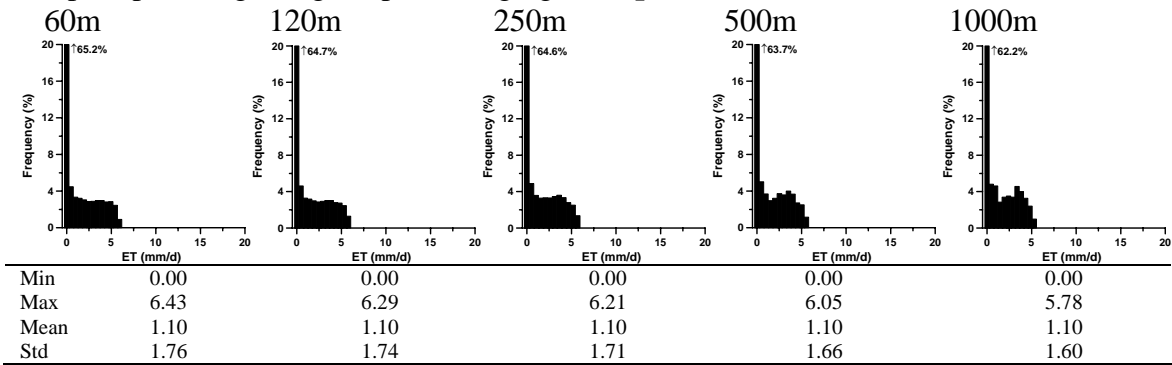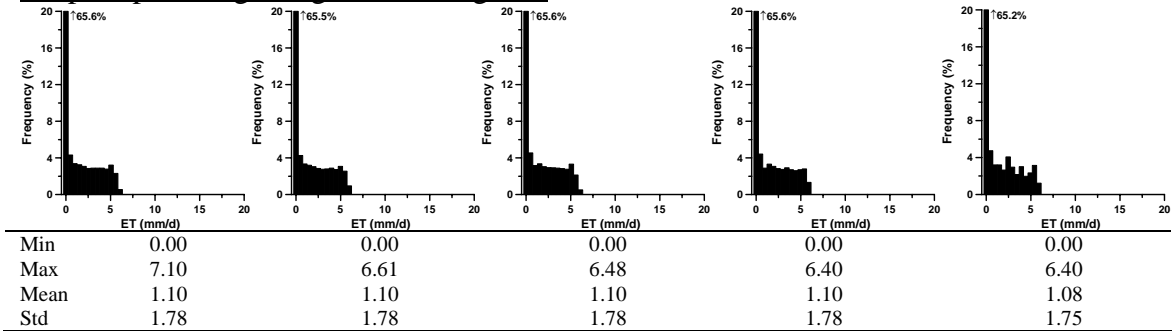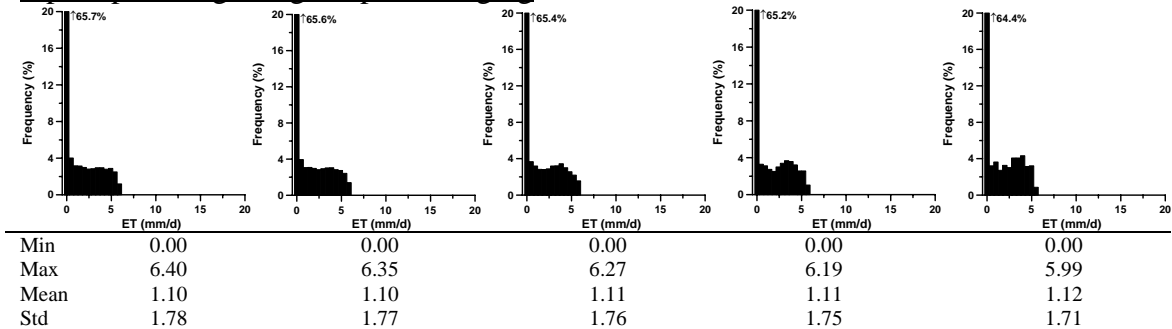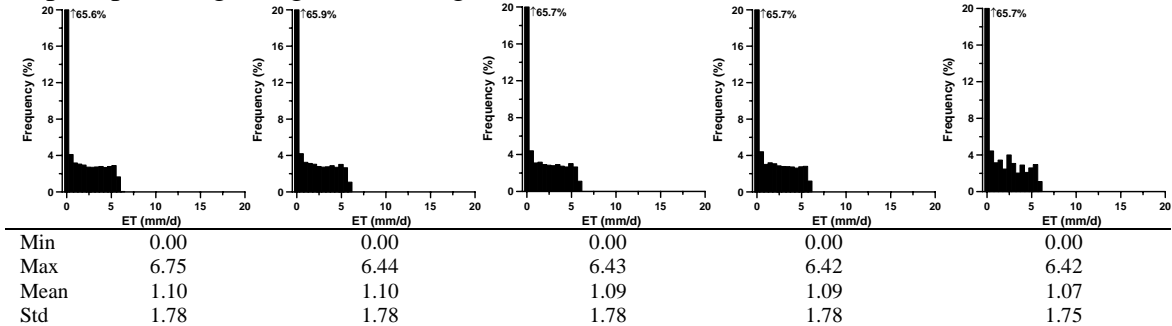
by input up-scaling using nearest neighbor resampling. An example for June 16, 2002 is

presented in Figure 5.11. Figures 5.12 and 5.13 present the histograms and statistics for

the different up-scaling methods on, respectively, June 16, 2002 and September 14, 2000.

Although spatial detail was lost with the increase in pixel size, the overall spatial

distribution of ET of each aggregated map (for example Figures 5.10 and 5.11) was in

agreement with the original ET maps in Figure 5.6.

All histograms of ET distribution (Figures 5.12 and 5.13) show the dominance of

close to zero ET values and this frequency decreases a few percent (3.4 to 1.3%) with

pixel size only when output up-scaling with simple averaging was applied. This feature

might be explained by the observation that desert areas along the riparian corridors are

classified to have zero ET in fine resolution of 30m. However, these desert areas are

easily mixed with riparian areas when applying simple averaging, while nearest neighbor

resampling schemes hardly affect the frequencies in the histogram since nearest neighbor

produces a subset of the original data. The 60 and 120m pixel sized histograms in Figures

5.12 – 5.13 exhibit an almost constant frequency occurrence of 2.0% for June imagery

and 3.0% for September imagery over ET rates ranging from 2.5 to 7.5 mm/d and from

1.0 to 5.0 mm/d, respectively. This constant frequency changes into a concave down

shape as pixel size is increased further with simple averaging resampling in both output

and input up-scaling. That is, the frequency of pixels having 5 – 6 mm/d ET increases but

the frequency of pixels having 3 – 4 mm/d decreases with simple averaging is applied.

Pixels having 5 – 6 mm/d of ET in this study area are mainly surface water, agricultural

fields and riparian vegetation pixels located along the Rio Grande riparian corridor. There are pixels having 3 – 4 mm/d of ET located inside of the riparian corridor as well as in the transition zone between riparian and surrounding desert. These pixels are mostly located along the transition zone between riparian areas and surrounding deserts areas and adjacent to the Rio Grande River. These pixels have low ET, but when averaged with adjacent higher ET pixels the contrast disappears. However, histograms from nearest neighbor resampling stayed rather consistent in shape at each resolution.

The basic statistics and histograms also show the statistical changes through aggregation. With either output up-scaling or input up-scaling, the mean values of the simple averaging and nearest neighbor images remain essentially constant across all aggregation levels in both days. However, ET maps derived using nearest neighbor show a more "blocky" pattern than those derived using from simple averaging (for example Figures 5.10 and 5.11). This difference in spatial distribution is due to the fact that simple averaging decreases the standard deviation with increasing pixel size, while the standard deviation from nearest neighbor aggregation stays fairly constant across all aggregation levels.

The differences in aggregation procedures between simple averaging and nearest neighbor cause the fundamental difference in statistics of the aggregated data. The simple averaging method aggregates based on data values, and the resulting values are confined to the mid range. However, the nearest neighbor resampling is based on location, its pixel value varying with the location of central pixels in new coordinates as the pixel size

changes. Therefore, the aggregated results are a systematically sampled subset of the

original data, and their values are expected to be less confined. This explains the

somewhat larger data ranges for the nearest neighbor resampling method, but the mean of

the data does not change significantly. Many regional-scale hydrological process models

require input parameters over a large area. Direct area averaging technique has often

been used to generate the regional-scale model input parameters (Shuttleworth, 1991;

Chehbouni and Njoku, 1995; Croley et al., 2005; Maayar and Chen, 2006). For example,

direct averaged values of air temperature, precipitation, humidity, surface roughness

length and so on were used as input parameters in hydrologic models (Brown et al., 1993;

Maayar and Chen, 2006). However, the standard deviation of the data set decreases as the

aggregation level increases, therefore users need to check the sensitivity of the range of

the variable of the model prior to applying direct averaging for data aggregation.

In fact, the SEBAL algorithm is nonlinear; that is the mean aggregated ET (output

up-scaled) at any given resolution does not equal the modeled ET value of an aggregated

input value (input up-scaled). However, as demonstrated by visual examination of the

spatial distribution of ET in Figures 5.10 – 5.13, the contrast as well as the basic patterns

(high and low values and their relative locations) of ET between output up-scaling and

input up-scaling show a slight disagreement. A slightly higher mean and standard

deviation was found in the results from input up-scaling with simple averaging than from

output up-scaling with simple averaging; however there is almost no difference between

input and output up-scaling when applying the nearest neighbor method. Overall,

statistical and spatial characteristics produced by input up-scaling show relatively good agreement with those of the output up-scaling method.

5.3.2.2. Difference of aggregated data versus original Landsat (30m) and MODIS (250m) estimated ET

First, aggregation difference was examined by comparing aggregated maps with the original ET map at 30m resolution derived from Landsat imagery. Tables 5.3 and 5.4 present the basic statistics of difference and relative difference against original Landsat derived ET on June 16, 2002 and September 14, 2000 produced by four different up-scaling. The mean values of absolute difference and relative difference range from 0.14 to 0.63 mm/d and from 0.55 to 0.82, respectively.

The mean and standard deviation values of absolute difference from September image are smaller than those from June image. The smaller mean difference and standard deviation is explained by the smaller values of the ET rates in the September image. Mean values of absolute difference from output up-scaled maps are similar with those from input up-scaled maps; however consistently higher standard deviations are found in input up-scaled maps (Tables 5.3 – 5.4). This result confirms that aggregated model output data provide the best estimate of model output at the coarser resolution.

The mean and standard deviation of the absolute differences also increase with pixel size. This is mainly due to the mixed pixel effect. Since aggregation tends to average out the small surface features, the difference between aggregated imagery and the original fine resolution imagery increases with aggregation levels. One interesting

Table 5.3. Basic statistics of the difference [mm/d] between up-scaled ET and original Landsat-based ET (30m). (note: statistics are calculated from absolute value of the difference)

Up-scaling approach	Up-scaling operation	June 16, 2002		September 14, 2000	
		Mean difference	Standard deviation	Mean difference	Standard deviation
Output	AVG_60[1]	0.20	0.34	0.14	0.24
	NN_60[2]	0.18	0.30	0.14	0.28
	AVG_120	0.30	0.48	0.17	0.27
	NN_120	0.32	0.35	0.23	0.33
	AVG_250	0.51	0.79	0.25	0.35
	NN_250	0.32	0.38	0.23	0.35
	AVG_500	0.54	0.81	0.27	0.36
	NN_500	0.38	0.41	0.27	0.36
	AVG_1000	0.63	0.90	0.30	0.38
	NN_1000	0.43	0.43	0.33	0.42
Input	AVG_60	0.28	0.50	0.14	0.25
	NN_60	0.18	0.31	0.15	0.28
	AVG_120	0.29	0.51	0.16	0.28
	NN_120	0.28	0.36	0.23	0.34
	AVG_250	0.53	0.85	0.24	0.36
	NN_250	0.32	0.38	0.23	0.35
	AVG_500	0.54	0.87	0.25	0.37
	NN_500	0.38	0.41	0.28	0.39
	AVG_1000	0.62	0.95	0.28	0.39
	NN_1000	0.43	0.43	0.32	0.42

[1]Aggregated to 60m by simple averaging, [2] Aggregated to 60m by nearest neighbor

Table 5.4. Basic statistics of the relative difference [-] between up-scaled ET and original Landsat-based ET (30m). (note: statistics are calculated from absolute value of the relative difference)

Up-scaling approach	Up-scaling operation	June 16, 2002		September 14, 2000	
		Mean relative difference	Standard deviation	Mean relative difference	Standard deviation
Output	AVG_60[1]	0.55	0.44	0.68	0.42
	NN_60[2]	0.56	0.45	0.69	0.43
	AVG_120	0.58	0.42	0.70	0.40
	NN_120	0.60	0.42	0.73	0.40
	AVG_250	0.64	0.40	0.74	0.37
	NN_250	0.65	0.41	0.75	0.38
	AVG_500	0.64	0.39	0.74	0.37
	NN_500	0.69	0.38	0.78	0.35
	AVG_1000	0.65	0.39	0.76	0.36
	NN_1000	0.72	0.37	0.82	0.32
Input	AVG_60	0.60	0.44	0.70	0.41
	NN_60	0.56	0.45	0.70	0.42
	AVG_120	0.61	0.42	0.71	0.40
	NN_120	0.62	0.42	0.73	0.39
	AVG_250	0.66	0.40	0.76	0.37
	NN_250	0.65	0.41	0.75	0.38
	AVG_500	0.67	0.40	0.76	0.37
	NN_500	0.69	0.39	0.78	0.35
	AVG_1000	0.68	0.39	0.77	0.36
	NN_1000	0.73	0.36	0.82	0.32

[1]Aggregated to 60m by simple averaging, [2] Aggregated to 60m by nearest neighbor

note is that the mean of the relative difference increase with pixel size, however standard deviation actually slightly decreases with pixel size. In this study relative difference is bounded to be not greater than 1.0. Therefore, as mean values increase to approach 1.0, the standard deviation of absolute difference actually decreases with increasing relative difference. Based on the mean and standard deviation of the absolute difference and relative difference, although the difference increases with aggregation levels, the ET of the original images seems to be better preserved from the output up-scaling than input up-scaling.

Both of the 3D frequency plots in Figure 5.14 between up-scaled ET and its relative difference against Landsat-based ET show patterns similar to those in Figure 5.9. That is, relative difference decreases with ET. However, points having 1.0 relative difference with daily ET greater than 1.0 mm/d are greatly diminished in Figure 5.14. In particular, the top portion of Figure 5.14, which shows the relative difference between the output up-scaled ET and the ET obtained from simple averaging, shows very few of these questionable points. In the bottom portion of Figure 5.14, which shows the relative difference between the input up-scaled ET and the nearest neighbor up-scaled ET, there are some points with a relative difference of 1.0, but there are far fewer such points than in Figure 5.9. This indicates that there are fewer georeferencing disagreements between Landsat-derived ET and output up-scaled ET than the one between Landsat and MODIS images.
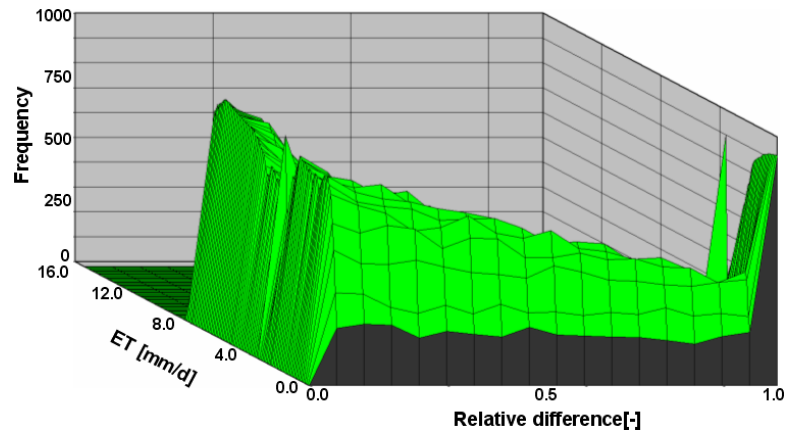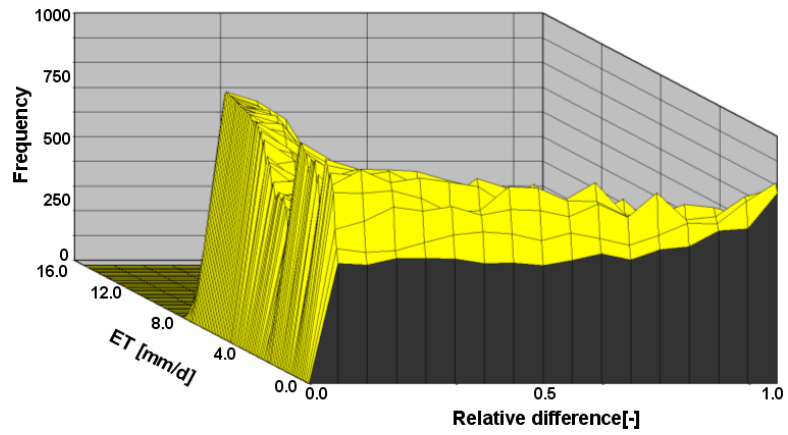
Figure 5.14. 3D frequency plot of the relative difference between up-scaled daily ET (250 m) and Landsat derived ET (30m) on June 16, 2002 against Landsat derived ET (30m) (top: up-scaling output with simple averaging and bottom: up-scaling input with nearest neighbor).

Table 5.5. Basic statistics of the difference [mm/d] and the relative difference [-] of up-scaled ET against original MODIS-based ET (250m). (note: statistics are calculated from absolute value of the difference)

Up-scaling approach	Up-scaling operation	June 16, 2002		September 14, 2000	
		Mean difference	Standard deviation	Mean difference	Standard deviation
Output	AVG_250[1]	0.41	0.39	0.31	0.37
	NN_250[2]	0.46	0.41	0.36	0.41
Input	AVG_250	0.43	0.40	0.32	0.38
	NN_250	0.46	0.41	0.36	0.41
		Mean relative difference	Standard deviation	Mean relative difference	Standard deviation
Output	AVG_250	0.60	0.38	0.71	0.36
	NN_250	0.67	0.37	0.78	0.34
Input	AVG_250	0.65	0.38	0.75	0.36
	NN_250	0.67	0.37	0.78	0.34

[1]Aggregated to 250m by simple averaging, [2] Aggregated to 250m by nearest neighbor

Next, we compare aggregation differences by comparing up-scaled maps at 250m resolution with the original ET map from MODIS. This requires that we first examine which aggregation scheme produces the best match with the original MODIS-based ET and then check the quality of the different aggregation schemes. Landsat-based ET maps at 30 m resolution were aggregated into 250 m resolution maps by applying the four different aggregation schemes already presented in Figure 5.5. Table 5.5 show the basic statistics of the absolute difference and relative difference of images from the four different up-scaling schemes at 250m resolution compared with MODIS-based ET of June and September. The mean and standard deviation of absolute difference and relative difference from output up-scaling with the simple averaging map are smaller than the one from input up-scaling (Table 5.5). Also the simple averaging method generates smaller absolute difference and relative difference than the nearest neighboring method. This implies that output up-scaling with simple averaging map has best agreement with MODIS derived ET. No difference between output and input up-scaling is found from the nearest neighbor aggregation method. As shown in the previous section, the maximum and standard deviation of the ET maps produced by simple averaging are decreased as data were aggregated to 250m resolution. However, the nearest neighbor aggregation method generated images having a similar maximum and standard deviation to the original image (Figures 5.12 – 5.13). This explains why the mean and standard deviation of absolute difference between aggregated Landsat ET image using simple averaging and MODIS-based ET are smaller than from nearest neighbor (Table 5.5).

Although the difference increases with aggregation levels, the ET of

the original images seems to be better preserved with output up-scaling than with input up-scaling. Out of the four different up-scaling procedures, output up-scaling with simple averaging performs best. However, all four aggregation schemes are still acceptable since the mean and standard deviation values of absolute difference are all less than those from the original Landsat ET imagery in Figure 5.7.

5.4.   CONCLUSIONS

Daily evapotranspiration rates were predicted using the SEBAL algorithm from Landsat 7 and MODIS imagery. The objectives of this study were to test the consistency of the SEBAL algorithm for the different satellite sensors and to investigate the effect of various proposed aggregation procedures.

Although ET maps derived from the Landsat 7 images showed higher maximum and standard deviation values than those derived from the MODIS images, the mean values of Landsat- and MODIS-based ET images were very similar. Discrepancy in direct pixel-by-pixel comparison between Landsat- and MODIS-based ET was due to mainly georeferencing disagreement as well as the inherent differences in spatial, spectral and radiometric resolutions between imagery from the different satellite sensors.

The output up-scaling scheme produced slightly better ET maps than the input up-scaling scheme. Both simple averaging and nearest neighbor resampling methods can

preserve the mean values of the original images across aggregation levels. However, the simple averaging resampling method resulted in decreasing standard deviation values as the resolution coarsened, while the standard deviation did not change across aggregation levels with the nearest neighbor resampling method. For difference analysis, large relative differences predominantly occur in areas having low ET (desert and bare soil) while areas having high ET (agricultural field and riparian vegetation) exhibit small relative differences. Out of the four different up-scaling procedures proposed in this study, output up-scaling with simple averaging performs best. However, other aggregation schemes are still acceptable.

ACKNOWLEDGEMENT

REFERENCES

Allen, R.G., L.S. Pereira, D. Raes, and M. Smith. 1998. Crop evapotranspiration. FAO Irrigation and drainage paper 56, FAO. Rome.

Allen, R.G., M. Tasumi, and R. Trezza. 2007. Satellite-based Energy Balance for Mapping Evapotranspiration with Internalized Calibration (METRIC) – Model. Journal of Irrigation and Drainage Engineering, ASCE 133:380-394.

Anselin, L., and A. Getis. 1993. Spatial statistical analysis and geographic information systems Springer-Verlag, New York.

Atkinson, P.M. 1985. Preliminary Results of the Effect of Resampling on Thematic Mapper Imagery. ACSM-ASPRS Fall Convention Technical Papers:929-936.

Bastiaanssen, W.G.M., M. Menenti, R.A. Feddes, and A.A.M. Holtslag. 1998. A remote sensing surface energy balance algorithm for land (SEBAL). Part 1: Formulation. Journal of Hydrology 212-213:198-212.

Bastiaanssen, W.G.M. 2000. SEBAL-based sensible and latent heat fluxes in the Irrigated Gediz Basin, Turkey. Journal of Hydrology 229:87-100.

Bastiaanssen, W.G.M., E.J.M. Noordman, H. Pelgrum, G. Davids, B.P. Thoreson, and R.G. Allen. 2005. SEBAL model with remotely sensed data to improve water-resources management under actual field conditions. Journal of Irrigation and Drainage Engineering 131:85-93.

Bian, L. 1997. Multiscale nature of spatial data in scaling up environment models CRC Press, Inc.

Bian, L., R. Butler, D.A. Quattrochi, and P.M. Atkinson. 1999. Comparing effects of aggregation methods on statistical and spatial properties of simulated spatial data. Photogrammetry and Remote Sensing 65:73-84.

Brown, D.G., L. Bian, and S.J. Walsh. 1993. Response of a distributed watershed erosion model to variations in input data aggregation levels. Computers and Geosciences 19:499-509.

Brutsaert, W. 1982. Evaporation into the atmosphere D. Reidel Pub. Co., Dordrecht, The Netherlands.

Brutsaert, W., and M. Sugita. 1992. Application of self-preservation in the diurnal evolution of the surface energy budget to determine daily evaporation. Journal of Geophysical Research 97:18,377-18,382.

Carmel, Y., J. Dean, and C.H. Flather. 2001. Combining location and classification error sources of estimating multi-temporal database accuracy. Photogrammetric Engineering and Remote Sensing 67:865-872.

Carmel, Y. 2004. Controlling data uncertainty via aggregation in remotely sensed data. IEEE Transaction on Geoscience and Remote Sensing Letters 1:39-41.

Chehbouni, A., and E.G. Njoku. 1995. Approaches for averaging surface parameters and fluxes over heterogeneous terrain. Journal of Climate 8:1386-1393.

Choudhury, B.J., S.B. Idso, and R.J. Reginato. 1987. Analysis of an empirical model for soil heat flux under a growing wheat crop for estimating evaporation by an infrared-temperature-based energy balance equation. Agriculture and Forest Meteorology 39:283-297.

Cihlar, J., H. Ly, Z. Li, J. Chen, H. Pokrant, and F. Hung. 1997. Multi-temporal, Multi-channel AVHRR data sets for land biosphere studies – Artifacts and corrections. Remote Sensing of Environment 60:35-57.

Clothier, B.E., K.L. Clawson, J. P.J. Pinter, M.S. Moran, R.J. Reginato, and R.D. Jackson. 1986. Estimation of soil heat flux from net radiation during growth of alfalfa. Agricultural and Forest Meteorology 37:319-329,.

Compaore, H., J.M.H. Hendrickx, S.-H. Hong, J. Friesen, N.C.v.d. Giesen, C. Rodgers, J. Szarzynski, and P.L.G. Vlek. 2008. Evaporation mapping at two scales using optical imagery in the White Volta Basin, Upper East Ghana. Physics and Chemistry of the Earth 33:127-140.

Cover, T., and P. Hart. 1967. Nearest neighbor pattern classification. IEEE Transactions on Information Theory 13:21- 27.

Crago, R.D. 1996. Conservation and variability of the evaporative fraction during the daytime. Journal of Hydrology 180:173-194.

Croley, I., T. E., C. He, and D.H. Lee. 2005. Distributed-Parameter Large Basin Runoff Model. II: Application. Journal of Hydrologic Engineering 10:182-191

Dai, X.L., and S. Khorram. 1998. The effects of image misregistration on the accuracy of remotely sensed change detection. IEEE Transaction on Geoscience and Remote Sensing 36:1566-1577.

Daughtry, C.S., W.P. Kustas, M.S. Moran, R.D. Jackson, and J. Pinter. 1990. Spectral estimates of net radiation and soil heat flux. Remote Sensing of Environment 32:111-124.

De Cola, L. 1994. Simulating and mapping spatial complexity using multi-scale techniques. International Journal of Geographical Information Systems 8:411-427.

Dodgson, N.A. 1997. Quadratic interpolation for image resampling. IEEE Transactions on Image Processing 6:1322-1326.

Ebleringer, J.R., and C.B. Field. 1993. Scaling Physiological Processes, Leaf to Globe Academic Press, Inc., New York.

ERDAS. 2002. Field Guide 6th ed. Atlanta, Georgia, ERDAS Inc.

Eugenio, F., and F. Marqués. 2003. Automatic Satellite Image Georeferencing Using a Contour-Matching Approach. IEEE Transactions on Geoscience and Remote Sensing 41:2869-2880.

Farah, H.O., W.G.M. Bastiaanssen, and R.A. Feddes. 2004. Evaluation of the temporal variability of the evaporative fraction in a tropical watershed. International Journal of Applied Earth Observation and Geoinformation 5:129-140.

French, A.N. 2001. Scaling of surface energy fluxes using remotely sensed data. PhD Thesis, University of Maryland, College Park.

French, A.N., T.J. Schmugge, and W.P. Kustas. 2002. Estimating evapotranspiration over El Reno, Oklahoma with ASTER imagery. Agronomie 22:105-106.

Gentine, P., D. Entekhabi, A. Chehbouni, G. Boulet, and B. Duchemin. 2007. Analysis of evaporative fraction diurnal behaviour. Agricultural and Forest Meteorology 143:13-29.

Gupta, V.K., I. Rodriguez-Iturbe, and E.F. Wood. 1986. Scale Problems in Hydrology D. Reidel Publishing Company, Boston.

Hendrickx, J.M.H., W.G.M. Bastiaanssen, E.J.M. Noordman, S.-H. Hong, and L.E. Calvo Gobbetti. 2005. Estimation of regional actual evapotranspiration in the Panama Canal watershed using SEBAL, p. 315-323, *In* R. S. Harmon, ed. The Rio Chagres: A multidisciplinary profile of a tropical watershed, Vol. 52. Kluwer Academic Publishers, Dordrecht, The Netherlands.

Hendrickx, J.M.H., and S.-H. Hong. 2005. Mapping sensible and latent heat fluxes in arid areas using optical imagery. Proceedings of International Society for Optical Engineering, SPIE 5811:138-146.

Hendrickx, J.M.H., S.-H. Hong, J. Friesen, H. Compaore, N.C. van de Giesen, C. Rodgers, and P.L.G. Vlek. 2006. Mapping energy balance fluxes and root zone soil moisture in the White Volta Basin using optical imagery. Proceedings of International Society for Optical Engineering, SPIE 6239:238-249.

Hong, S.-H., J.M.H. Hendrickx, and B. Borchers. 2005. Effect of scaling transfer between evapotranspiration maps derived from LandSat 7 and MODIS images. Proceedings of International Society for Optical Engineering, SPIE 5811:147-158.

Kustas, W.P., C.S.T. Daughtry, and P.J.V. Oevelen. 1993. Analytical treatment of the relationships between soil heat flux/net radiation ratio and vegetation indices. Remote Sensing and Environment 46:319-330.

Lam, N., and D.A. Quattrochi. 1992. On the issues of scale, resolution, and fractal analysis in the mapping sciences. Professional Geographer 44:88-98.

Lhomme, J.-P. 1992. Energy balance of heterogeneous terrain: Averaging the controlling parameters. Agricultural and Forest Meteorology 61:11-21.

Li, B., and R. Avissar. 1994. The impact of spatial variability of land-surface characteristics on land-surface fluxes. Journal of Climate 7:527-537.

Liang, S. 2000. Numerical experiments on spatial scaling of land surface albedo and leaf. area index. Remote Sensing Reviews 19:225–242.

Liang, S., H. Fang, M. Chen, C.J. Shuey, C. Walthall, C. Daughtry, J. Morisette, C. Schaaf, and A. Strahler. 2002. Validating MODIS land surface reflectance and albedo products: methods and preliminary results. Remote Sensing of Environment 83:149-162.

Liang, S. 2004. Quantitative Remote Sensing of Land Surfaces John Wiley and Sons, Inc.

Maayar, M.E., and J.M. Chen. 2006. Spatial scaling of evapotranspiration as affected by heterogeneities in vegetation, topography, and soil texture. Remote Sensing of Environment 102:33-51.

Mark, D.M., and P.B. Aronson. 1994. Scale dependent fractal dimensions of topographic surfaces: An empirical investigation with applications in geomorphology and computer mapping. Mathematical Geology 16:671-683.

Mecikalski, J.R., G.R. Diak, M.C. Anderson, and J.M. Norman. 1999. Estimating fluxes on continental scales using remotely-sensed data in an atmospheric-land exchange model. Journal of Applied Meteorology 38:1352-1369.

Mengelkamp, H.-T., F. Beyrich, G. Heinemann, F. Ament, J. Bange, F. Berger, J. Bösenberg, T. Foken, B. Hennemuth, C. Heret, S. Huneke, K.-P. Johnsen, M. Kerschgens, W. Kohsiek, J.-P. Leps, C. Liebethal, H. Lohse, M. Mauder, W. Meijninger, S. Raasch, C. Simmer, T. Spieß, A. Tittebrand, J. Uhlenbrock, and P. Zittel. 2006. Evaporation Over A Heterogeneous Land Surface. Bulletin of the American Meteorological Society 87:775-786.

Moran, M.S., R.B. Jackson, L.H. Raymond, L.W. Gay, and P.N. Slater. 1989. Mapping surface energy balance components by combing Landsat Thematic Mapper and ground-based meteorological data. Remote Sensing of Environment 30:77-87.

Morse, A., M. Tasumi, R.G. Allen, and W.J. Kramer. 2000. Application of the SEBAL methodology for estimating consumptive use of water and streamflow depletion

in the Bear river basin of Idaho through remote sensing. Final report submitted to the Raytheon Systems Company, Earth Observation System Data and Information System Project, by Idaho Department of Water Resources and University of Idaho.

Nellis, M.D., and J.M. Briggs. 1989. The effect of spatial scale on Konza landscape classification using textural analysis. Landscape Ecology 2:93-100.

Nishida, K., R.R. Nemani, S.W. Running, and J.M. Glassy. 2003. An operational remote sensing algorithm of land surface evaporation. Journal of Geophysical Research 108 (D9):doi:10.1029/2002JD002062.

Price, J.C. 1984. Land surface temperature measurements from the split window channel of the NOAA 7 Advanced Very High Resolution Radiometer. Journal of Geophysical Research 89:7231-7237.

Quattrochi, D.A., and M.F. Goodchild. 1997. Scale, multiscaling, remote sensing, and GIS Lewis Publishers, New York.

Seguin, B., J.-P. Lagouarde, and M. Saranc. 1991. The assessment of regional crop water conditions from meteorological satellite thermal infrared data. Remote Sensing of Environment 35:141-148.

Seyfried, M.S., and B.P. Wilcox. 1995. Scale and the nature of spatial variability: Field examples having implications for hydrologic modeling. Water Resources Research 31:173 - 184.

Shuttleworth, W.J., R.J. Gurney, A.Y. Hsu, and J.P. Ormsby. 1989. The variation in energy partition at surface flux sites. Proceedings of the IAHS Third International Assembly, Baltimore, MD. 186:67-74.

Shuttleworth, W.J. 1991. The modllion concept. Review of Geophysics 29:585-606.

Stoms, D. 1992. Effects of habitat map generalization in biodiversity assessment. Photogrammetric Engineering and Remote Sensing 58:1587-1591.

Tasumi, M., R.G. Allen, and W.G.M. Bastiaanssen. 2000. The theoretical basis of SEBAL. Appendix A of Morse et al. (2000). Idaho Department of Water Resources, Idaho.

Tasumi, M. 2003. Progress in operational estimation of regional evapotranspiration using satellite imagery, Ph.D. Thesis, University of Idaho, Moscow, Idaho.

Townshend, J.R.G., C.O. Justice, C. Gurney, and J. McManus. 1992. The impact of misregistration on change detection. IEEE Transaction on Geoscience and Remote Sensing 30:1054-1060.

Turner, M.G., R.V. O'Neil, R.H. Gardner, and B.T. Milne. 1989. Effects of changing spatial scale on the analysis of landscape pattern. Landscape Ecology 3:153-162.

Ulivieri, C., M.M. Castromouvo, R. Francioni, and A. Cardillo. 1992. A split window algorithm for estimating land surface temperature from satellite. Advances in Space Research 14.

Van Rompaey, A.J.J., G. Govers, and M. Baudet. 1999. A strategy for controlling error of distributed environmental models by aggregation. International Journal of Geographical Information Science 13:577-590.

Vazquez, D.P., F.J. Olmo Reyes, and L.A. Arboledas. 1997. A comparative study of algorithms for estimating land surface temperature from AVHRR data. Remote Sensing of Environment 62:215-222.

Vieux, B.E. 1993. DEM Aggregation and smoothing effects on surface runoff modeling. Journal of Computing in Civil Engineering 7:310-338.

Wolock, D.M., and C.V. Price. 1994. Effects of digital elevation model map scale and data resolution on a topography-based watershed model. Water Resources Research 40:3041-3052.

Zhang, W., and D.R. Montgomery. 1994. Digital elevation model grid size, landscape representation, and hydrologic simulations. Water Resources Research 30:1019-1028.

CHAPTER 6

DOWN-SCALING OF SEBAL DERIVED EVAPOTRANSPIRATION MAPS FROM MODIS (250m) TO LANDSAT (30m) SCALE

ABSTRACT

In the selection of satellite sensor imagery, there exists a trade-off between spatial and temporal resolution. The major problem with high spatial resolution satellite images like Landsat 7 is that imagery is not available very often (i.e. every 16 days or longer) and the coverage area is relatively small (swath width 185 km), while satellites of lower spatial resolution like MODIS are revisiting the same part of the Earth more often (daily) and one image covers a relatively large area (swath width 2,330 km). This paper considers the feasibility of applying various down-scaling methods to improve the spatial resolution of MODIS imagery to Landsat scale in order to obtain both high temporal and high spatial resolution. The Surface Energy Balance Algorithm for Land (SEBAL) was used to derive daily evapotranspiration distributions from Landsat 7 and MODIS images.

Landsat 7 has a spatial resolution of 30 to 60 m, and MODIS has a resolution of 250, 500 and 1000 m.

Two down-scaling procedures were evaluated: input down-scaling and output down-scaling. Input down-scaling consisted of disaggregating 250 m MODIS scale pixels of surface albedo, *NDVI*, and surface temperature values to obtain pixels at the 30m Landsat scale prior to applying the SEBAL algorithm to estimate daily evapotranspiration. Output down-scaling consisted of disaggregating SEBAL estimated daily evapotranspiration from MODIS to Landsat pixel scale. Disaggregation imagery was obtained by two different processes: (1) applying the difference between two MODIS scale images to previous or subsequent Landsat scale product covering the same area by assuming the fine scale variability of the area of interest is constant; (2) applying linear regression between two MODIS scale products to previous or subsequent Landsat scale product. The primary objective of this study was to investigate the effect of the different down-scaling schemes on the spatial distribution of SEBAL derived daily evapotranspiration, particularly how the relative accuracy of evapotranspiration changes with spatial resolution. This study shows that all of the 12 proposed down-scaling methodologies can generate reasonable spatial patterns of the disaggregated evapotranspiration map. Among the 12 different down-scaling schemes, the output down-scaling with regression between two MODIS-based images is the most preferred scheme and input down-scaling with subtraction between MODIS and aggregated (nearest neighboring) Landsat is the least preferred scheme.

6.1. INTRODUCTION

Monitoring surface characteristics with remote sensing data is dependent upon the relationship between the spatial resolution of the sensor (pixel size) and the scale of the surface features. The spatial resolution of each type of remote sensing imagery is among the most distinctive characteristics of the sensors. In order to assess the capabilities and the potential of remote sensing models, the remote sensing estimated surface flux estimates need to be compared against ground measurements (Valor and Caselles, 1996; Justice et al., 2000; Rigo et al., 2006). However, one of the major problems in validation of remote sensing estimates is the difference in spatial scale between ground point measurements and the spatial resolution of the remote sensing imagery (Ma et al., 2003; Liang, 2004). Moderate Resolution Imaging Spectroradiometer (MODIS) images provide useful opportunities to monitor the energy balance at meso-scale, but they cannot directly provide field specific data. Since most ground measurements are taken at the point/plot scale with footprints often not exceeding 100m, accurate validation of MODIS remote sensing evapotranspiration estimates can only be done using finer spatial resolution images like Land Satellite (Landsat) and Advanced Spaceborne Thermal Emission and Reflection Radiometer (ASTER).

Another issue in validation of remote sensing model flux estimates is that the remotely sensed imagery needs to be accurately georeferenced. The georeferencing is the image-processing technique to match the geolocation between remotely sensed image pixels and physical positions on the Earth surface. In fact the spatial accuracy of the

georeferenced images is dependent upon the accuracy of Ground Control Points (GCPs) and the mathematical transformation algorithm at the processing level (Schowengerdt, 1997; Carrion et al., 2002; Eugenio and Marqués, 2003). However, even the most sophisticated model cannot generate georeferenced imagery with errors of less than one pixel (Eugenio and Marqués, 2003). For example, the accuracy of the georeferenced 30m resolution Landsat imagery produced by professionals is still around 50m (personal communication with technician in MDA Federal Inc.). Therefore, there is difficulty in comparing flux estimates between remote sensing model and ground measurements; especially when the spatial scale of ground measurements is less than one or two pixel size.

Routine monitoring of surface conditions with high spatial resolution satellite data is difficult due to the long return period between successive satellite overpasses. Although the temporal resolution of Landsat is 16 days, even in arid regions only monthly coverage is a reasonable expectation for the availability of clear high-resolution satellite images due to periodic cloud cover (Moran et al., 1996). High-temporal resolution (daily or more frequent) but coarser spatial resolution satellite data including MODIS, Advanced Very High Resolution Radiometer (AVHRR) and Geostationary Orbiting Environmental Satellite (GOES) have therefore been used to conduct routine ET monitoring (e.g. Mecikalski et al., 1999; Sequin et al., 1991). Coarse resolution images like MODIS provide very useful opportunities to monitor the surface conditions at meso-scale with manageable amounts of data; however, they cannot directly provide detailed field-specific data. For the purpose of monitoring land cover changes accurately, thermal

band pixels of size less than 500 m are required (Townshend and Justice, 1988). Therefore, down-scaling from MODIS to Landsat scale is a very useful technique to combine the advantages of high temporal and spatial resolutions of surface conditions.

Down-scaling is defined as an increase in spatial resolution following disaggregation of the original data set (Bierkens et al., 2000; Liang, 2004). The process of down-scaling accomplishes a restoration of the variation at a specific scale by assuming that the values of the larger scale are the average of the values at the finer scale and that more uncertainties exist in down-scaled products than up-scaled products because infinite solutions of down-scaled products are possible (Bierkens et al., 2000). Down-scaling is generally required for the use of available information at a desired fine resolution (Price et al., 2000; Maayar and Chen, 2006). Traditionally, various down-scaling procedures have been tested in the fields of meteorology and climatology to obtain local climatological information from coarse-resolution remote sensing imagery, but only a few studies have applied disaggregation schemes to surface parameters to increase resolution (Liang, 2004).

In this study, high quality Landsat 7 and Terra MODIS images (Figure 6.1) were selected to test various down-scaling procedures. Disaggregated daily ET rates from MODIS imagery were compared with the ET rates derived from Landsat imagery. SEBAL-estimated daily ET from Landsat imagery was validated against ground-based eddy covariance measurements in previous research, demonstrating very good agreement

Landsat 7   MODIS

New Mexico

Landsat
Path 33: Row 36

Study area

City of Albuqueruqe
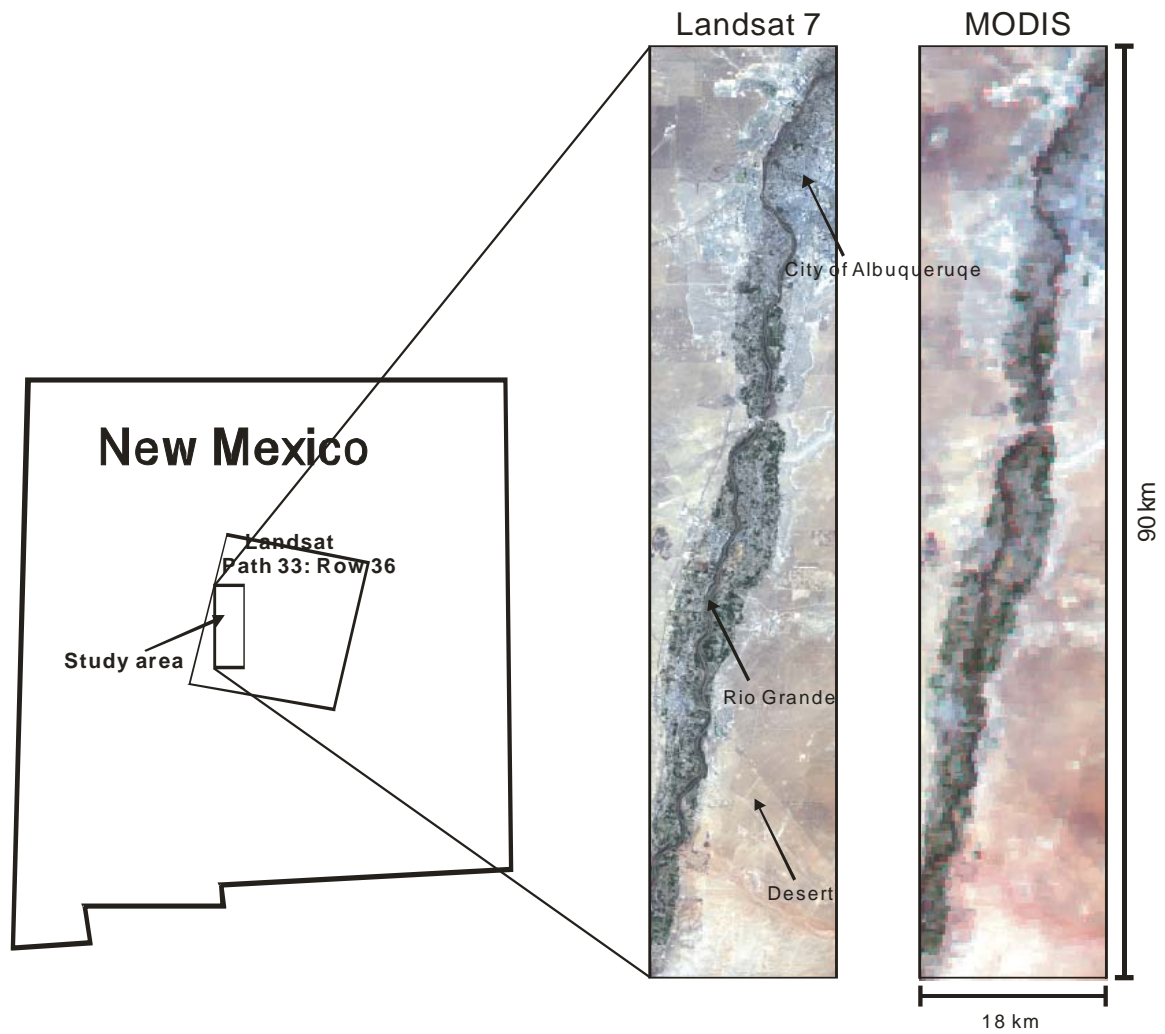
Rio Grande

Desert

90 km

18 km

Figure 6.1. Location of the study area (18km by 90km). True color Landsat 7 (30 m by 30 m resolution) and MODIS (250 m by 250 m resolution) images on June 16, 2002.

(Hendrickx and Hong, 2005). The primary objective of this research was to investigate the effect of various relatively simple down-scaling schemes on the spatial distribution of the SEBAL-derived daily ET rate, especially how the relative accuracy of ET changes with increasing spatial resolution. In the next section we provide a brief review of some existing down-scaling procedures.

6.2.   PREVIOUS RESEARCH ON DOWN-SCALING

In the last decade many studies have examined the effects of spatial resolution on surface characteristic representation, but information on down-scaling is limited since most studies have examined up-scaling procedures only (Nellis and Briggs, 1989; Turner et al., 1989; Lam and Quattrochi, 1992; Stoms, 1992; Brown et al., 1993; Vieux, 1993; De Cola, 1994; Mark and Aronson, 1994; Wolock and Price, 1994; Zhang and Montgomery, 1994; Bian et al., 1999).

In this section, several widely-used down-scaling procedures using remote-sensing imagery are presented. Each technique has achieved a certain amount of success at increasing spatial-resolution. Most previous research regarding down-scaling using remote sensing imagery has focused on attempting to disaggregate the land cover information. Among the most popular techniques for disaggregation of land cover are artificial neural networks (Kanellopoulos et al., 1992; Atkinson and Tatnall, 1997), mixture modeling (Settle and Drake, 1993; Kerdiles and Grondona, 1996), and supervised fuzzy c-means classification (Bezdek et al., 1984; Foody and Cox, 1994).

These techniques have been successfully applied to estimate the proportions of specific

classes that occur within each pixel. While this disaggregation information expressed

land cover composition, it did not provide any indication of spatial location within the

pixel. Atkinson (1997) proposed an idea for an alternative methodology called "sub-pixel

mapping". The proposed technique aimed to determine where the relative proportions of

each class are most likely to occur. The major assumption of this technique related to the

spatial dependence within and between pixels. The results showed a significant

improvement in the accuracy of land classification.

Several down-scaling techniques have been proposed for merging panchromatic

and multispectral data (for example, the combination of 10 m resolution of SPOT

panchromatic data with 30 m resolution of Landsat TM imagery). The most common

procedures for this technique include the intensity-hue-saturation transform based

methods (IHS), principal component analysis (PCA), and the Brovey transform.

However, those methods require complicated computations and time-consuming

processing. Detailed information can be found in several papers (Carper et al., 1990;

Chavez et al., 1991; Shettigara, 1992; Yocky, 1995; Zhou et al., 1998).

More recently, a sharpening thermal imagery algorithm called DisTrad was

introduced by Kustas et al. (2003). DisTrad sharpens thermal band data to that of the

VIS/NIR bands by using the relationship between radiometric surface temperature and

the Normalized Difference Vegetation Index (*NDVI*). The DisTrad technique is based on

fitting a second order polynomial between radiometric surface temperature (T_{rad}) and the

aggregated *NDVI* to the resolution of T_{rad}. Disaggregated sensible heat flux fields

estimated by the DisTrad technique using Landsat 7 imagery agreed with ground

measured fluxes to within 10 % (Anderson et al., 2004). Most of the very-fine resolution

(< 5 m) satellites like IKONOS and Quickbird do have VIS/NIR bands but do not have

thermal bands. DisTrad can generate IKONOS resolution for thermal imagery with

additional information. For example, since IKONOS provides 1.0 m resolution *NDVI*, 1.0

m resolution of thermal imagery can be generated with thermal imagery from other

sensors like Landsat and MODIS. DisTrad also can be a useful tool for disaggregating 60

m Landsat thermal imagery to 30 m resolution or 1000 m MODIS thermal imagery to

250 m resolution. However, it is not very practical to use DisTrad to disaggregate

MODIS resolution data to Landsat resolution since Landsat already has a thermal band.

6.3.   METHOD AND MATERIALS

6.3.1. Study Area and Satellite Imagery

The study area covers a portion of the Middle Rio Grande Valley in New Mexico

(Figure 6.1). The Middle Rio Grande setting is composed of agricultural fields and

riparian vegetation. The regional climate is classified as arid/semiarid; its annual

precipitation distribution is bimodal, with more than half of the rainfall due to monsoonal

patterns in the summer, although the proportion varies considerably from year to year.

The average annual air temperature is 15 °C. Summer daily temperatures range from 20

to 40 °C, while winter daily temperatures range from -12 to 10 °C. Mean annual

precipitation is about 25 cm and mean annual potential ET is approximately 170 cm. (Stromberg, 1998; Costigan et al., 2000; Scott et al., 2000; Cleverly et al., 2002; Elmore et al., 2002).

Clear-sky Landsat 7 and MODIS imagery from May 31 and June 16, 2002 was selected for the investigation of the effect of down-scaling processes. Table 6.1 shows the spectral bands of Landsat 7 and MODIS in the visible, near infrared and thermal infrared wavelength regions used for SEBAL application. These four satellite images were georeferenced to closely match the spatial coordinates each other. This was done by identifying several accurate Ground Control Points (e.g. road intersections and agricultural field boundaries) on the images and aligned them to fit on the images. The images used in this study covered an 18 km x 90 km area of the Middle Rio Grande Basin from city of Albuquerque to the Sevilleta LTER (Figure 6.1).

6.3.2. Surface Energy Balance Algorithm for Land (SEBAL)

SEBAL is a remote sensing flux algorithm that solves the surface energy balance on an instantaneous time scale and for every pixel of a satellite image (Bastiaanssen et al., 2005; Hendrickx and Hong, 2005; Allen et al., 2007). The method is based on the computation of surface albedo (α), surface temperature (T_s), and *NDVI* from multi-spectral satellite data (Figure 6.2). The albedo was calculated from visible to mid-infrared bands (Landsat 7: bands 1-5 and 7; MODIS: bands 1-4, 6 and 7); the T_s from thermal-infrared bands (Landsat 7: band 6; MODIS: bands 31 and 32); the *NDVI* from red and near-infrared bands (Landsat 7: bands 3 and 4; MODIS: bands 1 and 2). The albedo was

Table 6.1. Band spatial resolutions (m) and wavelengths (μm) of Landsat 7 and MODIS sensors.

Sensors		Band number								
		1	2	3	4	5[#]	6	7	31	32
Landsat 7	Pixel size [m]	30	30	30	30	30	60	30	NA*	NA*
	Band width [μm]	0.45–0.51	0.52–0.60	0.63–0.69	0.75–0.9	1.55–1.75	10.4–12.5	2.09–2.35	NA*	NA
MODIS	Pixel size [m]	250	250	500	500	500	500	500	1000	1000
	Band width [μm]	0.62–0.67	0.84–0.87	0.46–0.48	0.54–0.56	1.23–1.25	1.63–1.65	2.11–2.15	10.8–11.3	11.8–12.3

[#]MODIS band5 is not used in this study because of streaking noise, *Not available
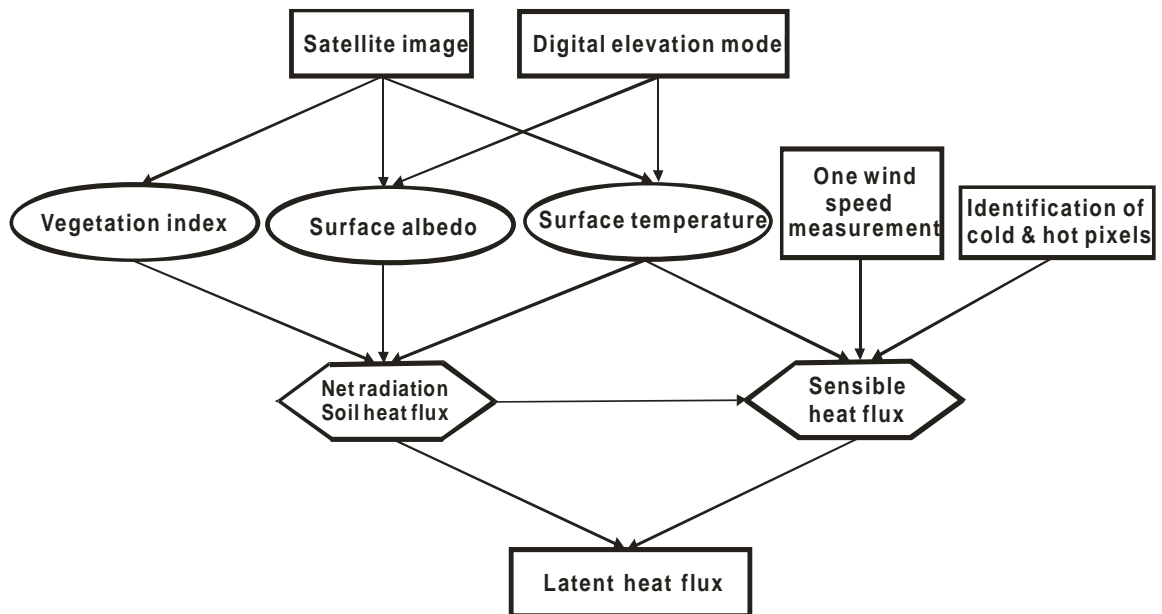
Figure 6.2. Schematic of SEBAL algorithm

used to calculate net short wave radiation, and T_s was used for the calculation of net long wave radiation, soil heat flux and sensible heat flux for each pixel. The *NDVI* governs the soil heat flux by incorporating light interception effects by canopies and was used to express spatial variability in aerodynamic roughness of the landscape. The latent heat flux was computed as the residue of the surface energy balance.

$$LE = R_n - G - H \qquad [6.1]$$

where R_n is the net radiation flux density [Wm^{-2}], G is the soil heat flux density [Wm^{-2}], H is the sensible heat flux density [Wm^{-2}] and $LE (= \lambda ET)$ is the latent heat flux density [Wm^{-2}], which can be converted to the ET rate [mms^{-1}] at the time of satellite passover using the latent heat of vaporization of water λ [Jkg^{-1}].

SEBAL estimates daily ET (mmd^{-1}) by assuming the value of evaporative fraction (*EF*) is assumed to be the same as the daily-averaged value (Shuttleworth et al., 1989; Brutsaert and Sugita, 1992; Crago, 1996; Farah and Bastiaanssen, 2001) and the soil heat flux is zero on a daily basis. Bastiaanssen et al. (1998) and Morse et al. (2000) show how to compute the daily net radiation and soil heat flux. Based on the known value of the instantaneous *EF*, the daily net radiation flux, and the soil heat flux over a daily period, daily ET can be estimated by the following:

$$ET_{24} = \frac{86400 \cdot EF \cdot (R_{n24} - G_{24})}{\lambda} \qquad [6.2]$$

where

$$EF = \frac{\lambda E}{\lambda E + H} \qquad\qquad [6.3]$$

and

$$R_{n24} = (1 - \alpha) \cdot R_{a24} \cdot \tau_{sw} - 110 \cdot \tau_{sw} \qquad\qquad [6.4]$$

where

$$R_{a24} = G_{SC} \cdot d_r \cdot \int_{\omega 1}^{\omega 2} \cos(\theta) \, d\omega \qquad\qquad [6.5]$$

where ET_{24} is daily ET [mmd^{-1}], R_{n24} is daily net radiation [Wm^{-2}], G_{24} is daily soil heat flux [Wm^{-2}], [-], EF is the evaporative fraction, α is the surface albedo [-], τ_{sw} is the transmissivity of air, G_{sc} is the solar constant [1367 Wm^{-2}], θ is solar incident angle, d_r is the inverse squared relative Earth-sun distance [-] and R_{a24} is the daily-averaged extraterrestrial shortwave radiation [Wm^{-2}] which is calculated using information on location, day of year, slope and aspect for each pixel (Tasumi et al., 2000).

The most difficult and complex issue involved in the SEBAL algorithm is solving the equation for the sensible heat flux density. The SEBAL sensible heat flux calculations are based on the Monin-Obukov similarity-stability theory accounting for effects on atmospheric stability on sensible heat flux (H) and aerodynamic resistance for heat transport (r_{ah}). Air temperature difference between two heights (dT) is needed for the calculation of sensible heat for each pixel. In order to determine the value of dT for each pixel, the SEBAL procedure assumes a linear relationship between dT and radiometric surface temperature (T_s). This relationship between dT and T_s is the most sensitive portion in SEBAL algorithm (Bastiaanssen et al., 1998; Hendrickx and Hong, 2005;

Allen et al., 2007). In order to minimize the effect of the dT-T_s relationship on the

SEBAL product, we restrained the relationship. Otherwise, the input down-scaled

imagery maybe affected more by the dT-T_s relationship rather than the down-scaled input

parameters. For the 30m resolution imagery whether it is Landsat or disaggregated

MODIS, $dT = 0.181 \cdot T_s - 54.71$ and $dT = 0.151 \cdot T_s - 45.29$ were used for June and May

images, respectively and $dT = 0.209 \cdot T_s - 64.13$ and $dT = 0.129 \cdot T_s - 38.63$ were used

for the 250m resolution June and May images, respectively. T_s expressed in degree

Kelvin. For more details of SEBAL algorithm, the reader is referred to the papers

(Bastiaanssen et al., 1998; Hendrickx and Hong, 2005; Allen et al., 2007).

We have selected SEBAL to estimate evaporation distributions in the Rio Grande

Basin for the following reasons: (1) SEBAL consists of physically-based image analysis

algorithms using standard satellites imagery and requires a minimum of ancillary

meteorological information from surface measurements or atmospheric models. (2)

SEBAL deals with a large number of environmental variables and does not assume

variables to be constant over space as do many other methods. For example, some

methods assume all variables besides surface and air temperatures are spatially constant

(Seguin and Itier, 1983; Jackson et al., 1996). (3) In SEBAL the need for atmospheric

correction of short-wave and thermal information in images is reduced (Tasumi, 2003),

since SEBAL evaporation estimates depend only on radiometric temperature differences

in the scene rather than on the absolute value of the surface temperature. This greatly

enhances the applicability of SEBAL, since the measurements needed for atmospheric

corrections are often not available (Bastiaanssen et al., 1998; Allen et al., 2007). (4)

SEBAL has not only been used successfully with Landsat images at spatial scales of 30-60 m, but also with AVHRR (Advanced Very High Resolution Radiometer) and MODIS (Moderate Resolution Imaging Spectroradiometer) images at spatial scales of 250-1000 m (Bastiaanssen et al., 2002; Hong et al., 2005; Hafeez et al., 2006). (5) Recent studies with SEBAL in the heterogeneous arid riparian and desert areas of the southwestern US have been successful using Landsat and MODIS images (Fleming et al., 2005; Hendrickx and Hong, 2005; Hong et al., 2005).

6.3.3. Down-Scaling (disaggregation) Process

Image down-scaling or disaggregation consists of using information taken at larger scales to derive processes at smaller scales. The total number of pixels increases and each output pixel represents a smaller area. Prior to applying the down-scaling procedures, we prepared maps of albedo, *NDVI*, surface temperature and daily ET from Landsat 7 and MODIS images on June 16, 2002 and May 31, 2002. Since down-scaling schemes require maps of 250m spatial resolution, the Landsat-based estimates of 30m resolution were aggregated to 250m by either applying simple averaging or nearest neighbor resampling. The schematic of preprocessing for down-scaling is shown in Figure 6.3. In this study, we have disaggregated MODIS scale imagery to Landsat scale imagery using twelve different down-scaling methods (Table 6.2 and Figure 6.4). First, disparities between input and output down-scaling procedures were evaluated. The "input down-scaling" consists of disaggregating MODIS-scale pixels of albedo, *NDVI*, and T_s values to obtain pixels at the Landsat scale prior to applying SEBAL to estimate daily ET.
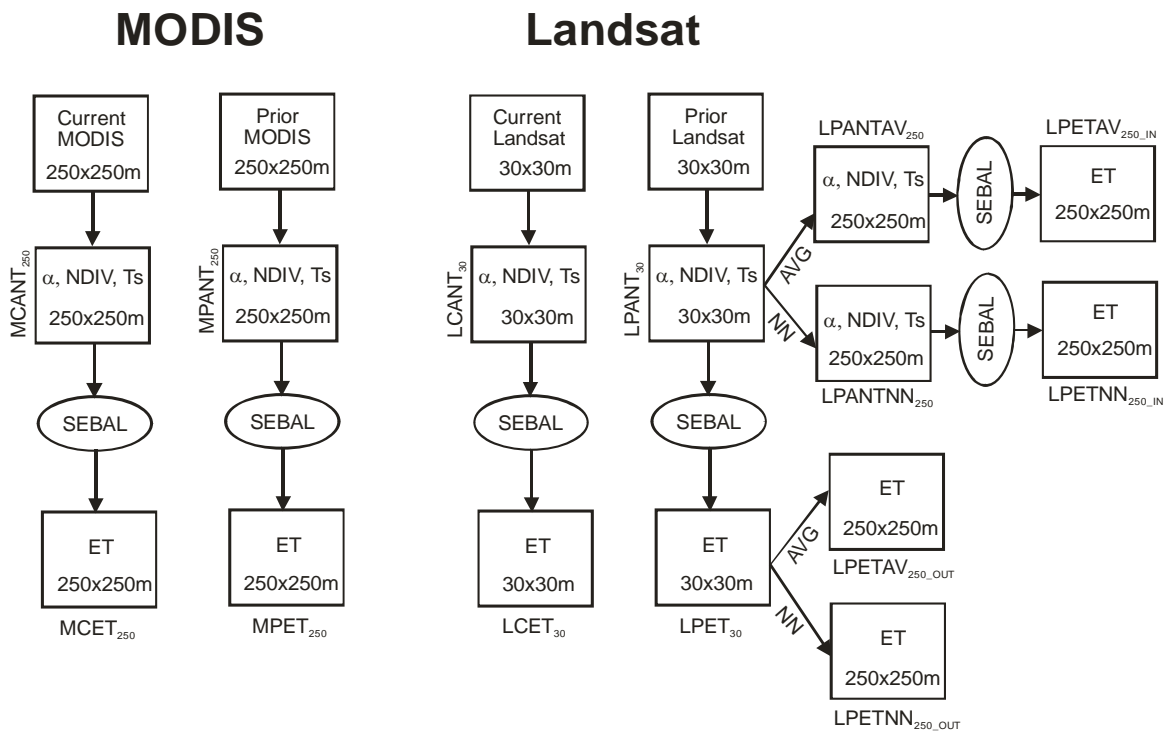
Figure 6.3. Preprocessing for down-scaling scheme

Table 6.2. Twelve different down-scaling methods used in this study.

Down-scaling approach	Down-scaling operation	ID	Method
Output	Subtraction	1a	$LCET_{30} = (MCET_{250} - MPET_{250}) + LPET_{30}$
		1b	$LCET_{30} = (MCET_{250} - LPETAV_{250\_OUT}) + LPET_{30}$
		1c	$LCET_{30} = (MCET_{250} - LPETNN_{250\_OUT}) + LPET_{30}$
	Regression	2a	$LCET_{30} = Regr*(MPET_{250}, MCET_{250})$ to $LPET_{30}$
		2b	$LCET_{30} = Regr(LPETAV_{250\_OUT}, MCET_{250})$ to $LPET_{30}$
		2c	$LCET_{30} = Regr(LPETNN_{250\_OUT}, MCET_{250})$ to $LPET_{30}$
Input	Subtraction	3a	$LCET_{30} = (MCANT_{250} - MPANT_{250}) + LPANT_{30}$
		3b	$LCET_{30} = (MCANT_{250} - LPANTAV_{250\_IN}) + LPANT_{30}$
		3c	$LCET_{30} = (MCANT_{250} - LPANTNN_{250\_IN}) + LPANT_{30}$
	Regression	4a	$LCET_{30} = Regr(MPANT_{250}, MCANT_{250})$ to $LPET_{30}$
		4b	$LCET_{30} = Regr(LPANTAV_{250}, MCANT_{250})$ to $LPET_{30}$
		4c	$LCET_{30} = Regr(LPANTNN_{250}, MCANT_{250})$ to $LPET_{30}$

$*1^{st}$ order regression, for example $Regr(x,y)$ to z represents applying 1st order regression between x (predictor) and y (response) to z as a predictor.

$LCET_{30}$: 30m resolution ET map from current (June 16, 2002) Landsat,

$LPET_{30}$: 30m resolution ET map from prior (May 31, 2002) Landsat,

$LPANT_{30}$: 30m resolution albedo, NDVI and T_s maps from prior Landsat,

$LCETAV_{250\_OUT}$: 250m resolution (output simple averaging) ET map from current Landsat

$LPETAV_{250\_OUT}$: 250m resolution (output simple averaging) ET map from prior Landsat

$LCETNN_{250\_OUT}$: 250m resolution (output nearest neighbor) ET map from current Landsat

$LPETNN_{250\_OUT}$: 250m resolution (output nearest neighbor) ET map from prior Landsat

$LPANTAV_{250}$: Aggregated (simple averaging) 250m resolution albedo, NDVI and T_s maps from prior Landsat,

$LPANTNN_{250}$: Aggregated (nearest neighbor) 250m resolution albedo, NDVI and T_s maps from prior Landsat,

$MCET_{250}$: 250m resolution ET map from current (June 16, 2002) MODIS,

$MPET_{250}$: 250m resolution ET map from prior (May 31, 2002) MODIS,

$MCANT_{250}$: 250m resolution albedo, NDVI and T_s maps from current MODIS,

$MPANT_{250}$: 250m resolution albedo, NDVI and T_s maps from prior MODIS,
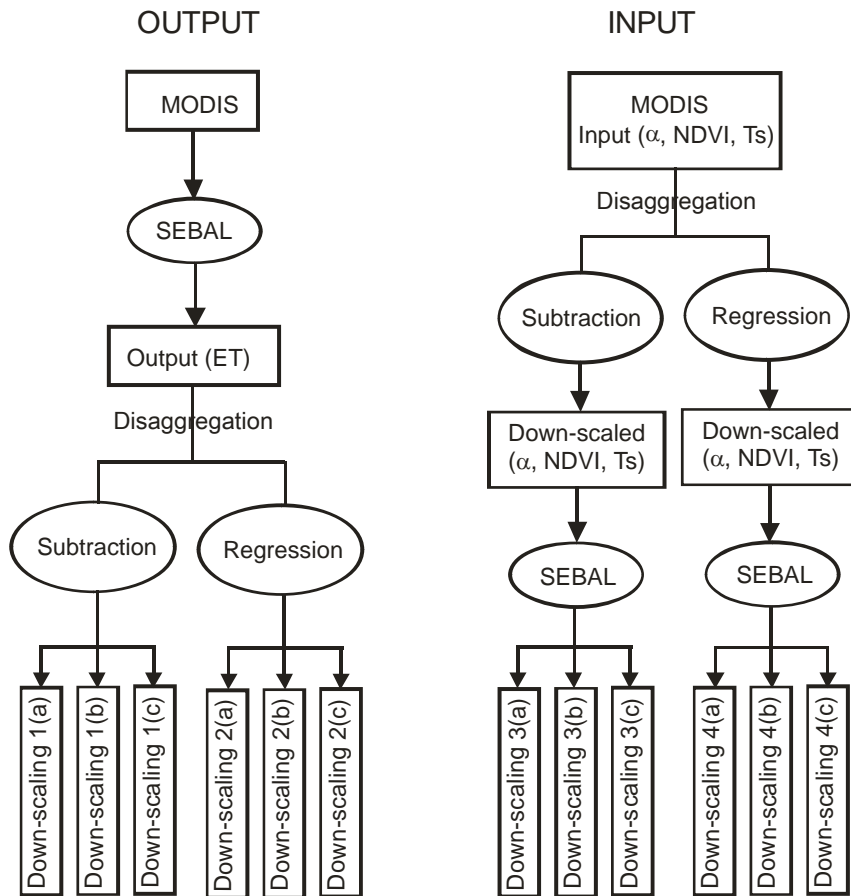
Figure 6.4. Schematic of down-scaling scheme (Downscalling1: down-scaling output with subtraction, Downscaling2: down-scaling output with regression, Downscaling3: down-scaling input with subtraction, Downscaling4: down-scaling input with regression).

The "output down-scaling" scheme required running SEBAL first and then disaggregated SEBAL estimated daily ET from MODIS to Landsat pixel scale. Second, disaggregation imagery was obtained by two different processes, subtraction and regression (Figure 6.5). Subtraction methodology disaggregated imagery by applying the distribution of pixel by pixel difference between two MODIS scale products to previous or subsequent Landsat scale images covering the same area. The fine-scale variability within a MODIS pixel is assumed unchanged during the time interval (16 days or longer) between two high quality Landsat images. For example in order to disaggregate ET imagery obtained from MODIS imagery of June with output-downscaling with subtraction (down-scaling 1(a) in Figure 6.4), first the pixel-by-pixel difference map between MODIS ET on June 16, 2002 and May 31, 2002 was calculated ((c) in Figure 6.6). Second, the calculated difference was added to prior Landsat ET imagery on May 31, 2002 to predict disaggregated ET imagery of June ((e) in Figure 6.6). Regression methodology disaggregated imagery by applying linear regression between two MODIS scale products to the previous or subsequent Landsat scale product. In this application of output down-scaling with regression (down-scaling 2(a) in Figure 6.4) as an example in Figure 6.7, a 1st order linear regression between two ET maps derived from MODIS on June 16, 2002 and May 31, 2002 was first calculated, and then the obtained regression was applied to ET map derived from prior Landsat on May 31, 2002 to predict disaggregated imagery of June. The obtained 1st order regression line was not constrained to zero intercept in order not to change the meaning of the regression coefficients. Regression methodology used in the study has an assumption that the linear relationship between coarse resolution images is valid between fine-scale resolution imagery and that
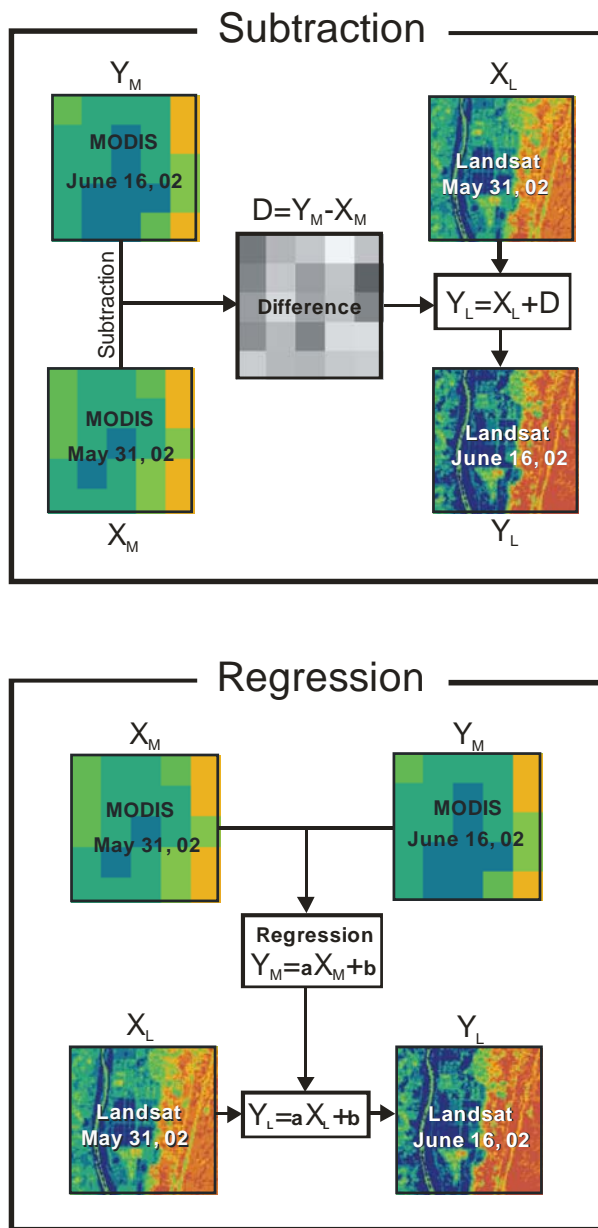
Figure 6.5. Example schematic of two disaggregation methods. MODIS scale imagery (250m resolution) on June 16, 2002 is MODIS-based estimate and May 31, 2002 MODIS scale imagery can be obtained from; (a) MODIS-based estimate at 250m resolution, (b) simple averaging of Landsat-based estimate at 30m to 250m resolution and (c) nearest neighbor of Landsat-based estimate at 30m to 250 resolution.
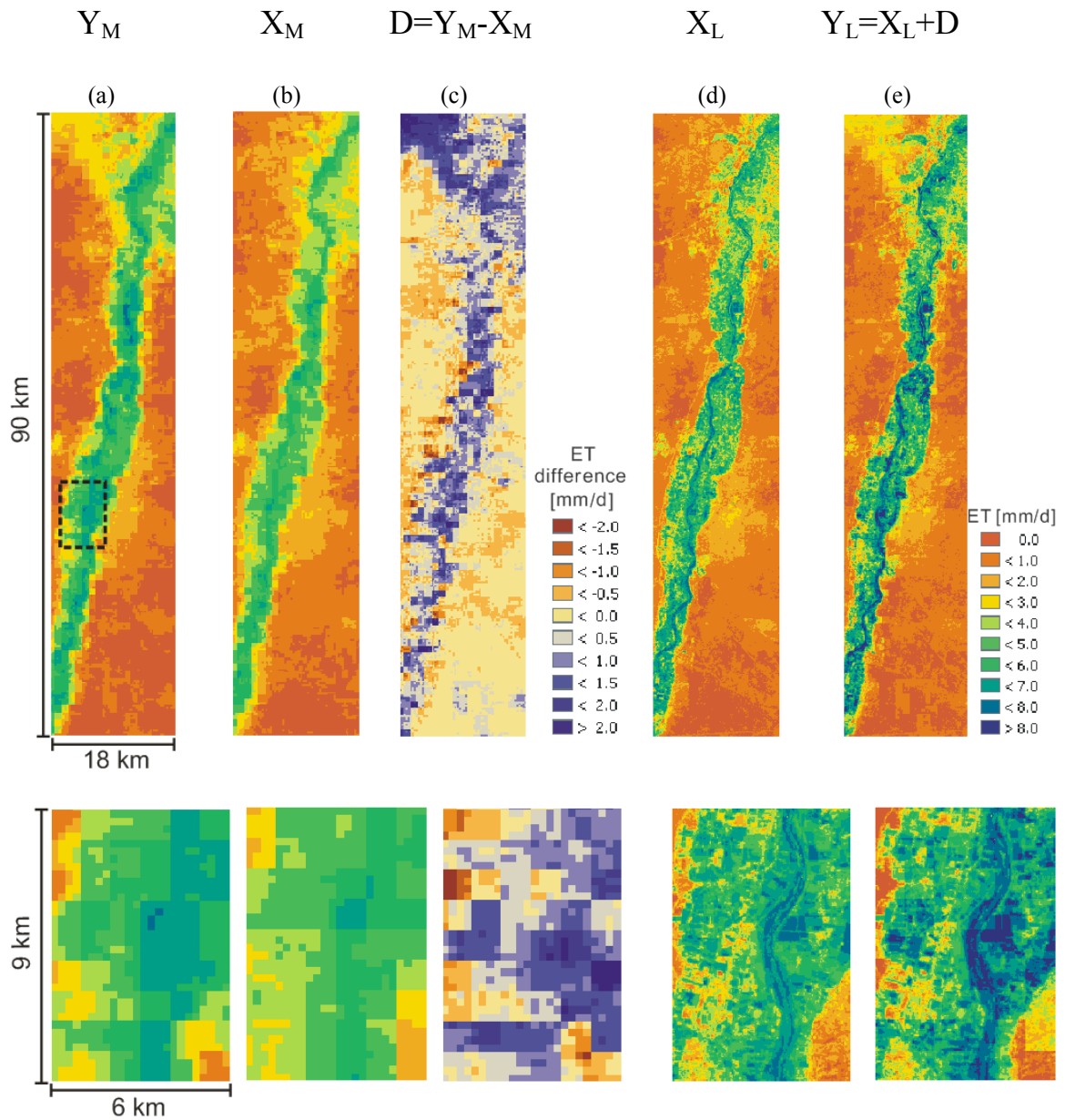
Figure 6.6. Example procedure of down-scaling output with subtraction. (a) MODIS-based ET map of June at 250 m resolution, (b) MODIS-based ET map of May at 250 m resolution, (c) Difference map between (a) and (b), (d) Landsat-based ET map of May at 30 m resolution and (e) Down-scaled ET map at 30 m resolution of June. Enlarged areas (6 by 9 km) shown at the bottom correspond to the dotted square of the upper images.
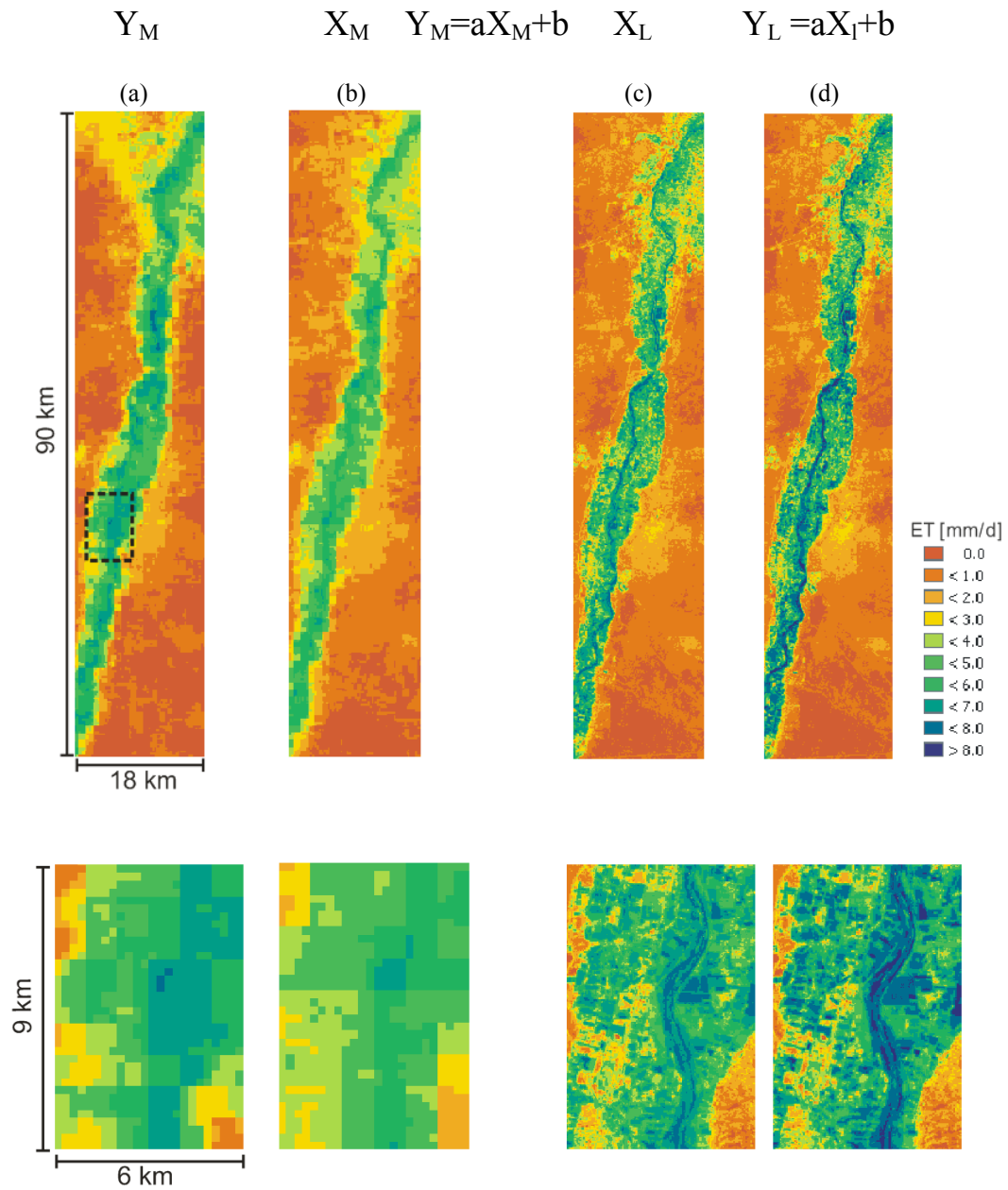
Figure 6.7. Example procedure of down-scaling output with regression. (a) MODIS-based ET map of June at 250 m resolution, (b) MODIS-based ET map of May at 250 m resolution, (c) Landsat-based ET map of May at 30 m resolution and (d) Down-scaled ET map at 30 m resolution of June. Regression line between (a) and (b) is; (a) = 1.135(b) - 0.15. Enlarged areas (6 by 9 km) shown at the bottom correspond to the dotted square of the upper images.

the fine-scale variability of the area of interest changes linearly during the time interval between two satellite-estimated maps.

Third, as illustrated in Figures 6.6 and 6.7, in order to disaggregate MODIS scale to Landsat scale imagery using subtraction and regression, two different dates' MODIS imagery at coarse resolution and/or one prior or subsequent Landsat imagery at fine resolution were required. The pixel-by-pixel difference and linear regression performed in subtraction and regression require two coarse 250m resolution images. These were obtained by three different methods as noted (a), (b) and (c) in Figure 6.4: (a) between two MODIS-derived estimates of ET, T_s, albedo or $NDVI$ on May 31, 2002 and June 16, 2002; (b) between a map estimated from MODIS imagery on June 16, 2002 and an aggregated map by simple averaging of Landsat imagery on May 31, 2002; and (c) between MODIS estimated map on June 16, 2002 and an aggregated map by nearest neighboring of Landsat imagery on May 31, 2002. To aggregate data from Landsat scale 30 m to MODIS scale250 m, first Landsat scale pixels were broken into 10 m pixels with the same pixel values. After that, the data resample to 250m resolution by simple averaging or nearest neighboring. The simple averaging method calculates the arithmetic mean over an n by n window to produce a new coarser resolution data set. The nearest neighbor method finds the pixel in the original image. The new data point is closest to the center of the grid in calculated coordinates. To determine the nearest neighbor, the algorithm uses the inverse of the transformation matrix to calculate the image file coordinates of the desired geographic coordinate.

The spatial distribution and statistical features of the disaggregated ET maps generated by 12 different down-scaling schemes were compared with each other. The down-scaled ET maps were also evaluated against the ET map directly derived from Landsat imagery. The performance of the different down-scaling schemes was examined by inspection of: (1) spatial distribution of disaggregated imagery by each down-scaling schemes to evaluate the changes in spatial pattern after disaggregation and (2) histograms and basic statistics of the disaggregated data from each down-scaling schemes.

The differences in spatial details between the disaggregated imagery and the original fine-resolution imagery from Landsat were considered disaggregation differences. In this study, difference images were created by subtracting the disaggregated pixels from the pixels of the direct Landsat-based estimates ($ET_{down\text{-}scaled}$ − $ET_{Landsat}$). Relative difference images were produced by diving absolute difference by direct Landsat-based ET imagery [$|(ET_{down\text{-}scaled} − ET_{Landsat})| / ET_{Landsat}$]. The statistical and spatial characteristics of the differences were evaluated by displaying their spatial distribution and calculating the mean and standard deviation of the absolute differences. Basic statistics were calculated based on the absolute value of the difference so that large positive and negative differences would not cancel each other out when the mean difference and relative difference were calculated.

6.4.   RESULTS AND DISCUSSION

6.4.1. Landsat and MODIS Imagery Preparation

Landsat- and MODIS derived surface albedo, *NDVI*, T_s and daily ET

distributions on May 31 and June 16 in 2002 are shown in Figures 6.8 – 6.11. The area of

coverage is 90 x 18 km^2 which contains 3000 x 600 pixels for Landsat scale (30m) and

360 x 72 pixels for MODIS scale (250m). The frequency distribution and basic statistics

including minimum, maximum, mean and standard deviation of SEBAL estimates are

also shown in Figures 6.8 – 6.11. In order to show the spatial distribution in detail, the

enlarged area of 6 x 9 km^2 in the Rio Grande riparian area is presented at the bottom of

the figures. Linear regressions of Landsat and MODIS scale pixels used in down-scaling

with regression methodology are presented in Figures 6.12 – 6.15.

6.4.1.1 Spatial distribution of Landsat- and MODIS-based maps

As shown in Figures 6.8 – 6.11 the SEBAL estimated maps support that the

SEBAL estimated albedo, *NDVI*, T_s and daily ET along the middle Rio Grande valley are

in good accordance between same date Landsat and MODIS imagery. The derived daily

ET rates have been validated and showed a good agreement with the eddy covariance

towers measurements located in the riparian areas (Hong et al., 2008). The frequency

distribution and basic statistics show a wide pixel value range due to the heterogeneous

surface covers including riparian vegetation, Rio Grande River, agricultural fields, bare

soil, desert vegetation and urban areas in the study area. Especially, great portion of the
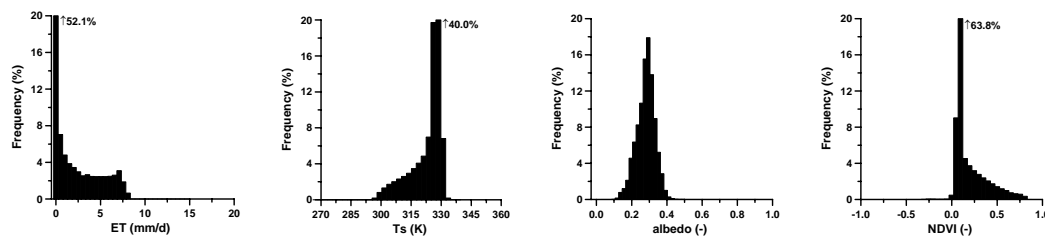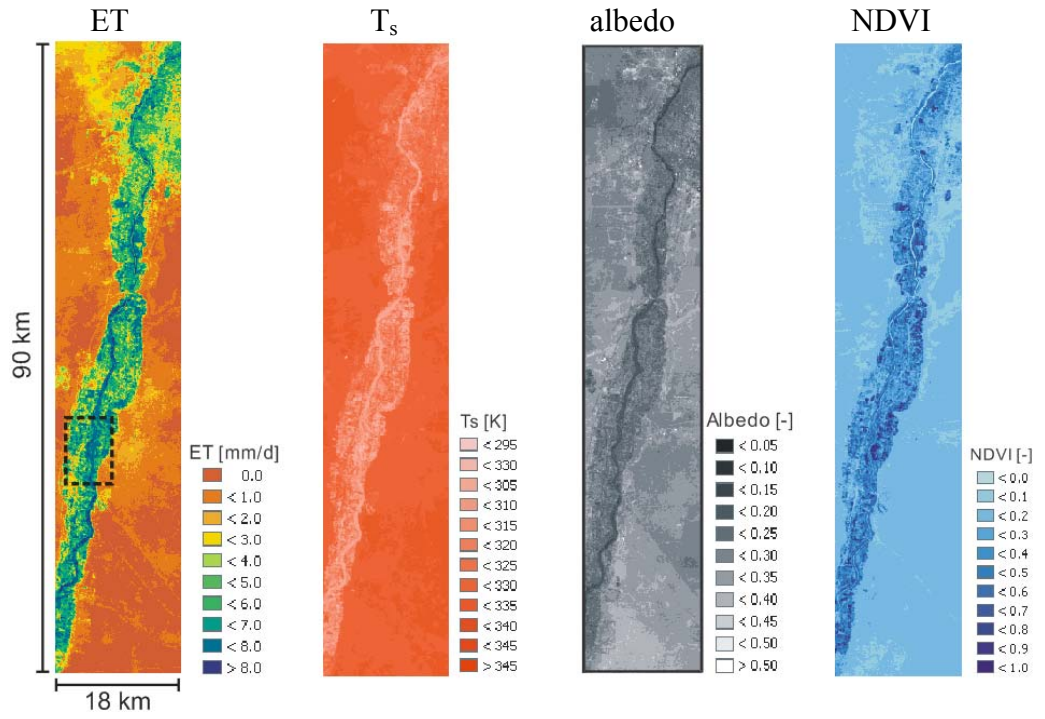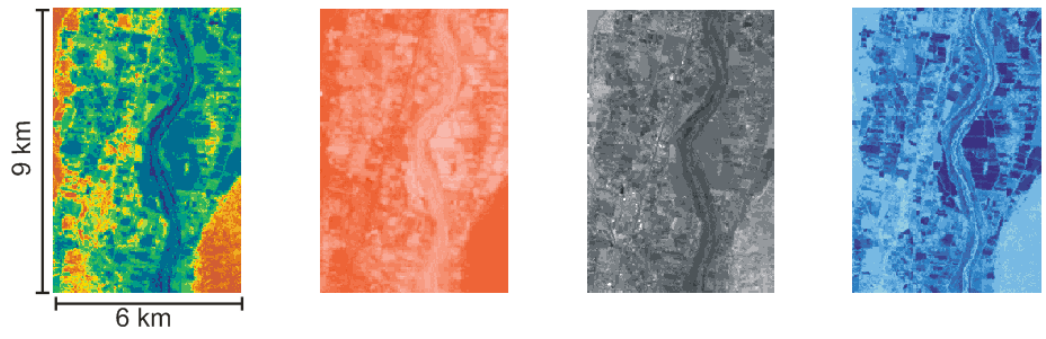
Figure 6.8. SEBAL estimated daily ET, surface temperature (T_s), surface albedo and NDVI from Landsat 7 on June 16, 2002 (30m by 30m resolution). Bin size of the ET, T_s, albedo and NDVI histogram is 0.5 mm/d, 2.5 K, 0.02, and 0.05, respectively. Enlarged areas (6 by 9 km) shown at the bottom correspond to the dotted square of the upper images.
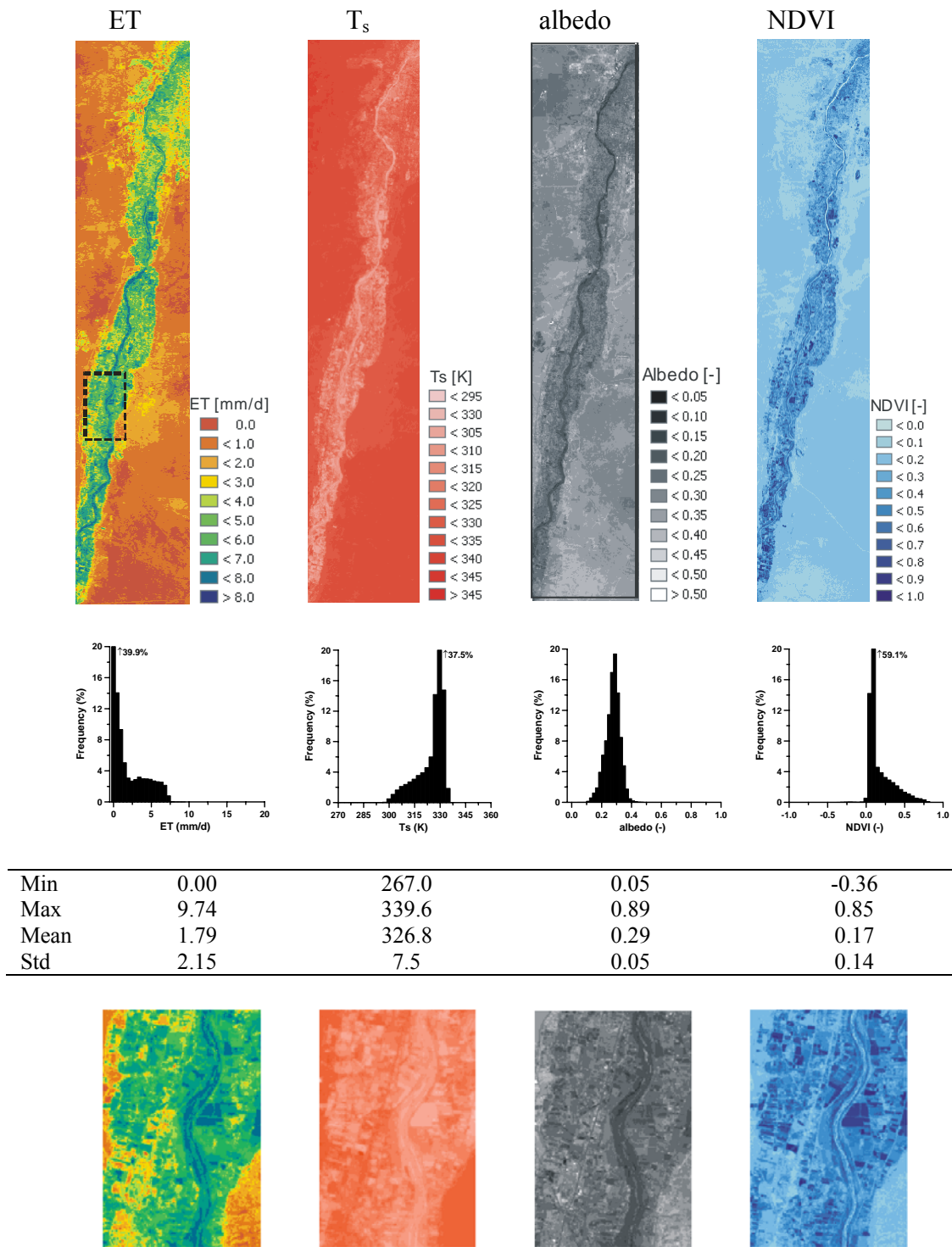
	ET	T_s	albedo	NDVI
Min	0.00	267.0	0.05	-0.36
Max	9.74	339.6	0.89	0.85
Mean	1.79	326.8	0.29	0.17
Std	2.15	7.5	0.05	0.14

Figure 6.9. SEBAL estimated daily ET, surface temperature (T_s), surface albedo and NDVI from Landsat 7 on May 31, 2002 (30m by 30m resolution). Bin size of the ET, T_s, albedo and NDVI histogram is 0.5 mm/d, 2.5 K, 0.02, and 0.05, respectively.

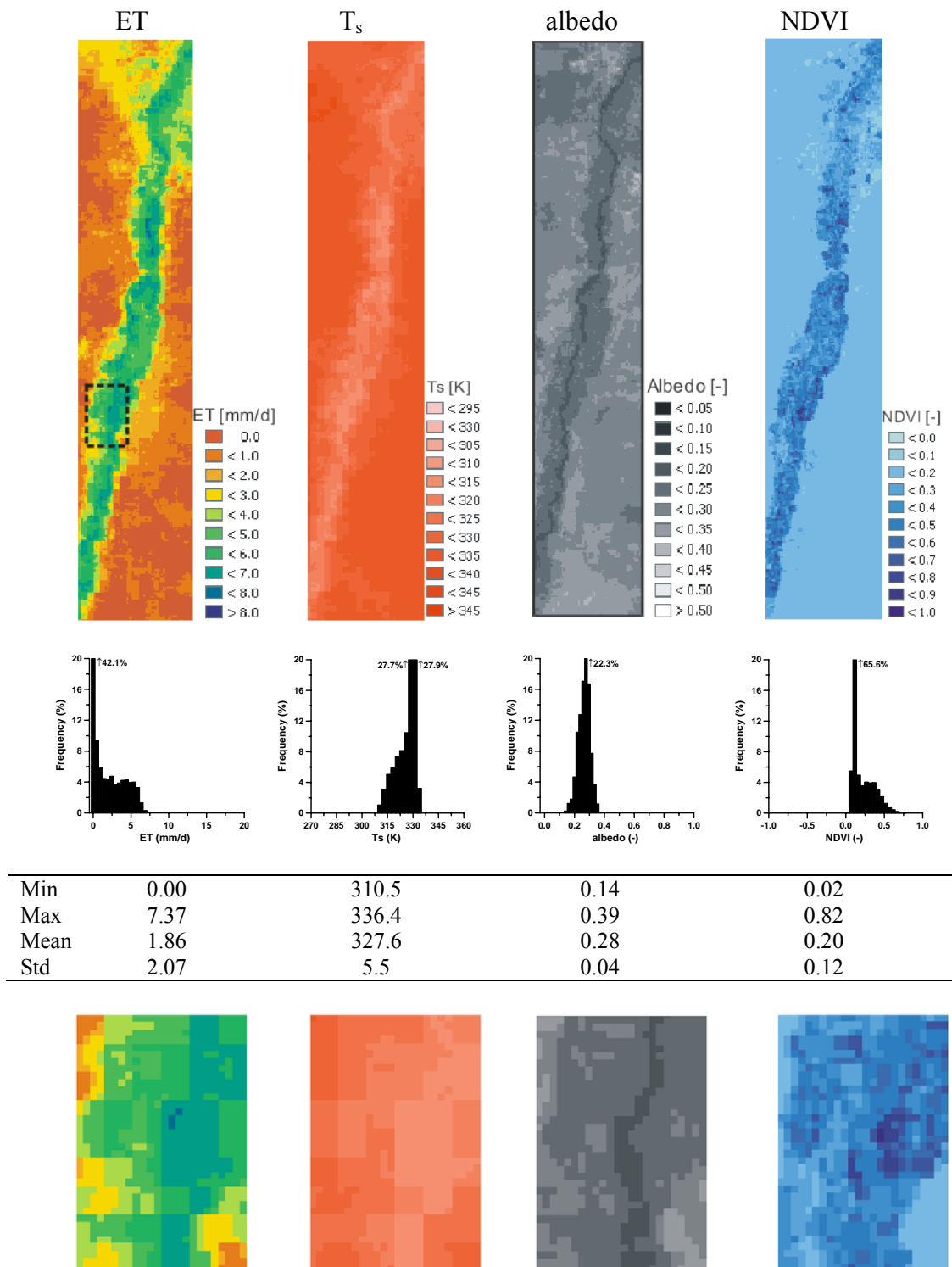|	ET	T_s	albedo	NDVI
Min	0.00	310.5	0.14	0.02
Max	7.37	336.4	0.39	0.82
Mean	1.86	327.6	0.28	0.20
Std	2.07	5.5	0.04	0.12

Figure 6.10. SEBAL estimated daily ET, surface temperature (T_s), surface albedo and NDVI from MODIS on June 16, 2002 (250m by 250m resolution). Bin size of the ET, T_s, albedo and NDVI histogram is 0.5 mm/d, 2.5 K, 0.02, and 0.05, respectively.

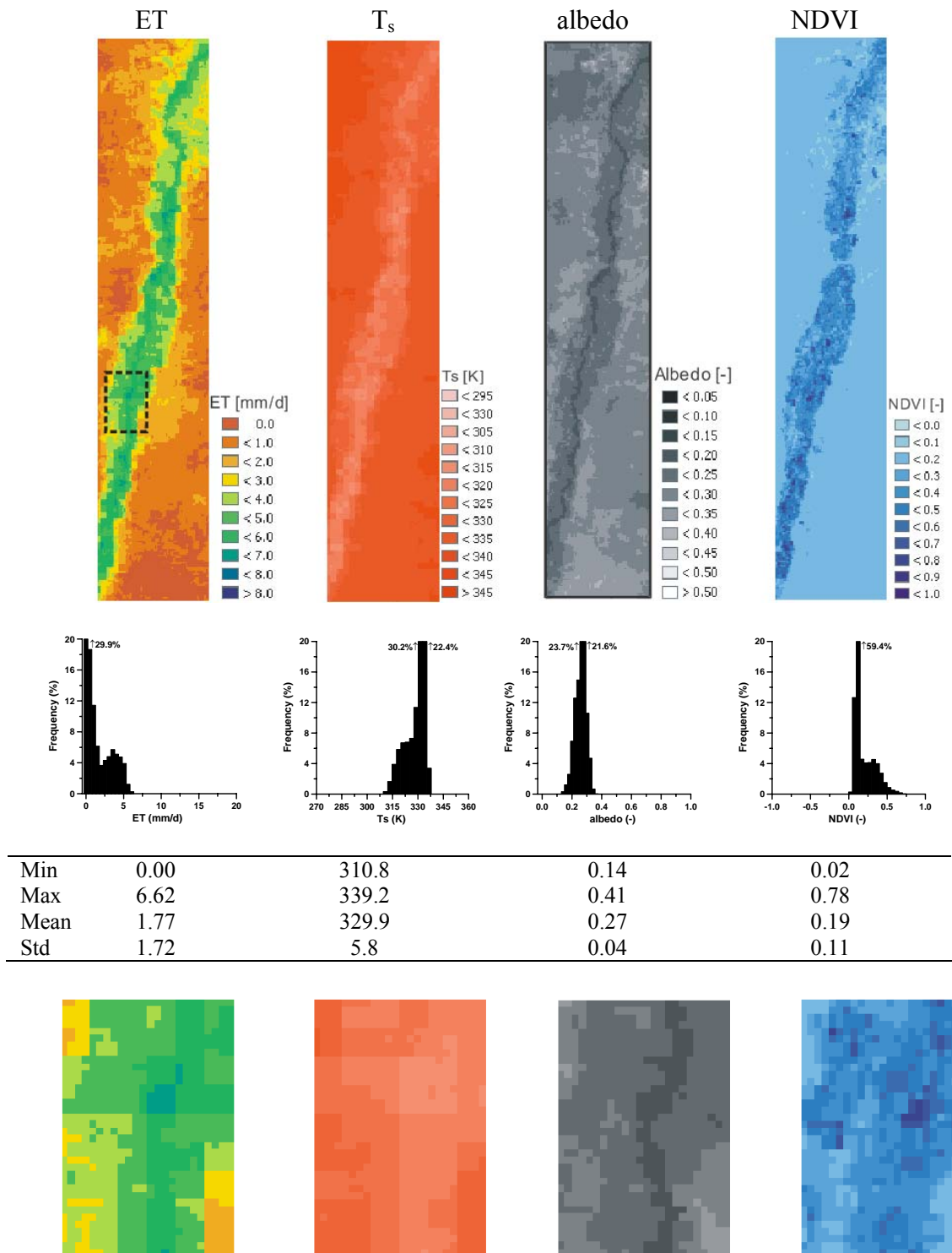|	ET	T_s	albedo	NDVI
Min	0.00	310.8	0.14	0.02
Max	6.62	339.2	0.41	0.78
Mean	1.77	329.9	0.27	0.19
Std	1.72	5.8	0.04	0.11

Figure 6.11. SEBAL estimated daily ET, surface temperature (T_s), surface albedo and NDVI from MODIS on May 31, 2002 (250m by 250m resolution). Bin size of the ET, T_s, albedo and NDVI histogram is 0.5 mm/d, 2.5 K, 0.02, and 0.05, respectively.
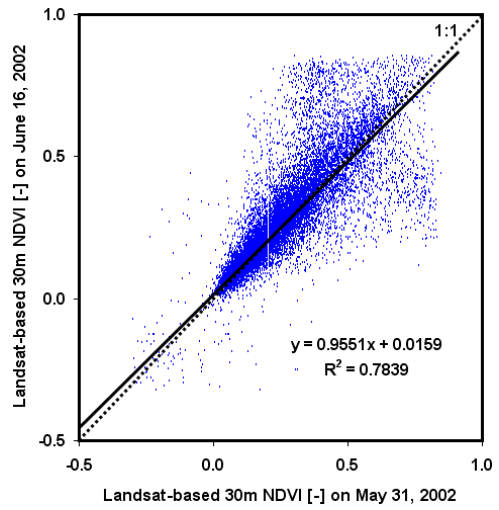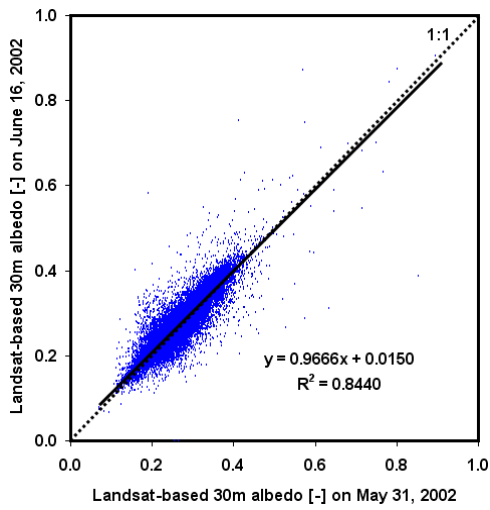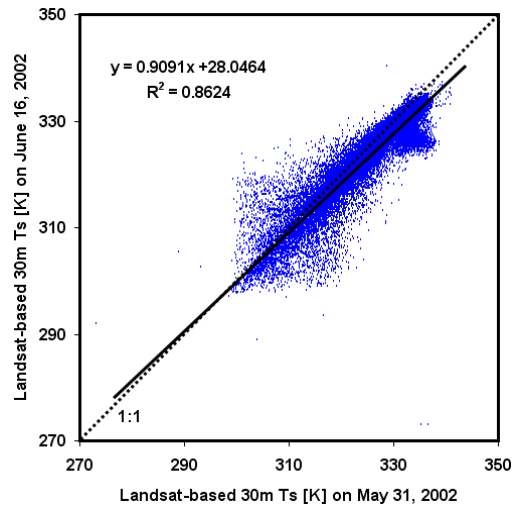
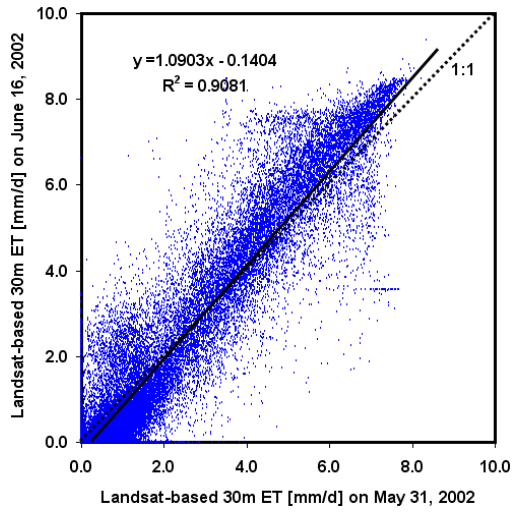Figure 6.12. Linear regression between Landsat-based estimates on May 31, 2002 and June 16, 2002 (30m resolution).

Figure 6.13. Linear regression between MODIS-based estimates on May 31, 2002 and June 16, 2002 (250m resolution).

Figure 6.14. Linear regression between Landsat-based estimates on May 31, 2002 (250m resolution by simple averaging) and MODIS-based estimates on June 16, 2002 (250m resolution).
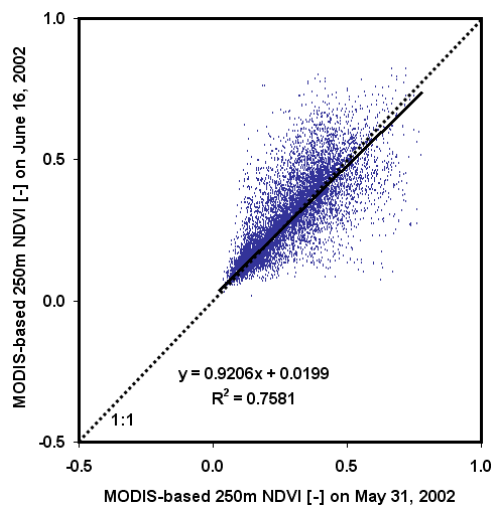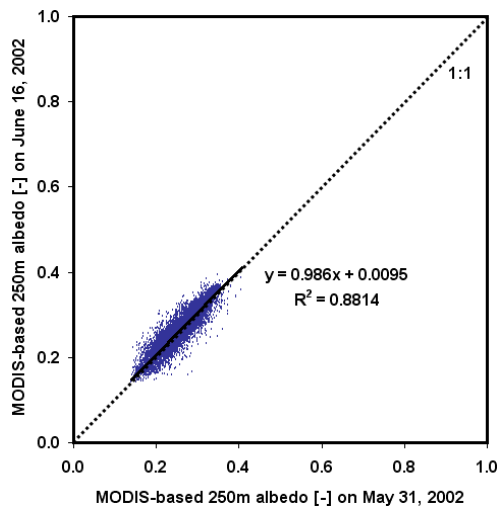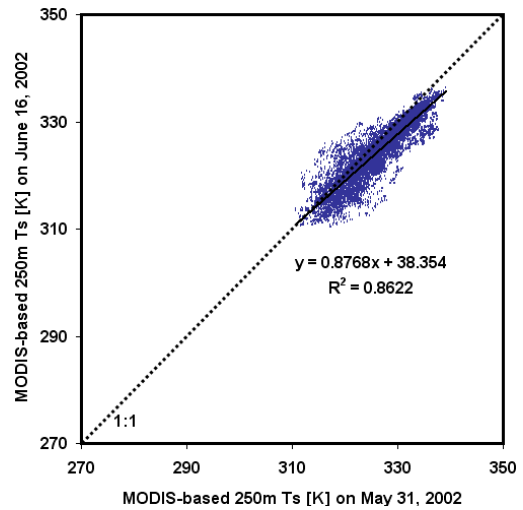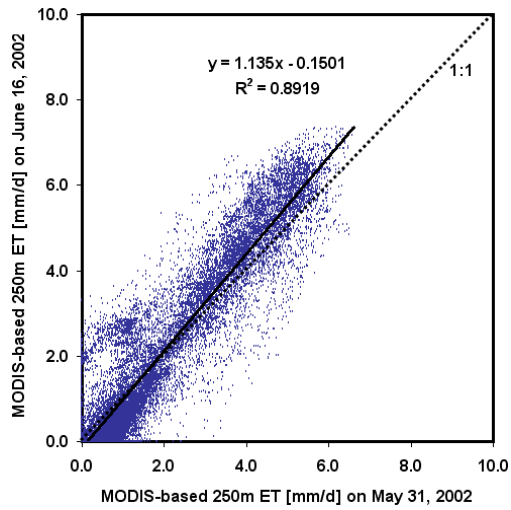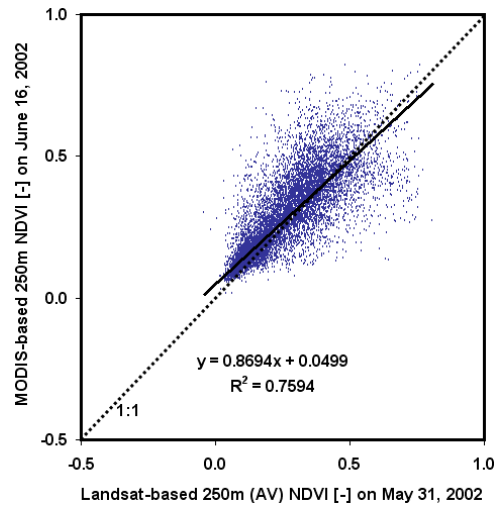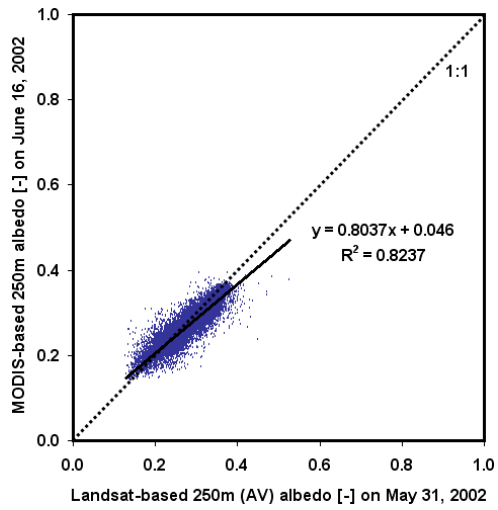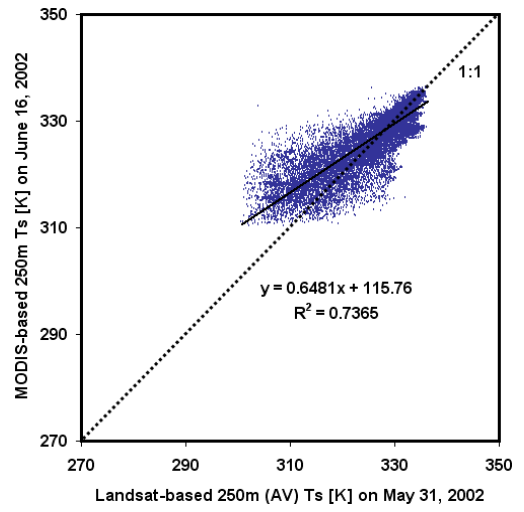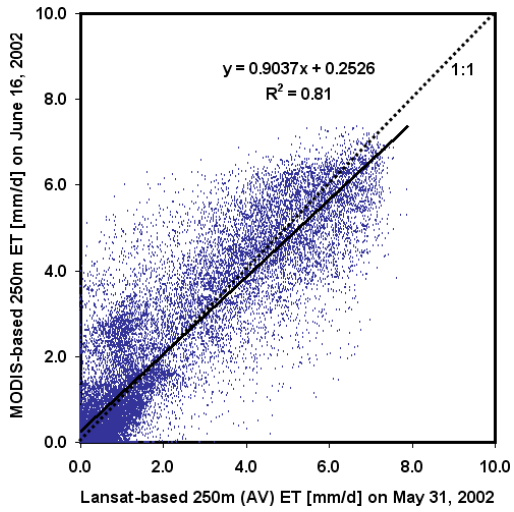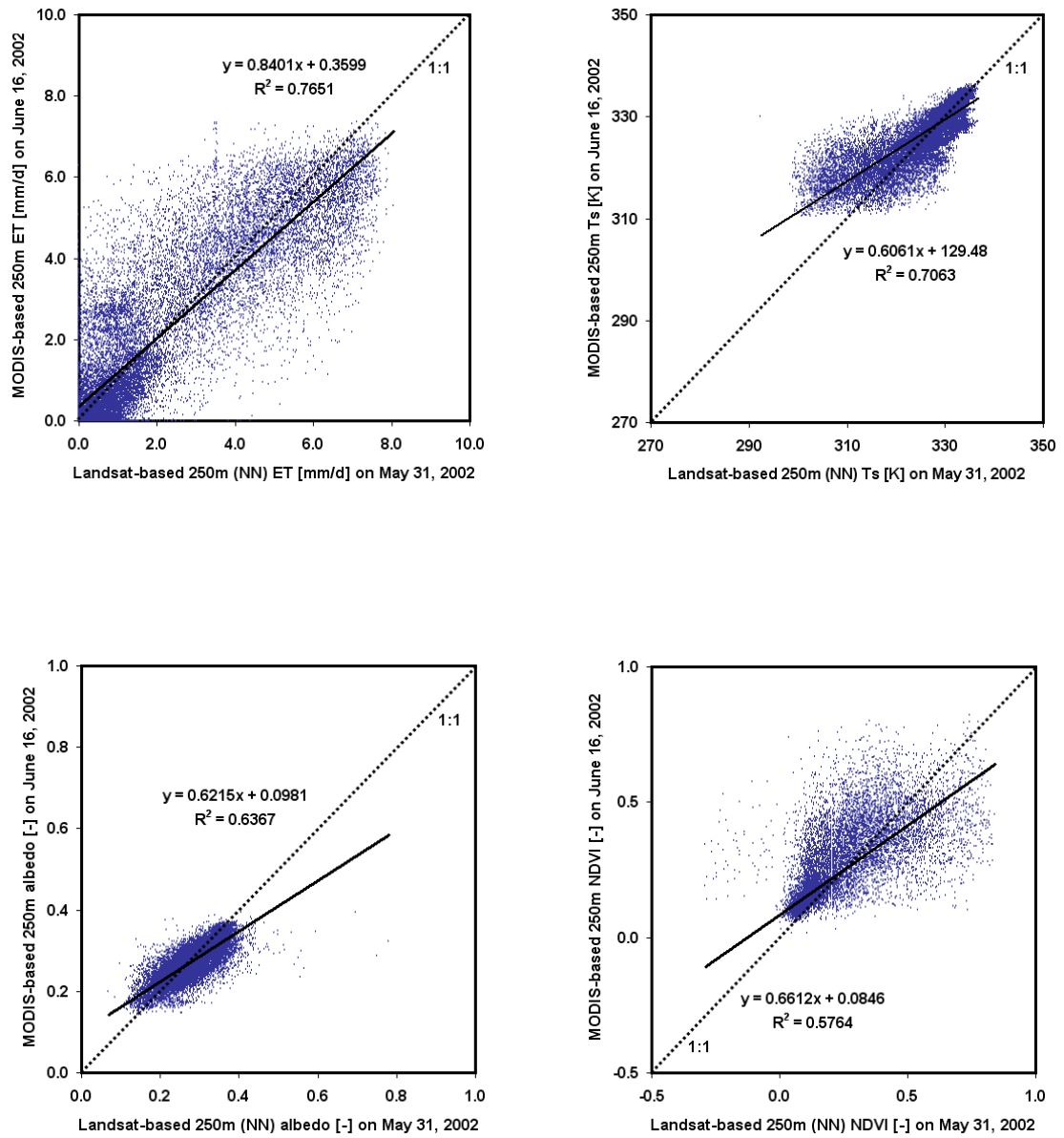
Figure 6.15. Linear regression between Landsat-based estimates on May 31, 2002 (250m resolution by nearest neighbor) and MODIS-based estimates on June 16, 2002 (250m resolution).

pixels (30 – 50%) in the study area have close to zero ET rates (0 – 0.5 mm/d). Lower ET rates correspond to the higher T_s and surface albedo and lower $NDVI$ values. In both Landsat and MODIS estimates, the mean values of ET and $NDVI$ were higher but T_s was lower for the June images than those from images were in May. This indicates that vegetation growth activity was increasing from the end of May to the middle of June. However, it is difficult to notice the difference in mean albedo values between the two dates. The full scene of Landsat- and MODIS-based ET, T_s, albedo and $NDVI$ maps on same date showed overall similar distribution, but many of the fine details found on the Landsat-based maps have disappeared on the MODIS-based maps. For example, all of the images clearly show that higher ET, low T_s, lower albedo and higher $NDVI$ occur in the irrigated fields and riparian areas along the Rio Grande Valley, while lower ET, higher T_s and albedo and lower $NDVI$ values occur in the adjoining desert areas. The city of Albuquerque has much higher ET rates than the surrounding desert due to the urban vegetations.

The high spatial resolution of the Landsat-based image resulted in many homogeneous pixels with either high or low ET, T_s, albedo and $NDVI$. The low spatial resolution of the MODIS-based map resulted in many mixed pixels consisting partly of high ET, T_s, albedo and $NDVI$ and partly of low ET, T_s, albedo and $NDVI$. The mixed pixels issue is well presented in the $NDVI$ maps. As shown in Figures 6.8 – 6.11, the minimum value of $NDVI$ in the Landsat-based estimate is negative (water pixel), but the MODIS-based $NDVI$ has a positive minimum number. This shows that the 250m by 250m MODIS pixel size is too big to be composed entirely or mainly of a water body in

our study area. Also in Figures 6.8 – 6.11, the increase in mixed pixels in the MODIS-based maps is clearly presented in the histograms and basic statistics. Due to the increase in mixed pixels as spatial resolution increases, MODIS-based ET, T_s, albedo and *NDVI* distributions produced a tighter and taller histogram than the one from Landsat imagery. As shown in the table of basic statistics, mean values of Landsat and MODIS estimated images are very similar (Figures 6.8 – 6.11). However, maps of ET, T_s, albedo, and *NDIV* derived from the Landsat 7 image show a greater maximum and standard deviation than the one derived from the MODIS images. The dynamic changes in ET, T_s, albedo and *NDVI* in the area of agricultural fields along the Rio Grande River between images of 16 days apart are significant. The abrupt changes are clearly shown in Landsat-based maps in 6 km by 9 km enlarged areas. These changes can be detected in the MODIS estimated maps, but are not as clearly represented as in Landsat scale images due to the coarse spatial resolution of the MODIS pixel.

6.4.1.2. Linear regression between Landsat- and MODIS-based maps

Figures 6.12 and 6.13 present the linear regressions of two Landsat and two MODIS estimates, respectively, on May 31, 2002 versus June 16, 2002. The linear regressions between MODIS and aggregated Landsat-based estimates with either simple averaging or nearest neighbor are also shown in Figures 6.14 and 6.15. The 1:1 line is also plotted in the graphs. Especially, Figures 6.12 and 6.13 were generated to answer to the question whether relationships between ET, T_s, albedo and *NDVI* are identical for a MODIS and Landsat image of the same day. The data show a decent agreement in linear regressions between Landsat and MODIS. Therefore, it confirms the feasibility to use the

downscaling methods, especially the regression based ones that are proposed in this study. Among the Figures 6.13 – 6.15, highest r^2 value is shown in relationship between two MODIS images (Figure 6.13) and the lowest r^2 value is shown between MODIS and aggregated Landsat by nearest neighbor (Figure 6.15). The regression lines in Figure 6.12 and 6.13 also support that the ET and *NDVI* were higher but T_s was lower for the June images than those from May images in both Landsat and MODIS estimates. However, regression lines in Figures 6.14 and 6.15 shows shallower slope than the ones in Figures 6.12 and 6.13. This shallow slope and lower r^2 of regressions in Figures 6.14 and 6.15 are mainly due to georeferencing disagreement between the MODIS and aggregated Landsat images that is discussed in detail in later section.

6.4.2. Comparison of Different Down-scaled Maps

Spatial and statistical characteristics of 12 different down-scaled products at 30m resolution from coarse 250m resolution MODIS-based imagery are presented in Figures 6.16 – 6.19. Examples of the difference maps of down-scaled daily ET map versus Landsat-based ET at 30m resolution are shown in Figures 6.20 and absolute relative difference maps of daily ET are presented in Figures 6.21. The enlarged area for the difference and absolute relative difference map is area of 12.5 km by 17 km and covers the east and west sides' boundary between riparian forest and desert areas.

6.4.2.1. Down-scaling with subtraction

In Figure 6.16, the down-scaled map shown in (a) is somewhat sharper than the maps in (b) and (c). The down-scaled map in (c) looks the most blurry. For example, it is

	(a)	(b)	(c)
Min	0.00	0.00	0.00
Max	10.86	12.01	11.72
Mean	1.94	1.89	1.88
Std	2.45	2.21	2.17
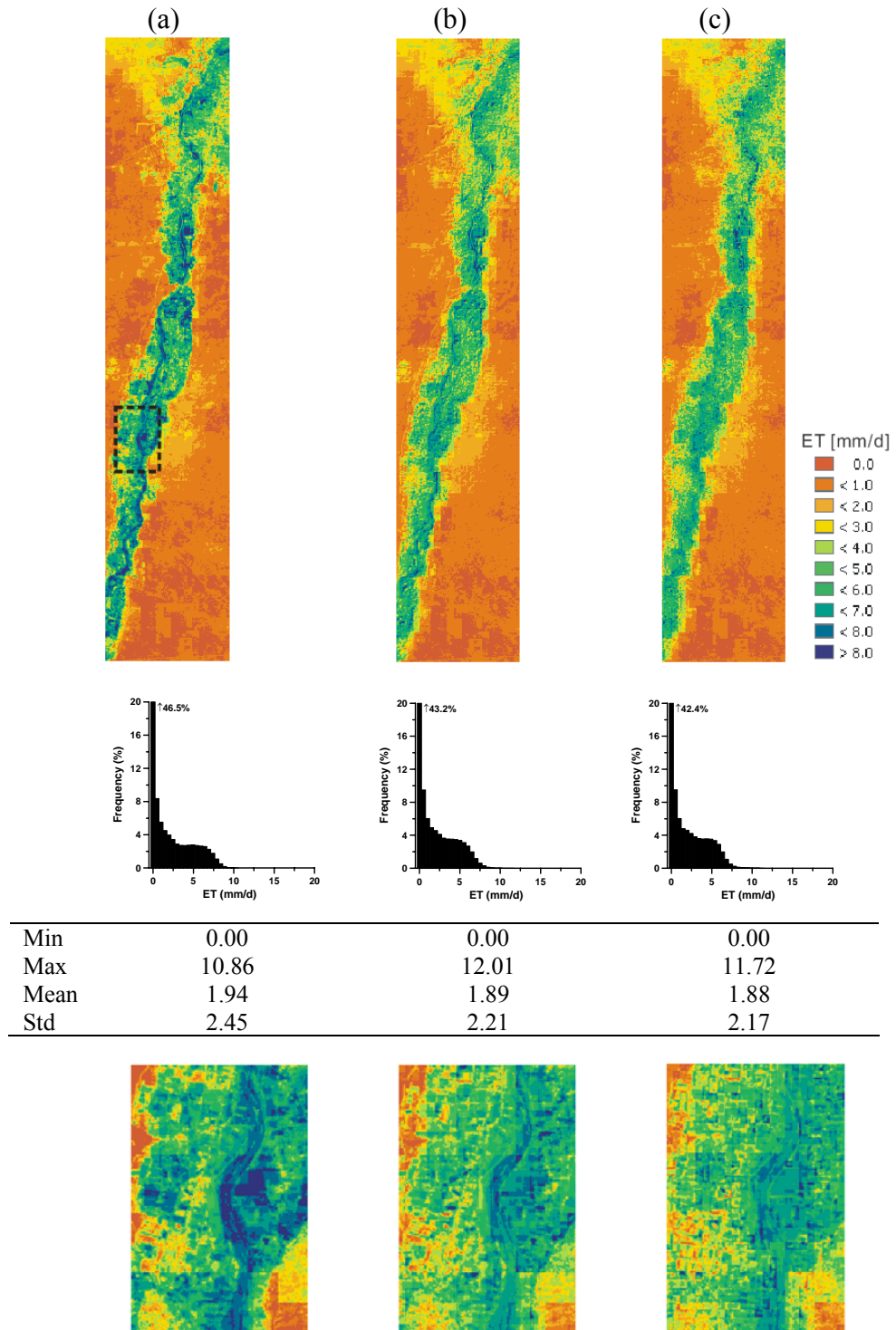
Figure 6.16. Down-scaled ET map from down-scaling output (daily ET) with subtraction. Pixel difference is calculated (a) between MODIS-based ET of June and May, (b) between MODIS-based ET of June and aggregated (simple averaging) Landsat-based ET of May and (c) between MODIS-based ET of June and aggregated (nearest neighbor) Landsat-based ET of May.

	(a)	(b)	(c)
Min	0.00	0.25	0.36
Max	10.90	9.07	8.55
Mean	1.92	1.86	1.85
Std	2.40	1.95	1.81
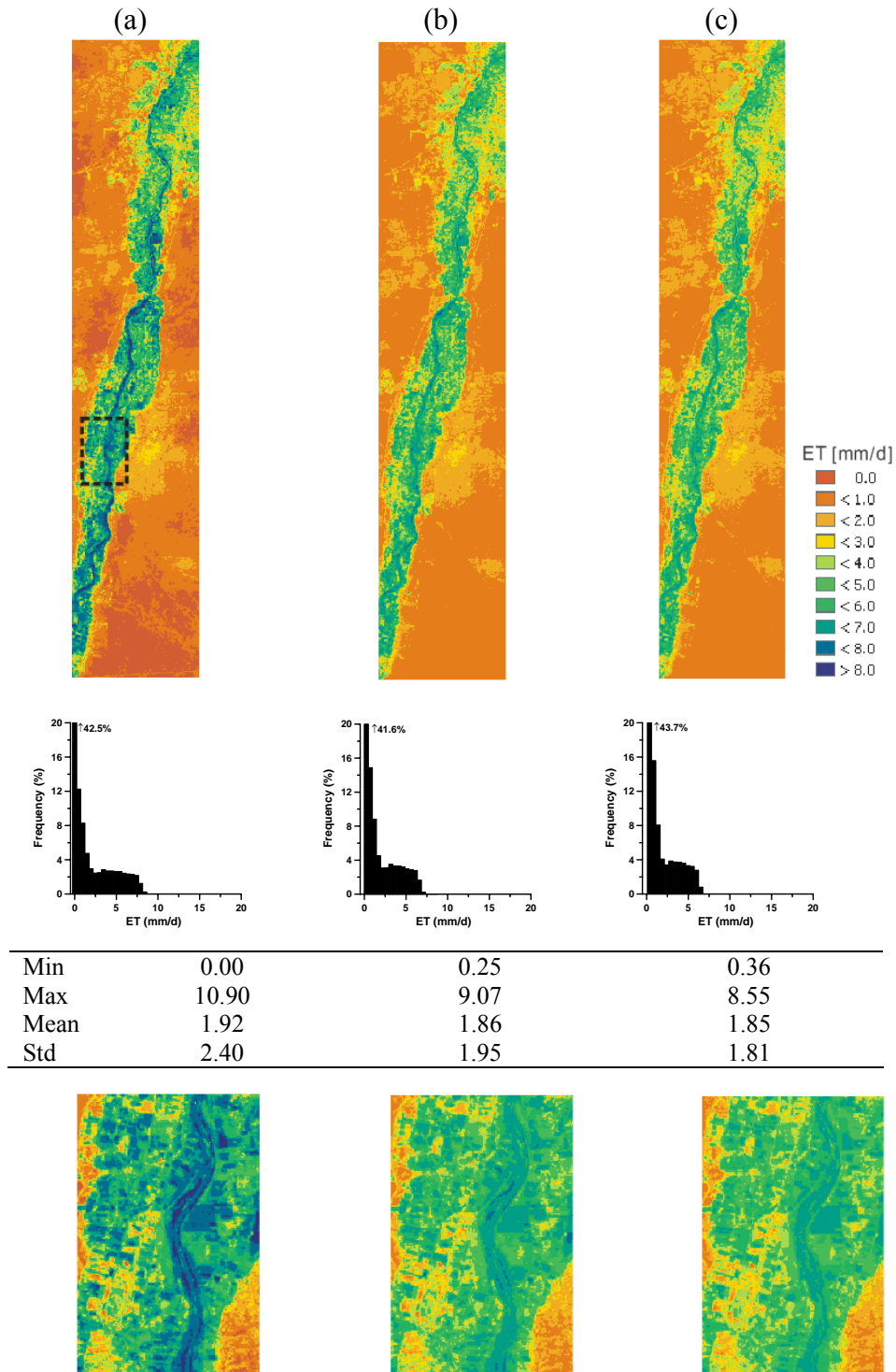
Figure 6.17. Down-scaled ET map from down-scaling output (daily ET) with regression. Linear regression is calculated (a) between MODIS-based ET of June and May, (b) between MODIS-based ET of June and aggregated (simple averaging) Landsat-based ET of May and (c) between MODIS-based ET of June and aggregated (nearest neighbor) Landsat-based ET of May.

|	(a)	(b)	(c)
Min	0.00	0.00	0.00
Max	15.00	12.39	20.00
Mean	1.97	1.52	1.53
Std	2.47	2.24	2.21
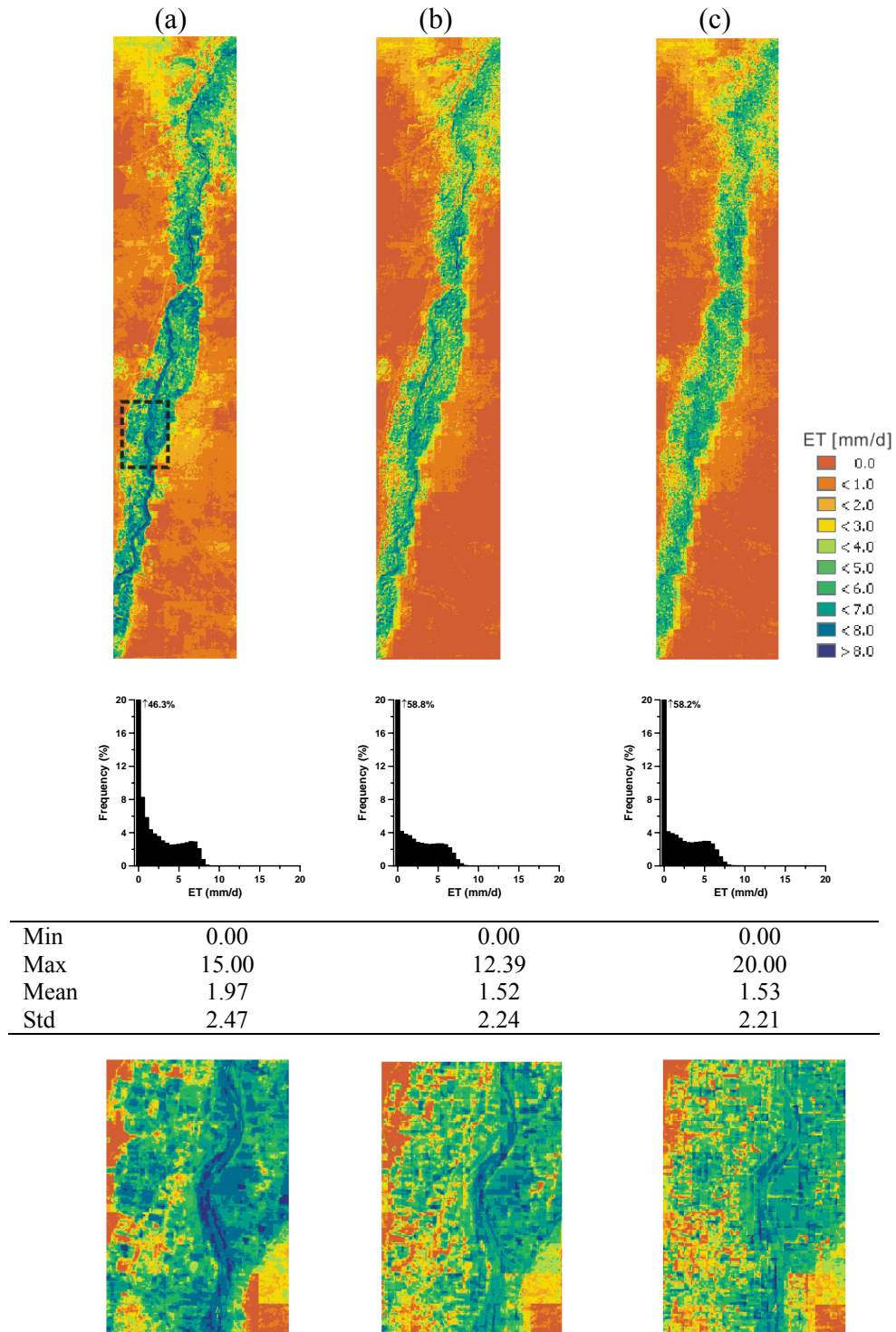
Figure 6.18. Down-scaled ET map from down-scaling inputs (T_s, albedo and NDVI) with subtraction. Pixel difference is calculated (a) between MODIS-based ET of June and May, (b) between MODIS-based ET of June and aggregated (simple averaging) Landsat-based ET of May and (c) between MODIS-based ET of June and aggregated (nearest neighbor) Landsat-based ET of May.

	(a)	(b)	(c)
Min	0.00	0.00	0.00
Max	17.27	8.08	7.45
Mean	1.85	1.34	1.29
Std	2.37	2.03	1.90
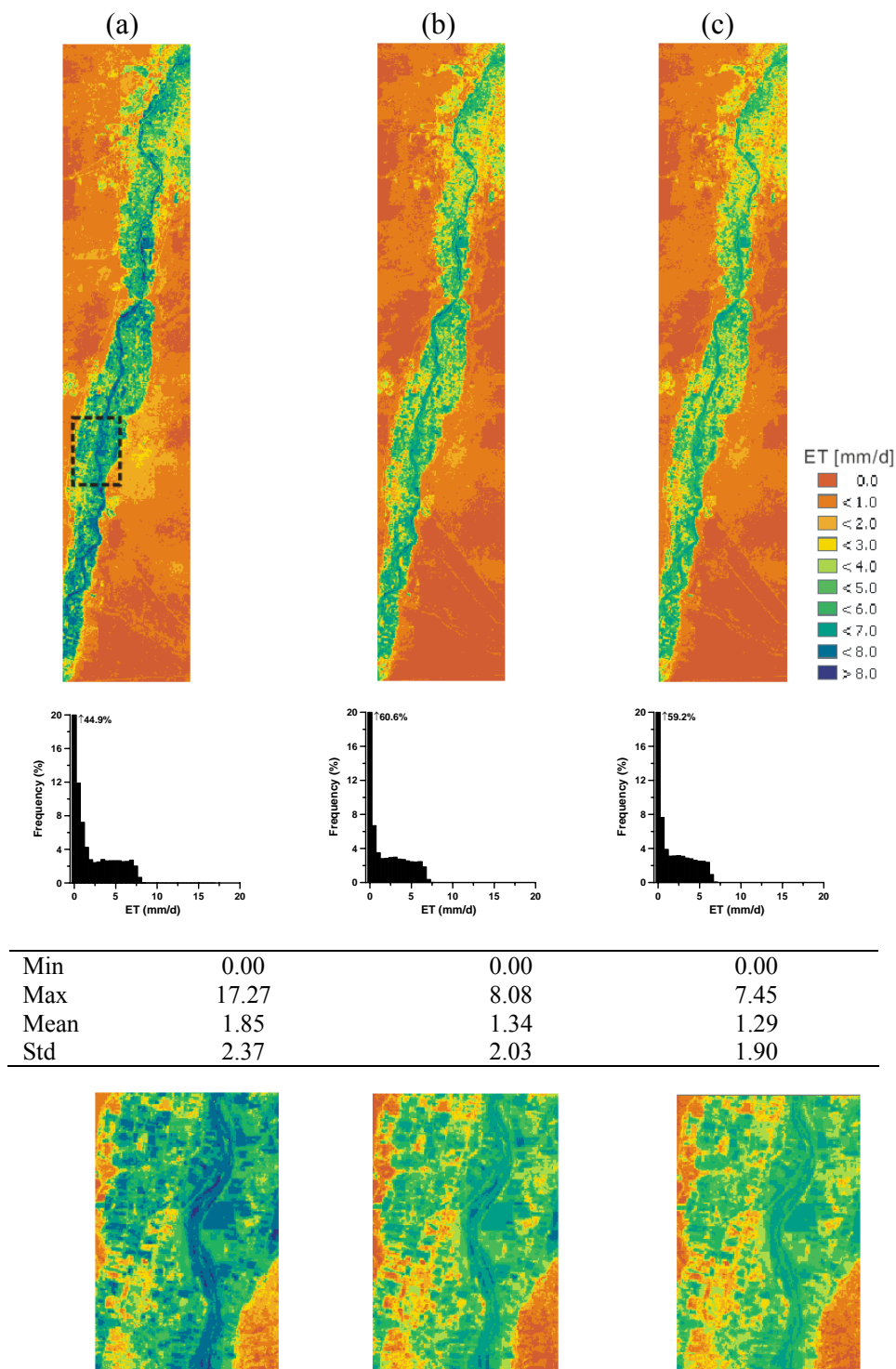
Figure 6.19. Down-scaled ET map from down-scaling inputs (T_s, albedo and NDVI) with regression. Linear regression is calculated (a) between MODIS-based ET of June and May, (b) between MODIS-based ET of June and aggregated (simple averaging) Landsat-based ET of May and (c) between MODIS-based ET of June and aggregated (nearest neighbor) Landsat-based ET of May.
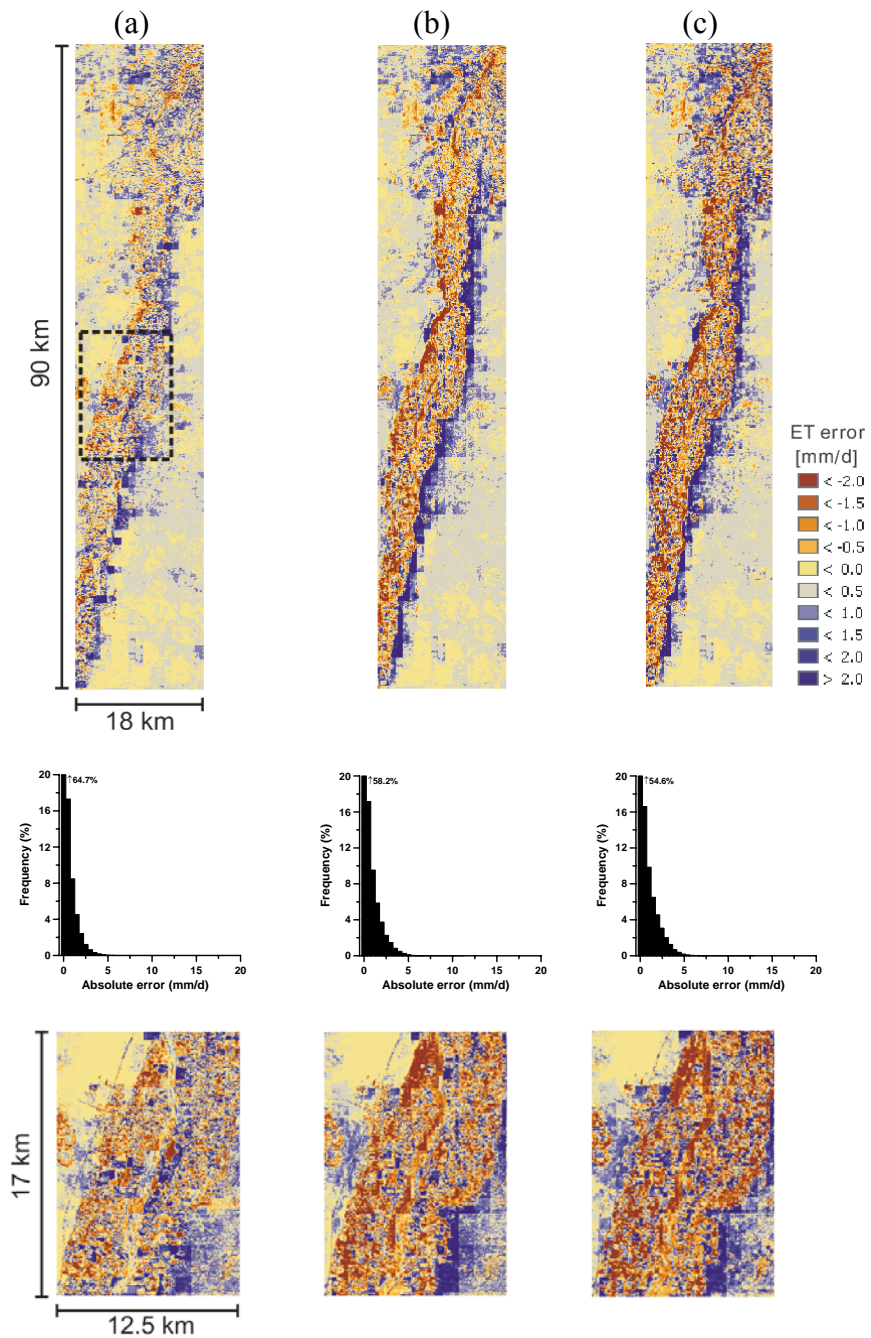
Figure 6.20. Example of the difference ET map between down-scaled ET (down-scaling output with subtraction) and Landsat-based ET of June at 30m resolution. Difference maps in (a), (b) and (c) were generated with the down-scaled maps shown in (a), (b) and (c) in Figure 6.12. Enlarged areas (12.5 by 17 km) shown at the bottom correspond to the dotted square of the upper images. Bin size of the difference histogram is 0.5 mm/d.
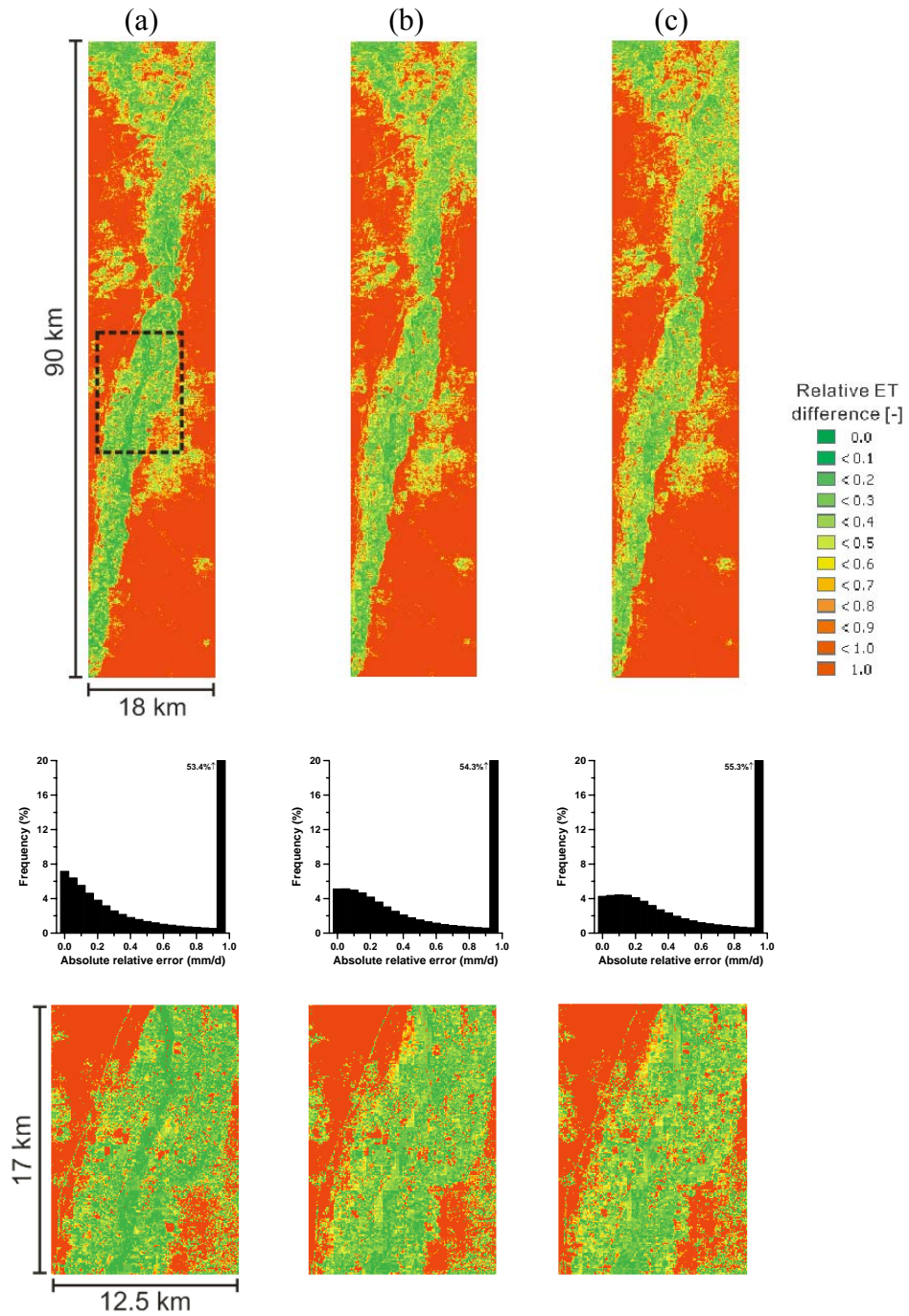
Figure 6.21. Example of the relative difference ET map between down-scaled ET (down-scaling output with subtraction) and Landsat-based ET of June at 30m resolution. Relative difference maps in (a), (b) and (c) were generated with the down-scaled maps shown in (a), (b) and (c) in Figure 6.12. Enlarged areas (12.5 by 17 km) shown at the bottom correspond to the dotted square of the upper images. Bin size of the relative difference histogram is 0.05 mm/d.

difficult to see where the location of the Rio Grande River is and to identify individual agricultural fields along the Rio Grande River in maps (b) and (c). Visual comparison of the spatial distribution of ET of down-scaled imagery against direct Landsat-based ET map on June 16, 2002 (Figure 6.8) reveals that visual agreement of (a) is best and (b) is better than (c). The somewhat blurrier pattern of down-scaled maps in (b) and (c) is also demonstrated in the basic statistics table. The standard deviation of down-scaled ET in (b) and (c) is smaller than the one from (a) as well as one from original Landsat-based ET (σ: 2.46 mm/d).

Mean values of the down-scaled ET map of June in Figure 6.16 are all greater than Landsat-based ET of May (μ: 1.79 mm/d), but interestingly the mean values are also greater than the mean value of the original June Landsat-based ET (μ: 1.81 mm/d). The greater mean values of the down-scaled ET map can be explained by the larger positive pixel-by-pixel difference between the two MODIS scale ET images than the difference between original Landsat-based ET of June and May. For instance, the differences in mean values between the MODIS-based ET in June and the May MODIS-based ET and aggregated ET maps from Landsat in May by using simple averaging and nearest neighboring are 0.09, 0.09 and 0.05 mm/d, respectively. Those differences are greater than the difference between original Landsat-based ET of June and May (0.02 mm/d). Therefore, when these differences between two MODIS-scale images were applied to Landsat-based ET on May 31, 2002, the down-scaled ET was higher than the original Landsat-based ET on June 16, 2002. The difference in the SEBAL outcome between Landsat 7 and MODIS is a result of slightly different band widths for each sensor. The

band widths of MODIS in the visible and near infrared, with the exception of Band 3, are narrower than those of Landsat 7. This results in different responses from the surface, which in turn may alter the computed surface albedo, *NDVI* and T_s.

6.4.2.2. Down-scaling with regression

The down-scaled maps in Figure 6.17 were produced by applying a linear regression obtained from two MODIS scale images to the Landsat-based ET map on May 31, 2002. Therefore, the overall spatial distribution of down-scaled imagery is similar to the original Landsat-based ET map of May. The down-scaled maps in Figure 6.17 show smoother pattern than those in Figure 6.16 since regression methodology is less vulnerable to the georeferencing difference between Landsat and MODIS images than the subtraction methodology. In Figure 6.17, the Rio Grande River and adjacent agricultural fields can be easily identified. Note that the standard deviation of the down-scaled maps in (b) and (c) is a lot smaller than the standard deviation from the direct Landsat-based ET of June (σ: 2.46 mm/d). This is because first the standard deviation of Landsat-based ET of May (σ: 2.15 mm/d) is smaller than the standard deviation of June imagery and second the slopes of the linear relationships between the two 250m resolution ET images in Figures 6.14 and 6.15 are smaller than 1.0. The minimum value of (c) in Figure 6.17 is greater and the maximum value of (c) is smaller than the ones from (a) and (b). The standard deviation of (c) is lowest. These differences are due to the fact that the regression line used to generate the down-scaled map of (c) has a bigger intercept (0.36) and smaller slope (0.84) than the ones from regression lines used for (a) and (b).

Regression methodology is a simpler procedure than subtraction methodology and produces a sharper imagery. Another advantage of regression over subtraction is that a few outliers hardly will affect the linear regression since so many pixels are available for the regression. Outliers can be caused by georeferencing disagreement among the different satellite images or by abrupt temporal changes between two different dates' images resulting from a rainstorm or irrigation over part of area. However, down-scaled maps with regression show that areas having low ET (desert and bare soil) can be relatively inaccurate, for example the minimum ET of (b) and (c) in Figure 6.16 is not zero but 0.25 and 0.36 mm/d respectively. The minimum of (a) in Figure 6.16 is zero. Smaller mean values of ET in Figure 6.18 than in Figure 6.16 are explained by the smaller slope (< 1.0) and bigger intercept (> 0.0) of T_s (Figure 6.13 – 6.15). This smaller slope and bigger intercept regression causes an increase in the pixel temperature of cold high ET areas, resulting in overall decreased ET.

6.4.2.3. Input and output down-scaling

The down-scaled ET maps in Figures 6.18 and 6.19 were generated after applying SEBAL with down-scaled 30m pixel size of SEBAL input parameters (T_s, albedo and *NDVI*) from 250m pixel size with subtraction and regression methodology, respectively. The disparity among the down-scaled ET maps of (a), (b) and (c) in Figures 6.18 and 6.19 is similar to the disparity among the maps in Figures 6.16 and 6.17. For example, maps of (a) in Figures 6.18 and 6.19 are sharper than the maps in (b) and (c) because again the georeferencing disagreement between the two MODIS images is a lot smaller than the one between MODIS and aggregated Landsat. The disparities in the

down-scaled maps between output and input down-scaling schemes were examined by

comparing the maps of Figure 6.16 against Figure 6.18 as well as Figure 6.17 against

Figure 6.19.

Comparing maps in Figures 6.16 and 6.18 reveals that the maximum values of

ET from input down-scaling (a: 10.9, b: 12.0 and c: 11.7 mm/d) are smaller than the ones

from the output down-scaling (a: 15.0, b: 12.4 and c: 20.0 mm/d). However, mean values

of (b: 1.52 mm/d) and (c: 1.53 mm/d) in Figure 6.18 are smaller than the ones (b: 1.89

and c: 1.88 mm/d) in Figure 6.16. This is because the maps in Figures 6.18 have more

pixels with low ET values (0 to 0.5 mm/d) and fewer high ET areas than the maps in

Figures 6.16. Few differences exist in standard deviation between maps in Figures 6.16

and 6.18. For the Figures 6.17 and 6.19, although maximum of (a) as 17.3 in Figure 6.19

is larger than the one (10.9 mm/d) in Figure 6.17, the mean values of (b) and (c) as 1.34

and 1.29 mm/d in Figure 6.19 are smaller than the ones (1.86 and 1.85) in Figure 6.17.

Just as was found in the comparison of Figures 6.16 and 6.18, the input down-scaled

maps in Figure 6.19 have more pixels with low ET values (0 to 0.5 mm/d) than the output

down-scaled maps in Figure 6.17, however the differences in standard deviations

between the maps in Figures 6.17 and 6.19 are small. A difference between input and

output down-scaled maps results from first the imperfection of down-scaling procedure

which leads a disparity between down-scaled input parameters and parameters from

original MODIS sensor. Second, the disparity between input and output down-scaling is

also due to the non-linearity of SEBAL model and application of different dT-T_s

relationship for different pixel size imagery. For the input down-scaling

$dT = 0.181 \cdot T_s - 54.71$ was used and $dT = 0.209 \cdot T_s - 64.13$ was used for the output

down-scaling. That is, even with the linearly related two input data set having different

spatial resolutions, the down-scaled SEBAL estimated ET (output down-scaled) is not

equal to the ET value from SEBAL after down-scaling input parameters (input down-

scaled). Nevertheless, as demonstrated by visual examination of the spatial distribution of

ET in Figures 6.16 (6.19, the contrast as well as the basic patterns (high and low values

and their relative locations) of ET between output down-scaling and input down-scaling

show only slight disagreement. The input down-scaling procedure is more complicated

than the output down-scaling, since it needs to disaggregates three images compare to one

image for output down-scaling. In addition, longer SEBAL process time is required for

input down-scaling because input images have a higher resolution and a larger file size.

6.4.3. Limitation of the Proposed Down-scaling Method

The proposed down-scaled methodology does not produce always a reliable

results. This section analyzes the differences in down-scaled images and investigates the

model limitations.

6.4.3.1. Difference between down-scaled ET and original Landsat-based ET

Figure 6.20 present examples of spatial distributions and frequency of the

difference images of down-scaled ET map which was created by down-scaling output

with subtraction. Basic statistics of absolute difference of 12 different down-scaled ET

maps against original Landsat-based ET of June 16, 2002 are shown in Table 6.3. Based

Table 6.3. Basic statistics of the difference [mm/d] of down-scaled ET against original Landsat-based ET of June 16, 2002. (note: mean and standard deviation are calculated from the absolute difference).

Down-scaling approach	Down-scaling operation	ID	Mean absolute difference	Standard deviation
Output	Subtraction	1a	0.53	0.72
		1b	0.70	0.90
		1c	0.78	0.99
	Regression	2a	0.57	0.70
		2b	0.72	0.64
		2c	0.80	0.64
Input	Subtraction	3a	0.55	0.77
		3b	0.67	0.86
		3c	0.78	1.15
	Regression	4a	0.54	0.70
		4b	0.62	0.86
		4c	0.66	0.90

on visual inspection of Figure 6.20, the spatial distribution of difference image of (a) is much smoother (fewer brown and blue points) than in (b) and (c). Basic statistics in Table 6.3 show that the mean and standard deviation values of (a) are smaller than those from (b) and (c). The greatest mean and standard deviation of differences are found in (c). The incidence of smoother difference and smaller mean in (a) than (b) and (c) indicates that down-scaling with MODIS-derived maps produces ET maps that are close to the original Landsat-based ET map. This is another confirmation that georeferencing disagreement is the most troublesome component in applying the disaggregation schemes suggested in this study.

Example of the spatial distributions and frequency of the absolute relative difference images of down-scaled ET map by applying down-scaling output with subtraction are shown in Figure 6.21. Basic statistics of absolute relative difference of 12 different down-scaled ET maps against original Landsat-based ET of June 16, 2002 are shown in Table 6.4. The absolute relative difference value ranges from zero to infinity. The infinity relative difference values occur when the original Landsat-based ET is much smaller than the down-scaled ET. The infinity values were constrained to 1.0. Pixels having zero values either in the Landsat-based ET or in the down-scaled ET images are also assigned an absolute relative difference of one (red-colored).

3-D frequency plots between down-scaled daily ET and absolute relative difference against Landsat-based ET created in Figure 6.21. Both of the spatial distribution of relative difference maps (Figure 6.20) and three 3-D plots (Figure 6.22)

Table 6.4. Basic statistics of relative difference [-] between down-scaled ET and original Landsat-based ET of June 16, 2002. (note: mean and standard deviation are calculated from the absolute relative difference).

Down-scaling approach	Down-scaling operation	ID	Mean absolute relative difference	Standard deviation
Output	Subtraction	1a	0.66	0.40
		1b	0.68	0.39
		1c	0.69	0.38
	Regression	2a	0.68	0.39
		2b	0.68	0.38
		2c	0.68	0.38
Input	Subtraction	3a	0.67	0.40
		3b	0.74	0.37
		3c	0.75	0.36
	Regression	4a	0.67	0.40
		4b	0.70	0.36
		4c	0.70	0.35
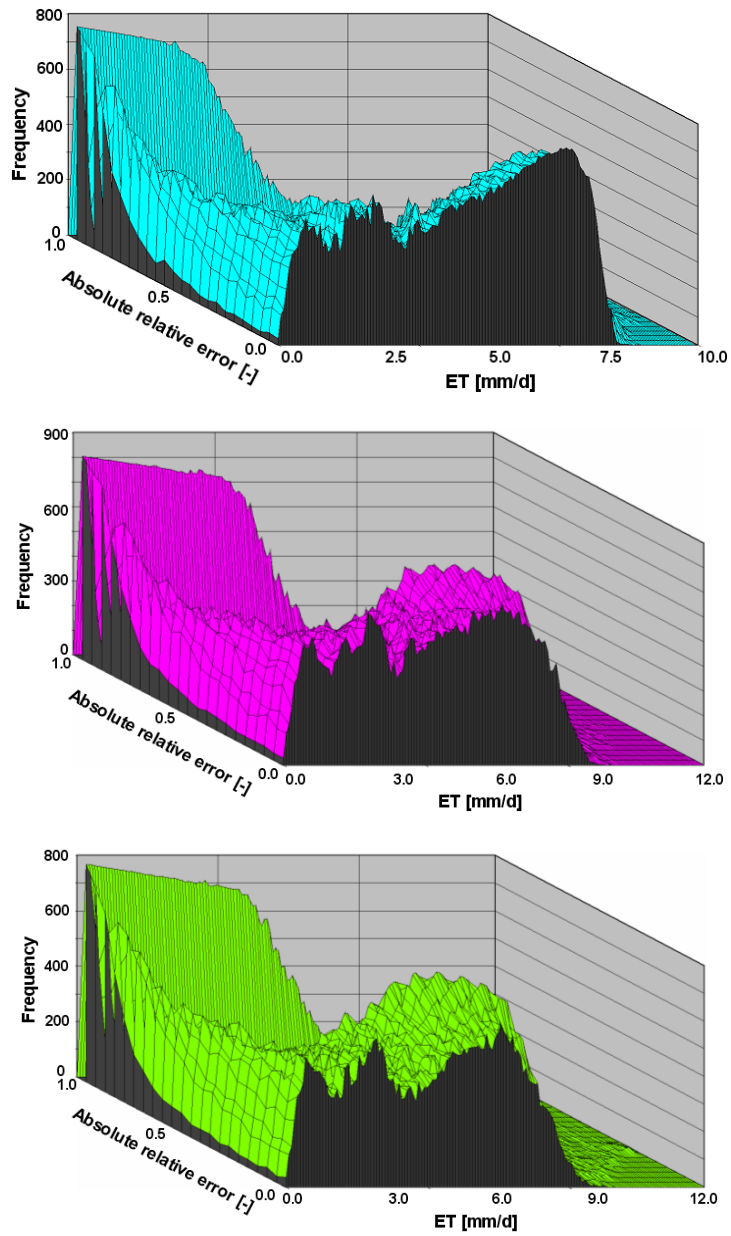
Figure 6.22. 3D frequency plot between down-scaled daily ET and absolute relative difference against Landsat estimated ET on June 16, 2002. Down-scaled image were generated by down-scaling output with subtraction (top) between MODIS-based ET of June and May, (middle) between MODIS-based ET of June and aggregated (simple averaging) Landsat-based ET of May and (bottom) between MODIS-based ET of June and aggregated (nearest neighbor) Landsat-based ET of May.

show that large absolute relative difference occurs in areas having low ET while areas

having high ET exhibit small relative differences. There are several areas inside of the

riparian area in Figure 6.21 having large relative differences. These are mainly

agricultural fields that show dynamic temporal changes in ET. Because it is impossible to

determine which field (at the MODIS sub-pixel scale) has received irrigation after the

previous Landsat image, it is impossible to derive the exact down-scaled ET distribution

within each MODIS pixel. In MODIS pixels with high frequency temporal changes the

proposed methods provide an average ET value but not a correct spatial distribution of

ET values. In Figure 6.22, there are some points having 1.0 relative difference with high

daily ET. These points are considered as unreliable down-scaled pixels where the down-

scaled ET is a lot higher than the original Landsat-based ET. These points are due to

either areas having dynamic temporal changes or by georeferencing disagreement

between down-scaled ET and original Landsat-based ET as discussed above.

The mean of the absolute difference ranged from 0.53 to 0.80 mm/d (Table 6.3).

The mean absolute difference of down-scaling ID #1 (subtraction or regression between

two MODIS-based estimates) is bigger than down-scaling ID #2 (subtraction or

regression between MODIS and simple averaged Landsat estimates). The mean absolute

difference of down-scaling ID #3 (subtraction or regression between MODIS and nearest

neighbored Landsat estimates) is lowest. This results also support that down-scaling with

two MODIS-derived maps produces better down-scaled ET maps compared to using

aggregated Landsat-derived map, because of smaller georeferencing disagreement exists

between two MODIS-based estimates. The mean of the absolute relative difference

ranged from 0.66 to 0.75 (Tables 6.3 and 6.4). The mean absolute difference of down-scaling ID #1 is bigger than down-scaling ID #2 and ID #3 except 'output down-scaling with regression'. This is because slopes of regression of ET in Figures 6.14 and 6.15 as 0.90 and 0.84, respectively, are smaller than the one in Figure 6.13 (1.14). The shallower slope generates down-scaled ET with tighter range therefore smaller standard deviation. Tables 6.3 and 6.4 also support that the difference in down-scaled ET maps between input and output down-scaling schemes was not significant. However, any slight difference between input and output down-scaling should be traced back to the difference between the down-scaled input parameters and the original parameters from MODIS imagery.

6.4.3.2. Georeferencing disagreement among images

Figure 6.23 presents the examples of a pixel-by-pixel difference map between two MODIS ET maps and between MODIS and aggregated Landsat-based ET maps to illustrate the georeferencing disagreement among images. Each image has a georeferencing difference of a size of one or two pixels; therefore, the disparity of the georeferencing accordance between images is easily more than a couple of pixels size. Also note that the georeferencing match between images from different satellite sensors is poorer than the ones from same sensors. As shown in Figure 6.23, the difference map between two MODIS-based ET maps in (a) shows a smoother pattern (less extreme values) than the ones in (b) and (c). Difference maps in (b) and (c), areas with apparently high ET differences (± 2.0 mm/d), shown with brown and blue colors, are observed along the boundary between Rio Grande River riparian areas and surrounding deserts. Since

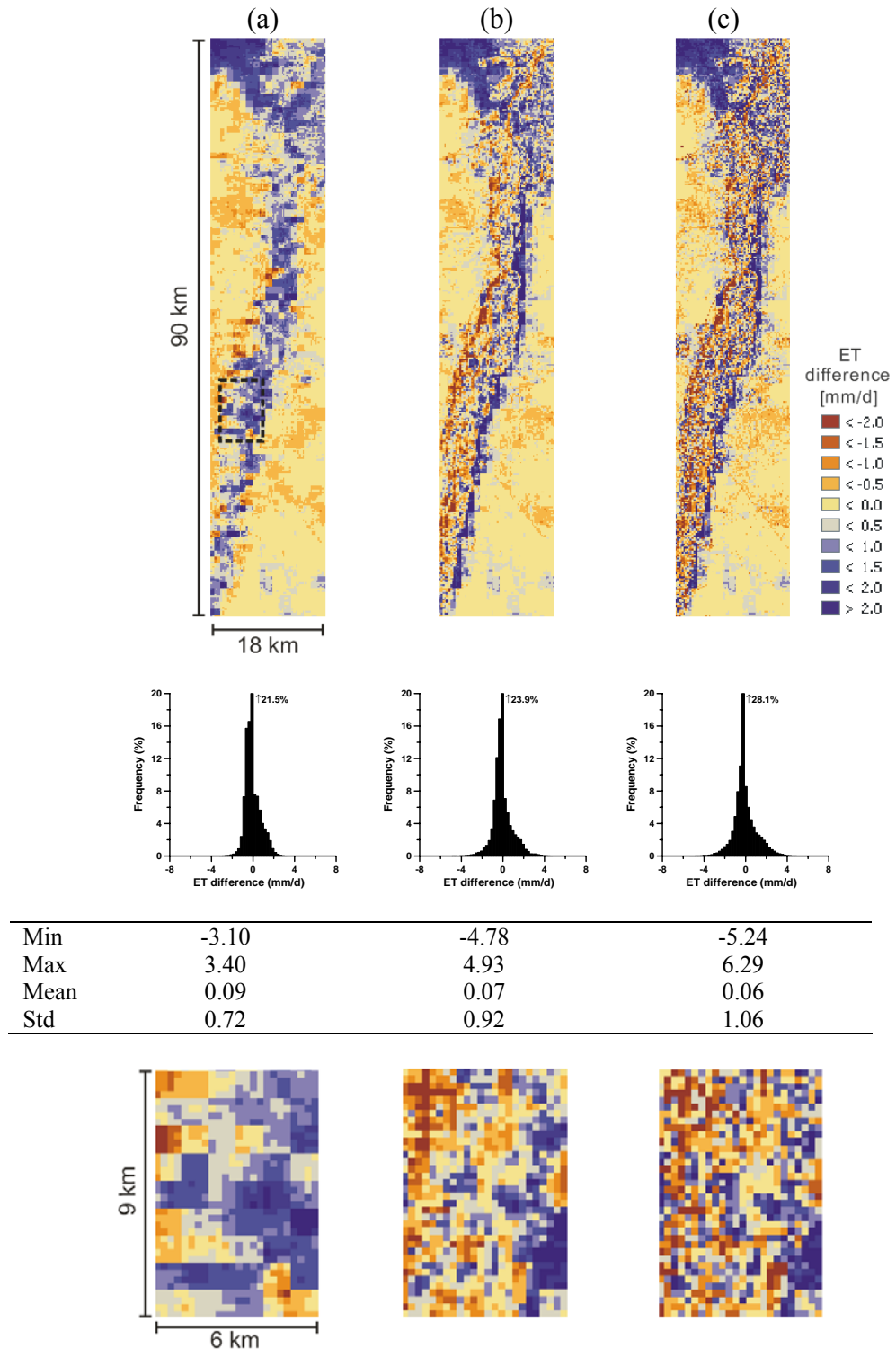|	(a)	(b)	(c)
Min	-3.10	-4.78	-5.24
Max	3.40	4.93	6.29
Mean	0.09	0.07	0.06
Std	0.72	0.92	1.06

Figure 6.23. Pixel by pixel difference ET map (a) between MODIS-based ET maps of June and May, (b) between MODIS-based ET of June and Landsat-based ET of May (250m resolution by simple averaging), (c) between MODIS-based ET of June and Landsat-based ET of May (250m resolution by nearest neighbor). Bin size of the ET difference in the histogram is 0.25 mm/d.

difference maps in (b) and (c) were produced by subtracting MODIS-based ET from

Landsat-based ET [$ET_{Landsat} - ET_{MODIS}$], blue-colored pixels of the difference maps of (b)

and (c) represent MODIS-based ET is considerably higher than Landsat-based ET. Of

course, areas showing brown-colored pixels represent points where the ET from Landsat

is considerably higher than the ET from MODIS-based imagery. These extremes are

mostly due to disagreement in image georeferencing match between Landsat- and

MODIS-scale imagery. Dealing with the georeferencing of two maps with spatial

resolutions differing by an order of magnitude is not an easy problem. In fact, it was

impossible for us to identify accurate common ground control points from both Landsat

and MODIS imagery directly because of the huge difference in the spatial resolution.

Therefore, it was very difficult to perform georeferencing two different-scale satellite

images correctly. Maps in Figure 6.23 show that georeferencing disagreement causes

abrupt ET changes at the boundaries between riparian (high ET) and desert (low ET)

areas. The georeferencing difference also appears in histograms. Histograms in Figure

6.23 show that the range between minimum and maximum of (b) and (c) is bigger than

the range in (a). In addition, since ET in the month of June is higher than the month of

May, histograms of ET difference ($ET_{June} - ET_{May}$) should be right-skewed because the

data have more positive values than negative values. However, as shown in histograms of

(b) and (c) compared to (a), it tends to be a normal distribution. This also indicates more

georeferencing difference in map (c) in which the Landsat-based ET map was aggregated

from 30 to 250 m resolution by nearest neighbor, while simple averaging was used to

generate map (b).

6.4.3.3. Areas having dynamic temporal changes

As mentioned earlier, subtraction methodology assumes fine-scale variability within one MODIS scale pixel is unchanged during the time interval between previous and subsequent imagery. To examine the difference of fine-scale variability in the time interval between previous and subsequent fine-resolution imagery, the spatial distribution of Landsat-based ET on May 31, 2002 and June 16, 2002 was examined. No precipitation was recorded during this 16 days period. Three different land use types including riparian, desert, and agricultural field are shown in the area of 1000 m by 1000 m (Figure 6.24). As shown in Figure 6.24, the spatial variability of daily ET in riparian and desert areas is consistent between the 16 days interval. However, agricultural fields show dynamic changes in daily ET between the 16 days apart due to irrigation. Therefore, subtraction methodology can produce a reliable down-scaled image in less dynamic (for example, no localized rainfall event) areas such as riparian and desert environments; however, it is impossible to precisely predict down-scaled imagery in areas experiencing dynamic changes such as agricultural fields.

Down-scaling with regression methodology is dependent upon regression slope and intercept between two 250m resolution images. Since the regression does not also allow abrupt changes between 16 days apart. For example, this study does not allow more than 20% in ET changes between May 31 and June 16. Therefore, regression method also has limitation to down-scale areas experiencing a dynamic temporal change in short period of time.
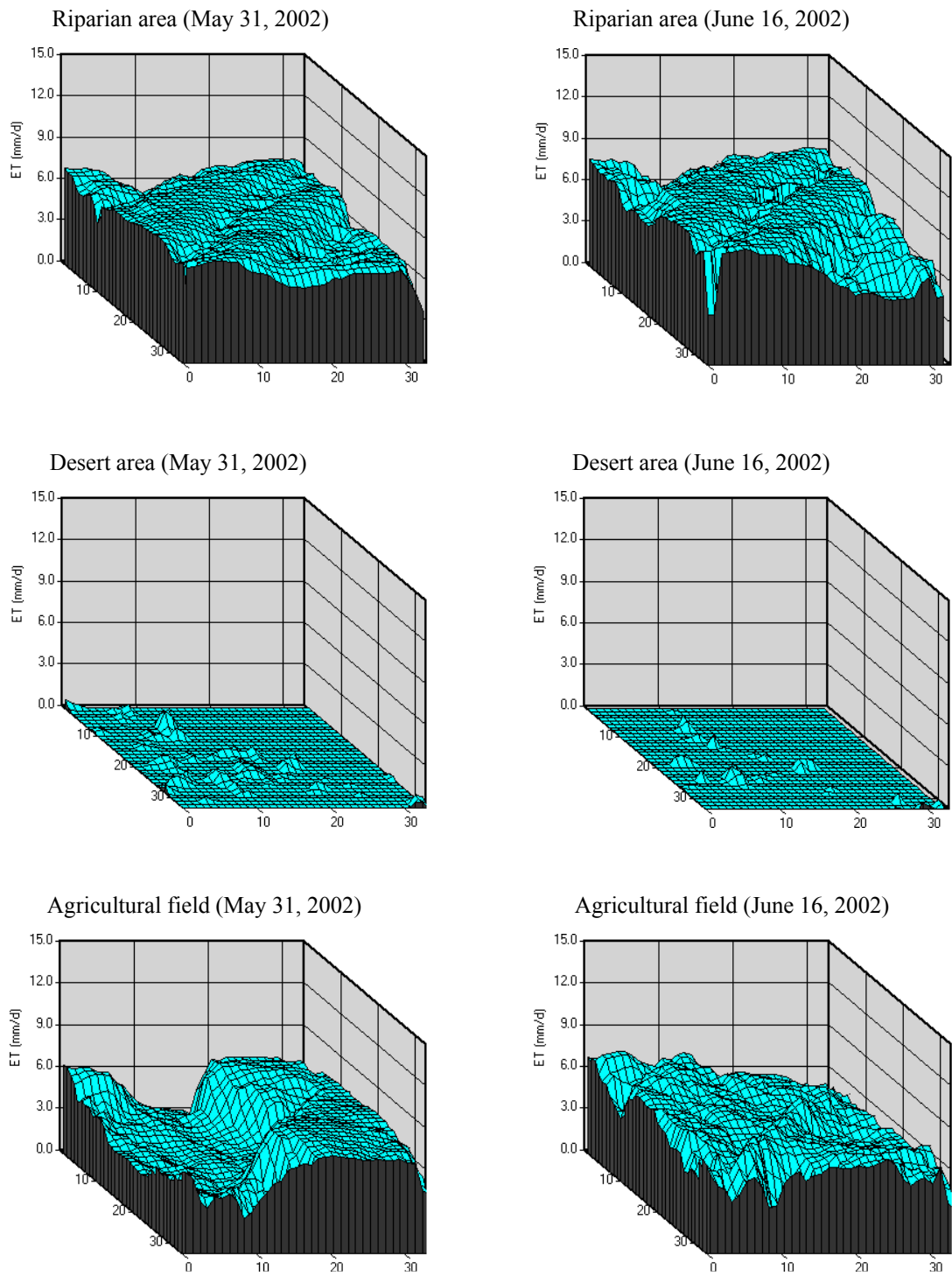
Figure 6.24. 3-D spatial distribution of Landsat-based ET of different land cover types at 30m resolution in area of MODIS pixel (1000m by 1000m) on May 31, 2002 and June 16, 2002.

6.5. CONCLUSIONS

Georeferencing disagreement between Landsat and MODIS images is a most significant issue for the application of the down-scaling schemes suggested in this study. Regression methodology is less vulnerable to the georeferencing difference than subtraction methodology. Using two MODIS-based estimates for pixel-by-pixel difference or linear regression in applying subtraction or regression produced more reliable results than using aggregated Landsat-based estimates. This is because difference due to georeferencing disagreement between two MODIS-based estimates is smaller than the difference between MODIS-based and aggregated Landsat-based estimates. When using aggregated Landsat-based estimates, simple averaging is preferred over the nearest neighboring. Because simple averaging produces images having less georeferencing disagreement. Nearest neighbor resampling selects only the middle pixel located in the calculated coordinates which causes larger differences. Difference images also confirm that down-scaling with two MODIS-derived maps rather than using an aggregated Landsat-based map produces ET maps that are better matched with the original Landsat-based map.

Based on our results, the difference in down-scaled ET maps between input and output down-scaling schemes was not significant. However, since input down-scaling procedure is more complicated and requires longer SEBAL process time than output down-scaling, we recommend the output down-scaling procedure over input down-scaling. This study also indicates that down-scaled ET values from coarse resolution

remotely sensed data are not always reliable. In particular, down-scaled sites need to be in less temporally dynamic conditions at the coarse MODIS scale in order to produce more reliable results. Relative difference images show that large relative difference occurs in desert areas with low to zero ET rates, while areas having high ET rates show small relative difference.

Despite encountering some issues, this study has shown that all of the proposed down-scaling methodologies could be used to predict reasonable spatial patterns of ET within each coarse MODIS-scale pixel over the Middle Rio Grande Basin. However, since output down-scaling is simpler than input down-scaling and regression methodology between MODIS images is the least vulnerable to georeferencing disagreement, it is concluded that output down-scaling with regression between two MODIS-based images (Down-scaling 2(a) in Figure 6.4) is the most preferred scheme among twelve proposed down-scaling schemes. The least preferred scheme is input down-scaling with subtraction between a MODIS image and a nearest neighbor aggregated Landsat image (Downscaling 3(c) in Figure 6.4).

ACKNOWLEDGEMENT

REFERENCES

Allen, R.G., M. Tasumi, and R. Trezza. 2007. Satellite-based Energy Balance for Mapping Evapotranspiration with Internalized Calibration (METRIC) – Model. Journal of Irrigation and Drainage Engineering 133:380-394.

Anderson, M.C., J.M. Norman, J.R. Mecikalski, R.D. Torn, W.P. Kustas, and J.B. Basara. 2004. A multiscale remote sensing model for disaggregating regional fluxes to micrometeorological scales. Journal of Hydrometeorology 5:343-363.

Atkinson, P.M., and A.R.L. Tatnall. 1997. Neural networks in remote sensing. International Journal of Remote Sensing 18:699-709.

Bastiaanssen, W.G.M., M. Menenti, R.A. Feddes, and A.A.M. Holtslag. 1998. A remote sensing surface energy balance algorithm for land (SEBAL). Part 1: Formulation. Journal of Hydrology 212-213:198-212.

Bastiaanssen, W.G.M., M.D. Ahmad, and Y. Chemin. 2002. Satellite surveillance of evaporative depletion across the Indus Basin. Water Resources Research 38:1273-1281.

Bastiaanssen, W.G.M., E.J.M. Noordman, H. Pelgrum, G. Davids, B.P. Thoreson, and R.G. Allen. 2005. SEBAL model with remotely sensed data to improve water-resources management under actual field conditions. Journal of Irrigation and Drainage Engineering 131:85-93.

Bezdek, J.C., R. Ehrlich, and W. Full. 1984. FCM: the fuzzy c-means clustering algorithm. Computers and Geosciences 10:191-203.

Bian, L., R. Butler, D.A. Quattrochi, and P.M. Atkinson. 1999. Comparing effects of aggregation methods on statistical and spatial properties of simulated spatial data. Photogrammetry and Remote Sensing 65:73-84.

Bierkens, M.F.P., P.A. Finke, and D.E. Willigen. 2000. Upscaling and downscaling methods for environmental research. Wageningen University and Research Centre, Kluwer Academic Publishers.

Brown, D.G., L. Bian, and S.J. Walsh. 1993. Response of a distributed watershed erosion model to variations in input data aggregation levels. Computers and Geosciences 19:499-509.

Brutsaert, W., and M. Sugita. 1992. Application of self-preservation in the diurnal evolution of the surface energy budget to determine daily evaporation. Journal of Geophysical Research 97:18,377-18,382.

Carper, J.W., T.M. Lillesand, and R.W. Kiefer. 1990. The use of intensity-hue-saturation transformations for merging SPOT panchromatic and multispectral image data. Photogrammetric Engineering and Remote Sensing 56:459-467.

Carrion, D., M. Gianinetto, and M. Scaioni. 2002. GEOREF: a Software for Improving the Use of Remote Sensing Images in Environmental Applications. In Proc. of IEMSS 2002 Int. Meeting, 24-27 June, Lugano, Switzerland:360-366.

Chavez, P.S., S.C. Sides, and J.A. Anderson. 1991. Comparison of three different methods to merge multiresolution and multispectral data: Landsat TM and SPOT Panchromatic. Photogrammetric Engineering and Remote Sensing 57:295-303.

Cleverly, J.R., C.N. Dahm, J.R. Thibault, D.J. Gilroy, and J.E.A. Coonrod. 2002. Seasonal estimates of actual evapotranspiration from Tamarix ramosissima stands using 3-dimensional eddy covariance. Journal of Arid Environments 52:181-197.

Costigan, K.R., J.E. Bossert, and D.L. Langley. 2000. Atmospheric/hydrologic models for the Rio Grande Basin: simulations of precipitation variability. Global and Planetary Change 25:83-110.

Crago, R.D. 1996. Conservation and variability of the evaporative fraction during the daytime. Journal of Hydrology 180:173-194.

De Cola, L. 1994. Simulating and mapping spatial complexity using multi-scale techniques. International Journal of Geographical Information Systems 8:411-427.

Elmore, A.J., J.F. Mustard, and S.J. Manning. 2002. Regional patterns of plant community response to changes in water: Owens Valley, California. Ecological Applications 13:443-460.

Eugenio, F., and F. Marqués. 2003. Automatic Satellite Image Georeferencing Using a Contour-Matching Approach. IEEE Transactions on Geoscience and Remote Sensing 41:2869-2880.

Farah, H.O., and W.G.M. Bastiaanssen. 2001. Spatial variations of surface parameters and related evaporation in the Lake Naivasha Basin estimated from remote sensing measurements. Hydrological Processes 15:1585-1607.

Fleming, K., J.M.H. Hendrickx, and S.-H. Hong. 2005. Regional mapping of root zone soil moisture using optical satellite imagery. Proceedings of International Society for Optical Engineering, SPIE 5811:159-170.

Foody, G.M., and D.P. Cox. 1994. Sub-pixel land cover composition estimation using a linear mixture model and fuzzy membership functions. International Journal of Remote Sensing 15:619-631.

Hafeez, M., M. Andreini, J. Liebe, J. Friesen, A. Marx, and N.v.d. Giesen. 2006. Hydrological parameterization through remote sensing in Volta Basin, West Africa. International Journal of River Basin Management 4:1-8.

Hendrickx, J.M.H., and S.-H. Hong. 2005. Mapping sensible and latent heat fluxes in arid areas using optical imagery. Proceedings of International Society for Optical Engineering, SPIE 5811:138-146.

Hong, S.-H., J.M.H. Hendrickx, and B. Borchers. 2005. Effect of scaling transfer between evapotranspiration maps derived from LandSat 7 and MODIS images. Proceedings of International Society for Optical Engineering, SPIE 5811:147-158.

Hong, S.-H., J. Kleissl, J.M.H. Hendrickx, R.G. Allen, W.G.M. Bastiaanssen, R.L. Scott, and A.L. Steinwand. 2008. Evaluation of SEBAL for mapping energy balance fluxes in arid riparian areas using remotely sensed optical imagery. Water Resources Research (in preparation).

Jackson, T.J., J. Schmugge, and E.T. Engman. 1996. Remote sensing applications to hydrology: soil moisture. Hydrological Sciences Journal 41:517-530.

Justice, C.O., A. Belward, J. Morisette, P. Lewis, J. Privette, and F. Baret. 2000. Developments in the 'validation' of satellite sensor products for the study of the land surface. International Journal of Remote Sensing 21:3383–3390.

Kanellopoulos, I., A. Varfis, G.G. Wilkinson, and J. Megier. 1992. Land cover discrimination in SPOT HRV imagery using an artificial neural network: a 20 class experiment. International Journal of Remote Sensing 13:917-924.

Kerdiles, H., and M.O. Grondona. 1996. NOAA-AVHRR NDVI decomposition and subpixel classification using linear mixing in the Argentinean Pampa. International Journal of Remote Sensing 16:1303-1325.

Kustas, W.P., J.M. Norman, M.C. Anderson, and A.N. French. 2003. Estimating subpixel surface temperatures and energy fluxes form the vegetation index-radiometric temperature relationship. Remote Sensing of Environment 85:429-440.

Lam, N., and D.A. Quattrochi. 1992. On the issues of scale, resolution, and fractal analysis in the mapping sciences. Professional Geographer 44:88-98.

Liang, S. 2004. Quantitative Remote Sensing of Land Surfaces John Wiley and Sons, Inc.

Ma, Y., J. Wang, R. Huang, G. Wei, M. Menenti, Z. Su, Z. Hu, F. Gao, and J. Wen. 2003. Remote sensing parameterization of land surface heat fluxes over arid and semi-arid areas. Advances in Atmospheric Sciences 20:530-539.

Maayar, M.E., and J.M. Chen. 2006. Spatial scaling of evapotranspiration as affected by heterogeneities in vegetation, topography, and soil texture. Remote Sensing of Environment 102:33-51.

Mark, D.M., and P.B. Aronson. 1994. Scale dependent fractal dimensions of topographic surfaces: An empirical investigation with applications in geomorphology and computer mapping. Mathematical Geology 16:671-683.

Mecikalski, J.R., G.R. Diak, M.C. Anderson, and J.M. Norman. 1999. Estimating fluxes on continental scales using remotely-sensed data in an atmospheric-land exchange model. Journal of Applied Meteorology 38:1352-1369.

Moran, M.S., A.F. Rahman, J.C. Washburne, and W.P. Kustas. 1996. Combining the Penman-Monteith equation with measurements of surface temperature and reflectance to estimate evaporation rates of semiarid grassland. Agricultural and Forest Meteorology 80:87-109.

Nellis, M.D., and J.M. Briggs. 1989. The effect of spatial scale on Konza landscape classification using textural analysis. Landscape Ecology 2:93-100.

Price, D.T., D.W. McKennery, I.A. Nalder, M.T. Hutchinson, and J.L. Kesteven. 2000. A comparison of two statistical methods for spatial interpolation of Canadian monthly mean climate data. Agricultural and Forest Meteorology 101:81-94.

Rigo, G., E. Parlow, and D. Oesch. 2006. Validation of satellite observed thermal emission with in-situ measurements over an urban surface. Remote Sensing of Environment 104:201-210.

Schowengerdt, R.A. 1997. Models and methods for image processing. Second edition ed. Academic Press, San Diego.

Scott, R.L., J.W. Shuttleworth, G. D.C., and M.I. T. 2000. The water use of two dominant vegetation communities in a semiarid riparian ecosystem. Agricultural and Forest Meteorology 105:241-256.

Seguin, B., J.-P. Lagouarde, and M. Saranc. 1991. The assessment of regional crop water conditions from meteorological satellite thermal infrared data. Remote Sensing of Environment 35:141-148.

Seguin, B.D., and B. Itier. 1983. Using midday surface temperature to estimate daily evapotranspiration from satellite thermal IR data. International Journal of Remote Sensing 4:371-383.

Settle, J.J., and N.A. Drake. 1993. Linear mixing and the estimation of ground cover proportions. International Journal of Remote Sensing 14:1159-1177.

Shettigara, V.K. 1992. A generalized component substitution technique for spatial enhancement of multispectral images using a higher resolution data set. Photogrammetric Engineering and Remote Sensing 58:561-567.

Shuttleworth, W.J., R.J. Gurney, A.Y. Hsu, and J.P. Ormsby. 1989. The variation in energy partition at surface flux sites. Proceedings of the IAHS Third International Assembly, Baltimore, MD. 186:67-74.

Stoms, D. 1992. Effects of habitat map generalization in biodiversity assessment. Photogrammetric Engineering and Remote Sensing 58:1587-1591.

Stromberg, J.C. 1998. Dynamics of Fremont cottonwood (Populus fremontii) and saltcedar (Tamarix chinensis) populations along the San Pedro River, Arizona. Journal of Arid Environments 40:133-155.

Tasumi, M., R.G. Allen, and W.G.M. Bastiaanssen. 2000. The theoretical basis of SEBAL. Appendix A of Morse et al. (2000). Idaho Department of Water Resources, Idaho.

Tasumi, M. 2003. Progress in operational estimation of regional evapotranspiration using satellite imagery, Ph.D. Thesis, University of Idaho, Moscow, Idaho.

Townshend, J.R.G., and C.O. Justice. 1988. Selecting the spatial resolution of satellite sensors required for global monitoring of land transformations. International Journal of Remote Sensing 9:187-236.

Turner, M.G., R.V. O'Neil, R.H. Gardner, and B.T. Milne. 1989. Effects of changing spatial scale on the analysis of landscape pattern. Landscape Ecology 3:153-162.

Valor, E., and V. Caselles. 1996. Mapping land surface emissivity from NDVI: Application to European, African, and South American areas. Remote Sensing of Environment 57:167-184.

Vieux, B.E. 1993. DEM Aggregation and smoothing effects on surface runoff modeling. Journal of Computing in Civil Engineering 7:310-338.

Wolock, D.M., and C.V. Price. 1994. Effects of digital elevation model map scale and data resolution on a topography-based watershed model. Water Resources Research 40:3041-3052.

Yocky, D.A. 1995. Image merging and data fusion by means of the discrete two-dimensional wavelet transform. Journal of Optical Society of America 12:1834-1841.

Zhang, W., and D.R. Montgomery. 1994. Digital elevation model grid size, landscape representation, and hydrologic simulations. Water Resources Research 30:1019-1028.

Zhou, J., D.L. Civco, and J.A. Silander. 1998. A wavelet transform method to merge Landsat TM and SPOT panchromatic data. International Journal of Remote Sensing 19:743-757.

CHAPTER 7

SUMMARY, CONCLUSIONS AND RECOMMENDATIONS

7.1.   SUMMARY AND CONCLUSIONS

Accurate information on the spatio-temporal distribution of the energy balance components (net surface radiation (R_n), soil heat flux (G), sensible heat flux (H) and latent heat flux (LE)) in arid riparian areas is critical knowledge for agricultural, hydrological and climatological investigations. Perhaps the most widely used energy balance component is the latent heat flux (evapotranspiration) because the amount of evapotranspiration is not only directly related to plant growth and carbon uptake but is also an important hydrological component affecting soil moisture, runoff, ground water recharge and atmospheric circulation. At different spatial scales, we have an interest in water use per field, per riparian unit, per range unit, per catchment and per entire river basin. At different temporal scales, we have an interest in daily and weekly water use for irrigation management, riparian vegetation, and range management as well as in seasonal and annual water budgets and in variability for long-term sustainable water management in large watersheds.

However, the distribution of surface fluxes over large areas is difficult to obtain from ground measurements alone since it is influenced by various parameters including soil type, soil moisture, plant type and development stage, and weather conditions. Therefore prediction of surface fluxes from remote sensing data is very attractive as it enables large area coverage and a high repetition rate. In this study, a cost-effective and fast remote sensing image processing technique, SEBAL, was selected to estimate all the energy balance components in the arid/semi-arid riparian areas of the Middle Rio Grande Basin (New Mexico), San Pedro River (Arizona), and Owens Valley (California).

Various types of remotely sensed images of the Earth's surface via satellite sensors provide information for estimation of the spatio-temporal distribution of land surface parameters. The spatial resolution of predictions from remote sensing imagery exclusively depends on the sensor type and there exists a trade-off between spatial and temporal resolution. The major problem with high spatial resolution satellite images like Landsat 7 is that imagery is not available very often (i.e. every 16 days or longer) and the coverage area is relatively small (swath width 185 km), while satellites of lower spatial resolution like MODIS are revisiting the same part of the earth more often (daily) and one image covers a relatively large area (swath width 2,330 km). Landsat 7 bands have spatial resolutions of 30 to 60 m, while MODIS bands have resolutions of 250, 500 and 1000 m.

Coarse resolution images like MODIS provide useful opportunities to monitor the surface conditions at meso-scale with manageable amounts of data; however, they cannot directly provide detailed field-specific data. For the purpose of monitoring land cover changes accurately, thermal band pixels of size less than 500 m are required. Therefore, down-scaling (disaggregation) from MODIS to Landsat scale is a very useful technique to combine the advantages of high temporal and spatial resolutions of surface conditions.

There exists a spatial resolution gap between the data requirements of regional-scale models and the output data from remote sensing energy balance algorithms such as SEBAL. For example, general circulation models or regional weather prediction models need input data with a spatial resolution of tens or hundreds of kilometers which is much larger than the spatial resolution of most satellite sensors. Therefore, an up-scaling (data aggregation) procedure is needed to fill the scale gap between satellite measurements and input requirements for large scale models.

The main objective of this study was to investigate the potential and limitations of remote sensing for the assessment of spatio-temporal distributions of surface energy balance components in the southwestern United States using optical imagery from Landsat and MODIS satellites. This study has compared instantaneous and daily SEBAL fluxes derived from Landsat 7 and MODIS images to surface-based measurements with eddy covariance flux towers; it also has investigated the effect of up- and down-scaling processes on the spatial distribution of evapotranspiration maps derived from SEBAL,

especially how the relative accuracy of evapotranspiration varies with different up- and down-scaling processes.

SEBAL yields reliable estimates for energy balance components at high spatial resolutions in heterogeneous riparian areas in the southwestern United States. The comparison study between SEBAL estimates of the energy balance components and ground measurements resulted in two main conclusions. The first one is that ground measurements of sensible heat flux should be used carefully for the calibration and validation of SEBAL in order to arrive at unbiased estimates of latent heat flux since the SEBAL sensible heat flux is biased and deviates from the ground measured sensible heat flux. The second conclusion is that SEBAL's internal calibration procedure is its greatest strength since it eliminates most bias in latent heat flux albeit at the expense of increased bias in sensible heat flux.

From the up-scaling study, I conclude that the output simple averaging method produced aggregated data with the most statistically and spatially predictable behavior among the four up-scaling methods compared. The input nearest neighbor method was the least predictable but was still acceptable. Overall, the daily evapotranspiration maps over the Middle Rio Grande Basin aggregated from Landsat images were in good agreement with evapotranspiration maps directly derived from MODIS images. In addition, good agreement exists between SEBAL estimated daily evapotranspiration maps on the same date directly derived from Landsat 7 and MODIS images, which confirms the consistency of the SEBAL algorithm for different satellite imagery.

From the down-scaling study, I conclude that all of the 12 proposed down-scaling methodologies can generate reasonable spatial patterns of the disaggregated evapotranspiration map. Georeferencing disagreement between Landsat and MODIS images is the most significant issue for the application of the down-scaling schemes suggested in this study. The regression method is less vulnerable to the georeferencing difference than the subtraction method and the difference in down-scaled ET maps between input and output down-scaling schemes was not significant. Among the 12 different down-scaling schemes, output down-scaling with regression between two MODIS-based images is the best scheme and input down-scaling with subtraction between MODIS and aggregated (nearest neighboring) Landsat is the worst scheme.

Finally, the spatio-temporal distributions of the surface energy balance components mapped in this study will provide useful information for water resources management as input and validation data sets for climate and hydrological models for understanding and predicting the global ecosystem and climate changes. Moreover, identifying up-scaling as well as down-scaling effects on statistical and spatial properties of spatial data can help to understand the characteristics of aggregated and disaggregated data sets.

7.2. RECOMMENDATIONS

The following section lists topics for further investigations for the advancement of our ability to estimate energy balance components using the remote sensing model SEBAL.

(1) Automatic implementation of the SEBAL model

This study indicates that the correct selection of the temperatures of the cold and hot pixel (anchor pixels) is the most critical step in the entire SEBAL process. An error of a few degrees in K will cause serious distortion of the distribution of the H and LE over an image. The selection of anchor pixels requires a thorough understanding of field micrometeorology and is somewhat subjective, i.e. different experts will select slightly different temperature values. Results of this study show that there is no significant difference in SEBAL products using the EC approach (selection of anchor pixel is calibrated using ground measurements) and EM approach (selection of anchor pixel is based on inspection of the hydrogeological features of the landscape and micrometeorological considerations as well as statistical relationship between surface parameters). Sound statistical relations among surface temperature, NDVI and albedo values inside of the image indicate a possibility for selection of anchor pixels in an automatic way. Since the selection of hot and cold pixel requires considerable knowledge and experience, the automatic implementation of SEBAL would be advantageous for users without such training or for the continuous automatic analysis of images in real time.

(2) SEBAL ET estimation in mountainous complex terrain

Quite a few studies, including this study, have used satellite imagery to estimate ET by using different modeling techniques with successful results over relatively flat areas including agricultural fields, riparian areas and semiarid rangeland basins. However, few studies have been conducted in mountainous complex terrain mainly because insufficient ground observations are available for model validation. The Valles Caldera National Preserve (VCNP) in New Mexico is a prime site for this type of study since VCNP represents a heterogeneous mountaneous region where direct ground measurements of heat fluxes from eddy covariance towers and scintillometers are available since 2006.

(3) SEBAL application in other environments

This study has confirmed that SEBAL accurately estimates the ET of heterogeneous semi-arid riparian areas in the southwestern USA. Its strong performance in this challenging environment suggests that SEBAL should perform well in most other environments. However, further studies are necessary to test the SEBAL approach under different climate/land conditions such as temperate climates and the humid tropics. For example, Dr. Hendrickx's research group is active with SEBAL applications in (1) the White Volta Basin with a tropical climate characterized by six months without and six months with rain, (2) the Panama Canal Watershed with a humid tropical climate, (3) Wyoming with a cold semi-arid climate, and (4) Michigan with a humid continental climate. Examples of different land surfaces in and outside of New Mexico in need of

further investigations are urban areas, water bodies, deserts, basalt flows, snow covered

ground, tropical vegetation, and bare soils. Of special interest in these areas is the further

development of algorithms for evaluation of R_n and G as well as the quantification of the

dT-T_s relationship for H estimation. An important criterion for the selection of new test

sites is that the availability of reliable ground measurements. Therefore, Dr. Hendrickx's

research group has installed 7 scintillometers and is measuring sensible heat fluxes in

agricultural fields, desert, mountain and basalt areas in New Mexico. These scintillometer

readings will be used to calibrate and validate SEBAL estimated surface fluxes.

(4) Comparison of SEBAL products from MODIS against scintillometry

There exist a scale disparity between the ground measurement of H and LE and

the spatial resolution of remote sensing images. While the spatial length scale of remote

sensing images covers a range from 60 m (Landsat), to 1000 m (MODIS) and 4000 m

(GOES) in the thermal band, direct methods to measure H and LE such as eddy

covariance (EC) and Bowen ratio (BR) only provide point measurements at a scale that is

considerably smaller than the estimate obtained from a remote sensing method. Therefore,

in order to validate MODIS products against ground measurements, the products of high

resolution remotely sensed imagery such as Landsat need to be first validated with

ground point measurements. MODIS products can then be compared against up-scaled

(aggregated) Landsat products. However, recent progress in scintillometry makes it now

possible to measure heat fluxes at footprint dimensions from 100 to 10,000 m.

Scintillometers are able to measure the vertical fluxes averaged over large areas (up to

about 5 MODIS thermal pixels), so coarse-resolution images can be directly validated and calibrated using scintillometer readings.

(5) Direct ET estimation from land cover

In regional hydrological studies, it is not uncommon to make the assumption that land cover is directly related to ET. This assumption then makes it possible to derive regional ET estimates based on a land cover map. It is often the only feasible alternative to the establishment of an expensive region wide network of meteorological sensors. Study of ET estimation directly from land cover is feasible in the area of the Middle Rio Grande Valley because good-quality detailed land cover maps of this area are available. In order to construct a relation between land cover and ET, first ET maps derived from SEBAL can be converted to maps of crop coefficients by dividing the ET of each pixel by the weather-based reference ET determined from measurements at a representative weather station. After that the spatial and temporal distributions of the crop coefficients and ET can be evaluated for each land cover class for the derivation of meaningful relationships between ET and land cover.

(6) Comparison of SEBAL with other remote sensing models

Satellite image-based remote sensing for examining spatial patterns or regional estimates of *H* and *LE* has been investigated by a number of investigators (e.g. SEBS, ALEXI, METRIC). Each model differs in terms of the complexity of the algorithms used in computing energy flux exchange, equations used to calculate fluxes and ancillary data requirements. In order to compare the performance of each model, products from

different models applied in various environments need to be compared to each other as well as validated with ground measurements. This will provide an opportunity for improvements in the algorithms used by the various models.

(7) Comparison of SEBAL with hydrological/numerical models

Remote sensing techniques and hydrological models (e.g. tRIBS, SVAT, HYDRUS) are advanced tools that are suited to estimate the ET, soil moisture and related hydrological processes at the regional scale. For the development of a practical cost-effective method for ET prediction at a fine spatio-temporal resolution, it will be necessary to use hydrologic models that assimilate data provided by SEBAL or other remote sensing methods as well as ground measurements. Previous research by Hong (2002) showed that ET estimated by SEBAL in a riparian area of the Middle Rio Grande was in reasonable agreement with ET derived from HYDRUS-1D simulations. We can investigate further how hydrological models can be combined with SEBAL in order to improve the quality of the ET and other surface parameters.